University of Ferrara

Doctoral Course in Physics – Cycle XXXVIII

Coordinator: Prof. Paolo Lenisa

Deconfinement phase transition in dense matter

and its effects on the formation of compact stars

Scientific-Disciplinary Sector (SDS): FIS/02

Ph.D. Candidate

Mirco Guerrini

Supervisor

Prof. Alessandro Drago

Co-supervisor

Prof. Giuseppe Pagliara

Academic Years 2022–2025

Abstract

The behavior of strongly interacting matter at densities above nuclear saturation and the associated deconfinement phase transition, whereby quarks are no longer confined within hadrons, remain open problems of broad interest. Such extreme conditions may be realized in compact stars and in related astrophysical phenomena, including core-collapse supernovae (CCSNe) and binary compact star mergers (BCSMs)
Phenomenological scenarios for compact stars depend crucially on whether the unknown energy per baryon of strange quark matter (SQM), a deconfined quark phase composed of u, d, and s quarks, is smaller or larger than that of iron in bulk at zero pressure and temperature, *i.e.*, whether SQM is absolutely stable or not. In the standard case where SQM is not absolutely stable, sufficiently high central densities may produce deconfined quark matter in the core, yielding *hybrid stars*, whereas stars with lower central densities remain purely hadronic neutron stars (NSs). Alternatively, the Bodmer–Witten hypothesis proposes that bulk hadronic matter is metastable under all conditions, while SQM is the absolute ground state. The two phases are separated in the space of configurations by an energy barrier that prevents the spontaneous decay of hadronic matter into SQM under ordinary conditions. If this hypothesis holds, a family of metastable NSs and a family of stable strange quark stars (QSs) may coexist, leading to the *two-families* scenario.

In this thesis I investigate the deconfinement phase transition in compact stars from two perspectives.
First, in the context of the one–family scenario, I develop a thermodynamically consistent framework for first–order phase transitions in multi–component matter that interpolates continuously between local and global electric charge neutrality. The resulting mixed–phase equation of state allows one to tune the strength and extent of the transition in a controlled manner and can be implemented directly in astrophysical simulations, thereby enabling systematic studies of how varying the transition properties in a thermodynamically consistent way affects astrophysical observables.
Second, I focus on the two–families scenario and on the decay of the metastable hadronic phase via nucleation which triggers the conversion of NSs into QSs. I formulate a nucleation scheme for SQM that incorporates strong–interaction constraints, local thermal fluctuations of the hadronic composition, a reduced–volume prescription for finite–time transport, and the effects of color superconductivity in the quark phase. This framework is applied to proto-neutron stars and to accreting compact binaries to identify the thermodynamic conditions under which NSs convert into QSs and how such conversions could manifest as delayed energetic transients. A qualitative application to CCSNe of massive progenitors is also discussed.

Table of Contents

Introduction

The behavior of strongly interacting matter under extreme conditions is a central open problem in contemporary nuclear physics and astrophysics. Quantum Chromodynamics (QCD) predicts that at low temperatures and low baryon densities, quarks and gluons are confined inside hadrons, whereas at sufficiently high temperatures or densities, they form a deconfined phase in which color is no longer confined. Between these two regimes, a transition region must exist where hadronic matter rearranges into deconfined quark matter [1, 2]. However, the location and nature of this transition at high baryon density remain unknown.

The QCD phase diagram is typically represented in the plane spanned by temperature and baryon chemical potential (or baryon number density), but in reality it is a multidimensional space that depends on several conserved charges, including baryon number, electric charge and strangeness. Different physical environments follow different trajectories in this multidimensional space and therefore correspond to different projections onto the usual two–dimensional diagram. As a consequence, the state that plays the role of the ground state within each sector (fixed set of conserved charges) at zero temperature and pressure can differ across projections. While in the zero–strangeness sector, the ground state at zero pressure and temperature is ordinary nuclear matter, this is not necessarily the case in projections where strangeness is allowed to equilibrate. In particular, the Bodmer–Witten hypothesis [3, 4] proposes that bulk strange quark matter (SQM), composed of up, down and strange quarks in weak equilibrium, could be more stable than bulk ordinary nuclear matter at zero pressure and temperature. In that case, hadronic matter would not be the global ground state, but rather a metastable phase separated from the SQM ground state by an energy barrier in configuration space. Whether this hypothesis is realized in nature has profound implications for both astrophysics and cosmology.

The high–density, low–temperature region of the phase diagram cannot be accessed directly by lattice QCD because of the sign problem, and it is not reproducible in terrestrial experiments. The only known systems that probe this regime are compact stars and related high–energy astrophysical phenomena. In the cores of compact stars, baryon densities reach several times nuclear saturation density at temperatures that are small on hadronic scales. During binary compact-star mergers, core–collapse supernovae and the early evolution of proto–neutron stars, matter can reach comparable densities at temperatures up to tens of MeV [5]. Cold, isolated compact stars therefore explore the nearly zero–temperature slice of the phase diagram, while mergers, proto–neutron stars and supernova cores populate finite temperature regions. In this sense compact objects serve as natural laboratories for QCD at high density.

The phenomenology of compact stars depends crucially on the realization of the deconfinement transition and on the stability of SQM. In the standard picture, SQM is not absolutely stable: at low density the ground state is hadronic, and deconfined quark matter appears only above a critical density, forming a quark core inside an otherwise hadronic star. Objects with a quark core are usually referred to as hybrid stars (HSs), and together with purely hadronic neutron stars (NSs) they form a single family in the mass–radius diagram described by a single equilibrium EOS. In this one–family scenario the main open question is the detailed structure of the hadron–quark transition and its impact on the equation of state (EOS).

If the Bodmer–Witten hypothesis holds, the picture changes qualitatively. In this case, SQM is absolutely stable, and all hadronic configurations are, in principle, metastable. Compact stars entirely composed of deconfined SQM, self–bound by the strong interaction, can then exist and are referred to as strange quark stars (QSs) [6, 7]. Whether a hadronic star actually converts into a QS depends on whether the conditions required to overcome the barrier separating the two phases are met during its evolution. If conversion is highly efficient, essentially all compact stars would eventually become QSs. If conversion is possible only for part of the population, a family of metastable NSs could coexist with a family of stable QSs. This is the so–called two–families scenario [8–10], in which the compact-star population consists of two distinct branches: one of NSs described by a metastable hadronic EOS, and one of absolutely stable QSs described by a stable SQM EOS, differing in radii, internal composition and maximum mass.

Multi–messenger observations in the last decade have begun to probe the structure of compact stars with increasing precision. Precise mass measurements of radio pulsars [11–13] indicate that some compact stars reach and exceed 2 $M_\odot$, requiring a sufficiently stiff EOS at high densities. At the same time, gravitational wave observation of binary compact stars merger GW170817 [14, 15], combined with X–ray timing of pulsars [16], suggest a comparatively soft EOS at intermediate densities, in agreement with constraints from heavy–ion collisions [17]. Additionally, intriguing, albeit debated, measurements, such as the extremely low mass inferred for HESS J1731–347 [18] and the nature of the secondary component of GW190814 [19], which lies in the mass gap between compact stars and black holes, further complicate the picture. Yet the available data do not single out a unique scenario: one–family models of compact stars, with [20, 21] or without [22] a deconfined quark core, as well as two–families models [8] with distinct NS and QS branches, remain viable. In particular, in the two–families scenario the tension is naturally resolved: NSs are characterized by a soft EOS, with a maximum mass below 2 $M_\odot$ and relatively small radii, whereas QSs possess a much stiffer EOS, capable of supporting maximum masses well above 2 $M_\odot$ [9, 10]. In contrast, in the one–family scenario, the observational constraints require a single equilibrium EOS that is comparatively soft at intermediate densities (*e.g.* due to the onset of quarks [21], hyperons [23] and/or attractive interactions) but stiffens again at higher densities (*e.g.* through repulsive interactions between hadrons [23–25] and/or quarks [21, 26]). Future constraints will increasingly probe the presence or absence of deconfined matter in compact stars.

To interpret the growing body of present and future data, it is not sufficient to establish whether deconfinement occurs; rather, one must also understand its detailed characteristics. In particular, in the high–density regime, the deconfinement transition may be

a genuine first–order phase transition (the case investigated in this thesis) [20, 27] or it may proceed as a smooth crossover [2]. In equilibrium, a first–order phase transition between a hadronic phase and a quark phase proceeds through the appearance of a mixed phase in which the two phases coexist. The detailed structure of this mixed phase depends on which charges are conserved globally and which are enforced locally. In many applications, only the baryon number is treated as a globally conserved quantity, while electric charge neutrality is imposed separately in each phase. This corresponds to the classical Maxwell construction and results in a sharp transition with constant pressure across the mixed phase (sometimes referred to as a strong first-order phase transition) [20, 27]. If electric charge is instead allowed to rearrange between the phases while only the overall charge neutrality is constrained, one obtains a Gibbs construction [20, 27] with a mixed phase in which the pressure varies smoothly (sometimes referred to as a weak first-order phase transition). In high-energy astrophysical environments, additional conserved charges, such as lepton number or the non–leptonic electric charge fraction, can be relevant [5, 28]. The corresponding equilibrium conditions modify the extent and properties of the mixed phase and, consequently, the global structure and stability of compact stars.

Even when the equilibrium conditions are known, they do not fully determine the dynamics of the transition. If there is a nonzero surface tension between the phases (namely, in first-order phase transitions), an energy barrier separates the hadronic and quark minima of the thermodynamic potential. The system can then remain trapped in the metastable hadronic state even when the quark phase is energetically favored. Conversion requires the decay of the metastable state via nucleation of a critical droplet of the new phase by a spontaneous fluctuation that overcomes the barrier [29, 30]. The nucleation rate depends on the height and shape of the barrier, as well as the transport properties of the medium. In the standard scenario, the metastability window may be relatively narrow, so nucleation mainly introduces a quantitative delay with respect to the equilibrium onset. In the two–families scenario, by contrast, hadronic matter is always metastable with respect to SQM, and nucleation is the only mechanism that determines when and where a hadronic star converts into a QS. Once a critical droplet has formed in this context, the subsequent conversion proceeds as a genuinely out–of–equilibrium, multi–stage process: the critical droplets grow and possibly merge, giving rise to a macroscopic deconfined region, and then to a conversion front that propagates through the star until a QS configuration is eventually reached [10, 31, 32]. Understanding nucleation is therefore essential for assessing the viability of the two–families picture and for identifying its potential observational signatures.

Deconfinement can, in principle, occur in a variety of astrophysical settings, and its manifestations differ between one–family and two–families scenarios. In binary mergers involving compact stars in the context of the one-family scenario, the remnant explores a wide range of densities and temperatures and may cross the hadron–quark transition line. Numerical–relativity simulations indicate that the detailed impact of deconfinement depends also on the strength (transition baryon density jump) and timing (transition baryon density onset) of the transition other than on the mere presence of quark matter: a very strong, early transition can drive rapid compactification and an early collapse to a black hole, while a strong but delayed transition may leave imprints on the post–merger gravitational–wave spectrum and on the lifetime of the remnant

[33]. In the two–families scenario the landscape is richer, because binaries can be composed of two NSs, two QSs, or a mixed NS-QS system [34]. In this case, the inspiral and merger dynamics reflect the coexistence of two distinct stellar families.

Core–collapse supernovae provide another promising site for deconfinement. In the early post–bounce phase, the central density and temperature of the proto–neutron star may reach the conditions for a deconfinement transition. Within the one–family scenario, the appearance of a mixed hadron-quark phase leads to a transient softening of the EOS, which can trigger a secondary collapse of the proto–neutron star. The subsequent restiffening of the EOS then produces a second bounce that may help to revive the stalled shock and lead to explosions of massive progenitors for which the standard neutrino–driven mechanism fails [35, 36]. In the two–families picture, the same conditions may instead trigger the nucleation of SQM in the core of an initially metastable hadronic proto–neutron star, followed by a rapid conversion into a QS. The associated release of gravitational binding energy may again contribute to the explosion, in a way that is qualitatively similar to the one–family case but with potentially different timescales, energetics and observable signatures. Moreover, if a hadronic proto–neutron star survives the standard neutrino–driven supernova explosion, the deconfinement phase transition leading to the formation of a HS (in the one–family scenario) or a QS (in the two–families scenario) can still occur during its subsequent evolution. In particular, deconfinement may be triggered as the star approaches its maximum temperature and undergoes deleptonization, roughly ten seconds after the explosion, before it has fully cooled [37].

Accreting systems offer yet another channel for deconfinement. In binaries where a NS accretes mass from a companion, the gradual increase in central density can eventually push the core into a deconfinement regime. In the one–family scenario, this typically results in the gradual growth of a quark core and in continuous, relatively modest changes in the stellar structure. In the two–families scenario, by contrast, accretion can push a metastable hadronic star over the nucleation threshold, triggering a conversion to a QS long after the original supernova. Such delayed conversions can lead to energetic transients, sudden changes in spin or orbit eccentricity, or additional neutrino and gravitational–wave emission [9].

Exploring all these channels, in both scenarios, requires dynamical simulations that consistently couple the EOS, a realistic treatment of the deconfinement phase transition, and detailed microphysics. Despite substantial theoretical and numerical efforts to identify robust, model–independent smoking–gun signatures of deconfinement in astrophysical systems related to compact stars, current observations have not yet provided unambiguous evidence for a hadron–quark phase transition. In the coming years, third–generation gravitational–wave detectors, such as the Einstein Telescope and Cosmic Explorer, will greatly increase the number and quality of observed events and may, for the first time, give access, *e.g.*, to post–merger signals that are particularly sensitive to the composition of strongly interacting matter [33]. In this context, it is essential to keep refining our modeling of dense matter by systematically exploring different EOSs, degrees of freedom, phases and out–of–equilibrium effects, and by quantifying their impact on astrophysical observables. The synergy between compact–star observations, heavy–ion experiments and constraints from the early Universe will be crucial for turning these future data into meaningful information on the QCD phase diagram.

The aim of this thesis is to contribute to this effort by developing and applying quantitative models of the deconfinement transition in dense matter and by investigating their consequences for the formation and evolution of compact stars. The work is organized around two complementary lines.

The first focuses on deconfinement in HSs and addresses how to describe a first–order phase transition in multi–component matter in a thermodynamically consistent way. In neutrinoless β–equilibrated systems (cold compact stars), the usual Maxwell and Gibbs constructions correspond to two limiting assumptions about charge neutrality: in the Maxwell case charge neutrality is enforced locally in each phase, whereas in the Gibbs case it is imposed only globally over the mixed phase [27, 38]. In many astrophysical applications, however, one expects an intermediate regime in which some fraction of the electric charge is effectively tied to each phase while the remainder can rearrange globally. Moreover, when β–equilibrium is not imposed and an additional globally conserved quantity is present (as in many astrophysical simulations where the electron fraction is treated as an independent EOS variable), a strict Maxwell construction is no longer a proper thermodynamic equilibrium solution [38], even if local charge neutrality is enforced. Nevertheless, simulations of core–collapse supernovae and binary compact-star mergers frequently adopt an effective Maxwell construction even when the EOS is tabulated in terms of the baryon density and a composition variable such as the charge fraction or the electron fraction [35, 36, 39]. In this situation, there are at least two globally conserved quantities, so enforcing phase coexistence through a Maxwell construction is thermodynamically inconsistent. The resulting transition is often artificially strong, with unphysically sharp jumps in pressure, and may therefore distort the predicted phenomenology if the evolution of the system is far from neutrinoless β-equilibrium.

A central motivation of this work is to develop a framework that enables control over the strength of the phase transition while maintaining full thermodynamic consistency. To this end, we introduce a general construction that interpolates continuously between local and global charge neutrality through a control parameter that quantifies the fraction of leptons participating in local versus global neutrality [40, 41]. The framework is based on free–energy minimization under the appropriate conservation laws and is applicable at finite temperature and in the presence of several conserved charges (*e.g.* both in and out of β-equilibrium). In the neutrinoless β–equilibrium regime, the standard Maxwell and Gibbs constructions are recovered as limiting cases of the mixed–phase EOS. The resulting effective EOS can be used directly in astrophysical simulations, permitting a controlled adjustment of the strength and extent of the phase transition in a thermodynamically consistent manner.

The second line of the thesis aims to investigate the decay of the metastable hadronic phase through nucleation and its implications for the two–families scenario. I will present a detailed description of the nucleation of SQM under conditions relevant for compact stars and related phenomena. The emphasis will be on the formation of the first critical droplet, while the subsequent macroscopic conversion of the star is beyond the scope of this work. The central question is whether a critical droplet of SQM can form within the stellar interior on the relevant timescales, thereby triggering the conversion of hadronic stars populating the QS branch of the mass–radius diagram.

The starting point is a thermodynamic description of nucleation in terms of an energy barrier in configuration space. The state of the system is characterized by the volume of the deconfined region (which, in a thermodynamic framework, plays the role of an order parameter) and by its thermodynamic properties, such as baryon density, charge fraction and strangeness fraction. A metastable hadronic configuration corresponds to a local minimum of the appropriate thermodynamic potential, while the fully converted SQM configuration corresponds to the global minimum. The critical droplet is identified with a saddle point of this potential: it is a maximum along the direction of the order parameter (the droplet volume) and a minimum along all other accessible directions [30]. The height and shape of the barrier determine how likely it is for spontaneous fluctuations to produce a droplet large enough to proceed to macroscopic conversion. The thesis discusses both thermal nucleation [30], in which the system overcomes the barrier through thermally induced fluctuations, and quantum nucleation [42], in which quantum tunnelling through the barrier becomes relevant.

The timescales of the relevant microscopic processes play a crucial role in determining which directions in configuration space are effectively accessible during the approach to the critical configuration. Fluctuations of the quark–droplet volume, being driven by deconfinement, proceed on strong–interaction timescales, which are many orders of magnitude shorter than those of weak processes. Within the nucleation window, strong interactions are therefore treated as active, while weak interactions are effectively frozen. This implies that the system can explore only configurations that respect the conservation laws associated with strong interactions. Under strong interactions, the conserved quantities are the baryon number, the non–leptonic electric charge and the strangeness, or equivalently the net numbers of up, down and strange quarks. Whether these conserved numbers are enforced locally within each phase or only globally across the whole system is a subtle issue. If the exchange of conserved numbers between the droplet and its surroundings is strongly inhibited, for instance by slow transport, the droplet composition is effectively "frozen" to that of the ambient hadronic matter. If, on the contrary, strong interactions and transport processes efficiently exchange quarks across the interface, the conserved numbers are shared globally, and the droplet composition can approach its own strong–interaction equilibrium. The literature brackets this uncertainty by analyzing two limiting prescriptions: a "frozen–flavor" limit, in which the droplet inherits the local composition of the hadronic phase, and a "strong–equilibrium" limit, in which the conserved numbers are allowed to redistribute globally between the phases.

The "frozen–flavor" approach is widely used in the literature on nucleation in compact stars [43, 44]. In addition, it assumes that the initial hadronic phase is compositionally homogeneous, *i.e.* that the local conditions coincide everywhere with the bulk averages. In this thesis, we relax this assumption and investigate the role of composition fluctuations in the initial hadronic phase [45, 46]: at the temperatures relevant for proto–neutron stars and merger remnants, the hadronic composition fluctuates around its bulk–equilibrium values. Since nucleation is a local process, the first critical droplet tends to form in those subregions whose instantaneous composition happens, by chance, to be more favourable to nucleation than the global average. This is captured by a "thermal–fluctuation" approach, in which fluctuations of the conserved charges in the initial hadronic phase are explicitly included in the construction of the barrier. In [45,

46] we assumed that all configurations compatible with the strong–interaction conservation laws are dynamically accessible, and showed that this prescription effectively converges to the strong–equilibrium limit. However, on the finite timescales relevant for compact–star evolution, not all thermodynamically allowed configurations need be dynamically accessible in practice. To account for these kinematic constraints, this thesis introduces a "reduced–volume" prescription, in which fluctuations and the exchange of conserved charges are allowed only within a finite reservoir surrounding the droplet. This construction interpolates between the frozen–flavor and fluctuation–assisted limits.

Moreover, I will also discuss how electric charge neutrality, Coulomb effects, charge screening, and color superconductivity in the quark phase modify the structure of the critical droplet and the resulting nucleation conditions.

The nucleation formalism will be applied to a set of astrophysical scenarios. A general strategy is proposed to combine astrophysical simulations, or simplified evolutionary models, with the nucleation framework developed in this thesis. For each thermodynamic trajectory, one can compute the nucleation rate as a function of time and determine whether, and when, a critical droplet is likely to form. In the absence of full simulations, a useful alternative is to compare the nucleation timescale (the typical time after which a nucleation event is statistically expected under given conditions) with the dynamical evolution timescale of the system (the time over which the thermodynamic conditions can be regarded as approximately constant).

In particular, the fluctuation–assisted approach with a framework that includes color superconductivity, is first used to study the evolution of proto–neutron stars and to assess the conditions under which they can convert to QSs before cooling and deleptonization. The results have direct implications for the possible coexistence of NSs and QSs.

Subsequently, the reduced–volume approach is explored qualitatively to discuss whether a hadronic NS that survives the proto–neutron star phase can later convert by mass accretion, after it has already cooled and deleptonized.

A simplified nucleation prescription is then employed in simulations of CCSNe in compact binaries, where a newborn NS and its NS companion accrete matter from the supernova ejecta [47]. If nucleation conditions are reached during the minutes–long accretion phase, one or both NSs convert into QSs, yielding NS–NS, NS–QS, or QS–QS remnants and releasing energy well after core collapse. This offers a concrete example of how delayed deconfinement in compact binaries could power energetic transients in the two–families scenario. Finally, the thesis qualitatively discusses a speculative application in the context of the two–families scenario, namely deconfinement–powered explosions of very massive progenitors, with a mechanism inspired by that proposed for the one–family scenario.

This work is organized as follows. Part I provides the general background. Chapter 1 reviews the present understanding of strongly interacting matter and the QCD phase diagram, introduces the Bodmer–Witten hypothesis and the one–family and two–families scenarios for compact stars, and summarizes the main constraints from multi–messenger astronomy. It also gives a qualitative overview of equilibrium phase

coexistence, metastability and nucleation, and of the phenomenology of deconfinement in astrophysics. Chapter 2 presents the EOS models used throughout the thesis for hadronic matter, deconfined quark matter, leptons and thermal bosons, and explains how they are combined into total homogeneous phases.

Part II is devoted to deconfinement in hybrid stars. Chapter 3 introduces the new framework for first–order phase transitions with partially local and partially global charge neutrality, and explores its consequences for mixed phases.

Part III focuses on deconfinement in the two–families scenario. Chapter 4 develops the nucleation formalism for the decay of the metastable hadronic phase into SQM, including the effects of flavor composition fluctuations, electric charge and color superconductivity. Chapter 5 applies this formalism to astrophysical systems, and discusses the implications for the formation of QSs and for possible observational signatures.

Technical details and complementary material are collected in the appendices. Appendix A summarizes the derivation of phase–equilibrium conditions for first–order transitions in multi–component systems. Appendix B recalls the Tolman–Oppenheimer–Volkoff equations used to compute stellar structure. Appendix C describes the numerical treatment of the relativistic Fermi and Bose integrals that enter the thermodynamic calculations.

Throughout this thesis, we will use natural units in which $\hbar = c = 1$. Moreover, we set $k_B = 1$.

Part I

General Background

Chapter 1

Background and motivation

This chapter introduces the physical context and the motivations of this thesis. We first recall the present understanding of strongly interacting matter at finite temperature and baryon density, with particular attention to the structure of the QCD phase diagram and to the possibility that strange quark matter is the absolute ground state. We then move to astrophysical systems in which such extreme conditions are realized. Finally, we review the theoretical description of the deconfinement transition in dense matter (equilibrium constructions, metastability and nucleation) and we outline the main channels in which deconfinement may occur in astrophysics, thereby setting the stage for the results presented in the following chapters.

1.1 Strongly interacting matter

The strong interaction among quarks is mediated by gluons and, within the Standard Model, is described by Quantum Chromodynamics (QCD), a non-Abelian gauge theory with local symmetry group $SU(3)_{\text{color}}$. Because gluons themselves carry color charge, they self-interact, introducing an essential nonlinearity that drives many of QCD's characteristic phenomena.

A central consequence of QCD's non-Abelian structure is the scale dependence of the coupling: the strong coupling "runs" with the momentum scale. At large momentum scales (short distances), the coupling decreases logarithmically (*asymptotic freedom*) and perturbation theory becomes reliable. Conversely, at low momentum scales (large distances), the coupling increases, rendering the dynamics intrinsically non-perturbative. This behavior may be intrinsically linked to *confinement*: the empirical observation that isolated colored states (quarks and gluons) are not found as physical asymptotic states in the vacuum.

For the light flavors, the QCD Lagrangian is approximately chirally symmetric. In the vacuum, however, chiral symmetry is *spontaneously broken* by the formation of a quark–antiquark condensate $\langle \bar{q}q \rangle \neq 0$. This mechanism acts to generate large constituent quark masses and gives rise to (nearly) massless Nambu–Goldstone bosons (pseudoscalar octet, *e.g.* pions). In this sense, the masses of hadrons are dominated

by dynamical QCD effects rather than the small current quark masses.

Beyond chiral symmetry, the QCD vacuum also breaks *scale* (dilatation) symmetry through the trace anomaly: the nonzero expectation value of the gluon operator $\langle F^a_{\mu\nu} F^{\mu\nu}_a \rangle$ defines a gluon condensate and a non-perturbative vacuum energy density.

These fundamental properties imply that the relevant degrees of freedom in strongly interacting matter are environment-dependent. At low temperature and baryon density, hadrons are the appropriate quasiparticles: strong correlations bind three quarks into color–singlet baryons and quark–antiquark mesons. As density (or temperature) increases, however, hadronic correlations weaken and quark wave functions begin to overlap. This allows colored constituents to propagate over distances exceeding the typical hadronic scale, and the medium enters a deconfined regime in which quarks and gluons become the relevant degrees of freedom, possibly through a phase transition. At low T and high baryon density, attractive color–magnetic interactions are expected to promote diquark pairing, $\langle qq \rangle \neq 0$, leading to a phase of color superconductivity.

For a comprehensive review of fundamental QCD properties and symmetries, see [1, 2] and references therein.

1.1.1 The QCD Phase Diagram

In summary, strongly interacting matter spans a range of regimes, from a confined, chirally broken hadronic phase at low temperature and baryon density to a deconfined regime with (approximate) chiral restoration as temperature and/or baryon density increase. These states are conventionally organized in the QCD phase diagram: a two–dimensional plot in the temperature–baryon chemical potential $T - \mu_B$ plane indicating the bulk equilibrium phase at given conditions (Fig. 1.1). It is crucial to keep in mind, however, that this is only a *projection* of a higher–dimensional variable space spanned by all conserved charges [48, 49], typically baryon number, electric charge (or isospin) and strangeness (μ_B, μ_C, μ_S), if only the three light quark flavors u, d, s are considered. The slice considered depends on the physical constraints: in heavy–ion matter one usually follows the strangeness–neutrality condition $Y_S = 0$ (where $Y_k = N_k/N_B$ is the fraction of the conserved charge k) with near–isospin symmetry $Y_C \simeq 0.4 - 0.5$, whereas in cold, weak–equilibrated matter (e.g., compact stars) a finite strangeness fraction can exist and charge neutrality together with β equilibrium relate μ_C to the baryon and lepton chemical potentials. Consequently, the apparent location and even the nature of boundaries in the (T, μ_B) plane are slice–dependent.

Knowledge of the diagram is anchored by several regimes where theory and experiment are under quantitative control. At the origin (T=0, μ_B=0) lies the vacuum with confinement and spontaneous chiral–symmetry breaking, characterized by nonzero quark and gluon condensates. Moving along the μ_B axis at $T \simeq 0$, the next anchor is bulk nuclear matter: at zero pressure the baryon chemical potential equals the energy per baryon of nucleons, $\mu_B \simeq 930$ MeV, and the equation of state up to a few times nuclear saturation density $n_0 \simeq 0.16$ fm^{-3} is constrained by chiral effective field theory [50, 51]. Along the temperature axis at $\mu_B \simeq 0$, *ab initio* lattice QCD demonstrates that the hadron–quark transition is a smooth crossover, not a true phase transition, with a

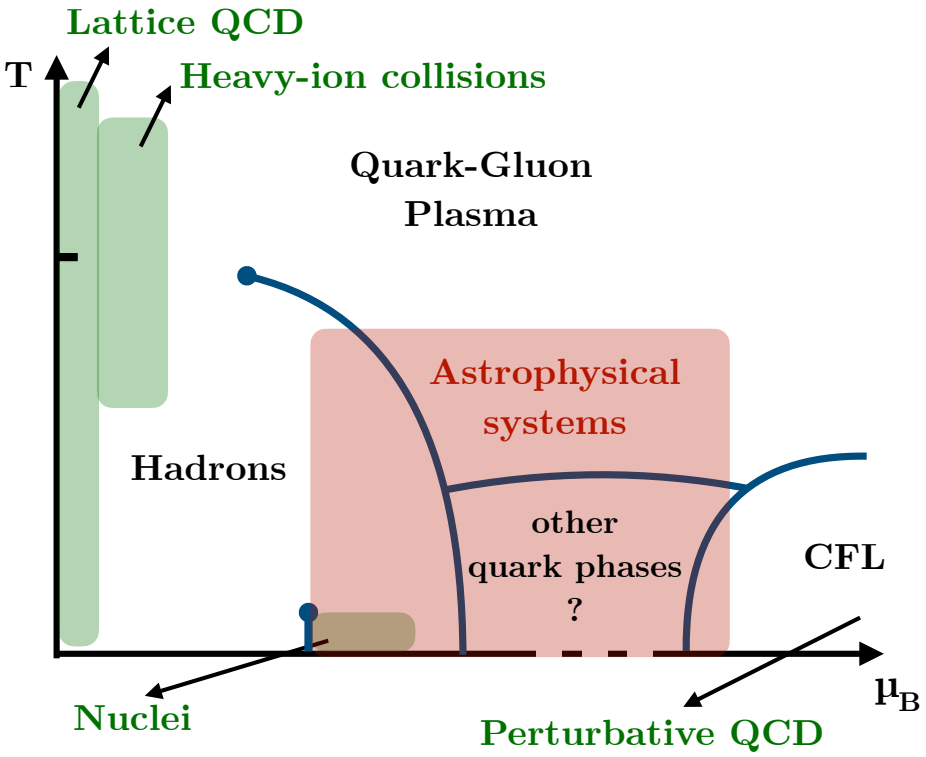

Figure 1.1: A schematic representation of the QCD phase diagram in the (T, μ_B) plane, showing the hadronic phase, the Quark-Gluon Plasma, and the Color Superconducting phases. The potential location of a first-order phase transition line ending in a Critical Point is also indicated.

pseudo–critical temperature $T_c \simeq 158$ MeV [52]. This sector is probed experimentally by high–energy heavy–ion collisions (RHIC/LHC) [53] and was realized in the early universe, where $\mu_B \approx 0$.

In the opposite corner, at $T \simeq 0$ and asymptotically large μ_B, asymptotic freedom renders perturbative QCD reliable: cold quark matter is deconfined and (approximately) chirally restored. Moreover, the one–gluon–exchange interaction is attractive in some channels and thus favors diquark pairing, leading to color–superconducting phases. The particular pairing pattern that minimizes the free energy depends on quark flavors and colors. For sufficiently high densities where three light quark flavors (u, d, s) are all present and nearly massless, the most energetically favored pairing pattern is the *Color-Flavor Locked* (CFL) phase. A complete review on the color-superconducting phases can be found in [54].

Finally, the broad intermediate region between these anchors remains uncertain. Theoretically, it is challenging because the *sign problem* renders direct lattice QCD simulations inapplicable at large μ_B. Progress is made by lattice QCD extrapolations from $\mu_B = 0$ (via Taylor expansions), which constrain the curvature of the crossover line [52], and the use of effective models and other functional methods (as will be discussed in Chapter 2). A widely discussed conjecture is that this region contains a first–order line at low T terminating at a critical endpoint; both the existence and the location of such a point are still open and depend on the chosen projection.

Heavy–ion beam–energy–scan programs probe the low and intermediate μ_B, high–T corner of this domain [53]. By contrast, the low–T, high–density regime is not reproducible in the laboratory and is realized only in high–density astrophysical environments: matter above nuclear saturation density exists in the interiors of compact stars, while comparable (or higher) densities together with high temperatures are transiently achieved during core collapse and in compact–binary mergers (see Sec. 1.2). These systems therefore serve as natural laboratories for probing strongly interacting matter at large baryon density and for investigating the deconfinement transition in this regime [55, 56].

1.1.2 Witten hypothesis

Since the usual (T, μ_B) diagram is only a projection of the full space of chemical potentials, one must specify which conserved charges are allowed to equilibrate when discussing the ground state at T=0 and P=0. Different choices of conserved charges (baryon number, electric charge, strangeness) define different sectors, each with its own lowest–energy state.

The Bodmer–Witten hypothesis [3, 4] posits that bulk three–flavor quark matter composed of up, down, and strange quarks (*strange quark matter*, SQM) in weak equilibrium could be the absolute ground state of strongly interacting matter. Concretely, the energy per baryon of bulk SQM at zero temperature and pressure would lie below that of the most stable nucleus (see Fig. 1.2),

$$E/N_B\Big|_{\mathrm{SQM}}(P=0,T=0) \;<\; E/N_B\Big|_{^{56}\mathrm{Fe}}(P=0,T=0) \;\simeq\; 930 \;\; \mathrm{MeV}. \tag{1.1}$$

In this picture, ordinary confined nuclear matter is not the absolute ground state of cold strongly interacting matter but a long–lived *metastable* configuration (a local energy minimum) separated from the SQM ground state by an energy barrier in the configuration space. Even if bulk SQM were energetically favored over bulk nuclear matter, not all intermediate configurations and not all finite systems are: finite–size effects (*e.g.* surface tension) raise the energy of small droplets, so the path in configuration space is not monotonically downhill. For example, at $T = P = 0$ the production of a single s quark via a weak process does not lower the energy of ordinary nuclear matter, since hyperons are heavier than nucleons; hence a sequence of isolated weak decays does not provide a downhill route to SQM. Reaching the three–flavor state would require the collective conversion of many u and d quarks into s quarks. Converting an iron nucleus into SQM with the same baryon number ($N_B = 56$) would entail an extremely high–order weak process (effectively the simultaneous flavor change of many quarks) with negligible probability. Conversely, at very small N_B the required weak order is lower, but the produced strangeness is typically insufficient to overcome finite–size penalties, so the strange droplet remains energetically disfavored [57].

Therefore, absolute stability of SQM does not conflict with the existence of ordinary nuclei in nature, since a significant fraction of strange quarks is required, and even if the SQM state were more energetically favorable than ordinary nuclear matter in bulk, the path in the configuration space would not be easily crossed.

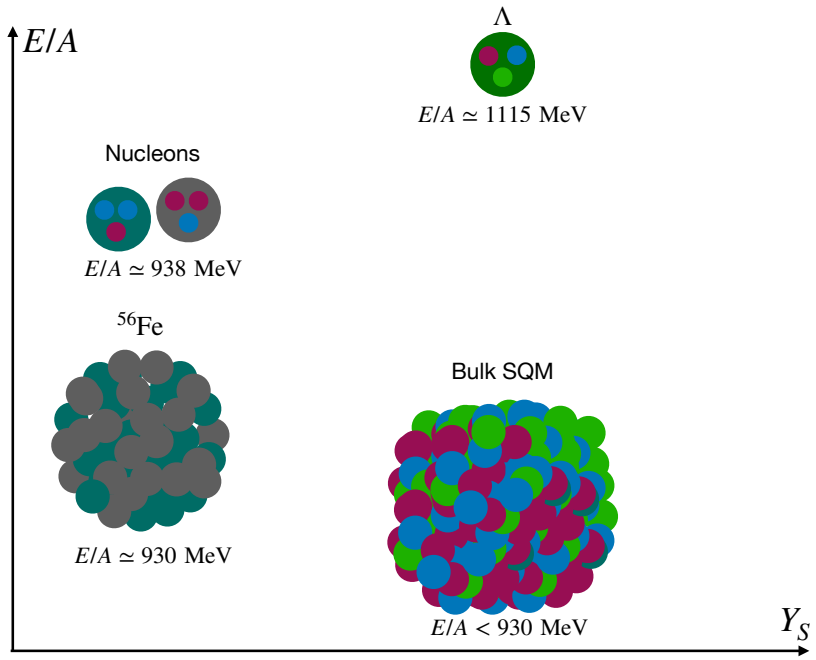

Figure 1.2: A schematic representation of the energy per baryon of different states of strongly interacting matter, having different strangeness fraction. See the text for the details.

Under the Bodmer–Witten hypothesis, the low–T structure of the phase diagram is qualitatively reshaped. For any finite baryon density n_B (equivalently, μ_B larger than the energy per baryon of the most stable phase), the energetically favored state is deconfined quark matter (SQM in particular) rather than confined hadronic matter. The hadron–quark first–order line usually drawn at low T is then not a boundary between *equilibrium* phases; instead, the only genuine $T \simeq 0$ transitions are within quark matter (*e.g.* from unpaired to superconducting phases [54] or among crystalline/partially gapped phases [58]), governed by pairing, neutrality, and flavor–mass effects [1].

Analyses in the literature identify parameter windows where the Bodmer–Witten criterion can be satisfied. In bag–like models [59], for α_s=0 and m_s=150 MeV, one requires 144 MeV $\lesssim B^{1/4} \lesssim$ 162 MeV, where the lower bound ensures two–flavor quark matter is unstable and the upper bound ensures bulk SQM is absolutely stable. For larger m_s the upper bound decreases; increasing α_s shifts both bounds to lower values [59, 60]. Diquark pairing further enlarges the stability window: within bag–like models, a larger pairing gap raises the allowed upper bound on B. Thus, the absolutely stable SQM phase could be either unpaired or color–superconducting.

The consequences of this hypothesis are far-reaching, with potential signatures in cosmology and astrophysics. For instance, macroscopic SQM nuggets (strangelets) formed in the early Universe and surviving to the present could account for a fraction of the dark matter [61, 62].

In Sec. 1.2.2 we discuss the implications for compact-star astrophysics.

1.2 Compact stars and astrophysical systems

The extreme densities and temperatures required to produce deconfined quark matter through a high-density QCD phase transition are rare in the Universe and can be realized only in a few astrophysical environments [56]. Densities above nuclear saturation naturally occur in compact stars (CS). Temperatures of several tens of MeV are reached during the collapse of the core of a massive star, where a core–collapse supernova (CCSN) explosion [5] gives rise to a hot, proto–neutron star (PNS) [63], which subsequently evolves into a cold CS or collapses to a black hole (BH). Comparable densities and temperatures are also obtained in the binary compact–star mergers (BCSMs) systems [64].

This section outlines the primary theoretical scenarios for compact star composition, the central puzzles, the key multi-messenger constraints and phenomenological signatures.

1.2.1 Astrophysical systems in the QCD phase diagram

Cold, isolated CSs [65] provide the cleanest thermodynamic setup. All relevant equilibria are attained: matter is in neutrinoless β equilibrium ($\mu_{\nu_e} = 0$), electric charge neutrality is enforced, and strangeness–changing weak reactions have equilibrated so that $\mu_S = 0$. In this regime, the EOS depends on a single control variable (either n_B or μ_B), and the structure of a non–rotating star follows from the TOV equations (Appendix B).

PNSs are one of the possible CCSN remnants and evolve on a timescale of tens of seconds at temperatures of tens of MeV. Immediately after bounce, neutrinos are trapped and in (near) equilibrium with the fluid, so lepton number is approximately conserved and one treats $Y_L \equiv Y_e + Y_{\nu_e}$ as a control variable with $\mu_{\nu_e} \neq 0$. As the star deleptonizes and cools, neutrinos diffuse out, $\mu_{\nu_e} \to 0$, and the configuration asymptotes to the cold, neutrinoless β–equilibrated limit. As for cold CSs, strangeness–changing weak processes are effectively equilibrated ($\mu_S \simeq 0$), and charge neutrality is enforced.

In the dynamical environments of CCSNe (tens of MeV) and BNS merger remnants (up to ~ 100 MeV), semi–leptonic β reactions generally cannot be assumed to maintain full equilibrium on dynamical timescales, and neutrinos are not in global thermal/chemical equilibrium. Consequently, simulations treat neutrinos via transport; Y_C (or, equivalently, Y_e, which is related to Y_C by electric charge neutrality) remains an independent variable of the EOS, while strangeness–changing weak reactions are still usually taken to be equilibrated ($\mu_S \simeq 0$). Electric charge neutrality is imposed. In practice, the EOS is queried at fixed (n_B, Y_C, T) (or (n_B, T, Y_L) where trapping neutrinos in equilibrium applies), with the neutrino sector provided by transport [5, 64].

The precise equilibrium constraints and control variables for pure phases are specified in Sec. 2.5; the corresponding conditions for mixed phases are detailed in Appendix A.

Let us also briefly discuss similar non-astrophysical systems for completeness. In heavy–ion collisions (HIC), the lifetime of the system is so short that weak interac-

Table 1.1: Indicative thermodynamic domains for some strongly interacting systems.

System	n_B/n_0	T [MeV]	C	S	e	ν
NS	$\lesssim 10$	~ 0	β eq. ($Y_C \sim 0.1$)	weak eq.	electric neut.	$Y_\nu = 0$
CCSN core	$\lesssim 10$	$0-50$	$Y_C \sim 0.35-0.45$	weak eq.	electric neut.	$Y_\nu \neq 0$ (out of eq.)
PNS	$\lesssim 10$	$0-50$	β eq. ($Y_C \sim 0.1$)	weak eq.	electric neut.	$Y_\nu \neq 0$
BCSM	$\lesssim 10$	0–100	$Y_C \sim 0.01-0.6$	weak eq.	electric neut.	$Y_\nu \neq 0$ (out of eq.)
Finite nuclei	1	0	$Y_C = Z/A \simeq 0.4-0.5$	–	–	–
HIC fireball	$\lesssim 5$	$\sim 10-150$	beam Z/A	$Y_S = 0$	–	–
Early Universe (QCD epoch)	$\simeq 0$	$30-500$	β eq.	weak eq.	electric neut.	lepton cons.

tions do not operate. Thus, strangeness is effectively conserved during the collision, $\mu_S \neq 0$, and the system also carries a fixed isospin/electric charge inherited from the colliding nuclei. At top RHIC/LHC energies the produced matter sits at high T and very small μ_B, in the crossover region that can be accessed by lattice QCD; at lower beam energies (BES, FAIR, NICA) the net baryon density increases and the system moves toward moderate T and moderate μ_B, but still under the constraint of (approximately) conserved strangeness and vanishing lepton number [53].

Finally, the early Universe followed an electric charge-neutral and nearly baryon–symmetric trajectory in which the baryon number and lepton numbers (usually referred to as baryon asymmetry, and lepton asymmetries to stress the "net" conservation of particles minus antiparticles) are conserved. Its path through QCD therefore lies along the high–T, low–μ_B edge of the diagram, where present lattice results indicate a crossover rather than a first–order transition. This makes the early–Universe QCD transition potentially qualitatively different from the deconfinement transition in compact stars, which occurs in a different corner of the full variable space [62].

In Table 1.1, a small qualitative summary of the thermodynamical conditions of some systems (which indicates their relevant region in the QCD phase diagram) is reported.

1.2.2 How many families of compact stars?

The phenomenology of compact stars depends critically on the (unknown) energy per baryon of β–stable strange quark matter (SQM) in bulk at zero pressure and temperature.

If $E/N_B|_{\rm SQM} > 930\,{\rm MeV}$, *i.e.* larger than the energy per baryon of iron, SQM and hadronic matter are separated by a phase–transition line in the QCD phase diagram (the *standard scenario*). As density increases (at fixed T), one encounters firstly a purely hadronic phase, then, at $n_B = n_B^{\rm mp}$, a hadron–quark mixed phase, and finally, at $n_B = n_B^{\rm pq}$, a pure deconfined quark phase. Stars with a central baryon density $n_B^{\rm c} < n_B^{\rm mp}$ are neutron stars[1] (NSs). If $n_B^{\rm mp} \leq n_B^{\rm c} \leq n_B^{\rm pq}$, the star has a hadronic outer layer and a mixed–phase core. If $n_B^{\rm c} > n_B^{\rm pq}$, a pure–quark core also develops. Both of the latter are referred as *hybrid stars* (HSs) [20, 60, 66–68]. In mass–radius diagram, NSs and HSs may form a single continuous branch (*one-family scenario*) or

[1]Throughout this work, we use the term neutron stars (NSs) to denote all hadronic stars, irrespective of whether additional hadronic degrees of freedom (e.g., hyperons and Δ resonances) are present.

be separated by an instability region, producing *twin* configurations with the same mass but different radii and compositions (*twin-stars scenario*) [69–72].

If instead $E/N_B|_{\rm SQM} < 930\,{\rm MeV}$, SQM is absolutely stable (the *Bodmer–Witten hypothesis*). Once a seed of deconfined quarks forms at suitable thermodynamic conditions, the entire star converts to SQM [31], yielding *strange quark stars* (QSs) that are self–bound by the strong interaction [6, 7]. In this case all NSs are, in principle, metastable against conversion. Two possibilities then arise: (i) if the conversion conditions are generically met during stellar evolution, all CSs are QSs; (ii) if they are met only in part of the population, NSs and QSs *coexist*, leading to the *two-families scenario* [8–10]. The former is generally viewed as unlikely because it struggles to reproduce crust–dominated phenomena such as glitches and quasi–periodic oscillations. Indeed, while QSs can be either bare or possess a thin crust [58], the microphysics of such crusts differs substantially from that of nuclear crusts, complicating the interpretation of timing and seismology data [73–75].

The key phenomenological difference between the *standard* and *Witten–hypothesis* scenarios is structural. In the standard case, both NSs and HSs are described by a *single equilibrium* EOS from crust to core. Under the Witten hypothesis, instead, NSs are *metastable* configurations: their hadronic EOS describes only a *local* equilibrium phase, and long lifetimes are possible only because an energy barrier inhibits conversion into the global equilibrium state (SQM), as discussed in Sec. 1.1.2. One may regard this as a limiting case of the standard picture in which the onset of the pure quark phase occurs at a baryon density below that corresponding to $P = 0$ at $T = 0$, so that the equilibrium ground state at finite density is deconfined SQM. See Fig. 1.3 for a qualitative representation of the two scenarios.

1.2.3 Constraints from multi-messenger astronomy

Any viable scenario, whether it involves one family, twins, or two families, must be compatible with the growing body of astrophysical observations. These observations, summarized in Table 1.2, place bounds on the mass-radius relation but have also revealed significant tensions and puzzles that any successful theory of dense matter must address.

The first and most robust constraint is the existence of massive pulsars. Observations of objects such as PSR J0348+0432 ($M = 2.01 \pm 0.04$ M$_\odot$) [11] and PSR J0740+6620 ($M = 2.08 \pm 0.07$ M$_\odot$) [76] established a firm lower limit for the maximum mass. More recently, the "black widow" pulsar PSR J0952-0607 has been measured at $M = 2.35 \pm 0.17$ M$_\odot$ [13]. This discovery sets the most stringent constraint to date, requiring any realistic EOS to support a maximum mass $M_{\rm max} \gtrsim 2.19$ M$_\odot$ (at 1σ confidence).

This observational fact is in direct conflict with a central theoretical challenge known as the "hyperon puzzle" [24, 77, 78]. At densities of just $(2-3)n_0$, the chemical potential is expected to becomes large enough to make the creation of hyperons (such as Λ, Σ, Ξ) and Δ resonances energetically favorable [79]. The appearance of these new, fermionic degrees of freedom softens the EOS, possibly dropping the predicted $M_{\rm max}$ below ~ 2 M$_\odot$, in contradiction with the pulsars listed above.

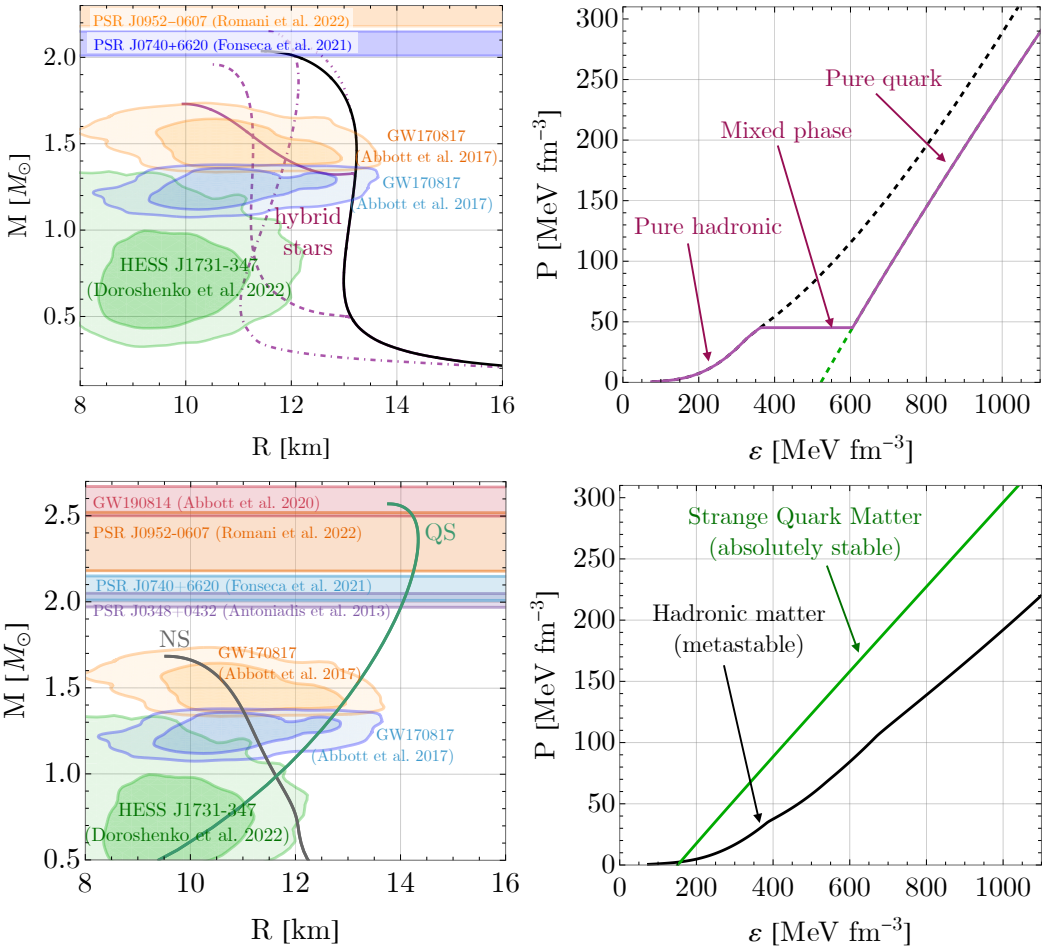

Figure 1.3: Comparison between the one-family scenario and the two-families scenario of compact stars. In the one-family scenario (*top panels*) all the compact stars are described with a single equilibrium EOS and stay on a continuous branch in the mass–radius diagram. The compact stars on the purples lines have a core with deconfined quark matter. In the two-families scenario (*bottom panels*), NSs are long-living metastable objects characterized by a soft EOS reaching small masses and low radii. QSs are characterized by the stable stiff SQM EOS and can reach very high masses.

While high-mass pulsars demand a stiff EOS, measurements of intermediate-mass stars suggest the opposite. The gravitational wave signal from GW170817 [14, 15, 80] and data from heavy-ion collisions [17] both indicate that the EOS is relatively *soft* at $(2-3)n_0$. This is broadly supported by several NICER radius measurements of canonical ~ 1.4 $M_\odot$ stars which point to relatively small radii, including PSR J0030+0451 [81], PSR J0437-4715 [82], and the recent PSR J0614–3329, which indicates a very compact radius of $R = 10.29^{+1.01}_{-0.86}$ km for a mass of $M = 1.44^{+0.06}_{-0.07}$ $M_\odot$ [16].

This creates the central tension of modern compact star physics: the EOS must be soft at intermediate densities (to satisfy GW170817 and small-radius pulsars) but must stiffen significantly at higher densities (to support $M_{\rm max} \gtrsim 2.19$ $M_\odot$). This implies a "back-bending" or "stiffening" in the M–R relation. This behavior is also supported by observations of massive stars that suggest larger radii, such as PSR J0740+6620 [12, 83] and analyses of the thermonuclear burster 4U 1702-429 [84].

Finally, some specific objects, though their interpretations are still debated, challenge our understanding of the mass spectrum itself.

The secondary component of the GW190814 merger had a mass of $M \simeq 2.6$ $M_\odot$ [19]. This object falls in the "mass gap" between the heaviest known CSs and the lightest known BHs. Supporting such a mass is extremely difficult for any hadronic EOS without violating causality or the radius constraints from GW170817. While analyses of GW170817 have suggested $M_{\rm max}$ is significantly below 2.6 $M_\odot$ [85], such results assume a one-family scenario and cannot be directly applied to the two-family scenario, where the merger remnant would be a differentially rotating QS with different properties.

At the other end, HESS J1731-347 has an exceptionally small mass and radius: $M = 0.77^{+0.20}_{-0.17}$ $M_\odot$ and $R = 10.4^{+0.86}_{-0.78}$ km [18]. Standard supernova theories struggle to produce a NS with a gravitational mass below ~ 1.1 $M_\odot$ [86]. This object can be explained in the context of the Bodmer-Witten hypothesis as a QS [87], even if other possibilities, including HSs, are not ruled out [88]. This picture is further complicated by data from another low-mass star, PSR J1231-1411, which instead suggests a large radius [89], creating a new tension at the low-mass end. However, this latter inference is still model–dependent and not yet as robust as J0030+0451 or J0740+6620, so its impact on EOS constraints should be treated with caution.

Reconciling a complex and often contradictory set of observational data (summarized in Table 1.2) and theoretical challenges (like the Hyperon Puzzle) is a primary goal of dense matter physics. The persistent large uncertainties, particularly in radius measurements, and the still ambiguous nature of observations like HESS J1731-347, PSR J1231-1411, and GW190814, preclude any definitive conclusions on the presence of deconfined quark matter in compact stars. Consequently, it is not yet possible to strongly advocate for one specific scenario over others.

One possible solution is the one-family (or twin-family) scenario in which hybrid stars feature a hadron–quark transition at a few times n_0. This transition initially softens the EOS at moderate baryon densities, but quark-matter repulsion and pairing (color superconductivity) re-stiffen it at higher densities. This "soft-to-stiff" mechanism allows the model to support a maximum mass of $M_{\rm max} \gtrsim 2$ $M_\odot$ while accounting for small

Table 1.2: Some representative mass–radius constraints for compact stars from NICER, HESS, and gravitational waves. Uncertainties are quoted at the level used in the cited work (typically 68% for NICER, 90% for GW).

Source / Dataset	$M\,[M_\odot]$	R [km]	Reference
PSR J0348+0432	2.01 ± 0.04	—	[11]
PSR J0030+0451	$1.44^{+0.15}_{-0.14}$	$13.02^{+1.24}_{-1.06}$	[99]
PSR J0030+0451	$1.34^{+0.15}_{-0.16}$	$12.71^{+1.14}_{-1.19}$	[100]
PSR J0740+6620	$2.072^{+0.067}_{-0.066}$	$12.39^{+1.30}_{-0.98}$	[83]
PSR J0740+6620	2.08 ± 0.07	$13.7^{+2.6}_{-1.5}$	[12]
PSR J0740+6620	2.073 ± 0.069	$12.49^{+1.28}_{-0.88}$	[101]
PSR J0740+6620	2.08 ± 0.07	$12.92^{+2.09}_{-1.13}$	[102]
PSR J0437−4715	1.42 ± 0.04	$11.36^{+0.95}_{-0.63}$	[82]
PSR J0614−3329	$1.44^{+0.06}_{-0.07}$	$10.29^{+1.01}_{-0.86}$	[16]
PSR J1231−1411	$1.04^{+0.05}_{-0.06}$	$12.6^{+0.3}_{-0.3}$	[89]
PSR J0952−0607	2.35 ± 0.17	—	[13]
HESS J1731−347	$0.77^{+0.20}_{-0.17}$	$10.4^{+0.86}_{-0.78}$	[18]
GW170817 (heavier comp.)	$1.36 - 1.60$	$R_1 = 10.8^{+2.0}_{-1.7}$ (90%)	[14, 15, 80]
GW170817 (lighter comp.)	$1.17 - 1.36$	$R_2 = 10.7^{+2.1}_{-1.5}$ (90%)	[14, 15, 80]
GW190814 secondary	$2.59^{+0.08}_{-0.09}$	—	[19]

radii of intermediate mass objects [21, 90–93]. Notably, an early onset of deconfined quarks (occurring before the hyperon onset) also naturally solves the Hyperon Puzzle.

The two-families scenario naturally accommodates the needed constraints. In this picture, hadronic NSs (possibly containing hyperons and Δ-resonances) form a soft branch with small radii and a maximum mass below 2 $M_\odot$. A distinct QS branch, characterized by a stiff SQM EOS, accounts for the most massive objects [8–10, 94] as well as for the sub-solar ones [87].

Examples of those scenarios are reported in Fig. 1.3.

Note that both the twin-family and two-families scenarios are able to support two compact stars with the same mass but different radii.

Finally, if one downweights the most uncertain (and most extreme) constraints, the allowed parameter space becomes less restrictive and several alternatives remain viable. These include neutron stars or hybrid stars featuring repulsive hyperon–hyperon interactions (e.g., repulsive hyperonic three–body forces) [95–97] and/or strong repulsive quark interactions [20, 98] at high baryon density. Moreover, even a purely nucleonic EOS without invoking deconfined degrees of freedom, predicting relatively low maximum central densities $\sim (4-5)\,n_0$ and nearly constant radii $R \sim 12$ km, is not ruled out [22].

Note that current astrophysical observables do not directly determine the microscopic composition of compact-star matter; possible evidence for deconfined quarks is necessarily indirect, entering through their impact on global properties such as mass–radius and tidal deformability. Some of the most incisive composition-sensitive signatures

are expected in the post–merger gravitational-wave (GW) spectrum of BCSMs. While present detectors primarily constrain the inspiral and are not yet sensitive enough in the kHz band to robustly detect post–merger features, third–generation instruments (Einstein Telescope, Cosmic Explorer) are forecast to resolve these modes and enable the "post–merger spectroscopy" [33, 103]. This would provide direct information on the presence (or absence) of deconfined quarks and on the nature of the hadron–quark transition. Accordingly, developing quantitatively controlled models of the transition in high–density astrophysical environments will be crucial in the coming years for interpreting next–generation GW data.

1.3 Deconfinement transition in astrophysics

The properties of the hadron–quark transition at supranuclear baryon densities, as may be realized in compact stars and related high–energy astrophysical environments, remain uncertain. First, deconfinement in this regime may proceed via a genuine first–order phase transition or, alternatively, via a smooth crossover similar to that observed at high temperature and low baryon density. Second, even once the order of the transition is specified, the structure of the mixed phase is fixed by which conserved charges (*e.g.* baryon number, non–leptonic electric charge, strangeness, total electric charge, lepton number) must be enforced *globally* in the environment. Third, if the transition is first order and thus the hadron–quark surface tension is nonzero, the system may fail to follow the equilibrium path and can remain trapped in a metastable hadronic state. These possibilities directly affect observable signatures in CCSNe, BNS mergers, and GRBs, as well as the macroscopic equilibrium structure of compact stars.

1.3.1 Equilibrium coexistence between phases

Let us consider two phases: a hadronic phase (H), in which quarks are confined, and a deconfined quark phase (Q). The transition between them in the high-density regime can proceed either as a *first–order* phase transition or as a *crossover*. In the first–order case, three thermodynamic regions can be identified at equilibrium: a pure hadronic phase, a pure quark phase, and a mixed phase within which the two phases coexist at the classical level and bounded by points where the thermodynamic potential is non-analytic. By contrast, in a crossover there is no sharply defined mixed phase: hadronic degrees of freedom are continuously reorganized into quark degrees of freedom at the quantum level and no thermodynamic discontinuity appears [2, 104]. This behavior is typically modeled by smooth interpolations between hadronic and quark EOSs [2, 98, 105, 106] or within quarkyonic frameworks in which quarks fill the Fermi sea while a shell of baryons survives near the Fermi surface [92, 107, 108].

In this thesis, I will focus on *first–order* deconfinement transitions in the high–density regime. For such transitions, for a specified set of conserved charges, equilibrium coexistence is obtained by minimizing the appropriate thermodynamic potential with respect to the independent variables under the relevant constraints, and it imply (i) thermal equilibrium (same temperature), (ii) mechanical equilibrium (same pressure), and (iii)

equality of the chemical potentials associated with all *globally* conserved charges in the two phases [27, 109].

The minimization of the thermodynamic potential favors charge rearrangement in the mixed phase. For example, the hadronic component becomes more isospin–symmetric by transferring negative charge to the quark component, the lepton fraction is correspondingly reduced, and strange quarks are produced in the quark phase to reduce other Fermi levels. This rearrangement naturally leads to positively charged domains of hadronic matter coexisting with negatively charged domains of quark matter [110–113]. The qualitative structure of the equilibrium mixed phase is set by the competition between surface and Coulomb energies. The hadron–quark surface tension σ tends to suppress interfaces and favor larger structures, while the electric field, screened over the corresponding Debye lengths in each phase, penalizes extended charge separations. The balance of these contributions can generate finite–size "pasta" configurations (droplets, rods, slabs, tubes, bubbles). What really impacts the *bulk* properties is not the exact shape sequence but the effective electric neutrality condition that emerges from this balance. If σ is large, the optimal structures are larger than (or comparable to) the Debye screening length, screening is efficient, and each phase is nearly neutral: the system behaves close to the locally neutral limit. If, instead, σ is small, the favored structures are smaller than the screening length, sizable charge separation is allowed, and only the mixture as a whole is neutral: the system approaches the globally neutral limit. In practice, one therefore considers the two extreme cases, $\sigma \to \infty$ (fully local neutrality) and $\sigma \to 0$ (fully global neutrality), as bracketing the realistic mixed phase [27, 109].

The description of first–order phase transitions under typical isolated compact–star conditions (cold, neutrino–less matter in β equilibrium) has been discussed extensively in the literature (see, *e.g.*, [20]). The two constructions most commonly used are the Maxwell (MC) and Gibbs (GC) constructions, which correspond to the two limiting cases discussed above [20, 27]. In the MC, only the baryon number is treated as a globally conserved quantity, while electric charge neutrality is imposed *locally* in each phase. At fixed T this leads to a mixed phase with *constant* pressure. In the GC, instead, both baryon number and electric charge are conserved *globally*; as a consequence, the pressure varies smoothly across the mixed phase. These distinct behaviors translate into different stellar structures: in the MC case the constant–pressure layer cannot provide support against gravity, so the mixed phase has essentially negligible radial extent and the star develops a sharp interface. In the GC case, a genuine mixed–phase region can be sustained inside the star.

Astrophysical environments often involve additional conserved charges. In dynamical systems such as CCSNe and BNS mergers, weak β-reactions do not necessarily reach equilibrium on hydrodynamic time scales. As a consequence, the net non–leptonic electric charge fraction Y_C must be treated as an independent, globally constrained quantity [5, 28]. Similarly, in these high–temperature phenomena, neutrinos can be trapped (their mean free path is shorter than the system size) [114, 115]. In that case, the total lepton number must be conserved globally, and the lepton fraction Y_L becomes an additional independent variable in the phase–equilibrium problem. By contrast, strangeness is *not* conserved on these time scales, because weak processes that create strange baryons or strange quarks are expected to operate fast enough at

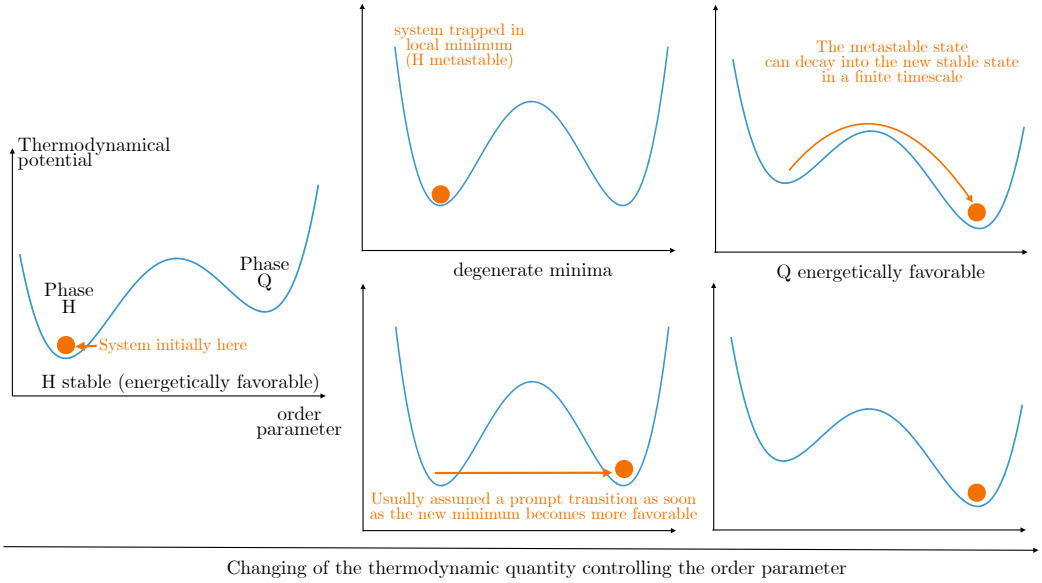

Figure 1.4: Schematic illustration of a first–order transition. The system can remain in the metastable minimum until it overcomes the barrier and converts to the stable phase.

the relevant densities and temperatures to drive s–content toward its equilibrium value [5].

In all these multi–component systems, the coexistence equilibrium characteristics depend explicitly on how many charges are taken to be globally conserved. A purely Maxwell–type construction, in which the pressure is constant, is an equilibrium solution if only one globally conserved charge is present [27, 109]. Thus, in the dynamical systems mentioned above, the MC is not a proper equilibrium solution for the mixed phase. A systematic discussion of these cases and the resulting equilibrium conditions is given in Appendix A (see also [109]).

In Chapter II, I will discuss a recent framework we developed [40, 41] that implements first–order transitions at finite T for high–energy astrophysical simulations, allowing charge neutrality to be fulfilled partially locally and partially globally in a thermodynamically consistent way.

Up to this point, we have described the *equilibrium* configuration of a first–order transition, *i.e.*, how the system would rearrange if it could move quasistatically from one minimum of the free energy (or, more generally, of the relevant thermodynamic potential) to another as soon as the new minimum (characterized by a given order parameter or, in a thermodynamic picture, by a given volume fraction of the new phase) becomes globally favored (see Fig. 1.4). In actual conditions, however, the system does not necessarily follow this ideal path. If a barrier separates the two minima (as in a first–order transition with nonzero surface tension σ), the system may remain trapped in the local minimum (metastable state) even after a lower–free–energy minimum exists. Thus, the phase transition occurs via *decay of the metastable state*.

1.3.2 Metastability and nucleation

In real systems, a first–order phase transition does not proceed as an instantaneous jump from one minimum of the thermodynamic potential to the other. Rather, the system must *decay* from the local minimum (metastable state) to the global one by overcoming the barrier generated, in configuration space, by the finite hadron–quark surface tension. This decay is initiated by fluctuations of the order parameter (and possibly of other thermodynamic quantities) that transiently create finite–size domains of the stable phase within the metastable background.

Two dynamical mechanisms can drive this decay [29, 116]. If the system is not driven far from the coexistence line, the dominant fluctuations are localized and of finite extent: a rare, sufficiently large fluctuation creates a droplet that reaches the critical size (*i.e.* overcomes the free–energy barrier) and then grows. The formation of such a critical droplet is called *nucleation*. If, instead, the system is pushed past the spinodal line into the mechanically unstable region, the free–energy barrier effectively disappears and long–wavelength modes grow spontaneously: this is *spinodal decomposition*. The latter can occur when the macroscopic evolution (expansion in heavy–ion collisions, cooling/expansion in the early Universe, rapid compression in CCSNe and BNSMs) carries the system into the unstable region on a timescale shorter than the nucleation time.

The approach adopted in this thesis cannot treat spinodal decomposition self–consistently, because it would require a single effective potential valid in both the hadronic and deconfined quark domains, whereas in Chapter 2 we construct the EOS from two distinct models. However, since the fluctuations that trigger nucleation are mediated by strong interactions and are therefore much faster than typical astrophysical dynamical timescales, a system brought close to the spinodal boundary (where the barrier is already low) will reasonably have enough time to nucleate. For these reasons, this thesis will focus on nucleation.

In principle, nucleation can be either *inhomogeneous* or *homogeneous*. Inhomogeneous nucleation, more common in nature, is initiated at impurities, defects, or boundaries that lower the effective barrier. Here, however, we are interested in *homogeneous* nucleation, in which the transition is triggered intrinsically by a spontaneous thermodynamic fluctuation (thermal or quantum) in an otherwise uniform medium.

In bulk, Q becomes thermodynamically favored when, at the same set of relevant chemical potentials, $P_Q(\{\mu_i\}, T) > P_H(\{\mu_i\}, T)$, and the two minima of the relevant thermodynamic potential, viewed as a function of the order parameter, are degenerate at the coexistence point (see Fig. 1.5). In the presence of a finite surface tension σ, however, the actual conversion is *delayed* because the metastable state must first decay: a critical droplet of Q inside H has to pay a finite–size energy, so nucleation requires an *overpressure* $\Delta P \equiv P_Q - P_H > 0$ (or, equivalently, superheating). A larger ΔP reduces the size of the critical fluctuation, lowers the free–energy barrier, and increases the nucleation rate. If the overpressure needed to obtain a nucleation rate comparable to the dynamical evolution timescale of the system is small, then using the equilibrium EOS with a mixed phase is an adequate approximation. If, instead, a sizeable overpressure is required, neglecting nucleation effects would underestimate the

true onset conditions of deconfinement.

In standard one–family scenarios, this delay is often a quantitative correction to the equilibrium picture. In contrast, in the Bodmer–Witten scenario, the hadronic phase is *always* metastable with respect to deconfined strange quark matter, so nucleation is the *only* way to determine when and where the conversion to a QS actually occurs (see Fig. 1.5). Note moreover that if the phase transition is triggered by the decay of a metastable hadronic state via nucleation, then the macroscopic conversion proceeds through a genuinely non–equilibrium process [10, 31, 32] that will be discussed in Sec. 4.1.

Pioneering applications to compact stars considered both thermal nucleation [117, 118] and quantum tunneling [42, 119]. Subsequent works have explored a wide range of astrophysical channels (*e.g.* quantum nucleation in cold compact stars, thermal nucleation in hot PNSs and CCSNe) and microphysical setups (*e.g.* different treatment of surface tension and flavor composition, role of hyperons, color–superconducting quark phases and neutrino trapping) [43, 44, 116, 120–130]. Possible connections with gamma–ray bursts have also been investigated, in particular in scenarios where the conversion provides a delayed energy release [43, 131–133]. In a recent study, we examined the impact of flavor composition fluctuations on the nucleation process [45, 46].

A broader literature addresses deconfinement nucleation in heavy–ion collisions [134, 135] and in the early Universe [29, 136]. Related studies of metastable–state decay in other contexts, such as atomic quantum gases [137] and ferromagnetic superfluids [138], may be particularly valuable because they may eventually provide laboratory–scale benchmarks for nucleation dynamics that cannot be probed directly in astrophysical systems.

A detailed development of the homogeneous–nucleation formalism for compact–star matter, and of its role in converting a metastable hadronic object into a QS within the two–families scenario, will be presented in Chapter 4, together with the extension that includes thermal fluctuations of the conserved charges [45, 46, 139]. The associated astrophysical implications are discussed in Chapter 5.

1.3.3 Phenomenology of deconfinement in astrophysics

Deconfinement leading to the formation of hybrid stars or strange quark stars can, in principle, occur in several astrophysical environments and leave multi–messenger imprints. Depending on the thermodynamic path followed by the system the transition may take place (i) during the evolution of a binary compact star merger remnant; (ii) in the hot, lepton–rich core of a core–collapse supernova (CCSN) or in the early life of a proto neutron star (PNS); (iii) later in the evolution of an ordinary neutron star, as accretion or spin–down drives its central density across the deconfinement threshold. Each of these channels is characterized by a different set of constraints (neutrino trapping vs. neutrino-free, local vs. global charge neutrality, flavor-conserved vs. equilibrated), and therefore by a different realization of the hadron–to–quark transition.

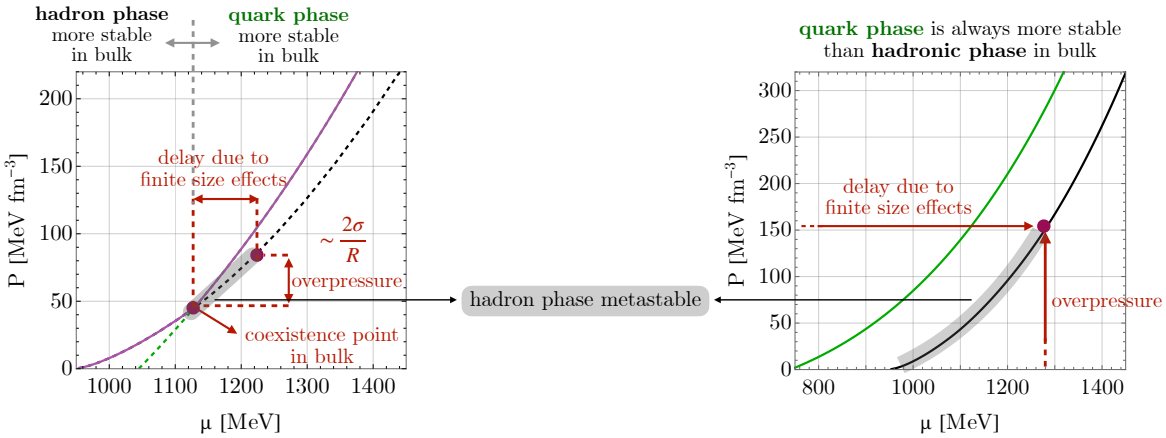

Figure 1.5: Schematic comparison of the role of finite-size effects in delaying the phase transition with respect to the coexistence point in the standard scenario and Bodmer-Witten scenario. For simplicity, in this image, only one global conserved quantity is considered. See the text for more details.

1.3.3.1 Deconfinement in binary compact star mergers

In the *one–family* scenario, where all cold compact stars follow a single hadronic–hybrid sequence, numerical–relativity simulations consistently show that the GW imprint of deconfinement depends more on the *strength and timing* of the hadron–quark transition than on the mere presence of a quark phase in the EOS.

The earliest simulations with a strongly, Maxwell–type first–order transition [39, 140], reached essentially immediately after merger, showed that the sudden softening drives a rapid compactification of the remnant and often an early (sometimes prompt) collapse to a BH. In this regime, the post–merger GW signal is short and its phase evolution departs from the purely hadronic case only mildly, so the effect of deconfinement can be confused with other high–density softening mechanisms (appearance of hyperons, thermal treatment, neutrino cooling) and even with numerical systematics. A different, and observationally more promising, regime is obtained when the transition is still Maxwell–like but the onset density/temperature is such that the remnant survives the transition. This is the setup explored by [141–143]: the merger remnant converts, becomes more compact than an equally massive hadronic remnant, and emits at a *systematically higher* dominant post–merger frequency f_2 than predicted by the tight hadronic f_2–$\tilde{\Lambda}$ relations [144–146]. In this case, a statistically significant upward deviation from the hadronic relations can be interpreted as evidence for a strong first–order transition active in the merger regime. In [147] authors made clear that such large, clearly identifiable shifts occur only if the transition does *not* trigger immediate collapse: if the onset is *delayed* by a few ms, the GW spectrogram can even show a two–stage structure (a first peak from the purely hadronic hypermassive NS and a later, higher–frequency peak from the hybrid remnant), providing a time–resolved imprint of deconfinement.

When the transition is *not* strong but proceeds over an extended mixed–phase region, the qualitative effect persists but is weaker. In [148] the hadronic EOS is matched to the quark EOS through a Gibbs–type construction: the merger remnants still experience

EOS softening, their post–merger spectra are modified, and in some cases the collapse is advanced, but the shift of f_2 and the change in the remnant lifetime are of the same order as those produced by varying the purely hadronic models. In other words, Gibbs–like transitions do leave a mark, but typically *inside* the current purely hadronic systematic band. Simulations with crossover transition models [149, 150], or using holographically motivated V–QCD frameworks [151, 152], show the same trend: the post–merger signal reacts to the gradual softening, but the resulting f_2 shift remains comparable to hadronic EOS scatter and is therefore hard to isolate with current detectors.

Summarizing these results, [33] shows that, unless the transition is *sufficiently strong* and actually crossed within the thermodynamic window explored by a non–negligible fraction of BNS remnants, current GW detectors cannot disentangle deconfinement–induced shifts of f_2 from the ordinary EOS–driven scatter of purely hadronic models. Third–generation interferometers, such as the Einstein Telescope and Cosmic Explorer, will be required to perform this discrimination systematically at the population level.

In general, a softening (stiffening) of the EOS in the post–merger phase produces a more (less) compact remnant and thus shifts the dominant f_2 peak to higher (lower) frequencies. The difference between the post–merger EOS and the inspiral EOS leads to violations of the quasi–universal relations that connect the post–merger spectrum to pre–merger properties such as the tidal deformability. However, these violations become observationally significant only if the phase transition modifies the EOS sufficiently strongly.

A smaller but growing set of simulations has explored mergers in the *two–families* scenario, in which NSs and QSs can both form binaries. Unlike the one–family case, three channels are now possible for the same values of chirp mass and mass asymmetry: NS–NS, NS–QS, and QS–QS [34, 153–156]. Because in this scenario NSs are deliberately more compact and with a relatively low $M_{\rm max}^{\rm NS}$, the merger of two such NSs produces a remnant that sits much closer to instability than in the one–family case: the threshold mass for prompt collapse is reduced and [34]. In mixed NS–QS systems, the QS is the less deformable component, so the inspiral already shows a smaller effective tidal deformability $\tilde{\Lambda}$; after contact, the NS material forms a outer layers/torus while the QS matter remains central [34]. QS–QS mergers are both rarer [34] and more collapse–prone: GR simulations of self–bound QS binaries show that the total mass for prompt or very early collapse sits very close to the mass–shedding limit, so in many cases, no post–merger GW can be measured. This behaviour stems from the fact that, for QSs, differential rotation increases the maximum mass only slightly above the uniformly rotating limit [157]. When a QS–QS remnant *does* survive, however, fully GR runs find a dynamical mass loss smaller than in the corresponding hadronic binary [154, 156].

Note that, in the two–families scenario, the quark phase is stiffer than the hadronic phase. Consequently, if quark matter is present in the post–merger remnant, the dominant frequency peak f_2 is shifted to lower values compared to the purely hadronic case.

In all mergers involving at least one QS, small amounts of SQM (strangelets) can be ejected. The subsequent evolution of these fragments has been studied in [156, 158],

where it was found that only a small fraction of the initially ejected strangelets survives evaporation and hadronization; the resulting Galactic strangelet density is therefore too low to convert all NSs into QSs, so the long–term coexistence of the two families is preserved.

Note that, while in QS–NS and QS–QS systems SQM is already present, in purely NS–NS mergers deconfinement can occur only via a nucleation–triggered conversion (see Chap. 4.1) if the remnant is compressed/heated to conditions for which the nucleation rate becomes relevant on dynamical timescales. We also stress that in [34] the onset of SQM is not obtained from a microscopic nucleation calculation, but is imposed through a phenomenologically motivated prescription (see Sec . 5).

1.3.3.2 Deconfinement in core-collapse supernovae

The idea that a hadron–quark phase transition can *trigger* a core–collapse supernova explosion goes back to [159]. The mechanism is the following: if, during the early PNS evolution, the central thermodynamic conditions enter the *soft* hadron-quark mixed phase, the core undergoes a brief secondary collapse; once the density rises enough to reach the *pure* quark phase, the EOS stiffens again and the core re–expands, launching a second shock that can revive the explosion.

This *deconfinement–driven* explosion can succeed even for progenitors for which the standard explosion mechanism (*e.g.* neutrino heating) fails. Recent CCSN simulations employing modern hybrid EOSs [35, 36] have confirmed this picture and, importantly, have demonstrated it for *massive* progenitors with zero–age main–sequence masses of $\sim 50\ M_\odot$, which would otherwise collapse to a black hole. In other words, deconfinement opens an additional explosion channel precisely in the high–mass regime.

These simulations [35, 36] employ a *Maxwell* construction, *i.e.* a strong transition with sizable latent heat, which naturally produces a pronounced dynamical collapse and bounce. A smoother, *Gibbs*–like construction would spread the softening over a broader density/temperature interval, so that both the bounce and the secondary shock are expected to be weaker. This has direct implications for EOS modelling: to assess how robust the deconfinement–driven mechanism really is, one needs thermodynamically consistent EOS families in which Maxwell and Gibbs are varied at fixed hadronic sector.

In the *two–families* scenario, no counterpart of the CCSN mechanisms discussed above for the one–family case has yet been explored in fully dynamical simulations. In Sec. 5.5 we will qualitatively outline a possible deconfinement–assisted explosion in this framework, inspired by the one–family scenario.

Note that in all the above simulations, the role of *nucleation* is neglected. See [116] for a discussion of quark–matter nucleation during a CCSN. In the two–families scenario, a consistent calculation of the nucleation rate would be *fundamental* to assess whether deconfinement can actually occur in a CCSN before collapsing into a BH.

Finally, a deconfinement–driven explosion naturally provides a larger energy budget than standard neutrino–driven CCSNe and can operate in the very massive progenitor

window that is also expected to produce a dense circumstellar medium [36]. These two ingredients make deconfinement–driven CCSNe plausible candidate progenitors of *superluminous* supernovae, i.e. events whose peak luminosity is $\gtrsim 10$ times that of ordinary CCSNe and that therefore require an additional power source.

Note that, in principle, deconfinement may also occur *after* a successful neutrino–driven CCSN explosion, during the subsequent evolution of the hot PNS remnant. This possibility, in the context of the two–families scenario, will be discussed in Sec. 5.2.

1.3.3.3 Deconfinement in binary accreting systems

Another channel for quark deconfinement is *accretion–induced* deconfinement in close binaries. If a hadronic NS in a low–mass X–ray binary (LMXB) accretes for long enough, its central density can be driven across the hadron–quark transition line. Once this happens, the star migrates to the HS or QS configuration and, if a latent heat is present (*i.e.* if the phase-transition is strong and/or triggered by the decay of a metastable system via nucleation), releases the corresponding binding–energy difference [9, 10]. The same transition can also be reached later, in the spin–down phase, when the loss of angular momentum increases the central density.

The resulting mass defect, possibly combined with an anisotropic neutrino burst, can *increase the eccentricity* (in some cases even enough to disrupt the binary, producing isolated millisecond pulsars) of a system that was previously circularized by tides and mass transfer. This provides a natural way to produce the otherwise puzzling population of *eccentric millisecond pulsars*. This idea has been quantified recently in [160] in the context of the twin–star scenario.

Unlike BNS mergers and CCSNe, where matter is hot, neutrino–rich, and not in β equilibrium, accreting NSs in LMXBs are effectively cold (the core temperature is only mildly affected by accretion) and reach neutrinoless β equilibrium. For this reason, in this channel, the *nucleation rate* of the first critical quark droplet must be computed for cold, slowly heated, rotating configurations, which is still largely unexplored.

An interesting accretion–driven deconfinement scenario within the two–families framework, in which both compact objects in a binary accrete ejected material from a CCSN and are thus pushed toward the quark branch, has been investigated in [47]; we will return to this mechanism in Sec. 5.4.

Finally, an analysis of the multi-messenger signals related to deconfinement in the two-family scenario (*e.g.* the possible link between deconfinement and GRB) can be found in [9, 10, 161–163].

Chapter 2

Equation of state of strongly interacting matter

The equation of state (EOS), namely, the relation between the system's thermodynamic quantities, is a key ingredient for computing the hydrostatic properties of isolated NSs, such as mass, radius, and tidal deformability, and for astrophysical simulations.

A fully microscopic, QCD–based description of strongly interacting matter over the wide range of baryon densities, temperatures, and conserved–charge contents is not yet available, because QCD at finite baryon chemical potential remains difficult to solve from first principles. For this reason, and following the strategy widely adopted in the literature, in this thesis the confined hadronic phase and the deconfined quark phase will be described with two different effective models, and the hadron–quark transition will be implemented through an appropriate construction between the two descriptions.

Astrophysical applications require an EOS that is thermodynamically consistent and spans a quite large region in the variable space (n_B, Y_C, Y_S, Y_L, T) so as to cover cold, β–equilibrated CSs, hot and neutrino–rich PNSs, matter in CCSNe and BNSMs which could be nearly isospin–symmetric ($Y_C \simeq 0.4$). In each of these subdomains, the EOS is constrained by different pieces of information. Around saturation density, $n_B \simeq n_0$, and at $T \simeq 0$, empirical properties of finite nuclei and of nearly symmetric nuclear matter fix the bulk parameters of hadronic models [164]. Up to $n_B \lesssim 2n_0$, state–of–the–art chiral effective field theory calculations with controlled truncation–error estimates provide robust bands for pure neutron matter and moderately asymmetric matter [50, 51]. At slightly higher densities, $n_B \simeq (2-4)\, n_0$, intermediate–energy heavy–ion collisions constrain the EOS for symmetric matter ($Y_C = 0.5$) and rule out very stiff behaviors [17]. At still higher densities, phenomenological extrapolations are needed and constrained by astrophysical observations (see Sec. 1.2.3).

Because we aim at high–energy astrophysical systems, the EOS must include, besides hadronic degrees of freedom (nucleons, hyperons, Δ resonances), quark degrees of freedom (up, down, and strange), leptons (electrons, muons, neutrinos when trapped), thermal bosons (photons and, for quark matter, gluons), and the corresponding antiparticles.

Reviews regarding the EOSs for astrophysical applications can be found in [5, 28].

In the rest of this Chapter I will present the EOS models employed in this work.

2.1 Homogeneous hadronic matter

In this work, hadronic matter will be described using two different approaches: (i) a purely nucleonic schematic model (ZL), based on an energy–density functional, and (ii) a relativistic mean–field model (SFHo-HΔ) that also includes hyperon and Δ degrees of freedom.

Note that the EOS models presented here are employed for the nuclear and supra-nuclear regimes. For the sub-nuclear regime, corresponding to the NS crust and the PNS envelope, we adopt the COMPOSE table[1] [23, 25, 38, 165].

2.1.1 Nucleonic EOS: ZL model

The Zhao–Lattimer (ZL) EOS was first proposed in [108] and has been employed both for cold, β–equilibrated matter at $T = 0$ [40, 98, 166, 167] and for out–of–equilibrium matter at $T \neq 0$ relevant to CCSNe and BCSMs [41, 45].

ZL is a schematic, density–functional model in which the nucleon–nucleon interaction is encoded in an interaction energy that depends on the baryon density and on the proton–neutron composition. Although it is not derived from a microscopic Lagrangian, the structure of the interaction term is close to what one would obtain from a relativistic mean–field model with vector interactions only. A key advantage of ZL is that with six parameters, $(a_0, b_0, a_1, b_1, \gamma, \gamma_1)$, one can reproduce standard bulk nuclear properties and, for suitable choices, remain consistent with theoretical, experimental, and astrophysical constraints [45, 98, 108].

The characteristic interaction part of the energy density is

$$V(n_B, Y_n, Y_p) = 4n_B^2 Y_n Y_p \left\{ \frac{a_0}{n_0} + \frac{b_0}{n_0} \left[\frac{n_B}{n_0}(Y_n + Y_p) \right]^{\gamma - 1} \right\} + n_B^2 (Y_n - Y_p)^2 \left\{ \frac{a_1}{n_0} + \frac{b_1}{n_0} \left[\frac{n_B}{n_0}(Y_n + Y_p) \right]^{\gamma_1 - 1} \right\}, \tag{2.1}$$

where $Y_i = n_i/n_B$ $(i = p, n)$ are the net proton and neutron fractions, n_i the corresponding number densities, n_B the baryon density, and n_0 the saturation density, fixed here to $n_0 = 0.16$ fm^{-3}. The parameter set used in this work is reported in Table 2.1 and coincides with the one adopted in [40, 41, 98].

The number density of nucleon i is

$$n_i = n_B Y_i = \frac{g_i}{2\pi^2} \int_0^{+\infty} k^2 \left[\mathbf{f}_i(k, \mu_i^*, T) - \mathbf{f}_i(k, -\mu_i^*, T) \right] dk, \tag{2.2}$$

[1] https://compose.obspm.fr/eos/118

Table 2.1: Parameters for the ZL model, corresponding to the parametrization used in [40, 41, 98]. See [98] for the implications for nuclear and NSs properties.

Parameter	Value	Units
m_p	939.5	MeV
m_n	939.5	MeV
n_0	0.16	fm^{-3}
a_0	-96.64	MeV
b_0	58.85	MeV
γ	1.40	
a_1	-26.06	MeV
b_1	7.34	MeV
γ_1	2.45	

where

$$\mu_i^* = \mu_i - \frac{1}{n_B}\left.\frac{\partial V}{\partial Y_i}\right|_{n_B, Y_{j\neq i}}, \tag{2.3}$$

is the chemical potential of species i, $g_i = 2J_i + 1$ the degeneracy ($g_p = g_n = 2$ due to the two spin states), and

$$\mathbf{f}_i(k, \pm\mu_i^*, T) = \frac{1}{\exp\left[\dfrac{E_i^*(k) \mp \mu_i^*}{T}\right] + 1} \tag{2.4}$$

is the Fermi–Dirac distribution, with single–particle effective energy

$$E_i^*(k) = \sqrt{k^2 + m_i^2}. \tag{2.5}$$

Note that the single–particle energy is

$$E_i(k) = E_i^*(k) + \frac{1}{n_B}\left.\frac{\partial V}{\partial Y_i}\right|_{n_B, Y_{j\neq i}} \tag{2.6}$$

and $E_i^* - \mu_i^* = E_i - \mu_i$. The total energy density is

$$\varepsilon_H = \sum_{i=p,n} \frac{g_i}{2\pi^2} \int_0^{+\infty} k^2 E(k, m_i) \left[\mathbf{f}_i(k, \mu_i^*, T) + \mathbf{f}_i(k, -\mu_i^*, T)\right] dk + V(n_B, Y_p, Y_n), \tag{2.7}$$

and the pressure reads

$$P_H = \sum_{i=p,n} \frac{g_i}{2\pi^2} \frac{1}{3} \int_0^{+\infty} \frac{k^4}{E_i^*(k)} \left[\mathbf{f}_i(k, \mu_i^*, T) + \mathbf{f}_i(k, -\mu_i^*, T)\right] dk + n_B \left.\frac{\partial V(n_B, Y_p, Y_n)}{\partial n_B}\right|_{Y_p, Y_n}. \tag{2.8}$$

All other thermodynamic quantities can be derived from these expressions; see [28, 41]. The numerical evaluation of the Fermi integrals is discussed in Appendix C.

2.1.2 Hadronic EOS: SFHo-HΔ model

The SFHo-HΔ model is a relativistic mean-field (RMF) description of dense hadronic matter in which baryons interact through the exchange of effective meson fields. It is built on the SFHo parametrization of [25] and extended to include the full baryon octet [23], the Δ-isobar quartet [79] and used in compact stars applications in [9, 34, 47, 94, 168].

The RMF Lagrangian density reads

$$\begin{aligned}
\mathcal{L} \;=\; & \sum_k \overline{\psi}_k \left[i\,\gamma_\mu\,\partial^\mu - (m_k - g_{\sigma k}\,\sigma) - g_{\omega k}\,\gamma_\mu\,\omega^\mu - g_{\phi k}\,\gamma_\mu\,\phi^\mu - g_{\rho k}\,\gamma_\mu\,\vec{t}\cdot\vec{\rho}^{\,\mu} \right] \psi_k + \\
& + \frac{1}{2}(\partial_\mu\sigma\partial^\mu\sigma - m_\sigma^2\sigma^2) - U(\sigma) + \\
& + \frac{1}{2}\,m_\omega^2\,\omega_\mu\omega^\mu + \frac{1}{4}\,c\,(g_{\omega N}^2\,\omega_\mu\omega^\mu)^2 - \frac{1}{4}F_{\mu\nu}F^{\mu\nu} + \\
& + \frac{1}{2}\,m_\phi^2\,\phi_\mu\phi^\mu - \frac{1}{4}P_{\mu\nu}P^{\mu\nu} + \\
& + \frac{1}{2}\,m_\rho^2\,\vec{\rho}_\mu\cdot\vec{\rho}^{\,\mu} + \frac{1}{4}\,d\,(g_{\rho N}^2\,\vec{\rho}_\mu\cdot\vec{\rho}^{\,\mu})^2 - \frac{1}{4}\vec{G}_{\mu\nu}\vec{G}^{\mu\nu} + \\
& + A(\sigma,\omega_\mu\omega^\mu)\,\vec{\rho}_\mu\cdot\vec{\rho}^{\,\mu} + \\
& + \overline{\psi}_{\Delta\,\nu}\left[i\gamma_\mu\partial^\mu - (m_\Delta - g_{\sigma\Delta}\sigma) - g_{\omega\Delta}\gamma_\mu\omega^\mu - g_{\rho\Delta}\gamma_\mu\vec{t}\cdot\vec{\rho}^{\,\mu} \right]\psi_\Delta^\nu
\end{aligned} \tag{2.9}$$

where the sum over k runs over the full octet of the lightest baryons (p, n, Λ, Σ^+, Σ^0, Σ^-, Ξ^0, and Ξ^-) interacting with the scalar isoscalar σ, vector isoscalars ω and ϕ, and vector isovector ρ meson fields, m_k is the vacuum baryon mass of the baryon k, $\vec{t}$ is the isospin operator, $U(\sigma)$ is the nonlinear self-interaction potential of the σ meson

$$U(\sigma) = \frac{1}{3}a\,(g_{\sigma N}\sigma)^3 + \frac{1}{4}b\,(g_{\sigma N}\sigma)^4, \tag{2.10}$$

the field-strength tensors for the ω, ϕ, and ρ mesons, are respectively

$$F_{\mu\nu} = \partial_\mu\omega_\nu - \partial_\nu\omega_\mu, \quad P_{\mu\nu} = \partial_\mu\phi_\nu - \partial_\nu\phi_\mu, \quad \vec{G}_{\mu\nu} = \partial_\mu\vec{\rho}_\nu - \partial_\nu\vec{\rho}_\mu, \tag{2.11}$$

and the function $A(\sigma,\omega_\mu\omega^\mu)$ introduces mixed ρ–σ and ρ–ω nonlinearities as in [25, 169]:

$$A(\sigma,\omega_\mu\omega^\mu) = g_{\rho N}^2\left[\sum_{i=1}^{6} a_i\sigma^i + \sum_{j=1}^{3} b_j(\omega_\mu\omega^\mu)^j\right]. \tag{2.12}$$

The last line of Eq. (2.9) contains the Δ-isobar contribution ($\Delta^{++},\Delta^+,\Delta^0,\Delta^-$), described by a Rarita–Schwinger spinor ψ_Δ^ν and coupled to σ, ω, and ρ with strength

$$x_{\sigma\Delta} \equiv \frac{g_{\sigma\Delta}}{g_{\sigma N}} = 1.15, \qquad x_{\omega\Delta} \equiv \frac{g_{\omega\Delta}}{g_{\omega N}} = 1.0, \qquad x_{\rho\Delta} \equiv \frac{g_{\rho\Delta}}{g_{\rho N}} = 1.0. \tag{2.13}$$

For the hyperons we adopt the SU(6)–motivated vector couplings and fit the scalar couplings to reproduce the empirical hyperon potentials at saturation,

$$U_\Lambda^{(N)} \simeq -28\ \text{MeV}, \qquad U_\Sigma^{(N)} \simeq +30\ \text{MeV}, \qquad U_\Xi^{(N)} \simeq -18\ \text{MeV}, \tag{2.14}$$

following [23, 170, 171]. In this way, the SFHo-HΔ model is consistent with nuclear data. With the parametrization adopted here, the maximum NS mass is below 2 $M_\odot$. This is not an issue for our purposes, since this EOS is meant to describe the *soft* hadronic branch in the two–families scenario. If one needs a hadronic EOS able to support 2 $M_\odot$ stars, stiffer parametrizations of the same SFHo family can be employed; see, *e.g.*, [23]. The used parameters are summarized in Table 2.2.

In the RMF approximation, baryons are treated as Dirac quasiparticles moving in classical (space–independent) meson fields. The field operators in Eq. (2.9) are replaced by their expectation values,

$$\begin{aligned}
\sigma &\rightarrow \langle\sigma\rangle \equiv \bar{\sigma} && (2.15)\\
\omega^\mu &\rightarrow \langle\omega^\mu\rangle = \delta^{\mu 0}\,\omega_0 \equiv \delta^{\mu 0}\,\bar{\omega} && (2.16)\\
\phi^\mu &\rightarrow \langle\phi^\mu\rangle = \delta^{\mu 0}\,\phi_0 \equiv \delta^{\mu 0}\,\bar{\phi} && (2.17)\\
\vec{\rho}^{\,\mu} &\rightarrow \langle\vec{\rho}^{\,\mu}\rangle = \delta^{\mu 0}\,\delta_{3a}\,\rho_{0,3} \equiv \delta^{\mu 0}\,\delta_{3a}\,\bar{\rho}, && (2.18)
\end{aligned}$$

so that only the time–like components of the vector mesons survive, and quantum fluctuations are neglected.

With these assumptions, the Dirac equations for the baryon octet ($k = p, n, \Lambda, \Sigma, \Xi$) and for the Δ–isobars read

$$\Big[i\gamma_\mu\partial^\mu - (m_k - g_{\sigma k}\bar{\sigma}) - \gamma_0\Big(g_{\omega k}\bar{\omega} + g_{\phi k}\bar{\phi} + g_{\rho k}\,t_{3k}\,\bar{\rho}\Big)\Big]\psi_k = 0, \tag{2.19}$$

where t_{3k} is the third component of the isospin of species k. From Eq. (2.19) one identifies the effective (Dirac) masses

$$m_k^* = m_k - g_{\sigma k}\bar{\sigma}, \tag{2.20}$$

and the effective single–particle energies

$$E_k^*(k) = \sqrt{k^2 + m_k^{*2}}, \tag{2.21}$$

where k labels the baryon octet and the delta quartet The corresponding effective chemical potentials are

$$\mu_k^* \;=\; \mu_k - g_{\omega k}\bar{\omega} - g_{\phi k}\bar{\phi} - g_{\rho k}\,t_{3k}\,\bar{\rho}. \tag{2.22}$$

The meson mean fields are fixed from the Euler–Lagrange equations applied to Eq. (2.9),

which reduces to self–consistent relations:

$$m_\sigma^2\bar{\sigma} + U'(\bar{\sigma}) - \bar{\rho}^2\frac{\partial A(\bar{\sigma},\bar{\omega})}{\partial\bar{\sigma}} = \sum_k g_{\sigma k}\, n_k^s, \tag{2.23}$$

$$m_\omega^2\bar{\omega} + c\, g_{\omega N}^4\,\bar{\omega}^3 + \bar{\rho}^2\frac{\partial A(\bar{\sigma},\bar{\omega})}{\partial\bar{\omega}} = \sum_k g_{\omega k}\, n_k, \tag{2.24}$$

$$m_\phi^2\bar{\phi} = \sum_k g_{\phi k}\, n_k, \tag{2.25}$$

$$m_\rho^2\bar{\rho} + d\, g_{\rho N}^4\,\bar{\rho}^3 + 2\,A(\bar{\sigma},\bar{\omega})\,\bar{\rho} = \sum_k g_{\rho k}\, t_{3k}\, n_k, \tag{2.26}$$

where the sums over k run over all populated baryons (octet and Δs). The scalar and number densities are

$$n_i^s = \langle\bar{\psi}_i\psi_i\rangle = \frac{g_i}{2\pi^2}\int_0^\infty \frac{m_i^*}{E_i^*(k)}\Big[\mathbf{f}_i(k,\mu_i^*,T) + \mathbf{f}_i(k,-\mu_i^*,T)\Big]k^2\,dk, \tag{2.27}$$

$$n_i = \langle\bar{\psi}_i\gamma^0\psi_i\rangle = \frac{g_i}{2\pi^2}\int_0^\infty \Big[\mathbf{f}_i(k,\mu_i^*,T) - \mathbf{f}_i(k,-\mu_i^*,T)\Big]k^2\,dk, \tag{2.28}$$

with spin–degeneracy $g_i = 2$ for octet baryons and $g_i = 4$ for deltas, and with Fermi–Dirac distribution in Eq. (2.4) with the single–particle energies in Eq. (2.21).

Inserting the solutions of Eqs. (2.23)–(2.26) back into the energy–momentum tensor gives the standard RMF expressions for energy density and pressure,

$$\varepsilon_B = \sum_i \frac{g_i}{2\pi^2}\int_0^\infty E_i^*(k)\,\Big[\mathbf{f}_i(k,\mu_i^*,T) + \mathbf{f}_i(k,-\mu_i^*,T)\Big]k^2\,dk + \tag{2.29}$$
$$+\frac{1}{2}m_\sigma^2\bar{\sigma}^2 + U(\bar{\sigma}) + \frac{1}{2}m_\omega^2\bar{\omega}^2 + \frac{3}{4}c\,g_{\omega N}^4\bar{\omega}^4 + \frac{1}{2}m_\phi^2\bar{\phi}^2 + \frac{1}{2}m_\rho^2\bar{\rho}^2 + \frac{3}{4}d\,g_{\rho N}^4\bar{\rho}^4 + A(\bar{\sigma},\bar{\omega}^2)\bar{\rho}^2,$$

$$P_B = \sum_i \frac{g_i}{6\pi^2}\int_0^\infty \frac{k^4}{E_i^*(k)}\Big[\mathbf{f}_i(k,\mu_i^*,T) + \mathbf{f}_i(k,-\mu_i^*,T)\Big]dk + \tag{2.30}$$
$$-\frac{1}{2}m_\sigma^2\bar{\sigma}^2 - U(\bar{\sigma}) + \frac{1}{2}m_\omega^2\bar{\omega}^2 + \frac{1}{4}c\,g_{\omega N}^4\bar{\omega}^4 + \frac{1}{2}m_\phi^2\bar{\phi}^2 + \frac{1}{2}m_\rho^2\bar{\rho}^2 + \frac{1}{4}d\,g_{\rho N}^4\bar{\rho}^4 + A(\bar{\sigma},\bar{\omega}^2)\bar{\rho}^2,$$

where the sum over i runs is for all the baryons. The entropy density, free energy density and all the other thermodynamic quantities can be computed with standard thermodynamic relations. The Fermi integrals are solved numerically as shown in Appendix C.

Since strong interactions conserve baryon number, electric charge, and strangeness, it is convenient to use these conserved quantities as inputs. Minimizing the appropriate thermodynamic potential under the constraints

$$n_B = \sum_i B_i n_i, \qquad Y_C = \sum_i C_i Y_i, \qquad Y_S = \sum_i S_i Y_i, \tag{2.31}$$

where B_i, C_i, and S_i[2] are, respectively, the baryon number, electric charge, and

[2]Note that in this work we define S_i as the number of s quarks in hadron i, so that $S_\Lambda = 1$. In much of the literature, however, the opposite convention is adopted and the strangeness quantum number of the Λ is taken to be $S_\Lambda = -1$.

strangeness carried by hadronic species i, and $Y_i \equiv n_i/n_B$, one finds that the chemical potentials of all species can be expressed in terms of the three chemical potentials conjugate to the conserved charges:

$$\mu_i = B_i\mu_B + C_i\mu_C + S_i\mu_S. \tag{2.32}$$

In a standard RMF treatment, the light pseudoscalar mesons (pions, kaons) do not contribute at the mean–field level, because the corresponding fields vanish. Following the phenomenological strategy of [165, 172, 173] we therefore include them (together with the light vector mesons) as an ideal Bose gas on top of the baryonic mean field, but with effective chemical potentials that are tied to the same meson fields that generate the baryonic interactions.

Concretely, for each meson species j (pseudoscalar: $\pi, K, \bar{K}, \eta, \eta'$; vector: $\rho, \omega, K^*, \bar{K}^*, \phi$) we add

$$P_M = \frac{1}{3}\sum_j g_j \int_0^\infty \frac{k^4}{2\pi^2\, E_j(k)}\, \mathbf{g}_j(k, \mu_j^*, T)\, dk, \tag{2.33}$$

$$\varepsilon_M = \sum_j g_j \int_0^\infty \frac{k^2}{2\pi^2}\, E_j(k)\, \mathbf{g}_j(k, \mu_j^*, T)\, dk, \tag{2.34}$$

$$n_j^M = g_j \int_0^\infty \frac{k^2}{2\pi^2}\, \mathbf{g}_j(k, \mu_j^*, T)\, dk, \tag{2.35}$$

with degeneracy $g_j = 1$ for pseudoscalar mesons and $g_j = 3$ for vector mesons, $E_j(k) = \sqrt{k^2 + m_j^2}$, and

$$\mathbf{g}_j(k, \mu_j^*, T) = \frac{1}{\exp\Big[(E_j(k) - \mu_j^*)/T\Big] - 1}, \qquad |\mu_j^*| \le m_j, \tag{2.36}$$

where the conditions $|\mu_j^*| \le m_j$ are related to the appearance of the Bose condensate after this threshold. The Bose integrals are solved numerically as shown in Appendix C.

The values of the effective meson chemical potentials μ_j^* are obtained from the physical meson chemical potentials μ_j, which follow from the strong–interaction equilibrium relations in Eq. (2.32) as functions of (μ_B, μ_C, μ_S), and are then rewritten in terms of the corresponding *effective* baryon chemical potentials [165, 172] (for instance, $\mu_{\pi^+} = \mu_C = \mu_p - \mu_n \;\rightarrow\; \mu^*_{\pi^+} = \mu^*_p - \mu^*_n$). In this way one finds

$$\mu^*_{\pi^+} = \mu^*_{\rho^+} = \mu^*_p - \mu^*_n \;=\; \mu_C - g_{\rho N}\,\bar{\rho}, \tag{2.37}$$

$$\mu^*_{K^+} = \mu^*_{K^{*+}} = \mu^*_p - \mu^*_\Lambda \;=\; (\mu_C - \mu_S) - (g_{\omega N} - g_{\omega\Lambda})\,\bar{\omega} - \tfrac{1}{2} g_{\rho N}\,\bar{\rho}, \tag{2.38}$$

$$\mu^*_{K^0} = \mu^*_{K^{*0}} = \mu^*_n - \mu^*_\Lambda \;=\; -\mu_S - (g_{\omega N} - g_{\omega\Lambda})\,\bar{\omega} + \tfrac{1}{2} g_{\rho N}\,\bar{\rho}, \tag{2.39}$$

while the other nonstrange neutral mesons have vanishing effective chemical potential, $\mu_j^* = 0$. The opposite–charge states are obtained by

$$\mu^*_{j^-} = -\,\mu^*_{j^+}. \tag{2.40}$$

Table 2.2: SFHo–HΔ parameters used in this thesis, written in the notation of Eq. (2.9).

Basic nuclear input			
n_0	0.1583 fm^{-3} (saturation density)		
Baryon masses			
m_p	938.2720 MeV	m_n	939.5653 MeV
m_Λ	1116 MeV	m_{Σ^+}	1189 MeV
m_{Σ^0}	1193 MeV	m_{Σ^-}	1197 MeV
m_{Ξ^0}	1315 MeV	m_{Ξ^-}	1321 MeV
m_Δ	1232 MeV		
Meson masses			
m_σ	467.9 MeV	m_ω	762.5 MeV
m_ρ	770 MeV	m_ϕ	1020 MeV
m_π	140 MeV	m_K	494 MeV
m_η	547 MeV	$m_{\eta'}$	958 MeV
m_{K^*}	892 MeV		
Nucleon–meson couplings			
$g_{\sigma N}$	7.536	$g_{\omega N}$	8.782
$g_{\rho N}$	9.384	$g_{\phi N}$	0
Hyperon–meson couplings (SU(6) + U_Y^N)			
Λ			
$g_{\sigma\Lambda}$	$0.605055\, g_{\sigma N}$	$g_{\omega\Lambda}$	$\frac{2}{3} g_{\omega N}$
$g_{\phi\Lambda}$	$-\frac{\sqrt{2}}{3} g_{\omega N}$	$g_{\rho\Lambda}$	0
Σ			
$g_{\sigma\Sigma}$	$0.346328\, g_{\sigma N}$	$g_{\omega\Sigma}$	$\frac{2}{3} g_{\omega N}$
$g_{\phi\Sigma}$	$-\frac{\sqrt{2}}{3} g_{\omega N}$	$g_{\rho\Sigma}$	$2 g_{\rho N}$
Ξ			
$g_{\sigma\Xi}$	$0.320371\, g_{\sigma N}$	$g_{\omega\Xi}$	$\frac{1}{3} g_{\omega N}$
$g_{\phi\Xi}$	$-\frac{2\sqrt{2}}{3} g_{\omega N}$	$g_{\rho\Xi}$	$g_{\rho N}$
Δ–isobar couplings			
Δ			
$g_{\sigma\Delta}$	$1.15\, g_{\sigma N}$	$g_{\omega\Delta}$	$g_{\omega N}$
$g_{\rho\Delta}$	$g_{\rho N}$	$g_{\phi\Delta}$	0
Nonlinear meson couplings			
a	7.0141 MeV (scalar self–interaction)	b	-4.0887×10^{-3} (scalar self–interaction)
c	-2.8355×10^{-4} (ω^4 self–interaction)	d	5.7542×10^{-4} (ρ^4 self–interaction)
Mixed ρ–σ and ρ–ω term $A(\sigma, \omega_\mu \omega^\mu)$			
a_1	-45.4168 MeV	a_2	5.7972×10^{-1}
a_3	1.74563×10^{-3} MeV^{-1}	a_4	8.88414×10^{-5} MeV^{-2}
a_5	1.7535×10^{-7} MeV^{-3}	a_6	4.35712×10^{-10} MeV^{-4}
b_1	5.8729	b_2	-4.22262×10^{-5} MeV^{-2}
b_3	2.07524×10^{-7} MeV^{-4}		

The total hadronic thermodynamics is then obtained as

$$X_H = X_B + X_M, \tag{2.41}$$

with $X = P,\, \varepsilon,\, s,\, f$.

2.2 Homogeneous deconfined quark matter

In this section we describe uniform deconfined quark matter using a family of bag–type models. The common ingredient of all of them is the bag constant B, which models confinement at the mean–field level by acting as an external vacuum pressure that

balances the quark kinetic and interaction pressure. In thermodynamic terms, B represents the energy–density difference between the non–perturbative QCD vacuum and the perturbative one, and appears as a positive shift in the energy density and a negative shift in the pressure of the quark phase.

I first introduce a vector–enhanced MIT bag (vMIT) model, which augments the classic MIT bag EOS with repulsive vector interactions to stiffen the quark matter at high density. I then move to the αBag model for unpaired quark matter, where leading–order perturbative QCD corrections in the strong coupling α_s are added on top of a finite–temperature MIT–like structure. Finally, I extend this framework to the color–superconducting CFL phase, in which pairing contributions are included explicitly in the thermodynamic quantities and the flavor densities are locked by the CFL pairing pattern.

Bag models provide a simple, flexible parametrization of quark matter, but they do not treat chiral symmetry breaking and encode confinement only through the phenomenological constant B. Other approaches, such as Nambu–Jona-Lasinio (NJL)–type models [1], can describe dynamical chiral symmetry breaking but lack confinement. Several extensions have been proposed to capture (at least partially) both aspects, including the Polyakov–loop–extended NJL (PNJL) [174, 175] models and color–dielectric models [176, 177], where an effective medium–dependent gluonic background mimics confinement. In this thesis, however, I adopt the bag–type EOSs introduced below because they are thermodynamically consistent, computationally efficient, and sufficiently flexible to explore the impact of deconfinement on astrophysics phenomenology.

2.2.1 vMIT model

The vMIT model [26] is a bag model [59] in which perturbative QCD corrections are neglected and replaced by a repulsive vector interaction among quarks, mediated by an isoscalar vector meson V^μ. The inclusion of a repulsive vector interaction stiffens the quark EOS and allows for larger HS and QS maximum masses [178]. The vMIT model has been widely used in astrophysical applications [20, 40, 41, 45, 98, 166, 179, 180].

The Lagrangian density of bulk quark matter in the vMIT model can be written as

$$\mathcal{L} = \left\{ \sum_{q=u,d,s} \bar{\psi}_q \left[i\gamma_\mu \partial^\mu - m_q - g_V \gamma_\mu V^\mu \right] \psi_q + \frac{1}{2} m_V^2 V_\mu V^\mu - B \right\} \Theta, \tag{2.42}$$

where ψ_q are the quark fields of flavor q, m_q are the current quark masses, g_V is the vector coupling, m_V is the mass of the vector meson, B is the bag constant, and Θ is the Heaviside step function implementing confinement ($\Theta = 1$ inside the bag and $\Theta = 0$ outside). For homogeneous bulk matter, we can simply set $\Theta = 1$.

The field equation at the mean–field level ($V^\mu \to \langle V^\mu \rangle = \delta^{\mu 0} V_0 \equiv \delta^{\mu 0} \bar{V}$) is

$$m_V^2 \bar{V} = g_V \sum_{q=u,d,s} \langle \bar{\psi}_q \gamma^0 \psi_q \rangle = g_V \sum_{q=u,d,s} n_q = g_V n_B \sum_{q=u,d,s} Y_q, \tag{2.43}$$

where n_q is the net number density of quarks of flavor q and $Y_q \equiv n_q/n_B$ its fraction.

It is convenient to define the kinetic single–particle energy

$$E_q^*(k) = \sqrt{k^2 + m_q^2}, \tag{2.44}$$

so that the total single–particle energy is $E_q(k) = E_q^*(k) + g_V \bar{V}$. The effective chemical potential is

$$\mu_q^* = \mu_q - g_V \bar{V} = \mu_q - a \sum_{i=u,d,s} n_i, \tag{2.45}$$

where we have introduced the parameter $a \equiv g_V^2/m_V^2$.

The net quark number densities are

$$n_q = Y_q n_B = \langle \bar{\psi}_q \gamma^0 \psi_q \rangle = \frac{g_q}{2\pi^2} \int_0^\infty \left[\mathbf{f}_q(k, \mu_q^*, T) - \mathbf{f}_q(k, -\mu_q^*, T) \right] k^2 \, dk, \tag{2.46}$$

where $g_q = 2_{spin} \times 3_{color} = 6$ is the degeneracy factor and $\mathbf{f}_q(k, \mu_q^*, T)$ are the Fermi–Dirac distribution functions defined in Eq. (2.4), with $E_q^*(k)$ given by Eq. (2.44). The baryon density is

$$n_B = \frac{1}{3} \sum_{q=u,d,s} n_q. \tag{2.47}$$

It is also useful to define the electric charge and strangeness fractions,

$$Y_C = \frac{2}{3} Y_u - \frac{1}{3} Y_d - \frac{1}{3} Y_s, \tag{2.48}$$

$$Y_S = Y_s. \tag{2.49}$$

The quark energy density is

$$\begin{aligned} \varepsilon_Q = & \sum_{q=u,d,s} \frac{g_q}{2\pi^2} \int_0^\infty E_q^*(k) \left[\mathbf{f}_q(k, \mu_q^*, T) + \mathbf{f}_q(k, -\mu_q^*, T) \right] k^2 \, dk \\ & + \frac{1}{2} a \left[n_B \left(\sum_{q=u,d,s} Y_q \right) \right]^2 + B, \end{aligned} \tag{2.50}$$

while the quark pressure is

$$\begin{aligned} P_Q = & \sum_{q=u,d,s} \frac{g_q}{6\pi^2} \int_0^\infty \frac{k^4}{E_q^*(k)} \left[\mathbf{f}_q(k, \mu_q^*, T) + \mathbf{f}_q(k, -\mu_q^*, T) \right] dk \\ & + \frac{1}{2} a \left[n_B \left(\sum_{q=u,d,s} Y_q \right) \right]^2 - B. \end{aligned} \tag{2.51}$$

The Fermi integrals are computed numerically as in Appendix C, and all the other thermodynamic quantities are obtained from standard thermodynamic relations.

The chosen parameters are reported in Table 2.3

Table 2.3: Parameter sets used in the present work for the vMIT EOS model.

Parameter	Value	Units
m_u	5.0	MeV
m_d	7.0	MeV
m_s	150.0	MeV
a	0.20	fm^2
$B^{1/4}$	180	MeV

2.2.2 αBag (unpaired) model

The αBag is a MIT Bag model supplemented by leading–order perturbative QCD corrections in α_s [59, 60]. The finite–temperature generalization follows the prescription of [181], in which kinetic contributions from massive quarks are combined with the analytic perturbative corrections for massless quarks. The same approach has been used in [46]. In this subsection we will discuss the *unpaired* case $Q_{\rm unp}$ while in the following subsection we will present the color superconducting *CFL* $Q_{\rm CFL}$ model.

For each flavor $q = u, d, s$ we define the net number density, pressure, energy density, and entropy density,

$$n_i^Q(\mu_i, T), \quad P_i^Q(\mu_i, T), \quad \varepsilon_i^Q(\mu_i, T), \quad s_i^Q(\mu_i, T), \tag{2.52}$$

from which the thermodynamic quantities of the unpaired quark sector are

$$n_B^{Q_{\rm unp}}(\{\mu_i\}, T) = \frac{1}{3} \sum_{i=u,d,s} n_i^Q(\mu_i, T), \tag{2.53}$$

$$P_{Q_{\rm unp}}(\{\mu_i\}, T) = \sum_{i=u,d,s} P_i^Q(\mu_i, T) - B_{\rm unp}, \tag{2.54}$$

$$\varepsilon_{Q_{\rm unp}}(\{\mu_i\}, T) = \sum_{i=u,d,s} \varepsilon_i^Q(\mu_i, T) + B_{\rm unp}, \tag{2.55}$$

$$s_{Q_{\rm unp}}(\{\mu_i\}, T) = \sum_{i=u,d,s} s_i^Q(\mu_i, T), \tag{2.56}$$

$$\tag{2.57}$$

where $B_{\rm unp}$ is the bag constant of the unpaired phase.

For massless quarks ($m_i = 0$) the flavor contributions can be computed analytically including the leading one–gluon–exchange corrections [59, 65]. For a given flavor i one

finds

$$n_q(\mu_i, T, m_i = 0, \alpha_s) = \left(\mu_i T^2 + \frac{\mu_i^3}{\pi^2}\right)\left(1 - \frac{2\alpha_s}{\pi}\right), \tag{2.58}$$

$$P_q(\mu_i, T, m_i = 0, \alpha_s) = \frac{7\pi^2}{60}T^4\left(1 - \frac{50\alpha_s}{21\pi}\right) + \left(\frac{1}{2}T^2\mu_i^2 + \frac{\mu_i^4}{4\pi^2}\right)\left(1 - \frac{2\alpha_s}{\pi}\right), \tag{2.59}$$

$$\varepsilon_q(\mu_i, T, m_i = 0, \alpha_s) = 3\,P_q(\mu_i, T, m_i = 0, \alpha_s), \tag{2.60}$$

$$s_q(\mu_i, T, m_i = 0, \alpha_s) = \frac{7\pi^2}{15}T^3\left(1 - \frac{50\alpha_s}{21\pi}\right) + T\mu_i^2\left(1 - \frac{2\alpha_s}{\pi}\right), \tag{2.61}$$

which correspond to the lowest–order gluon–exchange corrections to a massless Fermi gas with degeneracy $2_{\text{spin}} \times 3_{\text{color}} = 6$.

For non–interacting *massive* quarks ($\alpha_s = 0$), the finite–T thermodynamic quantities are given by relativistic Fermi integrals,

$$n_q(\mu_i, T, m_i, \alpha_s = 0) = \frac{6}{2\pi^2}\int_0^{+\infty} k^2\left[\mathbf{f}_i(k, \mu_i, T) - \mathbf{f}_i(k, -\mu_i, T)\right] dk, \tag{2.62}$$

$$P_q(\mu_i, T, m_i, \alpha_s = 0) = \frac{6}{2\pi^2}\frac{1}{3}\int_0^{+\infty} \frac{k^4}{E(k, m_i)}\left[\mathbf{f}_i(k, \mu_i, T) + \mathbf{f}_i(k, -\mu_i, T)\right] dk, \tag{2.63}$$

$$\varepsilon_q(\mu_i, T, m_i, \alpha_s = 0) = \frac{6}{2\pi^2}\int_0^{+\infty} k^2 E(k, m_i)\left[\mathbf{f}_i(k, \mu_i, T) + \mathbf{f}_i(k, -\mu_i, T)\right] dk \tag{2.64}$$

where $E(k, m_i) = \sqrt{k^2 + m_i^2}$ and $\mathbf{f}_i$ is the Fermi–Dirac distribution defined in Eq. (2.4) (with $\mu_i^* = \mu_i$). The integrals are computed as shown in Appendix C.

Following [181], we obtain the thermodynamic quantities for interacting massive quarks by combining the massive ideal–gas results with the analytic massless $\mathcal{O}(\alpha_s)$ corrections:

$$X_q^Q(\mu_i, T) = X_q(\mu_q, T, m_q, \alpha_s = 0) + \left[X_q(\mu_q, T, m_q = 0, \alpha_s) - X_q(\mu_q, T, m_q = 0, \alpha_s = 0)\right], \tag{2.65}$$

where $X = P, \varepsilon, s, f, n_i$. Thus,

$$n_i^Q(\mu_i, T) = n_q(\mu_i, T, m_i, \alpha_s = 0) - \frac{2\alpha_s}{\pi}\left(\mu_i T^2 + \frac{\mu_i^3}{\pi^2}\right), \tag{2.66}$$

$$P_i^Q(\mu_i, T) = P_q(\mu_i, T, m_i, \alpha_s = 0) - \frac{5\pi\alpha_s}{18}T^4 - \frac{2\alpha_s}{\pi}\left(\frac{1}{2}T^2\mu_i^2 + \frac{\mu_i^4}{4\pi^2}\right), \tag{2.67}$$

$$\varepsilon_i^Q(\mu_i, T) = \varepsilon_q(\mu_i, T, m_i, \alpha_s = 0) - \frac{15\pi\alpha_s}{18}T^4 - \frac{6\alpha_s}{\pi}\left(\frac{1}{2}T^2\mu_i^2 + \frac{\mu_i^4}{4\pi^2}\right), \tag{2.68}$$

$$s_i^Q(\mu_i, T) = s_q(\mu_i, T, m_i, \alpha_s = 0) - \frac{10\pi\alpha_s}{9}T^3 - \frac{2\alpha_s}{\pi}T\mu_i^2. \tag{2.69}$$

Operationally, the first term in each line represents the kinetic contribution of a massive, non–interacting Fermi gas, while the second term encodes the leading one–gluon–exchange correction extracted from the massless limit. The strong coupling α_s is treated as a fixed model parameter. Its effect is twofold: it stiffens the EOS as a function of density (increasing the pressure at fixed n_B), but it also decreases the pressure as a function

of the quark chemical potential (or equivalently, increases the free energy as a function of the quark density), making quark matter less thermodynamically favored.

All thermodynamic quantities can be expressed either in terms of $(\{\mu_i^Q\}, T)$ or, equivalently, in terms of $(n_B^Q, \{Y_i^Q\}, T)$:

$$n_i^Q(\mu_i, T) = n_B^Q\, Y_i^Q, \qquad Y_i^Q = \frac{n_i^Q}{n_B^Q}. \tag{2.70}$$

2.2.3 αBag (CFL) model

The color–superconducting color–flavor–locked (CFL) phase [54] is described with an αBag–inspired model, in which the pairing contribution is added on top of the unpaired αBag quark EOS in a way analogous to Refs. [66]. Denoting by $n_i^Q(\mu_i, T)$, $P_i^Q(\mu_i, T)$, $\varepsilon_i^Q(\mu_i, T)$, and $s_i^Q(\mu_i, T)$ the quantities of the quark flavor i as in Eqs. (2.66, 2.67, 2.68, 2.69) from Sec. 2.2.2, the CFL–modified thermodynamic quantities are

$$n_i^{Q_{\rm CFL}}(\{\mu_i\}, T) = n_i^Q(\mu_i, T) + \frac{2}{\pi^2}\,\mu_i\,\Delta(T)^2, \tag{2.71}$$

$$n_B^{Q_{\rm CFL}}(\{\mu_i\}, T) = \frac{1}{3}\sum_{i=u,d,s}\left[n_i^Q(\mu_i, T) + \frac{2}{\pi^2}\,\mu_i\,\Delta(T)^2\right], \tag{2.72}$$

$$P_{Q_{\rm CFL}}(\{\mu_i\}, T) = \sum_{i=u,d,s} P_i^Q(\mu_i, T) + \frac{\Delta(T)^2}{\pi^2}\sum_{i=u,d,s}\mu_i^2 - B_{\rm CFL}, \tag{2.73}$$

$$s_{Q_{\rm CFL}}(\{\mu_i\}, T) = \sum_{i=u,d,s} s_i^Q(\mu_i, T) + \frac{2}{\pi^2}\,\Delta(T)\,\frac{\partial\Delta(T)}{\partial T}\sum_{i=u,d,s}\mu_i^2, \tag{2.74}$$

$$f_{Q_{\rm CFL}}(\{\mu_i\}, T) = -P_{Q_{\rm CFL}}(\{\mu_i\}, T) + \sum_{i=u,d,s}\mu_i\, n_i^{Q_{\rm CFL}}(\{\mu_i\}, T), \tag{2.75}$$

$$\varepsilon_{Q_{\rm CFL}}(\{\mu_i\}, T) = f_{Q_{\rm CFL}}(\{\mu_i\}, T) + T\, s_{Q_{\rm CFL}}(\{\mu_i\}, T), \tag{2.76}$$

where $B_{\rm CFL}$ is the bag constant in the CFL phase and $\Delta(T)$ is the CFL pairing gap.

The temperature dependence of the gap is modeled as [54, 182]

$$\Delta(T) = \Theta(T_c - T)\,\Delta_0\sqrt{1 - \frac{T}{T_c}}, \tag{2.77}$$

where Θ is the Heaviside step function, Δ_0 is the zero–temperature gap, and the critical temperature is taken as

$$T_c \simeq 2^{1/3} \times 0.57\,\Delta_0. \tag{2.78}$$

In the CFL phase the pairing pattern enforces equal number densities of up, down, and strange quarks, so the quark chemical potentials are no longer independent. Instead, for a given baryon density and temperature, the set $\{\mu_i\}$ is determined by the conditions

$$n_u^{Q_{\rm CFL}}(\{\mu_i\}, T) = n_d^{Q_{\rm CFL}}(\{\mu_i\}, T) = n_s^{Q_{\rm CFL}}(\{\mu_i\}, T). \tag{2.79}$$

If not otherwise specified in the text, we consider two parametrizations for this model

as reported in Table 2.4. These parametrizations correspond to maximum non rotating QS masses of $2.20\,M_\odot$ for (Q1) and $2.57\,M_\odot$ for (Q2), the latter mainly considered to account for the possibility that the $\simeq (2.5-2.6)\,M_\odot$ object observed in GW190814 [19] is a compact star.

Table 2.4: Parameter sets used in the present work for the αBag EOS model.

Parameter	Value	Units
m_u	0	MeV
m_d	0	MeV
m_s	100	MeV
α_s	$\pi/2 \times 0.1$	
$B_{\rm unp}^{1/4}$	specified in text	MeV
$B_{\rm CFL}^{1/4}$	(Q1): 145 (Q2): 135	MeV
Δ_0	80	MeV

2.3 Leptons

Electrons and positrons are treated as a massive, non–interacting Fermi gas with spin degeneracy $g_e = 2$:

$$n_e(\mu_e,T) = \frac{2}{2\pi^2}\int_0^{+\infty} k^2\left[\mathbf{f}_e(k,\mu_e,T) - \mathbf{f}_e(k,-\mu_e,T)\right]\,dk, \tag{2.80}$$

$$P_e(\mu_e,T) = \frac{2}{2\pi^2}\frac{1}{3}\int_0^{+\infty} \frac{k^4}{E(k,m_e)}\left[\mathbf{f}_e(k,\mu_e,T) + \mathbf{f}_e(k,-\mu_e,T)\right]\,dk, \tag{2.81}$$

$$\varepsilon_e(\mu_e,T) = \frac{2}{2\pi^2}\int_0^{+\infty} k^2 E(k,m_e)\left[\mathbf{f}_e(k,\mu_e,T) + \mathbf{f}_e(k,-\mu_e,T)\right]\,dk, \tag{2.82}$$

$$s_e(\mu_e,T) = \frac{1}{T}\left[P_e(\mu_e,T) + \varepsilon_e(\mu_e,T) - \mu_e\, n_e(\mu_e,T)\right], \tag{2.83}$$

where $\mathbf{f}_e(k,\pm\mu_e,T)$ is the Fermi distribution and $E(k,m_e) = \sqrt{k^2+m_e^2}$. See Appendix C for the numerical solution of the Fermi integrals.

Neutrinos are treated as a massless, non–interacting Fermi gas with degeneracy $g_\nu = 1$:

$$n_\nu(\mu_\nu,T) = \frac{1}{6}\left(\mu_\nu T^2 + \frac{1}{\pi^2}\mu_\nu^3\right), \tag{2.84}$$

$$P_\nu(\mu_\nu,T) = \frac{1}{6}\left(\frac{7}{60}\pi^2 T^4 + \frac{1}{2}T^2\mu_\nu^2 + \frac{1}{4\pi^2}\mu_\nu^4\right), \tag{2.85}$$

$$\varepsilon_\nu(\mu_\nu,T) = 3\,P_\nu(\mu_\nu,T), \tag{2.86}$$

$$s_\nu(\mu_\nu,T) = \frac{1}{6}\left(\frac{7}{15}\pi^2 T^3 + T\mu_\nu^2\right). \tag{2.87}$$

As for the quark phase, the thermodynamic quantities of electrons (neutrinos) can

be written in terms of (n_e, T) $[(n_\nu, T)]$ as independent variables rather than (μ_e, T) $[(\mu_\nu, T)]$, by inverting the corresponding density relations when needed. Muons could also, in principle, play a role in high–energy astrophysical systems (see, for example, [183]), at least in the hadronic phase, but they will not be included explicitly in the present EOS.

2.4 Thermal bosons

Photons will be treated as an ideal boson gas with zero chemical potential (i.e., as blackbody radiation):

$$P_\gamma(T) = \frac{\pi^2}{45} T^4 \tag{2.88}$$

$$\varepsilon_\gamma(T) = 3P_\gamma(T) \tag{2.89}$$

$$s_\gamma(T) = \frac{4\pi^2}{45} T^3. \tag{2.90}$$

The contribution of thermal gluons is [65]

$$P_g(T) = \frac{8\pi^2}{45} T^4 \left(1 - \frac{15\alpha_s}{4\pi}\right) \tag{2.91}$$

$$\varepsilon_g(T) = 3P_g(T) \tag{2.92}$$

$$s_g(T) = \frac{32\pi^2}{45} T^3 \left(1 - \frac{15\alpha_s}{4\pi}\right). \tag{2.93}$$

2.5 Total homogeneous phases

The total thermodynamic quantities for the hadronic and quark phases can be written as

$$X_{HL\gamma}(n_B, \{Y_i\}, T) = X_H(n_B, \{Y_h\}, T) + X_L(n_B, \{Y_\ell\}, T) + X_\gamma(T), \tag{2.94}$$

$$X_{QL\gamma}(n_B, \{Y_i\}, T) = X_Q(n_B, \{Y_q\}, T) + X_L(n_B, \{Y_\ell\}, T) + X_\gamma(T) + X_g(T) \tag{2.95}$$

where $X = P, \varepsilon, s, f$, i runs over all particle species, h over hadrons, q over quark flavors, and ℓ over leptons (electrons and neutrinos). The leptonic contribution is

$$X_L(n_B, \{Y_\ell\}, T) = X_e(n_B, Y_e, T) + X_\nu(n_B, Y_{\nu_e}, T) + 2\, X_\nu(n_B, 0, T), \tag{2.96}$$

where the last term represents thermal μ and τ neutrinos and antineutrinos.

To avoid overloading the notation, in what follows we will denote by X_H and X_Q the *total* hadronic and quark phases, including leptons, photons, and thermal gluons, unless explicitly stated otherwise.

In principle, the independent variables are the set of particle densities $\{n_i\}$ (or equiv-

alently n_B and $\{Y_i \equiv n_i/n_B\}$), or the set of chemical potentials $\{\mu_i\}$, together with the temperature T. However, it is convenient to exploit conservation laws and chemical–equilibrium conditions and to work in terms of conserved charges and a reduced set of chemical potentials.

The relevant possible globally conserved charges for the systems considered in this thesis are

$$N_B = \sum_i B_i N_i \quad \Rightarrow \quad n_B = \sum_i B_i n_i, \tag{2.97}$$

$$N_C = \sum_i C_i N_i \quad \Rightarrow \quad Y_C \equiv \frac{n_C}{n_B} = \sum_i C_i Y_i, \tag{2.98}$$

$$N_S = \sum_i S_i N_i \quad \Rightarrow \quad Y_S \equiv \frac{n_S}{n_B} = \sum_i S_i Y_i, \tag{2.99}$$

$$N_{Q_{\rm tot}} = \sum_i q_i N_i \quad \Rightarrow \quad Y_{Q_{\rm tot}} \equiv \frac{n_{Q_{\rm tot}}}{n_B} = \sum_i q_i Y_i, \tag{2.100}$$

$$N_L = \sum_i L_i N_i \quad \Rightarrow \quad Y_L \equiv \frac{n_L}{n_B} = \sum_i L_i Y_i, \tag{2.101}$$

where each species i is characterized by its baryon number B_i, nonleptonic charge C_i (which can be mapped to isospin), strangeness S_i, electron–family lepton number L_i, and physical electric charge q_i (in units of e). Note that the three strong charges B, C, S can be mapped to quark flavor contents u, d, s of the specie i.

The quantum numbers for all particles used in this work are summarized in Table 2.5.

The total electric charge $Q_{\rm tot}$ is globally conserved and, for electrically neutral matter, vanishes:

$$Y_{Q_{\rm tot}} = Y_C - Y_e = 0. \tag{2.102}$$

Whenever a given set of charges is effectively conserved on the relevant timescales, chemical equilibrium (i.e. minimization of the appropriate thermodynamic potential under the corresponding constraints) implies that the chemical potential of species i can be written as

$$\mu_i = B_i\,\mu_B + C_i\,\mu_C + S_i\,\mu_S + L_i\,\mu_L, \tag{2.103}$$

where only the chemical potentials associated with the charges that are *actually conserved* in the physical situation under consideration are retained. Formally, one could also introduce a chemical potential $\mu_{Q_{\rm tot}}$ conjugate to $Q_{\rm tot}$, but for globally neutral matter $Q_{\rm tot} = 0$ implies $\mu_{Q_{\rm tot}} = 0$, so it does not appear explicitly.

Depending on which interactions have equilibrated, different subsets of charges remain conserved, and different reduced sets of independent variables can be used. In the following, we summarize the main cases relevant for this thesis.

If only strong interactions are operative (no weak processes), the strong charges B, C, S and the lepton number L are conserved. Chemical equilibrium under these constraints is obtained by imposing Eq. (2.103) and the conservation relations (2.97)–(2.101). In this case, the EOS can be parameterized as

$$(\{\mu_i\}, T) \;\longrightarrow\; (n_B, Y_C, Y_S, Y_L, T). \tag{2.104}$$

This corresponds to a situation in which the system is in equilibrium with respect to strong interactions, but weak processes have not yet altered the flavor or lepton content (e.g. very early stages of heavy–ion collisions or the initial configuration in nucleation calculations; see Chapter 4.3.4).

If nonleptonic weak processes such as

$$u + d \leftrightarrow u + s \tag{2.105}$$

are fast enough to reach equilibrium, strangeness S is no longer conserved. Then the minimization of the thermodynamic potential implies

$$\mu_S = 0. \tag{2.106}$$

In terms of microscopic chemical potentials this condition gives

$$\mu_s - \mu_d = 0, \tag{2.107}$$
$$\mu_\Lambda - \mu_n = 0, \tag{2.108}$$

which are precisely the equilibrium conditions for processes of the type (2.105). Such a situation can be approximately realized, for example, in hot/dense matter in CCSNe and binary compact–star mergers. In this case the EOS can be parameterized as

$$(\{\mu_i\}, T) \longrightarrow (n_B, Y_C, Y_L, T). \tag{2.109}$$

If, in addition, charged–current β processes such as

$$u + e^- \leftrightarrow d + \nu_e \tag{2.110}$$

have equilibrated, then the nonleptonic charge C is no longer conserved. The corresponding equilibrium condition is

$$\mu_C = 0, \tag{2.111}$$

which, in terms of hadronic and quark chemical potentials, reproduces the usual β–equilibrium relations

$$\mu_u + \mu_e = \mu_d + \mu_{\nu_e}, \tag{2.112}$$
$$\mu_p + \mu_e = \mu_n + \mu_{\nu_e}. \tag{2.113}$$

Such conditions are relevant, for instance, in proto neutron stars, where neutrinos are trapped on dynamical timescales. The EOS can be written as

$$(\{\mu_i\}, T) \longrightarrow (n_B, Y_L, T). \tag{2.114}$$

If neutrinos are no longer trapped (their mean free path exceeds the system size), electron–type lepton number is not conserved and $\mu_L = 0$, hence $\mu_{\nu_e} = 0$. In cold compact stars, all relevant weak processes have equilibrated, matter is globally charge

neutral, and neutrinos are untrapped, so the EOS reduces to

$$(\{\mu_i\}, T) \longrightarrow (n_B, T). \tag{2.115}$$

In simulations of CCSNe and BCSMs, neutrinos are typically treated via separate kinetic transport rather than as part of the hydrodynamic EOS. Consequently, neutrino contributions are omitted from the EOS tables used in the hydrodynamics, and one works with (n_B, Y_C, T) as independent variables [28]. This separation is well motivated by the thermodynamic role of neutrinos. Strict neutrinoless β–equilibrium ($\mu_n = \mu_p + \mu_e$) is exact only at $T = 0$ [114, 115]. At high temperatures the neutrino mean free path can become much smaller than the system size, so neutrinos are trapped and in equilibrium with matter, while at low temperatures they stream freely and effectively decouple. In the intermediate regime, where matter is too hot to neglect neutrinos entirely but not hot or dense enough for complete neutrino trapping, reaction rates must be treated explicitly. In particular, [114, 115] show that in this regime electron capture is much less suppressed than neutron decay (detailed balance is not satisfied), so the $T = 0$ β–equilibrium condition requires a model–dependent correction. A similar caveat applies to muons: at sufficiently high densities and/or temperatures, muons and muon neutrinos can be thermally and weakly produced in CCSNe and BNSMs, modifying charge and lepton balance and impacting the dynamics (see, e.g., [183]). However, they are typically not included in the tabulated EOS, and their contribution is instead accounted for either in post–processing approaches [183] or self–consistently through dedicated transport schemes [184].

In this section we have discussed only the equilibrium conditions at fixed conserved charges in homogeneous phases. The corresponding conditions for phase coexistence between hadronic and quark matter (mixed phases) are addressed in Appendix A.

Table 2.5: Quantum numbers for the hadrons (octet and Δ isobars), light quarks, mesons, and leptons included in this thesis. Here B_i is the baryon number, C_i the nonleptonic electric charge (which can be replaced by isospin), q_i the physical electric charge (in units of e), S_i the strangeness (defined such that $S_s = +1$), and L_i the electron–family lepton number.

Species i	B_i	C_i	q_i	S_i	L_i
		Baryons			
p	1	$+1$	$+1$	0	0
n	1	0	0	0	0
Λ	1	0	0	$+1$	0
Σ^+	1	$+1$	$+1$	$+1$	0
Σ^0	1	0	0	$+1$	0
Σ^-	1	-1	-1	$+1$	0
Ξ^0	1	0	0	$+2$	0
Ξ^-	1	-1	-1	$+2$	0
Δ^{++}	1	$+2$	$+2$	0	0
Δ^+	1	$+1$	$+1$	0	0
Δ^0	1	0	0	0	0
Δ^-	1	-1	-1	0	0
		Quarks			
u	1/3	$+2/3$	$+2/3$	0	0
d	1/3	$-1/3$	$-1/3$	0	0
s	1/3	$-1/3$	$-1/3$	$+1$	0
		Mesons			
π^+	0	$+1$	$+1$	0	0
π^0	0	0	0	0	0
π^-	0	-1	-1	0	0
K^+	0	$+1$	$+1$	-1	0
K^0	0	0	0	-1	0
K^-	0	-1	-1	$+1$	0
$\bar{K}^0$	0	0	0	$+1$	0
		Leptons			
e^-	0	0	-1	0	$+1$
e^+	0	0	$+1$	0	-1
ν_e	0	0	0	0	$+1$
$\bar{\nu}_e$	0	0	0	0	-1

Part II

Deconfinement in hybrid stars

Chapter 3

A new framework for local–global charge neutrality first–order phase transitions

The hadron–quark deconfinement phase transition in dense matter is usually modeled with either a Maxwell–like ("strong") or a Gibbs–like ("soft") construction. The *Maxwell construction* (MC) is the equilibrium solution for a first–order transition when only one global conserved charge is enforced. In this case the pressure remains constant throughout the mixed phase. The *Gibbs construction* (GC), instead, is the correct equilibrium solution when at least two independent charges are conserved globally; then the pressure varies continuously as a function of the other thermodynamic variables across the mixed phase.

In cold, neutrinoless β–equilibrated matter, as in cold compact stars, MC and GC correspond to two limiting prescriptions for electric charge neutrality. In the MC limit, the baryon number is the only globally conserved charge and electric charge neutrality is imposed *locally* in each phase (LCN). In the GC limit, both baryon number and total electric charge are conserved globally, so that charge neutrality is enforced only *globally* (GCN) across the mixed phase (see Sec. 1.3.1).

These two limits are commonly used as bulk approximations to mimic finite–size effects. In practice, the actual surface and Coulomb contributions are neglected and replaced by either an LCN or GCN treatment, depending on the competition between surface tension, Coulomb energy, and screening. Roughly speaking, LCN corresponds to the limit $\sigma \to \infty$, while GCN corresponds to $\sigma \to 0$ (see Sec. 1.3.1 for details).

For EOS tables used in simulations of CCSNe and BNSMs, however, β equilibrium is not assumed and Y_C (or equivalently Y_e) is treated as an independent input variable. Equivalently, the non–leptonic electric charge is globally conserved in addition to the baryon number. In many simulations a MC is nevertheless imposed even when Y_C is fixed, *i.e.* when at least two independent charges are conserved and the proper equilibrium solution would be of Gibbs type. This inconsistency can have a direct impact on observables in both merger and CCSN simulations (see Sec. 1.3.3).

The aim of this chapter is to introduce a thermodynamically consistent framework

that enables continuous interpolation between purely LCN and purely GCN, thereby treating all cases between these two extremes.

In cold β–equilibrated matter, the two endpoints reproduce the standard MC and GC; at finite temperature and out of β equilibrium, they correspond, respectively, to the fully LCN and GCN limits. The framework is designed to produce EOS tables with a mixed phase that can be used directly in high–energy astrophysical simulations.

In this work, we apply the framework to a hadron–quark transition modeled with the ZL EOS for nucleons (Sec. 2.1.1) and the vMIT EOS for quarks (Sec. 2.2.1). For simplicity we include only nucleons in the hadronic sector and only electrons in the leptonic sector; muons and neutrinos are neglected (see Sec. 2.5). The zero–temperature version of the framework was introduced in [40], while the finite–temperature, out–of–β generalization was presented in [41]. Here we summarize and adapt the formalism for use in this thesis.

3.1 Framework

In this framework we imagine that hadronic (H) and quark (Q) phases coexist in the mixed phase with a *quasi–permeable* interface for leptons. In the vicinity of this interface, the two phases can exchange leptons, which then help neutralize electric charge across both phases, while regions farther away remain effectively locally charge neutral.

Charge neutrality is therefore realized *partly locally* and *partly globally*.

To parametrize the degree of mixing we introduce a dimensionless parameter

$$\eta \in [0, 1], \tag{3.1}$$

which measures the fraction of electrons that enforce LCN separately in each phase. The remaining fraction $1 - \eta$ participates only in GCN.

An equivalent picture is that of pure–phase "lumps" forming in the coexistence region. If the characteristic size of these structures is much larger than the Debye screening length, electrons are effectively tied to individual lumps and charge neutrality is local. If their size is much smaller than the screening length, electrons experience an averaged background and charge neutrality becomes purely global. Intermediate sizes correspond to $0 < \eta < 1$.

We stress that we are *not* including finite–size effects (surface and Coulomb energies, screening, etc.) microscopically; instead, we emulate their net impact by tuning the balance between local and global neutrality through η. Similarly, we do not address nucleation dynamics here, but consider only the equilibrium mixed phase (see Sec. 1.3.2).

The equilibrium state at given (n_B, Y_C, T, η) is obtained by minimizing the total free energy density with respect to the independent variables, subject to the constraints associated with conserved charges. A detailed classification of the resulting equilibrium conditions, for different sets of conserved charges and for local versus global conserva-

tion, is given in Appendix A.

3.1.1 Free energy density of the mixed phase

In this chapter we take as input independent thermodynamic variables

$$n_B, \quad Y_C \equiv \frac{n_C}{n_B}, \quad T, \quad \eta, \tag{3.2}$$

and use *net number densities* as basic variables, in order to avoid ambiguities in the definition of Y_i (see Appendix A).

We denote by n_i^H the net number density of species i in the homogeneous hadronic phase, and by n_i^Q the corresponding quantity in the homogeneous quark phase. The volume fraction occupied by quark matter is $\chi \equiv V_Q/(V_H + V_Q)$, so that $1 - \chi$ is the hadronic volume fraction.

The free energy density of the mixed phase is written as

$$f_M(n_B, Y_C, T, \eta; \{n_h^H\}, \{n_q^Q\}, \chi) = (1-\chi)\, f_H(\{n_h^H\}, T, \eta) + \chi\, f_Q(\{n_q^Q\}, T, \eta), \tag{3.3}$$

where $h = p, n, e_L, e_G$ and $q = u, d, s, e_L, e_G$. Here e_L denotes the fraction of electrons that enforce *local* neutrality in each phase, whereas e_G denotes the fraction that enters only in *global* neutrality.

The hadronic and quark free energy densities are

$$f_H(\{n_h^H\}, T, \eta) = \sum_{h=p,n} f_h^H(n_h^H, T) + \eta\, f_e(n_{eL}^H, T) + (1-\eta)\, f_e(n_{eG}^H, T) + f_\gamma(T), \tag{3.4}$$

$$f_Q(\{n_q^Q\}, T, \eta) = \sum_{q=u,d,s} f_q^Q(n_q^Q, T) + \eta\, f_e(n_{eL}^Q, T) + (1-\eta)\, f_e(n_{eG}^Q, T) + f_\gamma(T), \tag{3.5}$$

where the sums collect the free energy densities of hadrons and quarks in the corresponding homogeneous EOS. We are working with models at the mean–field level (ZL and vMIT; see Sec. 2), in which bosons mediating the strong interaction are integrated out and replaced by mean fields that enter the single–particle potentials. Consequently the free energy of each phase can be written as a sum of quasiparticle contributions as in Eqs. (3.4)–(3.5).

3.1.2 Conservation laws and charge–neutrality constraints

In the applications of interest, the globally conserved strong charges are the baryon number B and the non–leptonic electric charge C. Their global conservation implies

$$n_B = (1-\chi)\, n_B^H + \chi\, n_B^Q, \tag{3.6}$$

$$n_C = (1-\chi)\, n_C^H + \chi\, n_C^Q, \tag{3.7}$$

Total electric charge neutrality is imposed partly locally (through e_L) and partly globally (through e_G):

$$n^H_{Q_{\rm tot}} = n^H_C - n^H_{eL} = 0, \tag{3.8}$$
$$n^Q_{Q_{\rm tot}} = n^Q_C - n^Q_{eL} = 0, \tag{3.9}$$
$$n^G_{Q_{\rm tot}} = (1-\chi)\Big(n^H_C - n^H_{eG}\Big) + \chi\Big(n^Q_C - n^Q_{eG}\Big) = 0. \tag{3.10}$$

The baryon and non–leptonic charge densities in each homogeneous phase are

$$n^H_B = n^H_p + n^H_n\,, \tag{3.11}$$
$$n^Q_B = \frac{1}{3}\Big(n^Q_u + n^Q_d + n^Q_s\Big), \tag{3.12}$$
$$n^H_C = n^H_p\,, \tag{3.13}$$
$$n^Q_C = \frac{2}{3}n^Q_u - \frac{1}{3}n^Q_d - \frac{1}{3}n^Q_s, \tag{3.14}$$

and, for completeness, the strangeness densities are

$$n^H_S = 0, \qquad n^Q_S = n^Q_s, \tag{3.15}$$

which simply reflects the absence of strange hadrons in the hadronic EOS adopted here and the identification of S with the net strange–quark content in the quark phase.

Equations (3.8)–(3.9) impose local neutrality in each phase for the fraction η of electrons (e_L), while Eq. (3.10) enforces global neutrality for the remaining fraction $1-\eta$ (e_G).

In terms of the variables just introduced, the sums over h and q in Eqs. (3.4)–(3.5) can equally well be taken over the charges B, C, S instead of the microscopic species, if desired.

3.1.3 Deriving equilibrium conditions

We now minimize the free energy density (3.3) with respect to the remaining degrees of freedom, under the constraints (3.6)–(3.10). In Appendix A, a class of similar problems is treated in terms of extensive variables N^I_i and V_I, which simplifies some of the algebra. Here we show explicitly the calculation using densities $\{n^I_i\}$ and the volume fraction χ.

We use the five constraints to eliminate five of the mixed–phase variables in favour of

(n_B, n_C, T, η) and a reduced set of densities:

$$n_B^Q = \frac{n_B - n_B^H(1-\chi)}{\chi}, \tag{3.16}$$

$$n_C^Q = \frac{n_C - n_C^H(1-\chi)}{\chi}, \tag{3.17}$$

$$n_{eG}^Q = \frac{n_C - n_{eG}^H(1-\chi)}{\chi}, \tag{3.18}$$

$$n_{eL}^Q = \frac{n_C - n_C^H(1-\chi)}{\chi}, \tag{3.19}$$

$$n_{eL}^H = n_C^H. \tag{3.20}$$

Thus the mixed–phase free energy can be viewed as a function of

$$(n_B, n_C, T, \eta; \{n_i^H\}, \{n_i^Q\}, \chi) \longrightarrow (n_B, n_C, T, \eta; n_B^H, n_C^H, n_S^H, n_{eG}^H, n_S^Q, \chi), \tag{3.21}$$

with $i = B, C, S, e_L, e_G$.

We now minimize f_M with respect to the remaining independent densities $(n_B^H, n_C^H, n_S^H, n_{eG}^H, n_S^Q, \chi)$, keeping (n_B, n_C, T, η) fixed. For brevity we denote by x the set of independent variables other than the one being varied.

Varying n_B^H we obtain

$$0 = \left.\frac{\partial f_M}{\partial n_B^H}\right|_{x \neq n_B^H} \tag{3.22}$$

$$= (1-\chi) \left.\frac{\partial f_H}{\partial n_B^H}\right|_{\{n_{i\neq B}^H\},T,\eta} + \chi \left.\frac{\partial f_Q}{\partial n_B^Q}\right|_{\{n_{i\neq B}^Q\},T,\eta} \left.\frac{\partial n_B^Q}{\partial n_B^H}\right|_{x \neq n_B^H}, \tag{3.23}$$

because n_{eL}^H does not depend on n_B^H and n_B^Q depends linearly on n_B^H via Eq. (3.16). Using $\partial f_I / \partial n_B^I = \mu_B^I$ and $\partial n_B^Q / \partial n_B^H = -(1-\chi)/\chi$ we find

$$(1-\chi)\,\mu_B^H - (1-\chi)\,\mu_B^Q = 0 \quad \Rightarrow \quad \mu_B^H = \mu_B^Q. \tag{3.24}$$

Similarly, varying n_C^H yields

$$0 = \left.\frac{\partial f_M}{\partial n_C^H}\right|_{x \neq n_C^H} \tag{3.25}$$

$$= (1-\chi)\left(\frac{\partial f_H}{\partial n_C^H} + \frac{\partial f_H}{\partial n_{eL}^H}\frac{\partial n_{eL}^H}{\partial n_C^H}\right) + \chi\left(\frac{\partial f_Q}{\partial n_C^Q}\frac{\partial n_C^Q}{\partial n_C^H} + \frac{\partial f_Q}{\partial n_{eL}^Q}\frac{\partial n_{eL}^Q}{\partial n_C^H}\right). \tag{3.26}$$

From Eqs. (3.17) and (3.19) we have $\partial n_C^Q / \partial n_C^H = -(1-\chi)/\chi$ and $\partial n_{eL}^Q / \partial n_C^H = -(1-\chi)/\chi$, while $n_{eL}^H = n_C^H$ implies $\partial n_{eL}^H / \partial n_C^H = 1$. Recognizing the chemical potentials we obtain

$$\mu_C^H + \eta\,\mu_{eL}^H = \mu_C^Q + \eta\,\mu_{eL}^Q. \tag{3.27}$$

Varying n_S^H and n_S^Q gives

$$0 = \left.\frac{\partial f_M}{\partial n_S^H}\right|_{x\neq n_S^H} = (1-\chi)\,\mu_S^H, \tag{3.28}$$

$$0 = \left.\frac{\partial f_M}{\partial n_S^Q}\right|_{x\neq n_S^Q} = \chi\,\mu_S^Q. \tag{3.29}$$

Thus, in equilibrium

$$\mu_S^H = 0, \qquad \mu_S^Q = 0, \tag{3.30}$$

which correspond to weak equilibrium with respect to non–leptonic flavor–changing reactions in each phase.

Finally, variation with respect to n_{eG}^H gives

$$0 = \left.\frac{\partial f_M}{\partial n_{eG}^H}\right|_{x\neq n_{eG}^H} \tag{3.31}$$

$$= (1-\chi)\,(1-\eta)\,\mu_{eG}^H + \chi\,(1-\eta)\,\mu_{eG}^Q \left.\frac{\partial n_{eG}^Q}{\partial n_{eG}^H}\right|_{x\neq n_{eG}^H}. \tag{3.32}$$

From Eq. (3.18) we have $\partial n_{eG}^Q/\partial n_{eG}^H = -(1-\chi)/\chi$, so that

$$\mu_{eG}^H = \mu_{eG}^Q. \tag{3.33}$$

Since electrons have the same EOS in both phases, Eq. (3.33) implies $n_{eG}^H = n_{eG}^Q$ and $f_e(n_{eG}^H, T) = f_e(n_{eG}^Q, T)$.

Equations (3.24), (3.27), (3.28), (3.29) and (3.33) summarize the *chemical equilibrium* conditions. There are three independent chemical potentials common to the two phases (associated with the three globally conserved quantities B, C, and the globally neutral part of the electric charge) plus the two conditions enforcing weak equilibrium in strangeness in the two homogeneous phases.

Mapping the charge degrees of freedom (B, C, S) to the microscopic ones (p, n, u, d, s) (see Appendix A), these conditions can be rewritten as

$$\mu_n^H = \mu_u^Q + 2\mu_d^Q, \tag{3.34}$$

$$\mu_p^H = 2\mu_u^Q + \mu_d^Q + \eta\left(\mu_{eL}^Q - \mu_{eL}^H\right), \tag{3.35}$$

$$\mu_d^Q = \mu_s^Q. \tag{3.36}$$

Mechanical equilibrium follows from minimizing f_M with respect to the volume frac-

tion χ:

$$0 = \left.\frac{\partial f_M}{\partial \chi}\right|_{x\neq\chi} \tag{3.37}$$

$$= -f_H + (1-\chi)\left.\frac{\partial f_H}{\partial \chi}\right|_{x\neq\chi} + f_Q + \chi\left.\frac{\partial f_Q}{\partial \chi}\right|_{x\neq\chi}. \tag{3.38}$$

The χ–dependence of f_H and f_Q enters only through the densities n_B^Q, n_C^Q, n_{eG}^Q, and n_{eL}^Q defined in Eqs. (3.16)–(3.19). Using the chain rule and the definitions of the corresponding chemical potentials, we obtain

$$\left.\frac{\partial f_H}{\partial \chi}\right|_{x\neq\chi} = 0, \tag{3.39}$$

$$\left.\frac{\partial f_Q}{\partial \chi}\right|_{x\neq\chi} = \mu_B^Q \left.\frac{\partial n_B^Q}{\partial \chi}\right|_x + \mu_C^Q \left.\frac{\partial n_C^Q}{\partial \chi}\right|_x + (1-\eta)\,\mu_{eG}^Q \left.\frac{\partial n_{eG}^Q}{\partial \chi}\right|_x + \eta\,\mu_{eL}^Q \left.\frac{\partial n_{eL}^Q}{\partial \chi}\right|_x. \tag{3.40}$$

From Eqs. (3.16)–(3.19) one finds

$$\frac{\partial n_B^Q}{\partial \chi} = -\frac{n_B^Q - n_B^H}{\chi}, \tag{3.41}$$

$$\frac{\partial n_C^Q}{\partial \chi} = -\frac{n_C^Q - n_C^H}{\chi}, \tag{3.42}$$

$$\frac{\partial n_{eG}^Q}{\partial \chi} = -\frac{n_{eG}^Q - n_{eG}^H}{\chi}, \tag{3.43}$$

$$\frac{\partial n_{eL}^Q}{\partial \chi} = -\frac{n_{eL}^Q - n_{eL}^H}{\chi}. \tag{3.44}$$

Inserting these relations, using the thermodynamic identity

$$f_I = -P_I + \sum_j n_j^I \mu_j^I, \tag{3.45}$$

for each phase $I = H, Q$, together with the chemical–equilibrium conditions and the charge–neutrality constraints we are left with the simple condition

$$P_H = P_Q, \tag{3.46}$$

i.e. the pressure is the same in the two phases. This is the usual mechanical equilibrium condition. Note that the contributions of photons and of the globally neutral electron component e_G cancel between the two phases, because $n_{eG}^H = n_{eG}^Q$ and f_γ is phase–independent.

For later reference we write the phase pressures explicitly as

$$P_H = \sum_{h=B,C,S} P_h^H(\{n_h^H\},T) + \eta\, P_e(n_{eL}^H,T) + (1-\eta)\, P_e(n_{eG}^H,T) + P_\gamma(T), \tag{3.47}$$

$$P_Q = \sum_{q=B,C,S} P_q^Q(\{n_q^Q\},T) + \eta\, P_e(n_{eL}^Q,T) + (1-\eta)\, P_e(n_{eG}^Q,T) + P_\gamma(T), \tag{3.48}$$

where the sums denote the hadronic and quark contributions in the homogeneous EOSs.

3.1.4 Computing the mixed phase

Collecting all constraints and equilibrium conditions, the mixed phase is determined by solving the coupled system

$$\begin{cases}
n_B = (1-\chi)\Big(n_p^H + n_n^H\Big) + \chi\left(\frac{1}{3}n_u^Q + \frac{1}{3}n_d^Q + \frac{1}{3}n_s^Q\right) \\
n_C = (1-\chi)\, n_p^H + \chi\left(\frac{2}{3}n_u^Q - \frac{1}{3}n_d^Q - \frac{1}{3}n_s^Q\right) \\
0 = n_p^H - n_{eL}^H \\
0 = \left(\frac{2}{3}n_u^Q - \frac{1}{3}n_d^Q - \frac{1}{3}n_s^Q\right) - n_{eL}^Q \\
0 = (1-\chi)\Big(n_p^H - n_{eG}^H\Big) + \chi\left[\left(\frac{2}{3}n_u^Q - \frac{1}{3}n_d^Q - \frac{1}{3}n_s^Q\right) - n_{eG}^Q\right] \\
\mu_n^H(n_p^H,n_n^H,T) = \mu_u^Q(n_u^Q,n_d^Q,n_s^Q,T) + 2\mu_d^Q(n_u^Q,n_d^Q,n_s^Q,T) \\
\mu_p^H(n_p^H,n_n^H,T) = 2\mu_u^Q(n_u^Q,n_d^Q,n_s^Q,T) + \mu_d^Q(n_u^Q,n_d^Q,n_s^Q,T) + \eta\Big[\mu_e(n_{eL}^Q,T) - \mu_e(n_{eL}^H,T)\Big] \\
\mu_d^Q(n_u^Q,n_d^Q,n_s^Q,T) = \mu_s^Q(n_u^Q,n_d^Q,n_s^Q,T) \\
\mu_e(n_{eG}^H,T) = \mu_e(n_{eG}^Q,T) \\
P_H(n_p^H,n_n^H,n_{eL}^H,n_{eG}^H,T,\eta) = P_Q(n_u^Q,n_d^Q,n_s^Q,n_{eL}^Q,n_{eG}^Q,T,\eta),
\end{cases} \tag{3.49}$$

for the unknowns

$$n_p^H,\ n_n^H,\ n_u^Q,\ n_d^Q,\ n_s^Q,\ n_{eL}^H,\ n_{eL}^Q,\ n_{eG}^H,\ n_{eG}^Q,\ \chi,$$

at given (n_B, Y_C, T, η), where $Y_C = n_C/n_B$. Note that the chemical potentials $\{\mu_i^I\}$ can be used as variables instead of $\{n_i^I\}$.

Once the system is solved, all densities become functions of the input variables:

$$(n_B, Y_C, T, \eta; \{n_i^H\}, \{n_i^Q\}, \chi) \longrightarrow (n_B, Y_C, T, \eta), \qquad i = B, C, S, e_L, e_G. \tag{3.50}$$

The mixed phase is defined by

$$0 < \chi(n_B, Y_C, T, \eta) < 1. \tag{3.51}$$

For $\chi \leq 0$ the system is in a pure hadronic phase and we set $\chi = 0$; for $\chi \geq 1$ it is in a pure quark phase and we set $\chi = 1$.

The total free energy density is therefore

$$f(n_B, Y_C, T, \eta) = \begin{cases} f_H(n_B, Y_C, T), & \chi(n_B, Y_C, T, \eta) \leq 0, \\ f_M(n_B, Y_C, T, \eta), & 0 < \chi(n_B, Y_C, T, \eta) < 1, \\ f_Q(n_B, Y_C, T), & \chi(n_B, Y_C, T, \eta) \geq 1, \end{cases} \tag{3.52}$$

with analogous expressions for P, ε, s, etc., obtained from Eqs. (3.3)–(3.5) by replacing the densities with their equilibrium values.

The particle fractions in the mixed phase are obtained from the corresponding densities. For hadrons ($h = p, n$) we have

$$Y_h(n_B, Y_C, T, \eta) = \begin{cases} n_h^H(n_B, Y_C, T)/n_B, & \chi(n_B, Y_C, T, \eta) \leq 0, \\ \left[1 - \chi(n_B, Y_C, T, \eta)\right] n_h^H(n_B, Y_C, T)/n_B, & 0 < \chi(n_B, Y_C, T, \eta) < 1, \\ 0, & \chi(n_B, Y_C, T, \eta) \geq 1, \end{cases} \tag{3.53}$$

for quarks ($q = u, d, s$)

$$Y_q(n_B, Y_C, T, \eta) = \begin{cases} 0, & \chi(n_B, Y_C, T, \eta) \leq 0, \\ \chi(n_B, Y_C, T, \eta)\, n_q^Q(n_B, Y_C, T)/n_B, & 0 < \chi(n_B, Y_C, T, \eta) < 1, \\ n_q^Q(n_B, Y_C, T)/n_B, & \chi(n_B, Y_C, T, \eta) \geq 1. \end{cases} \tag{3.54}$$

Finally, the total electron fraction can be written as the sum of all electrons terms with the proper weight

$$Y_e = \frac{(1-\chi)\left[\eta n_{eL}^H + (1-\eta) n_{eG}^H\right] + \chi\left[\eta n_{eL}^Q + (1-\eta) n_{eG}^Q\right]}{n_B}, \tag{3.55}$$

which, due to total charge neutrality, is equal to Y_C by construction.

In the mixed phase, the dependence on (n_B, Y_C, T) is determined by the solution of Eqs. (3.49), while in the pure phases it follows from the equilibrium relations and constraints for pure phases summarized in Sec. 2.5.

3.1.5 Limiting cases and β equilibrium

It is straightforward to verify that the chemical and mechanical equilibrium conditions, as well as all thermodynamic quantities, reduce to the standard expressions in the two limiting cases:

- $\eta = 1$ (purely local charge neutrality): local electric charge neutrality is enforced in each phase, but both B and C remain globally conserved. Therefore, if Y_C is kept as an independent EOS variable, a Maxwell construction with strictly constant pressure in the mixed phase is *not* a true equilibrium solution.
- $\eta = 0$ (purely global charge neutrality): charge neutrality is enforced only globally

and three globally conserved charges are present (B, C and $Q_{\rm tot}$).

The same framework can be straightforwardly adapted to other setups by following the prescriptions in Appendix A. For instance, in neutrinoless β–equilibrated compact star matter one removes C as an independently conserved quantity (no constraint (3.7)). Minimization of f_M then yields, in place of Eq. (3.27), the usual β–equilibrium conditions modified by η:

$$\mu_p^H + \eta\,\mu_{eL}^H + (1-\eta)\,\mu_{eG}^H = \mu_n^H\,, \tag{3.56}$$

$$\mu_u^Q + \eta\,\mu_{eL}^Q + (1-\eta)\,\mu_{eG}^Q = \mu_d^Q\,. \tag{3.57}$$

In this case the independent variables are (n_B, T, η), and the limits $\eta = 0$ and $\eta = 1$ correspond to the standard GC and MC with, respectively, two $(B, Q_{\rm tot})$ and one (B) globally conserved charges.

3.2 Results

In this section, we explore how the local–to–total lepton ratio η affects the EOS and the composition of matter. Unless otherwise specified, results are shown for different values of the net electron fraction Y_e (which coincides with the non–leptonic electric charge fraction Y_C in our setup) and for two representative temperatures.

3.2.1 Onset and extent of the mixed phase

Figure 3.1 shows the quark volume fraction χ as a function of the baryon density n_B, and Fig. 3.2 displays the corresponding phase boundaries in the T–n_B plane. Larger values of the local–to–total lepton ratio η (i.e. more local charge neutrality and, in our interpretation, effectively larger surface tension) shrink the mixed phase in density. For fixed (Y_e, η), increasing the temperature lowers the onset density of quarks; at fixed (T, η), lowering Y_e also shifts the onset to lower n_B.

The Y_e dependence can be understood from the symmetry energy of nucleonic matter. Smaller Y_e implies a smaller proton fraction in the pure hadronic phase, hence a larger symmetry energy and a higher free energy for nucleonic matter at fixed n_B. It then becomes energetically favorable to form quarks at lower densities. For each pair (Y_e, T), the curves for different η intersect approximately at the density where the free energy densities of the pure nucleonic and pure quark phases are equal.

At large Y_e, the sensitivity to η is strongly reduced. The origin of this behavior will become clear in the discussion of the mixed–phase composition below.

The density and temperature location of the mixed–phase boundaries are model dependent. With the choice of bag constant in Table 2.3, the onset of the mixed phase in nearly symmetric matter occurs at $n_B \sim (8.3\text{–}8.4)\,n_0$, depending on η, which is compatible with heavy–ion constraints [17]. We selected this value to obtain a mixed phase that spans a relatively wide density range, making the qualitative behavior of thermo-

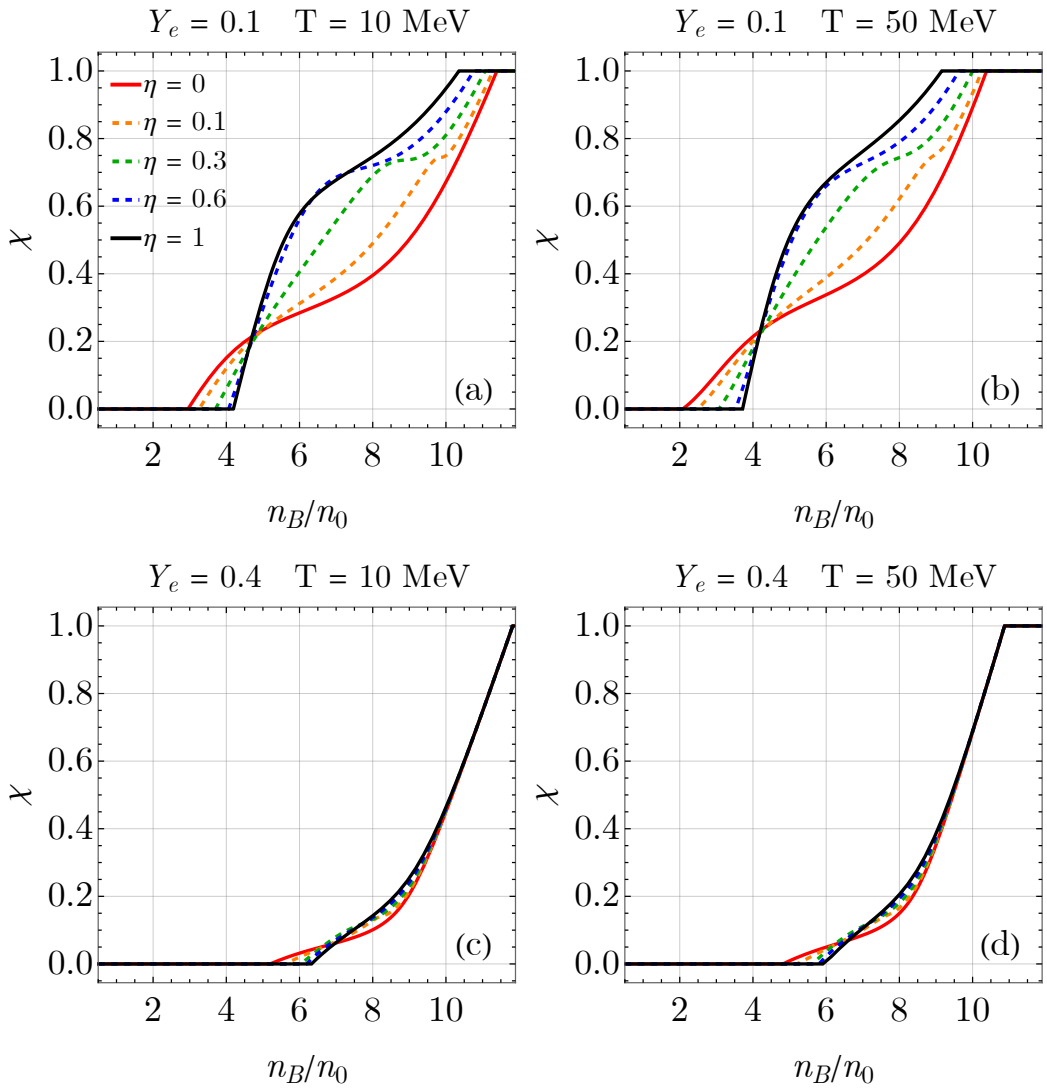

Figure 3.1: Volume fraction of quark matter χ vs. baryon density n_B (in units of nuclear saturation density n_0) for the indicated values of the local–to–total lepton ratio η, with net electron fraction $Y_e = 0.1$ and temperature $T = 10$ MeV [panel (a)], $Y_e = 0.1$ and $T = 50$ MeV [panel (b)], $Y_e = 0.4$ and $T = 10$ MeV [panel (c)], and $Y_e = 0.4$ and $T = 50$ MeV [panel (d)]. Figure adapted from [41].

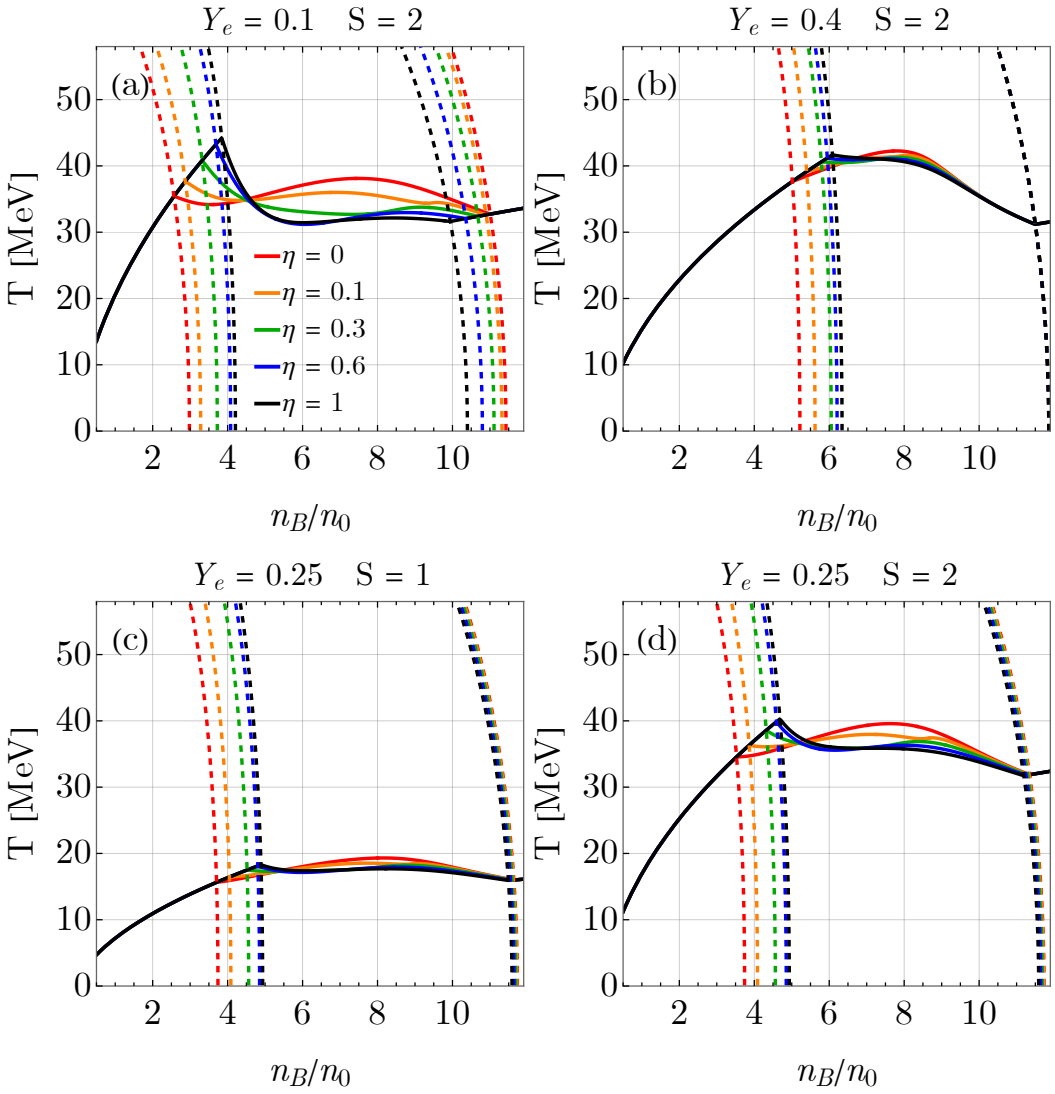

Figure 3.2: Phase diagram in the T–n_B plane for the indicated values of the local–to–total lepton ratio η. For each case, phase boundaries (T vs. n_B) are shown as dashed (solid) lines at fixed specific entropy $S = s/n_B$ (either $S = 1$ or $S = 2$) and fixed Y_e (either $Y_e = 0.1$ or $Y_e = 0.4$), as stated in the plot titles. The $Y_e = 0.25$ cases [panels (c) and (d)] are also shown, since [36] finds this as a typical central value after core bounce in CCSN simulations of massive progenitors. Figure from [41].

dynamic quantities easier to visualize. Other values of B could be chosen to shift the mixed region to densities more in line with EOSs used in astrophysical simulations such as [35, 36].

Figure 3.2 shows $T(n_B)$ at fixed specific entropy $S = s/n_B$, which approximates the evolution of the central region of the PNS after core bounce in a CCSN. Using the classification of [36], panel (c) with $S = 1$ corresponds roughly to a ~ 50 $M_\odot$ progenitor, while panel (d) with $S = 2$ resembles an ~ 80 $M_\odot$ progenitor. Simulations employing a Maxwell construction often find that, once the central density exceeds the transition density, a second shock can be launched by the quark–hadron transition [35, 36], potentially driving an explosion. Analogously, in BNSM simulations, EOSs with a sharp first–order transition can leave distinctive imprints on the post–merger gravitational–wave signal, such as phase shifts [39] or modifications of the peak frequency [141].

In our framework, when Y_C (or Y_e) is an input variable, pressure and density vary more smoothly across the mixed phase than in the idealized Maxwell case, even for large η. This softens the transition and may suppress the secondary shock in CCSNe and reduce strong phase–transition signatures in the BNSM post–merger signal. Moreover, BNSMs with a Gibbs–type transition are already known to be difficult to distinguish from purely hadronic mergers [33, 148]. A more realistic treatment of the interface (of which our scheme is a thermodynamically consistent bulk approximation) will therefore be crucial in future numerical simulations.

3.2.2 Pressure–energy relation

Figure 3.3 shows the pressure P as a function of the energy density ε. As expected, the onset of quark degrees of freedom softens the EOS, *i.e.* it lowers P at fixed ε. The qualitative dependence on (Y_e, T, η) closely parallels that of the volume fraction χ discussed above.

A central point is that, once Y_e is treated as an independent variable, the pressure is *not* constant in the mixed phase even for $\eta = 1$, *i.e.* even under fully local charge neutrality. For a first–order phase transition, a constant–pressure mixed phase is the correct equilibrium solution only if there is a single globally conserved charge [27].

In our finite–temperature setup, however, Y_e (or equivalently Y_C) is a free parameter, so there are at least two globally conserved strong charges: baryon number and non–leptonic electric charge. For $\eta \neq 1$, part of the total electric charge is also shared globally, providing an additional conserved quantity.

For comparison, Fig. 3.4 shows the pressure as a function of the energy density in neutrinoless β–equilibrium, where Y_e is no longer an input but is fixed for each (n_B, T) by the β–equilibrium condition. In this case, and for fully local charge neutrality ($\eta = 1$), the system has only one globally conserved charge (the baryon number), and the isothermal pressure is constant across the mixed phase as a function of both ε and n_B, reproducing the usual MC. Strictly speaking, however, neutrinoless β–equilibrium is exact only at $T = 0$; at finite temperature neutrinos would in general alter the equilibrium conditions (see Sec. 2.5 and Appendix A).

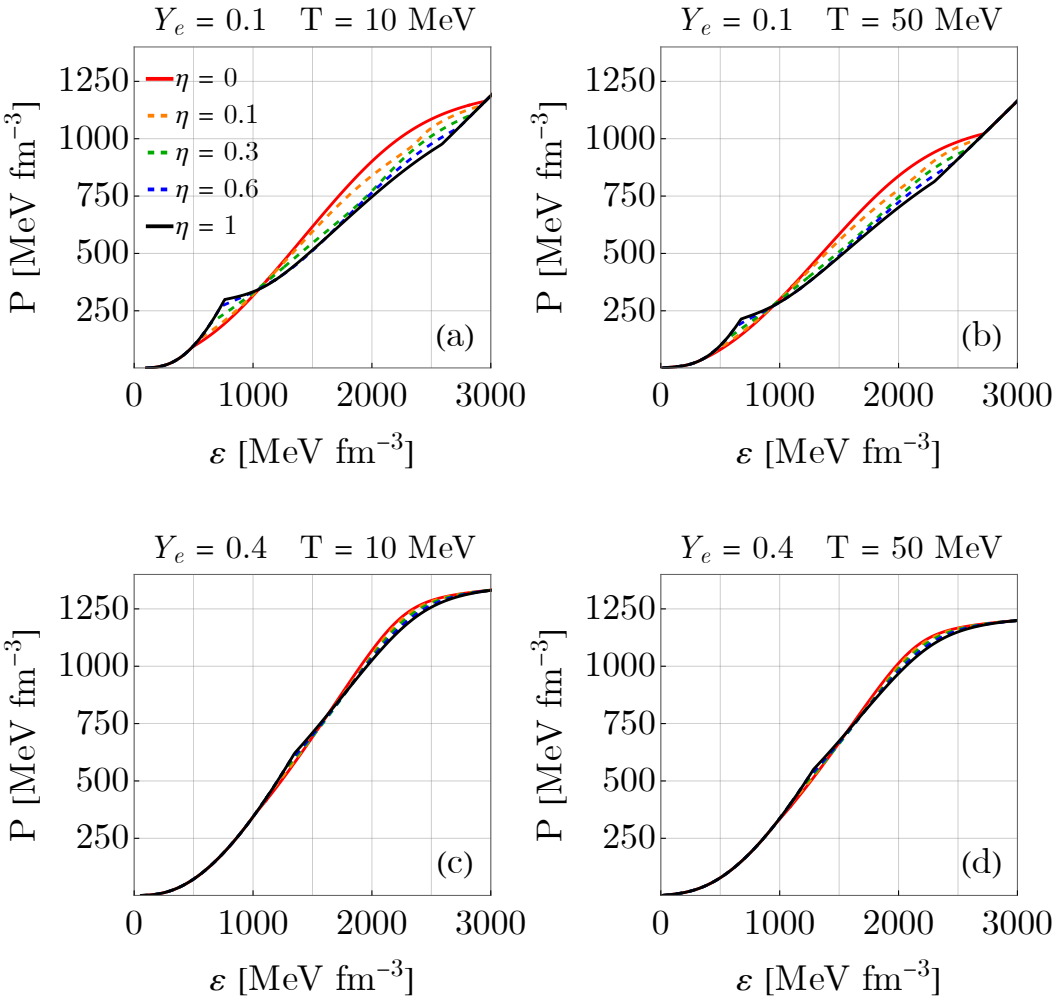

Figure 3.3: Pressure P vs. energy density ε for the indicated values of the local–to–total lepton ratio η, net electron fraction Y_e, and temperature T. In contrast to the β–equilibrium case, the pressure is not constant in the mixed phase, even for $\eta = 1$. Figure from [41].

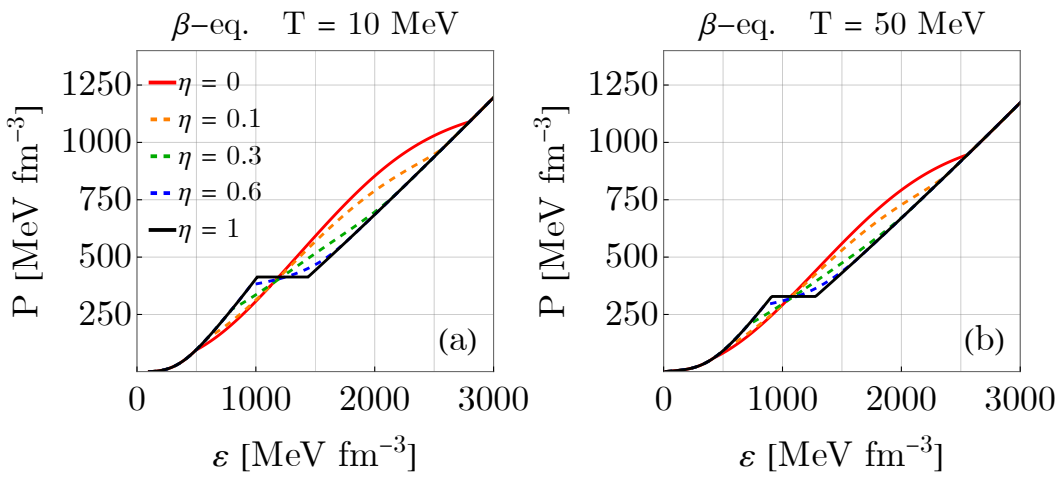

Figure 3.4: Pressure P vs. energy density ε in neutrinoless β–equilibrium for the indicated values of the local–to–total lepton ratio η and temperature T. For $\eta = 1$ and $T \simeq 0$ the mixed phase reduces to a constant–pressure plateau, as in the standard Maxwell construction. Figure from [41].

3.2.3 Composition

Figures 3.5 and 3.6 show the particle fractions Y_i as functions of n_B for $Y_e = 0.1$ and $Y_e = 0.4$, respectively. Electron and positron fractions are plotted separately, whereas for all other species net fractions are shown. Our formulation keeps track of all partial lepton populations even for $\eta = 1$, where standard MC typically lose this information.

The qualitative differences between $T = 10$ MeV and $T = 50$ MeV are modest, except for the shift of the mixed region to lower densities at higher temperatures. The main variations in particle fractions come from the interplay between the nucleonic symmetry energy and the strong equilibrium between nucleons and quarks.

For $\eta = 0$ (purely global neutrality), $Y_{eG} \equiv n_{eG}^H/n_B = n_{eG}^Q/n_B = Y_e$ in the mixed phase; electrons form a single global Fermi sea, with $\mu_{eG}^H = \mu_{eG}^Q \equiv \mu_{eG} \propto n_B^{1/3}$ for degenerate matter.

The onset of the quark phase allows for the reduction of the nucleonic symmetry energy by redistributing the isospin from the hadronic to the quark phase without any constraints of local electric charge neutrality. In particular, proton fraction Y_p in the hadronic phase rises rapidly until $Y_p \approx Y_n$, where the isovector contribution to the nucleon energy becomes small, compensated by negatively charged d and s quarks over u quarks at the onset of the mixed phase.

For $\eta = 1$ (purely local neutrality), the total Y_e is fixed, but the local electron components

$$Y_{eH} \equiv (1-\chi)\,\frac{n_{eL}^H}{n_B}, \qquad Y_{eQ} \equiv \chi\,\frac{n_{eL}^Q}{n_B}$$

are not. Initially, $Y_p = Y_{eH}$ increases modestly, while Y_{eQ} decreases because the quark phase hosts more positrons, again reflecting the presence of negatively charged d and

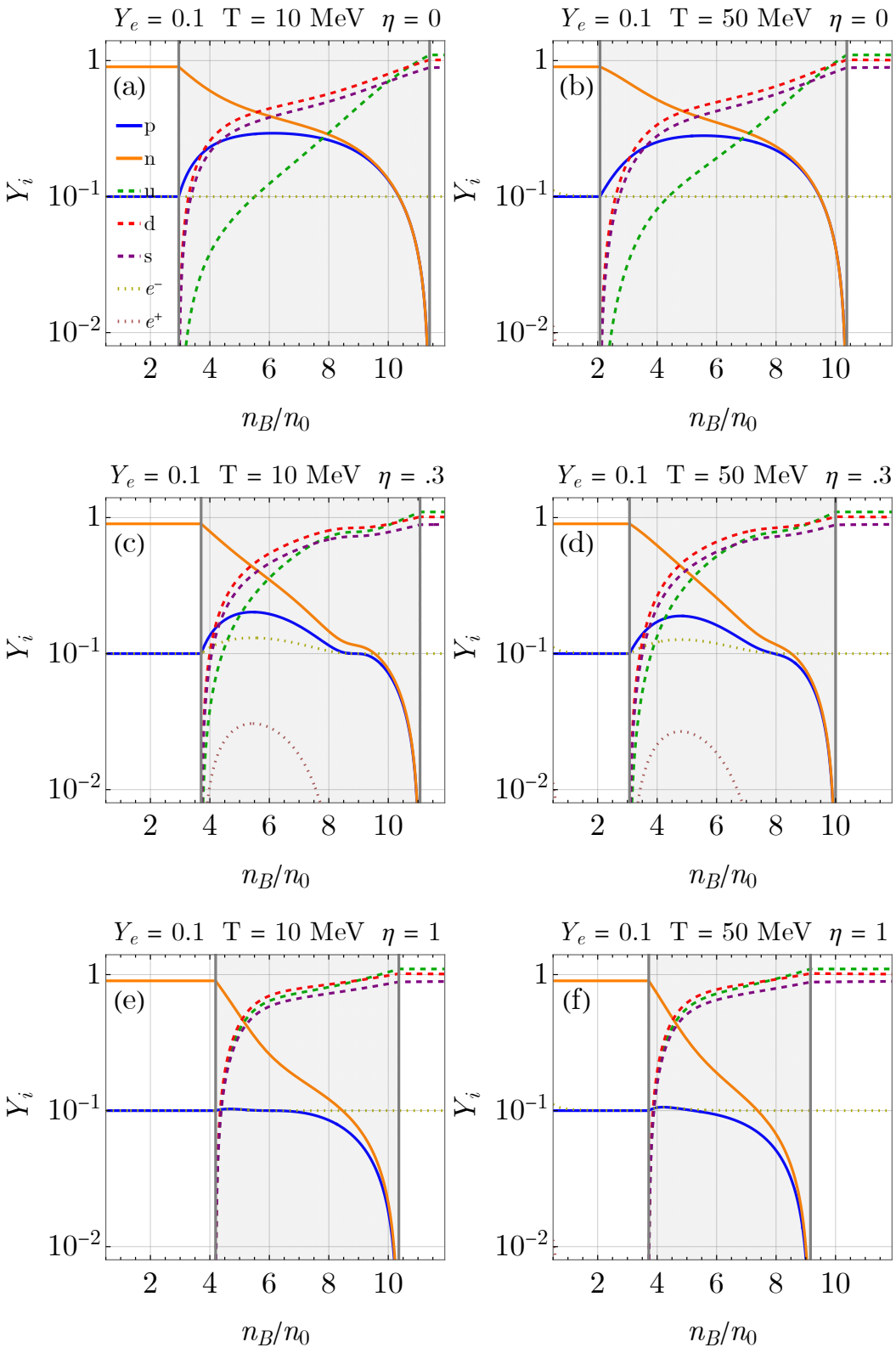

Figure 3.5: Particle fractions Y_i vs. baryon density n_B at net electron fraction $Y_e = 0.1$, for the indicated values of the local–to–total lepton ratio η and temperature T. Contributions from electrons and positrons are shown separately; for all other species net fractions are plotted. Figure from [41].

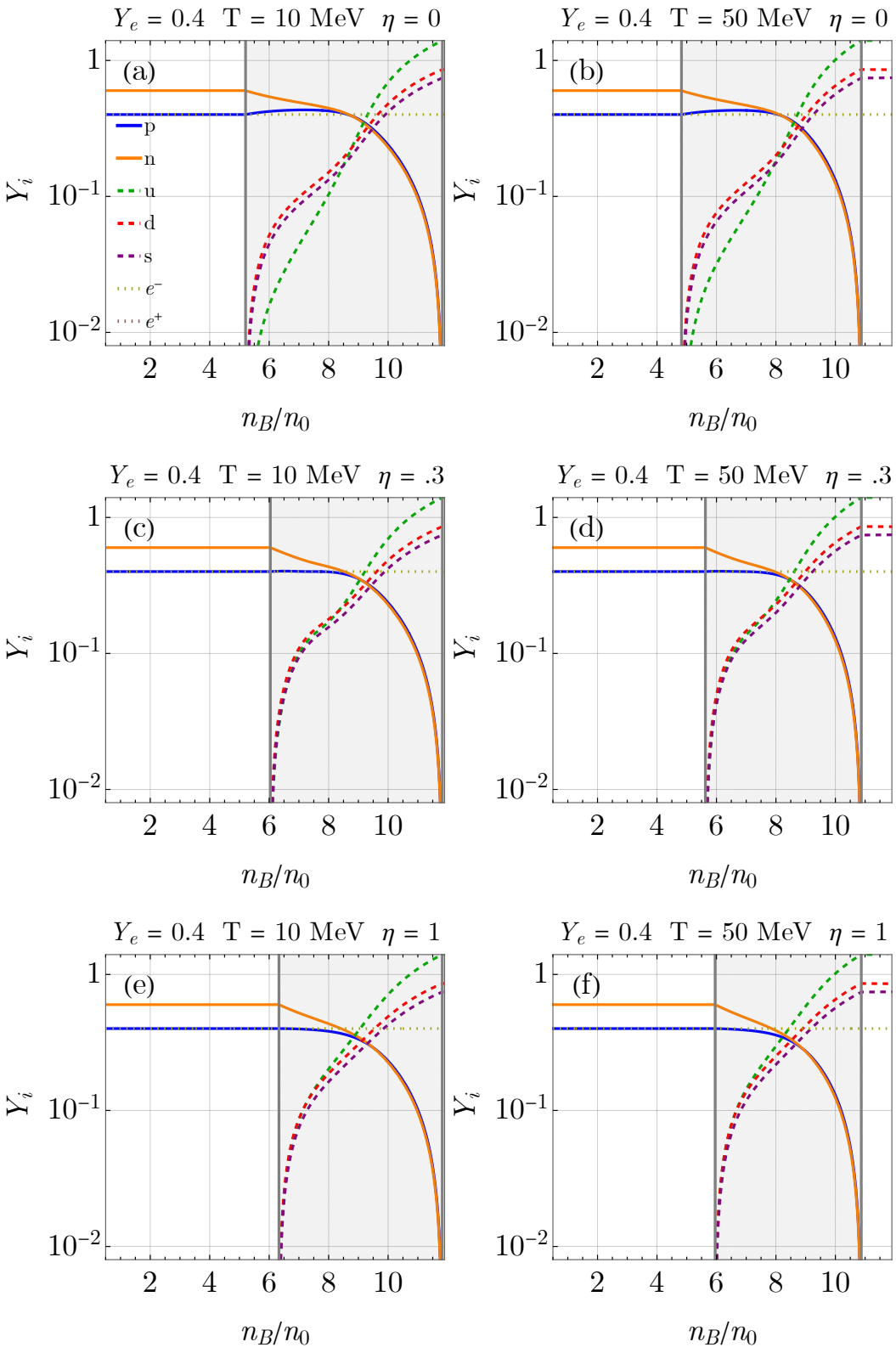

Figure 3.6: Same as Fig. 3.5 but at net electron fraction $Y_e = 0.4$. Figure from [41].

s quarks. At larger n_B, the hadronic sector becomes more symmetric, and strong equilibrium drives the quark phase toward a more positive net charge compensated by an increase in Y_{eQ}.

For intermediate η, the behavior lies between these two extremes. The early rise of Y_p is shared between a global electron component and a local one in the hadronic phase, partially compensated by positrons in the quark phase. The clearest qualitative difference is that for small η the proton fraction grows noticeably in the first part of the mixed phase, while for large η it remains nearly flat. The reason why, at large η, the initial increase of Y_p is weaker than at low η is that, in this regime, electric charge neutrality must be enforced locally in both phases. As a result, there is less freedom to redistribute electric charge between the hadronic and quark components, and the symmetry energy can be reduced only through a more constrained adjustment of Y_p.

At larger Y_e (e.g. Fig. 3.6), the symmetry energy penalty in the pure hadronic phase is smaller, so the onset of quarks is pushed to higher densities and the initial Y_p increase after the transition is reduced. As n_B increases further, the hadronic phase quickly approaches $Y_p \simeq Y_n$, and the symmetry energy prevents it from becoming proton–rich, keeping $Y_p \approx Y_n$.

A noteworthy limit is $Y_e \to 0.5$. The quark phase energetically favors a small non–leptonic charge fraction $Y_C^Q = n_C^Q/n_B^Q$ (namely a symmetric matter) thanks to the available negatively charged quarks. For $Y_e \leq 0.5$ in the mixed phase we find $Y_C^Q < Y_e < Y_C^H$, with smaller η giving larger Y_C^H and smaller Y_C^Q. However, the symmetry energy constrains Y_C^H to not become larger than 0.5. Therefore, for $Y_e \sim 0.5$ we obtain $Y_C^H \simeq 0.5$ almost independently of η, while $Y_p = (1-\chi)\, n_C^H/n_B$ then decreases with increasing χ. This explains why both composition and thermodynamics become nearly η–independent at high Y_e. The strong density dependence of the symmetry energy in the ZL model makes this effect particularly pronounced.

3.2.4 Entropy

Figure 3.7 shows the specific entropy $S = s/n_B$ as a function of n_B. In both pure phases the entropy decreases monotonically with density at fixed T, while in the mixed phase it develops non–monotonic features whose detailed shape depends on η. At fixed (n_B, Y_e, η) the entropy increases monotonically with T, and the difference in S between the pure nucleonic and pure quark phases becomes larger at higher temperatures, reflecting the larger number of active degrees of freedom in quark matter.

3.2.5 Response functions

It is useful to recall the relevant response functions and the role of the thermodynamic constraints under which derivatives are taken.

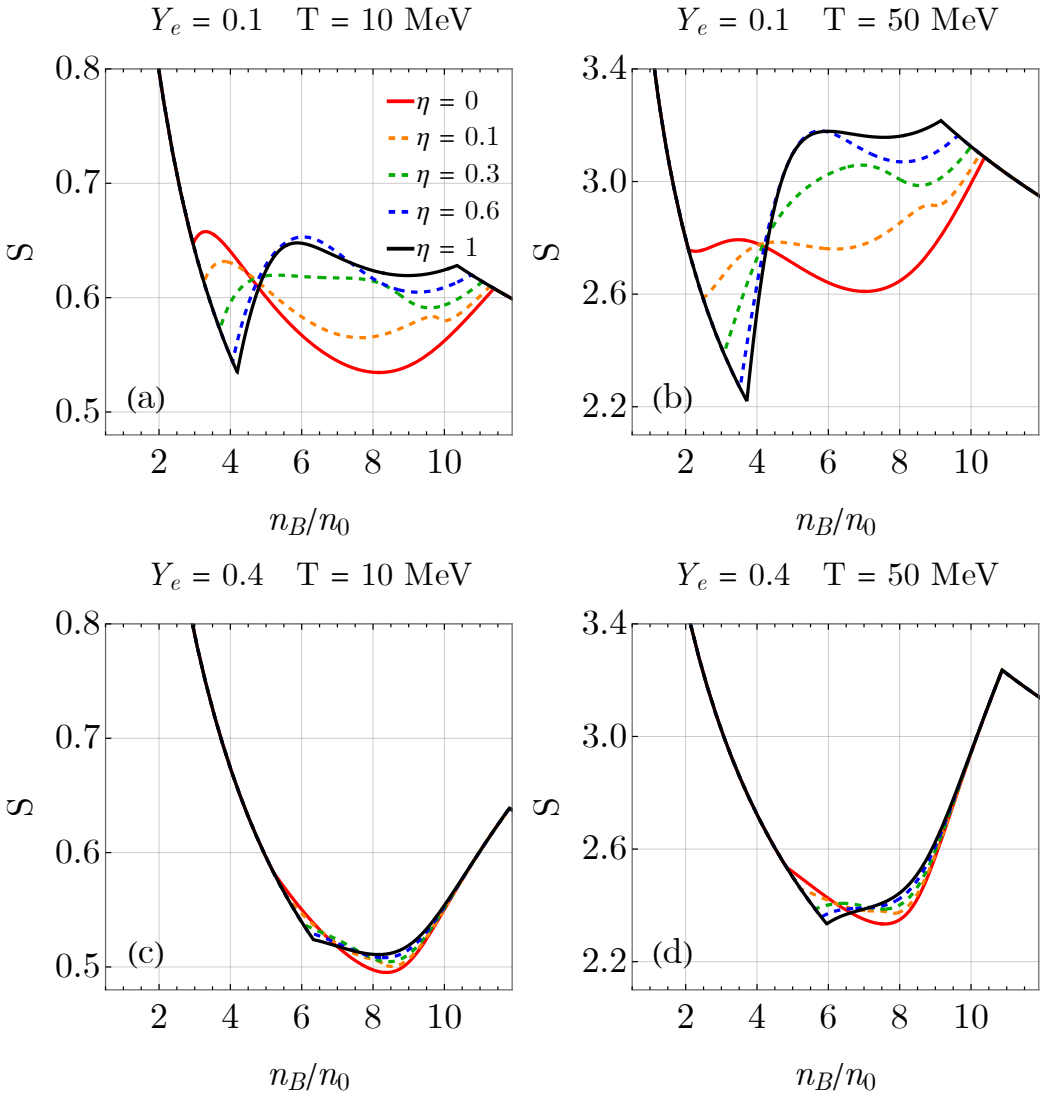

Figure 3.7: Specific entropy $S = s/n_B$ vs. baryon density n_B for the indicated values of the local–to–total lepton ratio η, net electron fraction Y_e, and temperature T. Figure from [41].

The specific heats per baryon at constant volume and constant pressure are defined as

$$C_V = \frac{1}{n_B} \left.\frac{\partial \varepsilon}{\partial T}\right|_{n_B,\{Y_i\}}, \tag{3.58}$$

$$C_P = \frac{1}{n_B} \left.\frac{\partial h}{\partial T}\right|_{P,\{Y_i\}}, \tag{3.59}$$

where ε is the energy density, $h = (\varepsilon + P)/n_B$ the enthalpy per baryon, and $\{Y_i\}$ denotes the set of particle fractions kept fixed during the differentiation. In practice, we often compute C_P from C_V and derivatives of P using the standard relation [185]

$$C_P = C_V + \frac{T}{n_B^2} \frac{\left(\partial P/\partial T|_{n_B,\{Y_i\}}\right)^2}{\partial P/\partial n_B|_{T,\{Y_i\}}}. \tag{3.60}$$

The adiabatic sound speed is

$$c_{\rm ad}^2 = \left.\frac{\partial P}{\partial \varepsilon}\right|_{S,\{Y_i\}} = \frac{C_P}{C_V} \frac{n_B}{\varepsilon + P - Ts} \left.\frac{\partial P}{\partial n_B}\right|_{T,\{Y_i\}}, \tag{3.61}$$

where the second equality follows from a Legendre transform to the variables $(n_B, \{Y_i\}, T)$. Chemical susceptibilities, which we do not display explicitly, are second derivatives of the free energy density with respect to conserved densities or, equivalently, derivatives of particle densities with respect to chemical potentials, e.g.

$$\chi_{ij} = \left.\frac{\partial n_i}{\partial \mu_j}\right|_{T,\{\mu_{k\neq j}\}}, \tag{3.62}$$

and encode the response of the system to changes in composition.

A crucial point, emphasized in [41], is that first derivatives of the free energy (e.g. P, ε, s) are independent of the order in which we impose thermodynamic equilibrium conditions and take derivatives: imposing equilibrium first or last gives the same result. In contrast, *second* and higher derivatives, such as C_V, C_P, $c_{\rm ad}^2$ or chemical susceptibilities, do depend on which variables are regarded as independent at the level of the derivatives.

Physically, this is related to the timescale over which perturbations propagate. If fluctuations are very fast compared with the timescales of reactions that change composition, the particle fractions and the phase volume fraction χ cannot readjust to maintain chemical equilibrium. In that *fast* limit, partial derivatives entering response functions must be taken at fixed $\{Y_i\}$ and fixed χ.

In the opposite *slow* limit, reactions mediated by strong and electromagnetic interactions are assumed to equilibrate, so chemical equilibrium relations among hadrons and quarks are imposed *before* taking derivatives. In that case, only globally conserved charges (such as B and C depending on the setup) remain independent, and the particle fractions $\{Y_i\}$ become implicit functions of (n_B, Y_e, T, η) via the equilibrium conditions. However, even in this slow limit, χ is kept fixed during differentiation to

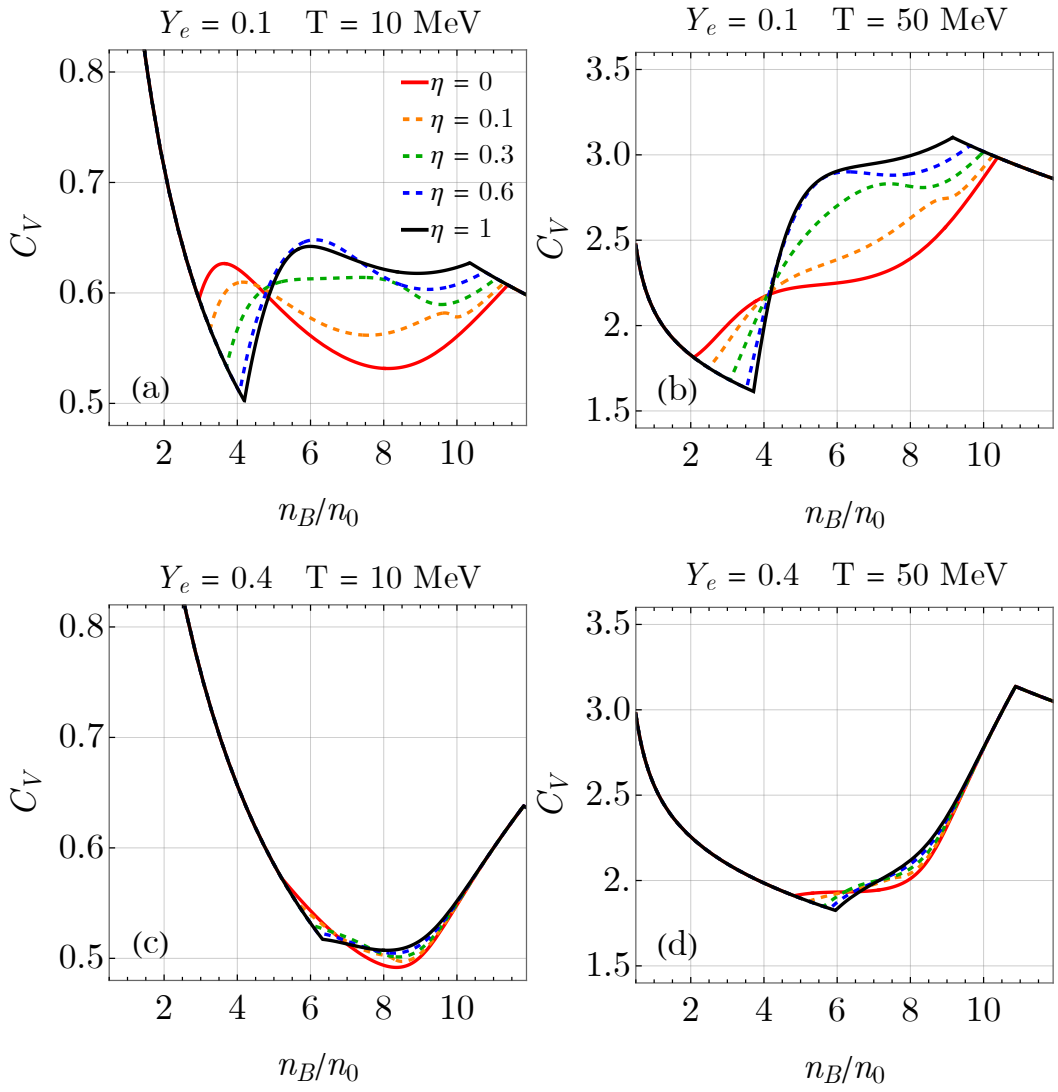

Figure 3.8: Specific heat per baryon at constant volume C_V vs. baryon density n_B for the indicated values of the local–to–total lepton ratio η, net electron fraction Y_e, and temperature T. Figure from [41].

ensure continuity of the response functions across the mixed phase; mechanical equilibrium ($P_H = P_Q$) is enforced only *after* the derivatives are evaluated.

The behavior of C_V and C_P is shown in Figs. 3.8 and 3.9. Both quantities increase with temperature and exhibit non–trivial structure in the mixed phase, reflecting the onset of quark degrees of freedom. At low densities the difference between C_P and C_V is largest, as expected in a relatively compressible regime; at higher densities, where the EOS stiffens, C_P and C_V become closer.

In a naive two–phase construction (simply stitching hadronic and quark EOSs at their crossing point) the adiabatic compressibility,

$$\left.\frac{\partial P}{\partial n_B}\right|_S , \tag{3.63}$$

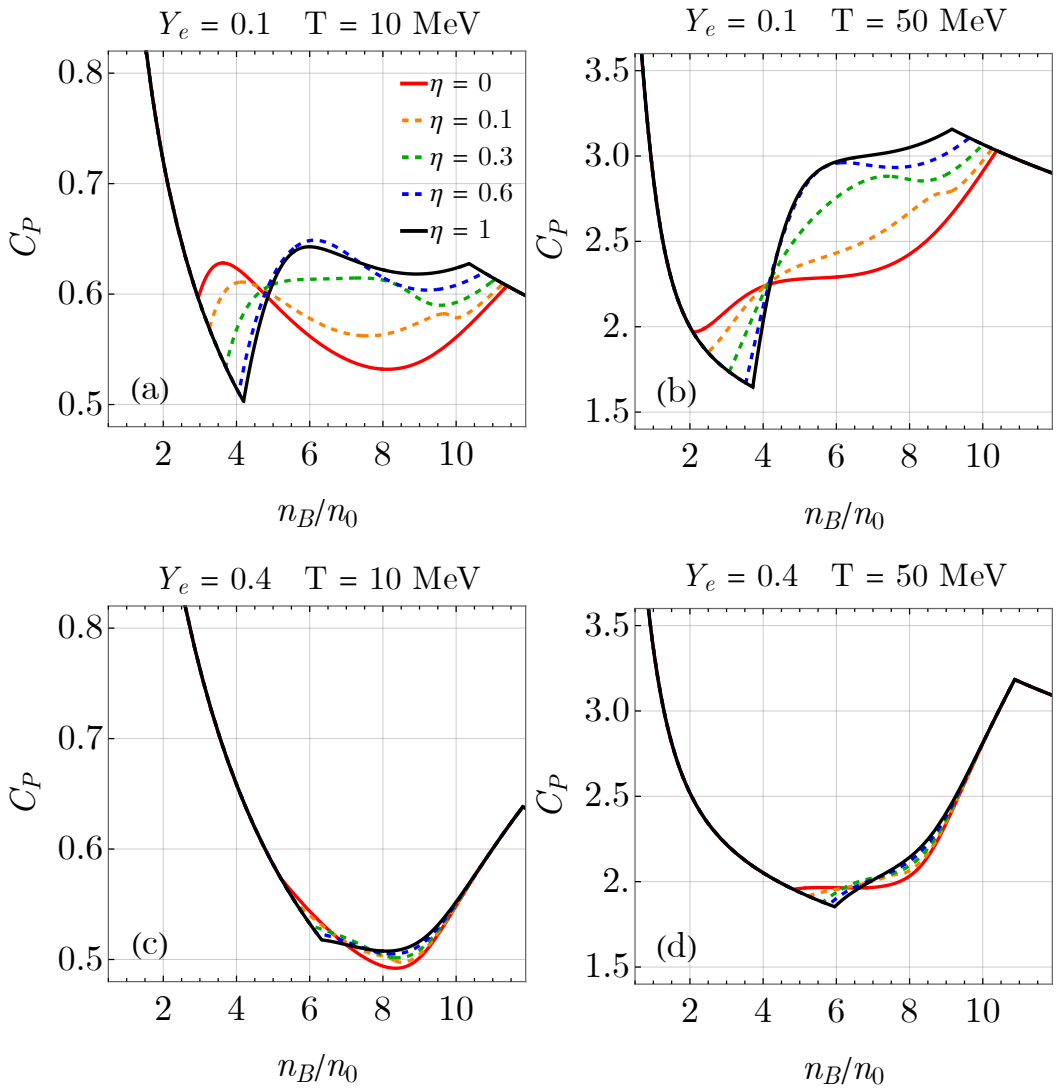

Figure 3.9: Specific heat per baryon at constant pressure C_P vs. baryon density n_B for the indicated values of the local–to–total lepton ratio η, net electron fraction Y_e, and temperature T. Figure from [41].

can become negative just above the transition density, because the quark phase is energetically favored but has a lower pressure at the same n_B. This signals a mechanical instability, and related response functions, such as C_P or chemical susceptibilities, may show divergences or discontinuities.

The Maxwell, Gibbs, and intermediate constructions cure this problem at the macroscopic level. Imposing mechanical equilibrium,

$$P_H = P_Q, \tag{3.64}$$

through a proper minimization of the free energy, the mechanical equilibrium condition ensures that the total pressure is a non–decreasing function of n_B in the mixed phase. Since all partial derivatives are computed at fixed χ and equilibrium is imposed only afterward, they remain continuous; in particular

$$\left.\frac{\partial P}{\partial n_B}\right|_S > 0 \tag{3.65}$$

everywhere. Consequently, any peaks or extrema in C_P and C_V should be interpreted as signatures of the mixed phase and the appearance of new degrees of freedom, not as physical instabilities. This remains true even in β–equilibrated, $\eta \simeq 1$ cases in which the pressure is nearly constant across the mixed phase: the stellar configurations built from such EOSs are mechanically stable, although the mixed region may occupy only a small radial range.

3.2.6 Adiabatic sound speed

Figure 3.10 shows the adiabatic sound speed squared c_{ad}^2 as a function of n_B in the two limiting regimes described above. In the *fast* regime, derivatives are taken at fixed pure–phase fractions $\{Y_i\}$ and fixed χ, corresponding to perturbations that do not allow composition to readjust. In the *slow* regime, derivatives are taken at fixed Y_C and χ since strong and electromagnetic equilibrium are imposed prior to differentiation.

In both regimes, c_{ad}^2 typically increases with density in the pure nucleonic phase, reaches a maximum near the onset of the mixed phase, then decreases across the mixed region before rising again in the pure quark phase. For large η, the peak tends to occur right at the hadron–quark transition; for small η, the sound speed starts from a lower value at the onset of mixing and reaches its maximum somewhat deeper in the mixed phase. The slow–perturbation sound speed in the mixed phase is generally slightly smaller than in the fast case, reflecting the additional softening associated with composition readjustment.

At high densities in the quark phase, c_{ad}^2 approaches values of order $\sim 1/2$, exceeding the conformal limit $1/3$. This is a direct consequence of the repulsive vector interaction in the vMIT model, which mimics non–perturbative effects expected at densities that are still far from the asymptotically free QCD regime.

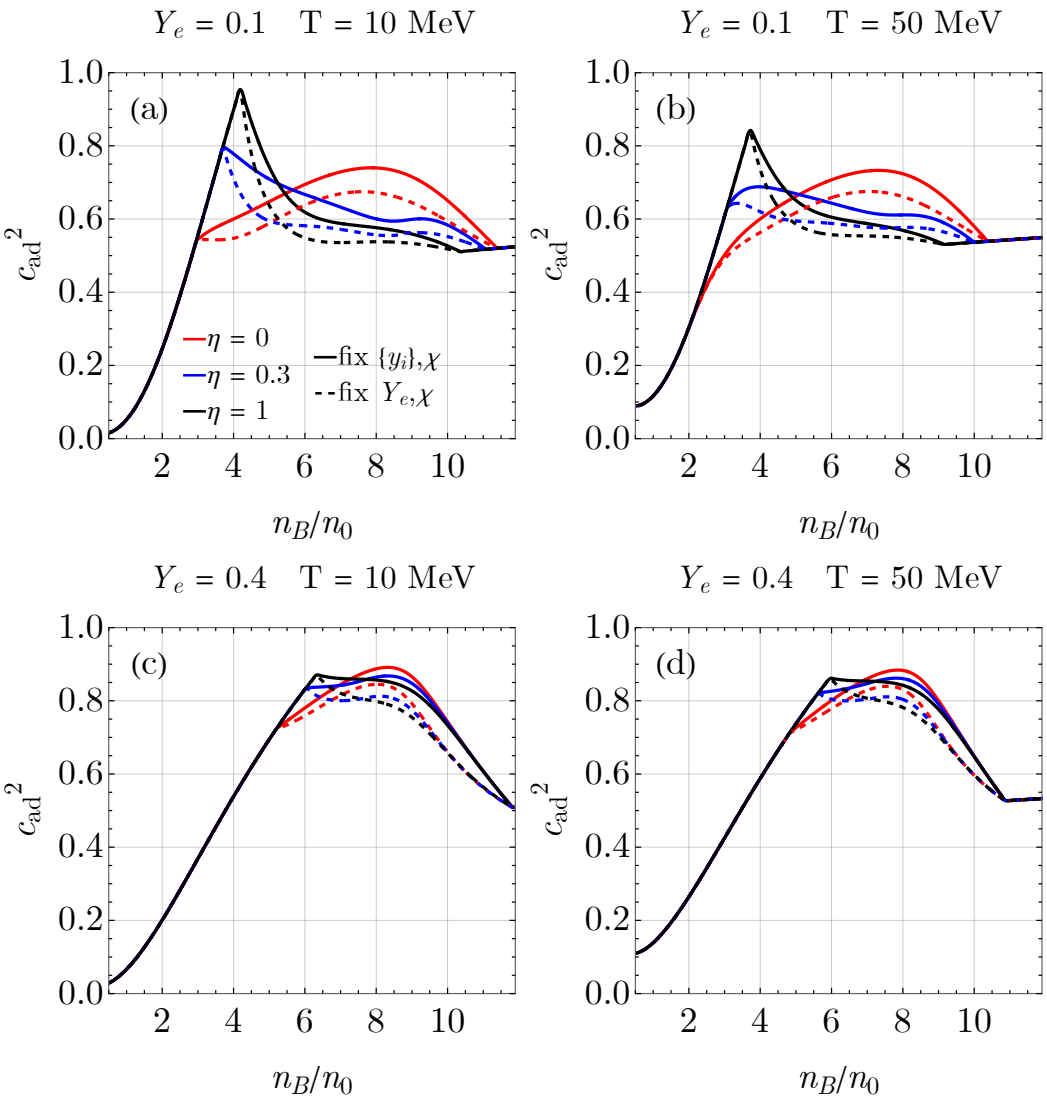

Figure 3.10: Adiabatic sound speed squared c_{ad}^2 vs. baryon density n_B in the fast–propagation (fixed $\{y_i\}, \chi$) and slow–propagation (fixed Y_e, χ with chemical equilibrium) regimes, for the indicated values of the local–to–total lepton ratio η, net electron fraction Y_e, and temperature T. Figure from [41].

3.2.7 Thermal index

In hydrodynamic simulations it is common to evolve conserved quantities such as the total energy density ε and baryon density n_B, and reconstruct other thermodynamic variables (e.g. T, P) from the EOS. A popular approximation is to decompose the pressure as

$$P(\varepsilon, n_B) = P(n_B, T = 0) + P_{\rm th}(n_B, T), \tag{3.66}$$

$$\Gamma(n_B, T) = 1 + \frac{P_{\rm th}(n_B, T)}{\varepsilon - \varepsilon(n_B, T = 0)}, \tag{3.67}$$

and approximate the thermal index Γ as a constant ("Γ–law" EOS). For a single degenerate Fermi species this works well: $\Gamma \simeq 5/3$ for non–relativistic and $\Gamma \simeq 4/3$ for ultra–relativistic matter. A more refined approach allows Γ to depend on density, $\Gamma = \Gamma(n_B)$, fit once and for all at $T = 0$.

For CCSN and BNSM EOSs, Y_e is also a free variable, so the cold EOS is $P(n_B, Y_e)$ and $\varepsilon(n_B, Y_e)$. In purely hadronic or purely quark matter, the dependence of $\Gamma(n_B, Y_e, T)$ on Y_e is usually mild, so a nearly constant Γ remains acceptable. This can be seen by comparing the top and bottom panels of Fig. 3.11. The situation changes qualitatively in a hybrid EOS with a mixed phase, where the volume fraction χ is itself determined by mechanical and chemical equilibrium.

In that case, several definitions of thermal pressure are possible:

(i) $P_{\rm th} = P[\{Y_i(T = 0)\}, \chi(T = 0), T] - P[\{Y_i(T = 0)\}, \chi(T = 0), 0]$,

(ii) $P_{\rm th} = P[\{Y_i(T)\}, \chi(T), T] - P[\{Y_i(T)\}, \chi(T), 0]$,

(iii) $P_{\rm th} = P[\{Y_i(T)\}, \chi(T), T] - P[\{Y_i(0)\}, \chi(0), 0]$,

where, for compactness, $P(\{Y_i\}, \chi, T)$ stands for $P(n_B, \{Y_i\}, \chi, T)$ and the implicit dependence $\{Y_i(T)\} \equiv \{Y_i(n_B, Y_e, T)\}$, $\chi(T) \equiv \chi(n_B, Y_e, T)$ arises from the equilibrium condition. The corresponding thermal energy density $\varepsilon_{\rm th}$ is defined analogously, and we compute

$$\Gamma = 1 + \frac{P_{\rm th}}{\varepsilon_{\rm th}}. \tag{3.68}$$

Definitions (i) and (ii) coincide in the $T \to 0$ limit and lead to very similar results at low T; we therefore show only definition (ii) in Fig. 3.11. In the mixed phase, Γ then decreases smoothly from $\simeq 5/3$ in nucleonic matter toward $\simeq 4/3$ in quark matter. As η is increased from 0 (GCN) to 1 (LCN), the mixed phase shrinks and the drop in Γ becomes sharper.

Figure 3.12 shows the thermal index computed with definition (iii), which is closer to what is done in many simulations that extend a cold EOS to finite T by adding a thermal component. The resulting behavior can be divided into five density regions (see also Refs. [186, 187]): At low n_B the system is purely nucleonic both at $T = 0$ and at finite T, and Γ is nearly constant with its hadronic value. At slightly higher densities, the system is in the mixed phase at finite T but still purely hadronic at $T = 0$. Here Γ

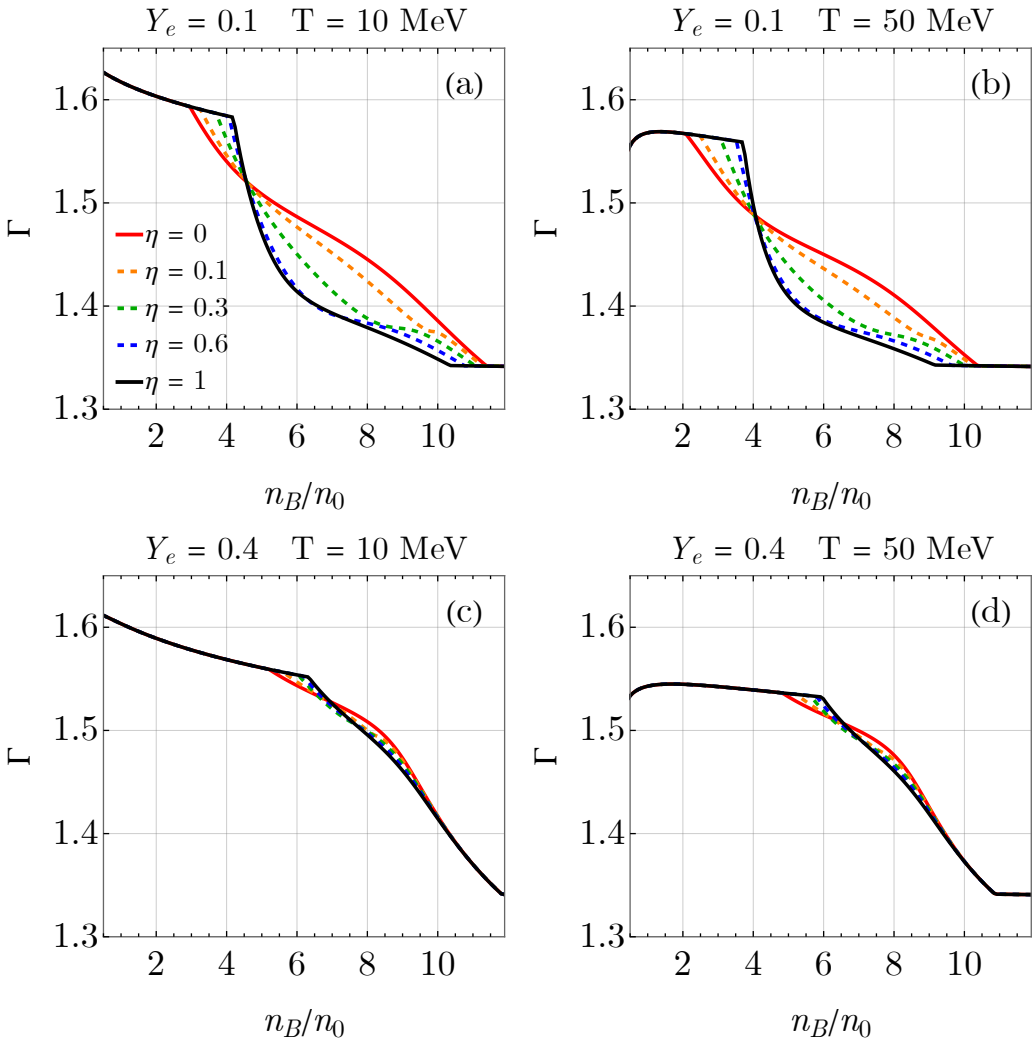

Figure 3.11: Thermal index Γ defined via prescription (ii) vs. baryon density n_B for the indicated values of the local–to–total lepton ratio η, net electron fraction Y_e, and temperature T. Figure from [41].

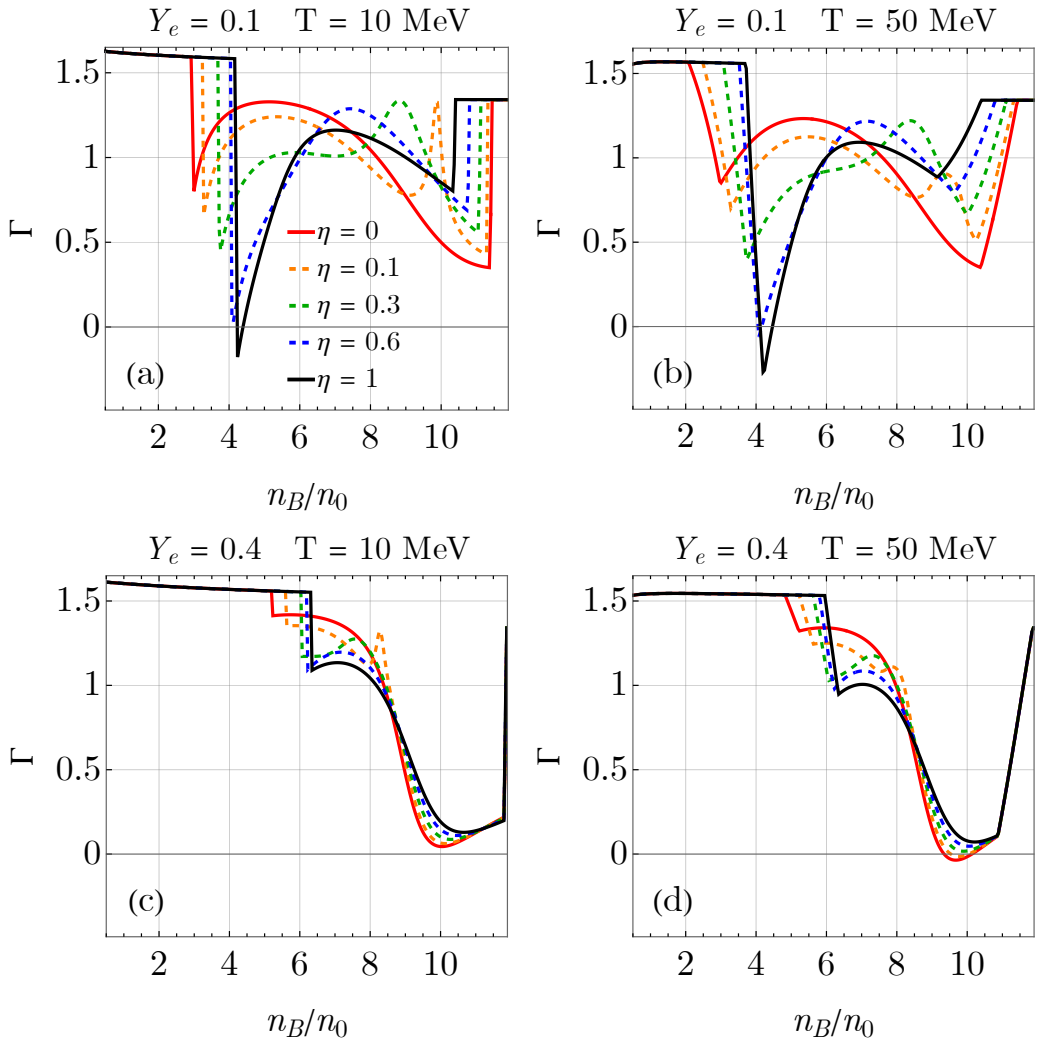

Figure 3.12: Thermal index Γ defined via prescription (iii) vs. baryon density n_B for the indicated values of the local–to–total lepton ratio η, net electron fraction Y_e, and temperature T. Figure from [41].

drops sharply and monotonically. In an intermediate range, the system is in the mixed phase at both temperatures. Γ is non–monotonic, may exhibit multiple peaks, and can be substantially smaller than in the pure phases, sometimes even dipping below zero for certain (n_B, Y_e). At higher densities, the system is in the quark phase at finite T but still mixed at $T = 0$, and Γ rises sharply. Finally, at the highest densities the system is purely quark at both temperatures and Γ again approaches a nearly constant value characteristic of pure quark matter.

The rapid variations in regions 2 and 4 might be misinterpreted as discontinuities; in reality, they are narrow but finite density intervals whose width grows with T. They arise because the mixed–phase boundaries occur at different densities at $T = 0$ and at finite T when definition (iii) is used. In definitions (i) and (ii), χ is kept fixed in the differentiation, so these extra structures do not appear. Only in the strict $T \to 0$ limit do regions 2 and 4 collapse into points, at which Γ is truly discontinuous.

These considerations show that a simple constant–Γ extension of a cold hybrid EOS to finite temperatures is generally inadequate to describe the mixed phase. Even an interpolation of two constant values for the hadronic and quark phases is only reasonable if one uses definitions (i) or (ii),*i.e.* if the finite–temperature extension is performed *before* enforcing chemical and mechanical equilibrium to determine $\{Y_i(n_B, Y_e, T)\}$ and $\chi(n_B, Y_e, T)$. Refinements of the constant–Γ approximation, tailored to definition (iii), have been proposed in Refs. [186, 187].

Part III

Deconfinement in the two-families scenario

Chapter 4

Decay of the metastable hadronic phase

In this chapter, wediscuss the nucleation of deconfined quark matter in a metastable hadronic medium, namely the formation of a microscopic critical deconfined droplet from spontaneous local fluctuations that trigger the phase transition on a macroscopic scale. Section 4.1 outlines, at a schematic level, the stages of the conversion of a hadronic object into a QS. Section 4.2 reviews fluctuation theory for multi-component thermodynamic systems, setting the notation used in the rest of the chapter. Section 4.3 then develops the nucleation problem in detail, deriving the critical-size condition and the corresponding rates.

4.1 Conversion of a hadronic star

On macroscopic scales, the deconfinement transition that converts a hadronic object into a QS proceeds through a sequence of out-of-equilibrium stages [10]. A useful working picture is (see Fig. 4.1):

(i) *Nucleation:* a fluctuation produces a deconfined droplet that exceeds the critical size and is therefore energetically favored to grow rather than shrink. This requires overcoming the energy barrier in the phase space through a spontaneous thermal fluctuation or quantum tunneling.

(ii) *Seed growth:* critical seeds expand or merge with others, until reaching a macroscopic size;

(iii) *Macroscopic conversion:* the subsequent propagation of the conversion front can be treated within a hydrodynamic framework and proceeds in two regimes: an initial, turbulent deflagration whose velocity is greatly enhanced by hydrodynamical instabilities that converts the stellar core in a few milliseconds [31, 32, 188, 189], followed by a slower, strangeness diffusion driven burning, governed by the production and transport of strangeness, that converts the outer layers over tens of seconds [31, 190, 191].

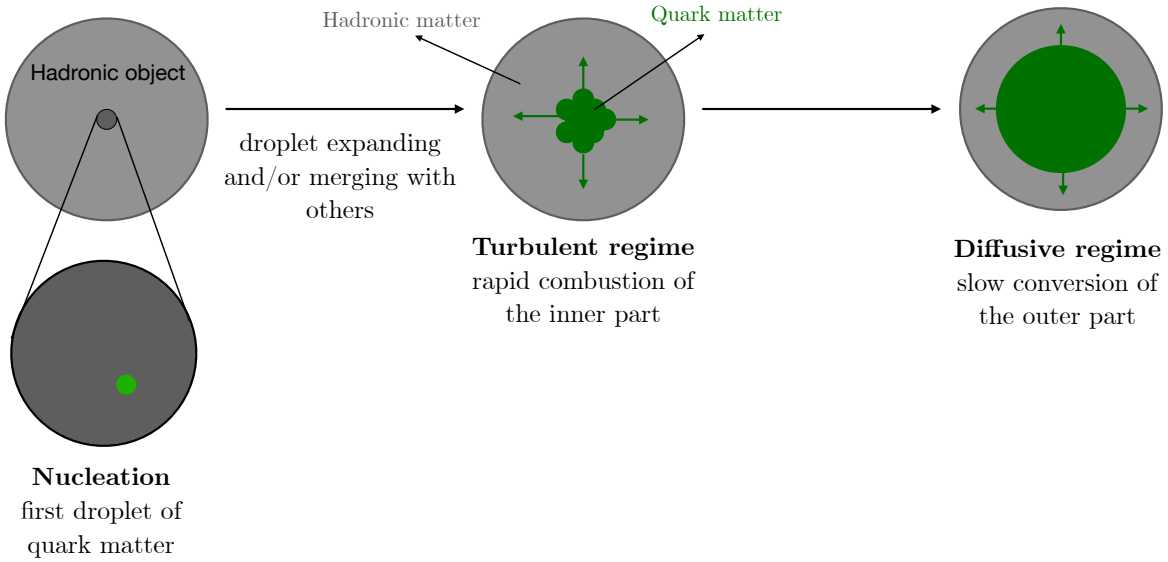

Figure 4.1: Schematic steps for a conversion of a hadronic compact star into a QS. See the text for the details.

Throughout this thesis, the emphasis is on identifying the thermodynamic conditions under which nucleation becomes possible and efficient in realistic astrophysical systems. The subsequent large-scale phase transition is summarized here only insofar as needed to connect microscopic nucleation to the final QS and related observables.

4.2 Fluctuations

Since thermal nucleation is an activated thermal fluctuation that overcomes an energy barrier, let us first review the theory of thermal fluctuations that underpins the nucleation calculations.

In macroscopic equilibrium, thermodynamic quantities are sharply peaked around their ensemble averages. Nevertheless, small deviations, namely *thermal fluctuations*, do occur.

4.2.1 Thermal fluctuations

Let us consider an isolated multicomponent system with fixed total energy E, volume V, and particle numbers $\{N_i\}$ for each component i. We coarse-grain the set of microstates in phase space into macrostates (or *configurations*) that will be labeled with x. According to the Boltzmann principle, the probability associated with a macrostate is proportional to the number of microstates that realize it

$$\mathcal{P}(x) \propto \mathcal{W}(x) = e^{S(x)}, \tag{4.1}$$

where

$$S(x) = \ln \mathcal{W}(x), \tag{4.2}$$

is the entropy of that macrostate and $\mathcal{W}(x)$ is the number of microstates (or phase–space measure) compatible with macrostate x. The equilibrium macrostate $\bar{x}$ is the most probable one, namely the one that maximizes S under the proper constraints. Then the probability that a system in the equilibrium configuration explores a fluctuated macrostate x' is the relative weight between the two

$$\mathcal{P}(\bar{x} \to x') \propto e^{\Delta S(x')} \equiv e^{S(x')-S(\bar{x})}. \tag{4.3}$$

To explore the fluctuations around the equilibrium configuration, let us consider a fluctuated macrostate x' in which a certain small subsystem of the system is characterized by the homogeneous thermodynamic quantities $(E^*, V^*, \{N_i^*\})$ while the homogeneous surroundings by $(E^o, V^o, \{N_i^o\})$, such that

$$\begin{aligned} E &= E^o + E^* && (4.4)\\ V &= V^o + V^* && (4.5)\\ N_i &= N_i^o + N_i^* \qquad \forall\, i. && (4.6) \end{aligned}$$

On the other hand, in the equilibrium macrostate $\bar{x}$, the thermodynamic variables are homogeneous everywhere $(\bar{E}, \{\bar{N}_i\}, \bar{V}) = (E, \{N_i\}, V)$. The entropy difference between the two macrostates is

$$\begin{aligned} \Delta S(x') &= S(x') - S(\bar{x}) && (4.7)\\ &= [S(E^*, \{N_i^*\}, V^*) + S(E^o, \{N_i^o\}, V^o)] - S(\bar{E}, \{\bar{N}_i\}, \bar{V}) && (4.8)\\ &= \Delta S^* + \Delta S^o && (4.9) \end{aligned}$$

where ΔS^* and ΔS^o are the entropy difference in the subsystem and in the surroundings, respectively, between the macrostates x and x'. The subsystem can be identified, for example, with a certain volume or with a certain number of a component. Let us assume that the subsystem is much smaller than the surroundings, such that $V^* \ll V^o$, $N_i^* \ll N_i^o$, $E^* \ll E^o$. Expanding to the first order $S^o(E^o, V^o, \{N_i^o\})$ around the equilibrium quantities $(\bar{E}^o, \bar{V}^o, \{\bar{N}_i^o\})$:

$$\begin{aligned} \Delta S^o &\equiv S^o - \bar{S}^o && (4.10)\\ &= \left(\frac{\partial S^o}{\partial E^o}\right)_{V,\{N_i\}} \Delta E^o + \left(\frac{\partial S^o}{\partial V^o}\right)_{E,\{N_i\}} \Delta V^o + \sum_i \left(\frac{\partial S^o}{\partial N_i^o}\right)_{E,V} \Delta N_i^o + \mathcal{O}(\Delta^2) \\ &= \frac{\Delta E^o}{\bar{T}} + \frac{\bar{P}\Delta V^o}{\bar{T}} - \frac{\sum_i \bar{\mu}_i \Delta N_i^o}{\bar{T}} + \mathcal{O}(\Delta^2), && (4.11) \end{aligned}$$

where ΔE^o, ΔV^o and ΔN_i^o are respectively the differences in energy, volume and number of the component i of the surroundings in the fluctuated macrostate x' with respect to the equilibrium macrostate $\bar{x}$. Thus, to first order, the surroundings intensives in x' are the *equilibrium* ones $\bar{x}$. Thus, processes involving the subsystem do not lead to any appreciable change in intensive thermodynamical quantities of the surroundings (μ_i^o, T^o, P^o), which acts as a thermodynamic bath,

$$P^o \simeq \bar{P}\,, \qquad \mu_i^o \simeq \bar{\mu}_i \;\forall\, i\,, \qquad T^o \simeq \bar{T}. \tag{4.12}$$

The Eq. (4.9) becomes

$$\Delta S(x') = \Delta S^* + \frac{\Delta E^o + \bar{P}\Delta V^o - \sum_i \bar{\mu}_i \Delta N_i^o}{\bar{T}} \tag{4.13}$$

$$= \frac{\bar{T}\Delta S^* + \Delta E^o + \bar{P}\Delta V^o - \sum_i \bar{\mu}_i \Delta N_i^o}{\bar{T}}, \tag{4.14}$$

The conservation of the total energy, volume and numbers Eqs. (4.4, 4.5, 4.6), implies that the variations in the surroundings are opposite to the variations in the subsystem $\Delta E^o = -\Delta E^*$, $\Delta V^o = -\Delta V^*$, $\Delta N_i^o = -\Delta N_i^*$. Thus,

$$\Delta S(x') = -\frac{\Delta E^* - \bar{T}\Delta S^* + \bar{P}\Delta V^* - \sum_i \bar{\mu}_i \Delta N_i^*}{\bar{T}}. \tag{4.15}$$

The numerator of Eq. (4.15) is the *minimum reversible work* W needed from an external source to create the fluctuation under the imposed constraints [185]

$$W = \Delta E^* - \bar{T}\Delta S^* + \bar{P}\Delta V^* - \sum_i \bar{\mu}_i \Delta N_i^*. \tag{4.16}$$

Thus, the probability of a fluctuation from the equilibrium macrostate $\bar{x}$ into a fluctuated macrostate x' characterized by a subsystem (small with respect to the system) in which the thermodynamic quantities fluctuate by ΔE^*, ΔS^*, ΔV^*, ΔN_i^* and a surroundings acting as thermodynamic bath is

$$\mathcal{P}(\bar{x} \to x) = \mathcal{Z}\, e^{-\frac{W}{T}}, \tag{4.17}$$

where $\mathcal{Z}$ is the prefactor that normalize the probability over all the *accessible macrostates*. Note that

$$\Delta E^* = E^* - \bar{E}^* = -P^*V^* + S^*T^* + \sum_i \mu_i^* N_i^* - \left(-\bar{P}\bar{V}^* + \bar{S}^*\bar{T} + \sum_i \bar{\mu}_i \bar{N}_i^*\right), \tag{4.18}$$

where $\bar{E}^*$, $\bar{V}^*$, $\bar{S}^*$ and $\bar{N_i}^*$ are the energy, volume, entropy and component numbers (namely, the extensive quantities) of the same subsystem evaluated in the equilibrium macrostate $\bar{x}$. The intensive quantities are equal everywhere in the macrostate $\bar{x}$.

Replacing Eq. (4.18) in Eq. (4.16), the minimum work becomes

$$W = -V^*\Delta P^* + S^*\Delta T^* + \sum_i N_i^* \Delta \mu_i^*. \tag{4.19}$$

If the considered system is not isolated (namely, the total energy is not conserved), but is instead kept at constant temperature T, the macrostate probability is $\propto \exp(S)\exp(-E/T) = \exp(-F/T)$, where $F = E - ST$ is the free energy. Following similar steps as before,

it can be shown that Eq. (4.17) holds, where

$$\begin{aligned} W &= F(x') - F(\bar{x}) && (4.20)\\ &= (F^* + F^o) - \bar{F} && (4.21)\\ &= \left[-P^*V^* + \sum_i \mu_i^* N_i^* - P^oV^o + \sum_i \mu_i^o N_i^o\right] + \bar{P}(V^* + V^o) - \sum_i \bar{\mu}_i(N_i^* + N_i^o) \\ &= -(P^o - \bar{P})V^o - (P^* - \bar{P})V^* + \sum_i N_i^o(\mu_i^o - \bar{\mu}_i) + \sum_i N_i^*(\mu_i^* - \bar{\mu}_i) && (4.22)\\ & && (4.23) \end{aligned}$$

where the global conservation of the volume and of the conserved numbers i are used. Moreover, using the assumptions $V^* \ll V^o \simeq V$ and $N_i^* \ll N_i^o \simeq N_i$, and expanding up to the first order ΔF^o as done before with ΔS^o, Eqs. (4.12) hold, and

$$\begin{aligned} W &\simeq -(P^* - \bar{P})V^* + \sum_i N_i^*(\mu_i^* - \bar{\mu}_i) && (4.24)\\ &\equiv -V^*\Delta P^* + \sum_i N_i^* \Delta\mu_i^*. && (4.25) \end{aligned}$$

Finally, it is interesting to note that, for small fluctuations, Eq. (4.17) is a multivariate gaussian peaked at the equilibrium conditions [185]. Indeed, by expanding $\Delta E^*(S^*, \{N_i\}^*, V^*)$ up to the second order and replacing it in Eq. (4.16), linear terms cancel exactly and only higher orders remain. For example, assuming P and T constant [45],

$$\exp\left(-\frac{W}{\bar{T}}\right) \simeq \exp\left[-\frac{1}{2T}\sum_{i,j}\left(\frac{\partial\mu_i}{\partial N_j}\right)_{T,V} \Delta N_i^*\, \Delta N_j^*\right], \qquad (4.26)$$

with the derivative (*i.e.* chemical susceptibilities) evaluated at the equilibrium.

4.2.2 Fluctuations in finite-time strongly interacting systems

Let us consider a single–phase multicomponent hadronic system at fixed volume V, temperature T and a set of conserved numbers $\{N_i\}$. The weights in Eq. (4.1) describe the *equilibrium* distribution: on asymptotically long times every macrostate x' compatible with the thermodynamic constraints is accessible and contributes according to its thermodynamic potential. For a *finite* observation window Δt, instead, the system can only explore configurations that can be assembled by microscopic reactions and transport taking place within Δt. In other words, one samples a restricted ensemble determined by kinetics.

In particular, the accessible macrostates are limited by:

- Charge–changing reaction timescales: Only channels with characteristic times $\tau_r \lesssim \Delta t$ are effectively active; the others are frozen. For hadronic matter, strong processes act on $\tau_{\rm strong} \sim 10^{-23}$ s, whereas weak processes are much slower and strongly ambient dependent: nonleptonic flavor–changing reactions ($u + d \leftrightarrow u + s$) have $\tau_{\rm weak(s)} \sim (10^{-10} - 10^{-6})$ s [192, 193], while semileptonic β processes

(*e.g.* $u + e^- \leftrightarrow d + \nu_e$) are even slower [114, 115, 194].

  - If $\tau_{\text{strong}} \ll \Delta t \ll \tau_{\text{weak}}$: only strong interactions act. Net quark flavors u, d, s (equivalently, the linear combinations B, C, S) are separately conserved on Δt, so macrostates with different net flavor content are inaccessible.
  - If $\tau_{\text{strong}} \ll \tau_{\text{weak}} \ll \Delta t$: weak processes are active and net flavors are *not* separately conserved.
    * If only nonleptonic weak channels operate on Δt: S can change, but B and C remain conserved.
    * If β processes also operate: C can change via exchange with leptons, while total electric charge is always conserved (and lepton numbers may or may not be conserved depending on neutrino trapping).

- Transport (diffusion) constraints: to reach a fluctuated macrostate x' within a finite window Δt, the system must physically rearrange the relevant conserved charges across a characteristic distance L. With diffusive transport, the typical distance a conserved quantity can be moved in time Δt is the *diffusion length*

$$\ell_D(\Delta t) \equiv \sqrt{D_{\text{eff}}\,\Delta t}, \tag{4.27}$$

  where D_{eff} is the effective diffusivity for the charge being transported. A necessary (and in practice, near-sufficient) condition for kinetic accessibility on the window Δt is therefore

$$L \lesssim \ell_D(\Delta t). \tag{4.28}$$

  Macrostates that require transporting conserved charge over distances $L \gg \ell_D(\Delta t)$ are *not reachable* in time Δt and should be excluded from the finite-time ensemble, even if they possess a well-defined equilibrium weight. Conversely, for $L \ll \ell_D(\Delta t)$, the corresponding fluctuated macrostates are reachable and should be included. When only strong interactions are active on Δt (*i.e.* $\tau_{\text{strong}} < \Delta t \ll \tau_{\text{weak}}$), no local sources can create the excess charge inside the fluctuated subsystem, so x' can be built only by diffusive rearrangement from the surroundings.

The lepton numbers (*e.g.* L_e for electrons) are conserved on the timescale of interest only if neutrinos are *trapped*. Operationally, if the neutrinos' mean free path is much shorter than the system, neutrinos remain in equilibrium with matter and carry nonzero chemical potentials μ_{ν_e}.

In compact-star applications, we could identify the "system" with a volume that is (i) much larger than the fluctuating subregion (so it acts as a thermodynamic bath) and (ii) small enough to ensure that spatial gradients due to gravity across the cell can be ignored and thus average thermodynamic variables can be defined.

A concrete example is a grid cell in a numerical simulation: at each snapshot, the cell is specified by fixed control variables (typically the baryon density n_B, charge fraction Y_C, and temperature T) which define the local equilibrium state. Representative values are a cell size $\sim 10^2$ m and a "lifetime" set by the time step, of order the dynamical time $\tau_{\text{dyn}} \sim 10^{-4}$ s. It is worth specifying that throughout this chapter we focus on

microscopic, fluctuations *within* a cell (namely, deviations from the local equilibrium established by processes faster than the lifetime of the cell), rather than on *macroscopic*, out-of-equilibrium variations over larger spatial or temporal scales (*e.g.*, the fact that simulation cells are not in β equilibrium), which are instead described within a hydrodynamic framework.

4.3 Nucleation

If a phase transition is of first order, *i.e.* it involves latent heat, there exists a nonzero surface tension between the two phases. Thermodynamically, the surface tension is the extra free energy per unit area required to create an interface, reflecting the fact that particles near a boundary have different interactions than those in the bulk.

Thus, a first-order phase transition at macroscopic scales proceeds via *nucleation*[1], whereby a spontaneous (thermal or quantum) fluctuation in an initially metastable system creates a *critical* seed of the new phase that overcomes the interfacial free–energy cost and grows, thereby triggering the decay of the metastable state.

Let us consider a system of volume V and at temperature T initially in a stable H phase. By increasing density (*e.g.* raising pressure) or temperature, the globally favored state may become the Q phase filling the entire volume[2].

Since the system sits in a local minimum corresponding to the pure H state, a finite Q volume V_Q must be created to reach the global minimum. However, although the fully converted configuration ($V_Q = V$) is more stable than the pure H state ($V_Q = 0$), not all intermediate configurations with $0 < V_Q < V$ are necessarily energetically favorable: because of the finite-size cost of the surface tension, small droplets are disfavored. In particular, a configuration with volume V_Q is more stable than a pure H state only if V_Q is sufficiently large for the energetically favorable bulk term to outweigh the unfavorable surface contribution. As a result, there is an energy barrier between the metastable configuration (pure H state) and the global minimum (pure Q state). The maximum of the energy as a function of V_Q defines the *critical volume* V_{Q*} and the *energy barrier height* W^* (which is the free energy difference between this maximum configuration and the initial local minimum configuration H).

Namely, V_{Q*} is the critical droplet volume of phase Q in H medium such that a slightly larger configuration ($V_Q = V_{Q*} + \epsilon$, with ϵ infinitesimal) is energetically favored over $V_Q = V_{Q*}$. Droplets with $V_Q < V_{Q*}$ tend to shrink, whereas those with $V_Q \geq V_{Q*}$ to grow. Hence, to trigger conversion one needs a spontaneous thermal fluctuation that produces a droplet at least as large as V_{Q*} (*thermal nucleation*), or a quantum tunneling event that crosses the barrier (*quantum nucleation*). See Fig. 4.2 for a schematic picture. Note that a fluctuation of the droplet volume V_Q can be viewed as a fluctuation of the *order parameter* of the phase transition.

[1] Another possible pathway is *spinodal decomposition*, which occurs if the system is driven into a mechanically unstable region before nucleation can take place in the metastable one. See Sec. 1.3.2.

[2] For simplicity, we ignore here the possibility that the minimum–energy configuration is a mixed ("pasta") phase [112, 113]. In that case the same discussion holds after replacing V with the equilibrium Q-phase structure volume $V_{Q,\mathrm{eq}} \leq V$.

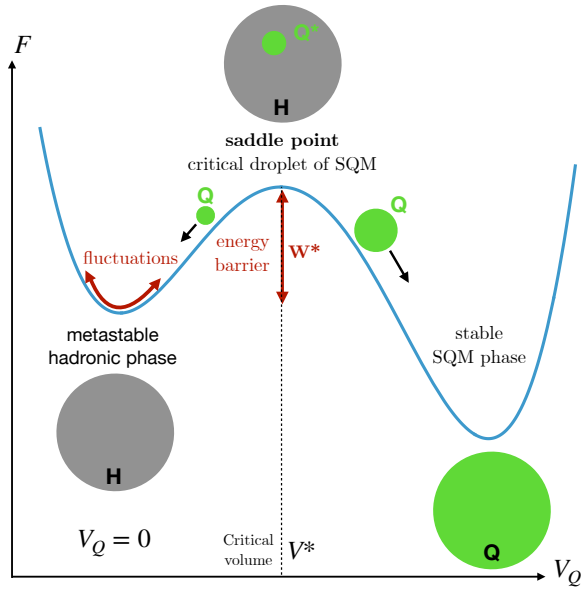

Figure 4.2: Nucleation is the formation, by a spontaneous fluctuation (thermal or quantum), of a *critical* droplet of the stable phase Q within the metastable medium H. In a thermodynamic description the droplet is parameterized by its volume V_Q. The metastable H macrostate is the pure–H configuration, a local minimum of the relevant thermodynamic potential $F(V_Q)$. The *critical* macrostate corresponds to a small Q droplet surrounded by H at which F attains a maximum along V_Q; droplets with $V_Q < V_{Q*}$ shrink, whereas those with $V_Q > V_{Q*}$ grow. Once the critical configuration is reached, the system relaxes toward the global minimum at $V_Q = V$, where the entire system is in phase Q. The barrier height W^* is the difference of the relevant potential between the metastable minimum and the critical configuration.

It is worth stressing two points. The framework developed here concerns only the *trigger* (the formation of the first critical droplet) and not the subsequent macroscopic evolution. Moreover, we do not model the microphysical mechanism of quark deconfinement that creates the deconfined droplet within hadronic matter. Instead, we assume that deconfinement proceeds on strong–interaction timescales, producing a volume V_Q of quark matter as a spontaneous fluctuation (interpretable as a fluctuation of the order parameter), and we ask under which conditions such a fluctuation can be large enough to overcome the barrier and initiate macroscopic conversion (see, *e.g.*, [104] for a tentative microscopic mechanism).

Besides V_Q, other thermodynamic variables can fluctuate spontaneously [185]. Hence, one must first identify which directions in variable space are kinematically accessible on the relevant timescale in approaching the critical configuration. As discussed above, if the initial hadronic phase is metastable, fluctuations in V_Q can lower the free energy of the system if V_Q is large enough. Conversely, if the initial system is already in chemical equilibrium with respect to the active interactions, a fluctuation in any other variable (*e.g.* n_B^Q, Y_C^Q, Y_S^Q) always increases the total free energy. Therefore, the most favorable critical configuration (namely, the one with the lowest possible W^*) is a *saddle point* of the relevant thermodynamic potential F, namely a maximum along the V_Q direction and a minimum along all other directions [30, 195].

In what follows, we present the detailed calculation of the nucleation work and rate for quark matter droplets.

4.3.1 Energy barrier

We now compute the work $W(R_Q)$ to form a spherical droplet of the new phase of radius R_Q, and the associated barrier $W^* \equiv W(R_{Q*})$ that enters the thermal and quantum nucleation rates. Consider a system at fixed $(T, V, \{N_i\})$ with $i = B, C, S, e, \nu$, initially in the local equilibrium pure hadronic state $\bar{x}$. The barrier is the free–energy difference between the *critical* configuration x^* (*i.e.* the saddle point configuration characterized by a spherical droplet in the quark phase Q labeled as Q^* and a surrounding in the H phase labeled as H^o) and the initial configuration $\bar{x}$ Equivalently, it is the minimum reversible work required to build x^* from $\bar{x}$ (Eq. 4.19). For a generic radius R_Q, $W(R_Q)$ is the work to create the droplet, and

$$W^* \equiv W(R_{Q*}) = \max_{R_Q} W(R_Q), \tag{4.29}$$

with R_{Q*} the critical radius.

Since we use two distinct EOS models for the hadronic and quark phases (rather than a single unified potential), we adopt the thin–wall approximation: the $Q - H$ interface is taken to be infinitely thin and characterized by a surface tension σ. In this approximation, the order parameter (and thus, the phase) changes from inside to outside the droplet over a negligible layer, while it is constant inside and outside the droplet (namely, it is a step function), thus the droplet free energy decomposes into

bulk, surface, and Coulomb terms. The corresponding energy barrier splits as

$$W^* = W^*_{\rm bulk} + W^*_{\rm finite\,size} + W^*_{\rm Coulomb}. \tag{4.30}$$

The bulk contribution, proportional to R^3_{Q*}, reads (see Eq. 4.24)

$$\begin{aligned} W^*_{\rm bulk} &= \Delta F^* & (4.31)\\ &= -V_{Q*}(P_{Q*} - P_{\bar{H}}) + \sum_i N_i^{Q*}\left(\mu_i^{Q*} - \mu_i^{\bar{H}}\right), \qquad i = B, C, S, e, \nu_e, & (4.32) \end{aligned}$$

with

$$\begin{aligned} X_{\bar{H}} &\equiv X_H\left(n_B^{\bar{H}}, \{Y_i^{\bar{H}}\}, T\right) & (4.33)\\ X_{Q*} &\equiv X_Q\left(n_B^{Q*}, \{Y_i^{Q*}\}, T\right), & (4.34) \end{aligned}$$

for any thermodynamic quantity X (*e.g.* P, μ_i), evaluated using the EOSs described in Sec. 2. Writing $N_i^{Q*} = n_B^{Q*}\, Y_i^{Q*}\, V_{Q*}$ and $V_{Q*} = 4\pi/3 R^3_{Q*}$, Eq. (4.32) becomes

$$W^*_{\rm bulk} = -\frac{4\pi}{3} R^3_{Q*}\left[(P_{Q*} - P_{\bar{H}}) - n_B^{Q*}\sum_i Y_i^{Q*}\left(\mu_i^{Q*} - \mu_i^{\bar{H}}\right)\right] \tag{4.35}$$

This term is negative (favorable) in the metastable region and positive (unfavorable) when the hadronic phase is stable. As discussed in Sec. 4.2, Eq. (4.32) assumes $V_{Q*} \ll V$ so that the surroundings act as a bath.

The second term in Eq. (4.30) collects all finite-size corrections, such as the surface term $\propto \sigma R^2_{Q*}$, with σ the surface tension, and the curvature term $\propto \varsigma R_{Q*}$, with ς the curvature tension. Both coefficients should ideally be computed self-consistently from the underlying EOS and can depend on temperature and density. Various microscopic approaches exist (see, *e.g.*, field-theoretic calculations [29, 196, 197] and thermodynamic treatments based on multiple reflection expansion [122, 124, 198, 199]), yielding model-dependent values of σ that are highly uncertain, typically $\sigma \sim$ (5–50) MeV/fm^2, but occasionally as low as a few MeV/fm^2 or exceeding 100 MeV/fm^2 [29, 42, 113, 116, 118, 124, 196, 198–203]. Given these uncertainties, we neglect curvature and subsume all finite-size effects into an effective surface tension σ, treated as a free parameter:

$$W^*_{\rm finite\,size} = \sigma\, A_{Q*} = 4\pi\sigma R^2_{Q*}, \tag{4.36}$$

where A_{Q*} is the droplet surface area.

The third contribution in Eq. (4.30) is the electrostatic (Coulomb) term associated with a possible net electric charge of the droplet:

$$W^*_{\rm Coulomb} = E^{\rm Coulomb}_{Q*} \tag{4.37}$$

whose form depends on how charge neutrality is enforced (local or global) and on screening by the electrically charged components. A complete treatment is given in Sec. 4.3.5.

Note that, while $W^*_{\rm bulk}$ can be either positive or negative depending on whether the hadronic phase is stable or metastable, both $W^*_{\rm finite\,size}$ and $W^*_{\rm Coulomb}$ are strictly positive, reflecting the extra cost of creating a *finite* droplet instead of an infinite bulk region. The terms dominate on different scales: for small radii the surface term $W^*_{\rm finite\,size} \propto R^2_{Q*}$ dominates, whereas for larger radii the bulk term $W^*_{\rm bulk} \propto R^3_{Q*}$ controls the behavior. As will be discussed in Sec. 4.3.5, if the droplet and its surroundings carry different electric charge densities, the unscreened Coulomb energy scales as $W^*_{\rm Coulomb} \propto R^5_{Q*}$ and would dominate at sufficiently large R_{Q*}. However, charge screening mitigates its effect.

In the absence of Coulomb effects, if the hadronic phase is stable ($W^*_{\rm bulk} > 0$), $W(R_Q)$ has a minimum at $R_Q = 0$ and increases monotonically for $R_Q > 0$; if it is metastable ($W^*_{\rm bulk} < 0$), $W(R_Q)$ has a minimum at $R_Q = 0$, a maximum at $R_Q = R_{Q*}$, and then decreases without bound as $R_Q \to \infty$. Including the Coulomb term modifies this picture: a maximum may not exist at all, or a second minimum can appear at large R_Q. In an intermediate regime, $W(R_Q)$ may develop such a second minimum with $W > 0$, in which case growth stalls at a configuration still less favorable than the initial state, and thus no critical radius exists in the usual sense. In practice, charge screening strongly suppresses the Coulomb contribution. In the cases considered here, $W(R_Q)$ retains the standard "barrier" shape: a maximum at the critical radius, followed by $W(R_Q) < 0$ for sufficiently large droplets. The additional minimum, when present with screening, occurs only at $R_Q \gg R_{Q*}$, so the qualitative behavior remains close to the Coulomb–free case. Numerically, the resulting R_{Q*} and W^* lie between the limiting scenarios of global charge neutrality with negligible Coulomb corrections and local charge neutrality. Further details are given in Sec. 4.3.5.

Note that in this discussion, we have used a thermodynamic framework to compute the energy barrier. However, the same equation can be found using a field-theoretical approach (see *e.g.* [116]).

At this stage, the independent thermodynamical variables are $n_B^{\bar{H}}, \{Y_i^{\bar{H}}\}, T, n_B^{Q*}, \{Y_i^{Q*}\}, R_{Q*}$ Our aim, however, is to recast the problem in terms of the initial control variables only, namely $n_B^{\bar{H}}, \{Y_i^{\bar{H}}\}, T$. The thermodynamical variables of the quark phase $n_B^{Q*}, \{Y_i^{Q*}\}$ are related to which configurations can be explored by the system.

In following subsections, n_B^{Q*}, R_{Q*} and $\{Y_i^{Q*}\}$ will be discussed.

4.3.2 Baryon density of the critical droplet

We now discuss two prescriptions to fix the baryon density of the quark phase inside the droplet, n_B^{Q*}.

4.3.2.1 Small Degrees of Metastability

A first option is the *small degree of metastability* approximation [185], used *e.g.* in [43, 45]. The system has a low degree of metastability if

$$\delta P_{\bar{H}} \equiv |P_{\bar{H}} - P_x| \;\ll\; P_x, \tag{4.38}$$
$$\delta P_{Q*} \equiv |P_{Q*} - P_x| \;\ll\; P_x, \tag{4.39}$$

where P_x is the bulk coexistence pressure at temperature T, defined by

$$\mu_k^H(P_x, T) = \mu_k^Q(P_x, T), \tag{4.40}$$

for each globally conserved charge k (with μ_k its conjugate chemical potential). In words, P_x is the equilibrium pressure of the two phases in the infinite-system (planar interface) limit. A low degree of metastability means that the overpressure needed to compensate the finite-size cost is small.

Under this condition, one may expand the quark Gibbs energy $\Phi_{Q*}(P_{Q*}, T) = \sum_i \mu_i^Q N_i^Q$ around $P_{\bar{H}}$:

$$\begin{aligned}\Phi_{Q*}(P_{Q*}, T) &\simeq \Phi_{Q*}(P_{\bar{H}}, T) + \left.\frac{\partial \Phi_{Q*}}{\partial P}\right|_T (P_{Q*} - P_{\bar{H}}) \\ &\simeq \Phi_{Q*}(P_{\bar{H}}, T) + V_{Q*}\,(P_{Q*} - P_{\bar{H}}).\end{aligned} \tag{4.41}$$

Substituting Eq. (4.41) into Eq. (4.32) gives

$$W^*_{\rm bulk} \;=\; \sum_i N_i^{Q*}\left(\mu_i^{Q*} - \mu_i^{\bar{H}}\right) \;=\; \frac{4\pi}{3}\, R_{Q*}^3\, n_B^{Q*} \sum_i Y_i^Q\left(\mu_i^{Q*} - \mu^{\bar{H}}\right), \tag{4.42}$$

with n_B^{Q*} determined by the *leading-order*

$$P_{Q*} = P_{\bar{H}}. \tag{4.43}$$

4.3.2.2 Saddle–point approach

In this approach, n_B^{Q*} is not fixed a priori by hard constraints and thus can, in principle, take any value (it sets the fluctuation size in baryon content, $N_B^{Q*} = n_B^{Q*} V_{Q*}$). Formally, the total nucleation probability requires integrating over all admissible values of n_B^{Q*}. The dominant contribution comes from the value of n_B^{Q*} that minimizes the barrier W^* (or, for quantum nucleation, the Euclidean action). In the spirit of the saddle–point picture of barrier crossing, we therefore fix n_B^{Q*} by imposing that the most probable path from the local to the global minimum passes near the lowest intervening saddle of the potential [30, 195]. Thus, we determine n_B^{Q*} by *minimizing* the barrier W^* with respect to n_B^{Q*} (at fixed T and $\{Y_i^{Q*}\}$).

Extremizing Eq. (4.35) with respect to n_B^{Q*} yields

$$\sum_i Y_i^{Q*}\,\mu_i^{\bar{H}} \;=\; \sum_i Y_i^{Q*}\,\mu_i^{Q*}, \tag{4.44}$$

which fixes n_B^{Q*} once T and $\{Y_i^{Q*}\}$ are specified. Using Eq. (4.44) in Eq. (4.35), the bulk part of the barrier reduces to

$$W^*_{\rm bulk} \;=\; -\,V_{Q*}\,(P_{Q*}-P_{\bar{H}}) \;=\; -\,\frac{4\pi}{3}\,R^3_{Q*}\,(P_{Q*}-P_{\bar{H}})\,, \tag{4.45}$$

to be combined with the surface and Coulomb terms for the full W^*.

Throughout this chapter we assume isothermal conditions, $T_{Q*} = T_{Ho} = T_{\bar{H}}$. If this assumption is relaxed, the bulk work in Eq. (4.35) acquires an additional entropic term $S_{Q*}\,(T_{Q*}-T_{\bar{H}})$, and the saddle–point condition with respect to T_{Q*} yields $T_{Q*} = T_{\bar{H}}$. Thus, the isothermal assumption is self–consistent at the level of the critical configuration.

4.3.3 Critical radius

The critical radius R_{Q*}, namely the radius of the quark droplet in the critical configuration, corresponds to the maximum of W^* (Eq. 4.35)

$$W(R_{Q*}) = \max_{R_Q}\left[W(R_Q)\right]. \tag{4.46}$$

The extremum condition is

$$P_{Q*} = P_H + n_B^{Q*}\sum_i Y_i^{Q*}(\mu_i^{Q*}-\mu_i^{\bar{H}}) + \frac{2\sigma}{R_{Q*}} - P_{Q*}^{\rm Coulomb}(R_{Q*}). \tag{4.47}$$

Using the saddle–point approach for n_B^{Q*} (Eq. 4.44),

$$P_{Q*} = P_{\bar{H}} + \frac{2\sigma}{R_{Q*}} - P_{Q*}^{\rm Coul.}(R_{Q*}), \tag{4.48}$$

which corresponds to the (unstable) mechanical equilibrium between the two phases. The Coulomb pressure term $P_{Q*}^{\rm Coul.}(R_{Q*})$ depends on the approach used for the charge neutrality and screening (see Sec. 4.3.5). If the Coulomb interaction does not play a role, then the critical radius is

$$R_{Q*} = \frac{2\sigma}{P_{Q*}-P_{\bar{H}}}. \tag{4.49}$$

4.3.4 Composition of the critical droplet

We now discuss the configurations of the system that can be explored in terms of the composition of the quark phase droplet $\{Y_i^{Q*}\}$.

The typical timescale of a fluctuation in the volume of the deconfined quark phase within a system initially in the phase H (which can be interpreted as a fluctuation in the order parameter) is the typical time over which a mechanically unstable droplet is created, shrinks back to the metastable phase, and disappears to restore the local

equilibrium of the system. The timescale for generating a critical droplet is set by the time needed to reach the critical configuration.

Since deconfinement is mediated by the strong interaction, the formation time is set by $\tau_{\text{strong}} \sim 10^{-23}$ s, whereas weak processes are many orders of magnitude slower. On the nucleation window, we therefore treat only strong interactions as *active*. Consequently, the system can explore only configurations that respect the strong–interaction conservation laws.

Under strong interactions, the conserved numbers are the baryon number B, the nonleptonic electric charge C, and the strangeness S. Equivalently, these map one-to-one to the net quark flavors u, d, s, which are conserved by strong reactions. Lepton number L_e is conserved only if neutrinos are trapped (mean free path $\ll$ system size). In that case, neutrinos carry nonzero μ_{ν_e}. If neutrinos are not trapped, L_e is *not* conserved locally and $\mu_{\nu_e} = 0$. Moreover, if the initial hadronic phase is charge-neutral $Y_C^{\bar{H}} - Y_e^{\bar{H}} = 0$, and since N_C is conserved, N_e is also conserved.

While the B, C, S conservation is generally accepted in the literature on quark nucleation, it is debated whether they are locally or globally conserved. As suggested in [27, 109], the total free energy is minimized if the two phases can share the conserved numbers. Thus, number conservations are global (and not local) unless the reactions that exchange conserved numbers from one phase to the other are suppressed because of some microphysical mechanisms. These mechanisms could include charge screening effects caused by long–range forces, the slowness of specific reactions, or the suppression of diffusion processes.

A fully microscopic treatment would consider all strong reactions and transport rates that both form the droplet and exchange conserved numbers across the interface. Within a thermodynamic framework, this can be emulated by two limiting prescriptions:

(i) Local flavor conservation: exchange of conserved numbers between droplet and surroundings is ineffective on the nucleation window. The droplet inherits the local composition ("frozen" flavors).

(ii) Global flavor conservation with strong chemical equilibrium: exchange is fast enough so that the conserved numbers are in strong chemical equilibrium between the droplet and the surroundings.

In the former (latter) limit, the equilibration time for the exchange of strong conserved numbers between the quark droplet and the surroundings is much longer (shorter) than the timescale of formation of the critical droplet.

In [43, 124] (and the references therein), local number conservation is assumed. On the other hand, in some works addressing the effect of phase transitions in heavy-ion collisions, global number conservation is assumed. For example, in [173, 204, 205], the strangeness is globally (and not locally) conserved, leading to the so-called *strangeness distillation* effect. The same approach, but with global isospin conservation, was used in [134].

Another aspect, neglected in [43, 124], is the presence of *thermal (statistical) fluctuations* of the composition at finite temperature, which can affect nucleation efficiency, as suggested by [116, 125, 134]. In [43, 124], beyond assuming frozen flavors, the hadronic phase is considered compositionally homogeneous, meaning each subsystem has the same composition as the bulk average. At finite T, however, the flavor composition fluctuates around its bulk average. Because nucleation is a local process, the first critical droplet may form within a subregion whose instantaneous composition deviates from the average in a way that is more favorable for nucleation.

In what follows, we present the different approaches to treating the flavor composition in nucleation. The neutrinos will be treated in chemical equilibrium between the two phases, namely with a μ_{ν_e} equal everywhere (if trapped) or neglected $\mu_{\nu_e} = 0 \Rightarrow Y_{\nu_e} = 0$ (if untrapped). In both cases, neutrinos do not give a direct contribution to W^*, since their contribution is canceled out at the droplet surface. The neutrino trapping effect impacts W^* only by modifying the composition of the initial phase. On the other hand, electrons will be discussed in Sec. 4.3.5.

4.3.4.1 Frozen flavor composition

This approach has been widely used in the literature (see *e.g.* [42, 43, 117, 124]). The droplet composition $\{Y_i^{Q*}\}$ is fixed by assuming (i) the initial hadronic phase is compositionally homogeneous (does not fluctuate) and (ii) the exchange of strong–conserved charges with the surroundings is ineffective during the formation of the deconfined droplet (local flavor conservation):

$$\begin{aligned} Y_C^{Q*} &= Y_C^{\bar{H}} \\ Y_S^{Q*} &= Y_S^{\bar{H}}. \end{aligned}$$

Assumption (i) excludes pre–existing thermal composition fluctuations in H (every subvolume has the bulk $\{Y_i^{\bar{H}}\}$), while (ii) states that during the short droplet lifetime neither weak reactions nor diffusive transport of the strong charges can appreciably modify the composition inside the droplet. Consequently, chemical potentials generally *mismatch* across the interface, $\mu_C^{Q*} \neq \mu_C^{\bar{H}}$ and $\mu_S^{Q*} \neq \mu_S^{\bar{H}}$. These gradients would drive diffusion to requilibrate the chemical potentials, but in the frozen limit, the diffusion length is negligible on the window, $\ell_D(\Delta t) \ll R_{Q*}$, so equilibration cannot occur before the fluctuation collapses or grows.

4.3.4.2 Thermal fluctuations of the flavor composition

We now relax the assumption of local compositional homogeneity in the hadronic phase. As suggested in [116, 125, 134] and formalized in [45, 46], at finite temperature the bulk composition $\{Y_i^{\bar{H}}\}$ represents only an average: locally, thermodynamic variables (including the flavor fractions) fluctuate about these mean values. Since nucleation is a *local* process, the first critical droplet may form in a subregion whose instantaneous composition $\{Y_i^{H*}\}$ differs from $\{Y_i^{\bar{H}}\}$ in a way that favors deconfinement.

To separate ingredients, we split the total work as $W^* = W_1^* + W_2^*$: W_1^* is the cost

to realize a subregion with fluctuated hadronic composition, and W_2^* is the additional cost to form the quark droplet inside that subregion.

Consider a system at fixed $(V, T, \{N_i^{\bar{H}}\})$ initially in the homogeneous state $\bar{H}$. Let a small subvolume V_{H*} fluctuate to composition $\{Y_i^{H*}\}$ (state H^*), while the surrounding is labeled as $H^{o(1)}$. The work to create this fluctuation is the free–energy difference

$$\begin{aligned} W_1^* &= \Big(F_{H*} + F_{H^{o(1)}}\Big) - F_{\bar{H}} \\ &= -V_{H^{o(1)}}(P_{H^{o(1)}} - P_{\bar{H}}) - V_{H*}(P_{H*} - P_{\bar{H}}) \qquad (4.50) \\ &\quad + \sum_i N_i^{H^{o(1)}}\Big(\mu_i^{H^{o(1)}} - \mu_i^{\bar{H}}\Big) + \sum_i N_i^{H*}\Big(\mu_i^{H*} - \mu_i^{\bar{H}}\Big), \qquad (4.51) \end{aligned}$$

which, using $V_{H*} \ll V_{H^{o(1)}} \simeq V$ (the surroundings act as a bath: $P_{H^{o(1)}} \simeq P_{\bar{H}}$, $\mu_i^{H^{o(1)}} \simeq \mu_i^{\bar{H}}$, see Sec. 4.2.1), reduces to

$$W_1^* \simeq -V_{H*}\,(P_{H*} - P_{\bar{H}}) + N_B^{H*} \sum_i Y_i^{H*}\Big(\mu_i^{H*} - \mu_i^{\bar{H}}\Big), \qquad (4.52)$$

with thermodynamic quantities in the fluctuated subsystem given by

$$X_{H*} = X_H\Big(n_B^{H*}, \{Y_i^{H*}\}, T\Big), \qquad X = P, \mu_i, ... \qquad (4.53)$$

Let us still assume, for the moment, that the conserved strong charges C, S cannot be exchanged with the surroundings (local conservation). The critical quark droplet then inherits the composition of the pre–existing hadronic subregion:

$$\begin{aligned} Y_C^{Q*} &= Y_C^{H^*} \qquad (4.54) \\ Y_S^{Q*} &= Y_S^{H^*}. \qquad (4.55) \end{aligned}$$

To fix $n_B^{H^*}$ we follow [185] and assume that the composition fluctuation attains *mechanical* equilibrium with the bath much faster than it can re–equilibrate chemically, so

$$P_{H^*} = P_{H^{o(1)}} \simeq P_{\bar{H}}, \qquad (4.56)$$

which, for given $\{Y_i^{H^*}\}$ and T, determines $n_B^{H^*}$ from the hadronic EOS. To set the size of the fluctuation, we define the subvolume so that it contains the same baryon number as the final critical droplet,

$$N_B^{H^*} = N_B^{Q*} = n_B^{Q*}\, V_{Q*}. \qquad (4.57)$$

With Eqs. (4.56, 4.57), the work to create the compositional fluctuation becomes

$$\begin{aligned} W_1^* &= N_B^{Q*} \sum_i Y_i^{Q*}\Big(\mu_i^{H^*} - \mu_i^{\bar{H}}\Big) \qquad (4.58) \\ &= \frac{4\pi}{3}\, R_{Q*}^3\, n_B^{Q*} \sum_i Y_i^{Q*}\Big(\mu_i^{H^*} - \mu_i^{\bar{H}}\Big), \qquad (4.59) \end{aligned}$$

Note that for small deviations $\Delta Y_i^H \equiv Y_i^{H^*} - Y_i^{\bar{H}}$ one may expand W_1^* to quadratic order, obtaining a multivariate Gaussian peaked at $Y_i^{H^*} = Y_i^{\bar{H}}$ (see Sec. 4.2.1).

Since H^* is not a distinct phase, no interfacial (surface tension) cost enters W_1^* at leading order. Gradient penalties would be higher–order corrections and are neglected here. If the fluctuation induces a local electric charge imbalance, an additional Coulomb term $W^*_{1,\text{Coulomb}}$ arises.

The work W_2^* is the free–energy difference between the configuration with a quark droplet Q^* embedded in H^o and the composition–fluctuated configuration:

$$W_2^* \;=\; \Big(F_{Q*} + F_{H^o}\Big) - \Big(F_{H^*} + F_{H^{o(1)}}\Big) \;+\; W^*_{2,\text{finite size}} \;+\; W^*_{2,\text{Coulomb}}. \tag{4.60}$$

Using $V_{Q*} \sim V_{H^*} \ll V_{H^{o(1)}} \simeq V_{Ho} \simeq V$ (see Sec. 4.2.1), so that $P_{H^{o(1)}} \simeq P_{H^o} \simeq P_{\bar{H}}$ and $\mu_i^{H^{o(1)}} \simeq \mu_i^{H^o} \simeq \mu_i^{\bar{H}}$, we obtain

$$W_2^* \simeq -V_{Q*}\Big(P_{Q*} - P_{\bar{H}}\Big) + \sum_i N_i^{Q*}\Big(\mu_i^{Q*} - \mu_i^{H*}\Big) + W^*_{\text{finite size}} + W^*_{2,\text{Coul.}} \tag{4.61}$$

$$= \frac{4\pi}{3} R_{Q*}^3 \left[-\Big(P_{Q*} - P_{\bar{H}}\Big) + n_B^{Q*} \sum_i Y_i^{Q*}\Big(\mu_i^{Q*} - \mu_i^{H*}\Big)\right] + 4\pi\sigma R_{Q*}^2 + E_{Q*}^{\text{Coul.}}(R_{Q*}). \tag{4.62}$$

The total work is

$$W^* = W_1^* + W_2^* \tag{4.63}$$

$$= \frac{4\pi}{3} R_{Q*}^3 \left[-\Big(P_{Q*} - P_{\bar{H}}\Big) + n_B^{Q*} \sum_i Y_i^{Q*}\Big(\mu_i^{Q*} - \mu_i^{\bar{H}}\Big)\right] + 4\pi\sigma R_{Q*}^2 + E_{Q*}^{\text{Coul.}}(R_{Q*}). \tag{4.64}$$

A given subvolume has probability $\mathcal{P}_1 \propto e^{-W_1^*/T}$ to realize a composition $\{Y_i^{H*}\}$ by thermal fluctuation, and, conditional on that, a quark droplet forms with probability $\mathcal{P}_2 \propto e^{-W_2^*/T}$ for thermal activation, or $\mathcal{P}_2 \propto e^{-S_E(W_2^*)/\hbar}$ for quantum tunneling, where S_E is the Euclidean action of the critical trajectory (see Sec. 4.3.7). A fully consistent calculation would integrate the total probability over all admissible compositions. However, since nucleation probability is a negative exponential of the work W^*, the dominant contribution comes from the composition that *minimizes* the total work W^*. In the spirit of the saddle-point approach, we therefore fix $\{Y_i^{Q*}\}$ by minimizing W^* at fixed n_B^{Q*} and T (and with the proper electric charge neutrality prescription).

Using Eq. (4.64), it is convenient to rewrite the bulk bracket as

$$-\Big(P_{Q*} - P_{\bar{H}}\Big) + n_B^{Q*} \sum_i Y_i^{Q*}(\mu_i^{Q*} - \mu_i^{\bar{H}}) = f_{Q*} + P_{\bar{H}} - n_B^{Q*} \sum_i Y_i^{Q*} \mu_i^{\bar{H}},$$

where f_{Q*} is the Helmholtz free–energy density of the Q^* phase. Then

$$0 = \left.\frac{\partial W^*}{\partial Y_C^{Q*}}\right|_{n_B^{Q*}, Y_S^{Q*}, T} = \frac{4\pi}{3} R_{Q*}^3 \, n_B^{Q*} \left[\mu_C^{Q*} - \mu_C^{\bar{H}} \;+\; \delta_{\text{loc}}\,(\mu_e^{Q*} - \mu_e^{\bar{H}})\right], \tag{4.65}$$

$$0 = \left.\frac{\partial W^*}{\partial Y_S^{Q*}}\right|_{n_B^{Q*}, Y_C^{Q*}, T} = \frac{4\pi}{3} R_{Q*}^3 \, n_B^{Q*} \left(\mu_S^{Q*} - \mu_S^{\bar{H}}\right), \tag{4.66}$$

where $\delta_{\rm loc} = 1$ if local electric neutrality is imposed ($Y_e^{Q*} + Y_C^{Q*} = 0$) and $\delta_{\rm loc} = 0$ for globally enforced neutrality, see Sec. 4.3.5 for details. Thus, the minimizing conditions are

$$\mu_C^{Q*} + \delta_{\rm loc}\mu_e^{Q*} = \mu_C^{\bar{H}} + \delta_{\rm loc}\mu_e^{\bar{H}}, \tag{4.67}$$

$$\mu_S^{Q*} = \mu_S^{\bar{H}}. \tag{4.68}$$

Combining Eqs. (4.67, 4.68) with the saddle–point condition for n_B^{Q*}, Eq. (4.44), yields also

$$\mu_B^{Q*} = \mu_B^{\bar{H}}. \tag{4.69}$$

In this section, we have interpreted a droplet composition different from the bulk hadronic one as arising from a prior *local* fluctuation of the hadronic composition. However, note that Eqs. (4.67, 4.68, 4.69) are precisely the strong–interaction *chemical–equilibrium* relations across the interface, enforced under the constraint of *global* conservation of the strong charges B, C, and S (with the electric channel modified according to the chosen neutrality prescription).

This means that, independently on how the droplet attains a composition more favorable to nucleation, whether via (i) a pre–existing thermal fluctuation of the hadronic composition in the nucleating subvolume, (ii) rapid exchange of strong charges across the phase boundary (including $q\bar{q}$ pair separation), or (iii) a combination of both, the same relations apply, namely Eqs. (4.67, 4.68, 4.69).

Let us investigate what happens when the initial hadronic phase is in β equilibrium with trapped (untrapped) neutrinos. At given $n_B^{\bar{H}}, Y_L^{\bar{H}}, T$ ($n_B^{\bar{H}}, T$) values, the β equilibrium composition $\{Y_i^{H_{\beta\nu}}\}$ ($\{Y_i^{H_\beta}\}$) is the one that solves the equilibrium conditions

$$\mu_C^{\bar{H}} + \mu_e^{\bar{H}} - \mu_{\nu_e}^{\bar{H}} = 0 \tag{4.70}$$

$$\mu_S^{\bar{H}} = 0 \tag{4.71}$$

(with $\mu_{\nu_e}^{\bar{H}} = 0$ if neutrinos are untrapped) together with the electromagnetic charge neutrality condition ($Y_C^{\bar{H}} - Y_e^{\bar{H}} = 0$). By replacing the conditions in Eqs. (4.67) and (4.68), we obtain

$$\mu_C^{Q*} + \mu_e^{Q*} - \mu_{\nu_e}^{Q*} = 0 \tag{4.72}$$

$$\mu_S^{Q*} = 0, \tag{4.73}$$

which are the conditions of β equilibrium for quark matter (but with a different leptonic fraction with respect to the initial hadronic phase $Y_L^{Q*} \neq Y_L^{\bar{H}}$). Thus, the composition that minimizes W^* is precisely the β–equilibrium quark composition, with the appropriate leptonic constraint, even if the weak interaction does not play a role.

Applying Eqs. (4.67, 4.68, 4.69) to Eq. (4.35), the work to form a droplet of radius R_Q in the saddle–point approach reduces to

$$W\left(R_Q, n_B^{\bar{H}}, \{Y_i^{\bar{H}}\}, T\right) = -\frac{4\pi}{3}R_Q^3\left(P_{Q*} - P_{\bar{H}}\right) + 4\pi\sigma R_Q^2 + E_Q^{\rm Coul.}(R_Q), \tag{4.74}$$

with $P_{Q*} \equiv P_Q(n_B^{Q*}, \{Y_i^{Q*}\}, T)$, where n_B^{Q*} and $\{Y_i^{Q*}\}$ are fixed by Eqs. (4.67, 4.68, 4.69). The critical radius R_{Q*} is the value of R_Q that maximizes $W(R_Q)$. Namely, it is the solution of Eq. (4.48) corresponding to the mechanically unstable equilibrium of the critical configuration. The barrier height is then $W^* \equiv W(R_{Q*})$.

In [45] the critical radius was identified as the R_2 that maximizes the work $W_2(R_Q)$. This underestimates the true R_{Q*}. The critical droplet must be *mechanically unstable* against growth into its actual surroundings $H^o \simeq \bar{H}$ so that, once R_Q exceeds R_{Q*} by an infinitesimal δR, the system can roll down toward the global minimum. A droplet with R_2 that maximizes W_2 can still correspond to a configuration where the bulk Q_* is more stable than the subvolume H_* it replaced (namely $\mu_{Q*}(P,T) < \mu_{H_*}(P,T)$, where μ is the Gibbs energy per baryon) yet not more stable than the surrounding bath $\bar{H}$ at the same (P,T) (namely $\mu_{Q*}(P,T) > \mu_{\bar{H}}(P,T)$). By contrast, R_{Q*} that maximize W^* guarantee the correct (unstable) mechanical balance with the bath, and thus the proper criterion for barrier crossing.

4.3.4.3 Reduced volume approach

The previous treatment implicitly assumes that all macrostates compatible with the thermodynamic constraints (global numbers conservation) are dynamically accessible, so that the system can, in practice, reach the composition $\{Y_i^{Q*}\}$ and density n_B^{Q*} that minimize W^*, either via a prior composition fluctuation in H and/or via exchange of strong–conserved charges across the interface. This is appropriate for an effectively infinite (in space and time) reservoir, see Sec. 4.2.2).

However, if we identify the "system" *e.g.* with a portion of a compact star that is much larger than V_{Q*} yet small enough that spatial gradients of the control variables are negligible (namely, gravity across it can be ignored), then it has a *finite* lifetime. For instance, if the system is taken to be a cell of an astrophysical simulation at a given snapshot, its effective lifetime is the simulation timestep, typically equal to the dynamical timescale $\tau_{\rm dyn} \sim 10^{-4}$ s: the interval over which the cell-averaged thermodynamic quantities can be treated as approximately constant. Consequently, even configurations that are in principle allowed by thermodynamics may be *kinematically inaccessible* within the finite time available.

In our framework, there are two relevant timescales:

(i) the lifetime of the system, of order the dynamical timescale $\tau_{\rm dyn} \sim 10^{-4}$ s;

(ii) the lifetime of the quark droplet (*i.e.*, the fluctuation in the thermodynamic variable V_{Q*}, interpretable as an order–parameter fluctuation), set by strong interactions, $\tau_{\rm strong} \sim 10^{-23}$ s, which mediate local deconfinement.

and two relevant mechanisms that can modify the flavor composition:

(i) *Background composition fluctuations* in the hadronic phase during the system lifetime, uncorrelated with the specific droplet–forming fluctuation. A practical

way to exclude kinematically inaccessible macrostates is to require that any rearrangement of conserved charges not exceed their diffusion length within $\tau_{\rm dyn}$ (only configurations compatible with the available diffusive transport are admitted).

(ii) *Interfacial exchange* of strong–conserved charges (flavors) between the droplet and its surroundings during the droplet lifetime, driven by chemical–potential gradients. This exchange may proceed via diffusion of already existent net charges or via charge distillation through continuous $q\bar{q}$ pair creation and separation [134, 204, 205]. For example, an $s\bar{s}$ pair forms and separates, with the s entering the quark droplet and the $\bar{s}$ entering the hadronic surroundings (*e.g.*, as a kaon). However, charge transport cannot extend beyond the diffusion length available within $\tau_{\rm strong}$.

In general, the thermal–fluctuation saddle–point approach of the previous section (Sec. 4.3.4.2) may overestimate nucleation by counting configurations that are *kinematically* unreachable on the finite window, whereas the frozen–flavor limit may be overly restrictive by discarding all local composition fluctuations. A complete treatment would require a detailed microphysical calculation with a unified Lagrangian for hadronic and quark degrees of freedom, treated beyond the mean-field approximation, as well as transport properties.

In the absence of a fully microscopic framework, we introduce an intermediate *reduced–volume* prescription that contains the previous limits as special cases. We allow *separate* finite reservoirs for each strong–conserved charge by defining three volumes

$$V_{Q*} \;\leq\; V_{r.v.}^{(k)} \;\leq\; V, \qquad k = B, C, S$$

within which the corresponding charge must be conserved. In addition, we introduce an independent volume

$$V_{Q*} \;\leq\; V_{r.v.}^{(\rm mec.)} \;\leq\; V,$$

interpreted as the reservoir over which the surroundings can readjust to establish mechanical balance with the droplet. A reasonable constraint would be $V_{r.v.}^{(\rm mec.)} \geq \max_k \left[\{V_{r.v.}^{(k)}\}\right]$, since the mechanical equilibrium can be driven by inelastic scattering between any charges.

Thus, the effective "surroundings" is now a *finite* reservoir, not necessarily much larger than the droplet. Consequently, the bath approximation (constant intensive quantities in the surroundings) no longer applies: any excess of a conserved charge k carried by the droplet must be compensated within a subvolume $V_{r.v.}^{(k)}$ that includes the droplet itself.

Let us assume, without losing generality, that $V_{r.v.}^{(S)} \leq V_{r.v.}^{(C)} \leq V_{r.v.}^{(B)} \leq V_{r.v.}^{(\rm mec.)}$, and suppose that all of these volumes refers to a sphere centered in the center of V_{Q*}. We can identify four spherical shells $V_{H\vartheta(j)}$ $(j = 1 - 4)$ around the spherical quark droplet

(see Fig. 4.3) such that

$$N_B^{Q*} + N_B^{H\vartheta(1)} + N_B^{H\vartheta(2)} + N_B^{H\vartheta(3)} = N_B^{r.v.} \equiv n_B^{\bar{H}} V_{r.v.}^{(B)} \tag{4.75}$$
$$N_C^{Q*} + N_C^{H\vartheta(1)} + N_C^{H\vartheta(2)} = N_C^{r.v.} \equiv n_B^{\bar{H}} Y_C^{\bar{H}} V_{r.v.}^{(C)} \tag{4.76}$$
$$N_S^{Q*} + N_S^{H\vartheta(1)} = N_S^{r.v.} \equiv n_B^{\bar{H}} Y_S^{\bar{H}} V_{r.v.}^{(S)} \tag{4.77}$$
$$V_{Q*} + V_{H\vartheta(1)} + V_{H\vartheta(2)} + V_{H\vartheta(3)} + V_{H\vartheta(4)} = V_{r.v.}^{(\mathrm{mec.})} \tag{4.78}$$

Thus, for each strong charge k, only the number N_k that is inside $V_{r.v.}^{(k)}$ in the initial configuration participate in the formation of the quark droplet. Moreover, let us assume that the intensive quantities of the charge k in the region not participating the the quark droplet formation are unaffected. The Eqs. (4.75–4.78) can be rewritten as

$$V_{Q*} n_B^{Q*} + V_{H\vartheta(1)}\, n_B^{H\vartheta(1)} + V_{H\vartheta(2)}\, n_B^{H\vartheta(2)} + V_{H\vartheta(3)}\, n_B^{H\vartheta(3)} = N_B^{r.v.} \equiv n_B^{\bar{H}} V_{r.v.}^{(B)} \tag{4.79}$$
$$V_{Q*} n_B^{Q*} Y_C^{Q*} + V_{H\vartheta(1)}\, n_B^{H\vartheta(1)}\, Y_C^{H\vartheta(1)} + V_{H\vartheta(2)}\, n_B^{H\vartheta(2)}\, Y_C^{H\vartheta(2)} = N_C^{r.v.} \equiv n_B^{\bar{H}} Y_C^{\bar{H}} V_{r.v.}^{(C)} \tag{4.80}$$
$$V_{Q*} n_B^{Q*} Y_S^{Q*} + V_{H\vartheta(1)}\, n_B^{H\vartheta(1)}\, Y_S^{H\vartheta(1)} = N_S^{r.v.} \equiv n_B^{\bar{H}} Y_S^{\bar{H}} V_{r.v.}^{(S)} \tag{4.81}$$
$$V_{Q*} + V_{H\vartheta(1)} + V_{H\vartheta(2)} + V_{H\vartheta(3)} + V_{H\vartheta(4)} = V_{r.v.}^{(\mathrm{mec.})} \tag{4.82}$$

The energy barrier is

$$W^* = \left(F_{Q*} + F_{Q*}^{\text{finite size}} + E_{Q*}^{\text{Coulomb}} + F_{H\vartheta(1)} + F_{H\vartheta(2)} + F_{H\vartheta(3)} + F_{H\vartheta(4)}\right) - F_{\bar{H}} \tag{4.83}$$
$$= V_{Q*} f_Q(n_B^{Q*}, Y_C^{Q*}, Y_S^{Q*}, T) + A_{Q*}\sigma + F_{Q*}^{\mathrm{Coul.}}(R_{Q*}) + \tag{4.84}$$
$$+ V_{H\vartheta(1)} f_H(n_B^{H\vartheta(1)}, Y_C^{H\vartheta(1)}, Y_S^{H\vartheta(1)}, T) + \tag{4.85}$$
$$+ V_{H\vartheta(2)} f_H(n_B^{H\vartheta(2)}, Y_C^{H\vartheta(2)}, Y_S^{H\vartheta(2)}, T) + \tag{4.86}$$
$$+ V_{H\vartheta(3)} f_H(n_B^{H\vartheta(3)}, Y_C^{H\vartheta(3)}, Y_S^{H\vartheta(3)}, T) + \tag{4.87}$$
$$+ V_{H\vartheta(4)} f_H(n_B^{H\vartheta(4)}, Y_C^{H\vartheta(4)}, Y_S^{H\vartheta(4)}, T) + \tag{4.88}$$
$$- V_{r.v.}^{(\mathrm{mec})} f_H(n_B^{\bar{H}}, Y_C^{\bar{H}}, Y_S^{\bar{H}}, T), \tag{4.89}$$

where we have already neglected the external part of the system that does not participate in the nucleation. In the spirit of the saddle–point approach, let us minimize the energy barrier W^* with respect to $n_B^{Q*}, Y_C^{Q*}, Y_S^{Q*}, n_B^{H\vartheta(j)}, Y_i^{H\vartheta(j)}$ under the constraints in Eqs. (4.79–4.81) or, equivalently, with respect to $N_i^{Q*}, N_i^{H\vartheta(j)}$ under the constraints in Eqs. (4.75–4.77):

$$\mu_B^{Q*} = \mu_B^{H\vartheta(1)} = \mu_B^{H\vartheta(2)} = \mu_B^{H\vartheta(3)} \equiv \mu_B^{H\vartheta}, \tag{4.90}$$
$$\mu_C^{Q*} = \mu_C^{H\vartheta(1)} = \mu_C^{H\vartheta(2)} \equiv \mu_C^{H\vartheta}, \tag{4.91}$$
$$\mu_S^{Q*} = \mu_S^{H\vartheta(1)} \equiv \mu_S^{H\vartheta}. \tag{4.92}$$

Note that, in general, the surround differs from the initial configuration, so $\mu_i^{H\vartheta} \neq \mu_i^{\bar{H}} \equiv \mu_i^H(n_B^{\bar{H}}, \{Y_i^{\bar{H}}\}, T)$.

Similarly, the critical volume and radius are obtained by extremizing W^* with respect

to V_{Q*} and $V_{\vartheta(j)}$ with Eq. (4.78) as constraints:

$$P_{Q*} = P_{H\vartheta} + \frac{2\sigma}{R_{Q*}} - P^{\text{Coul.}}_{Q*}(R_{Q*}), \tag{4.93}$$

where

$$P_{H\vartheta} \equiv P_{H\vartheta(1)} = P_{H\vartheta(2)} = P_{H\vartheta(3)} = P_{H\vartheta(4)}. \tag{4.94}$$

The unknowns $n_B^{Q*}, \{Y_i^{Q*}\}, \{n_B^{H\vartheta(j)}\}, \{Y_i^{H\vartheta(j)}\}, V_{Q*}, \{V_{H\vartheta(j)}\}$ with $i = B, C, S$ and $j = 1, 2, 3, 4$, are then fixed by the Eqs. (4.79–4.82, 4.90–4.94), $n_B^{\bar{H}}, \{Y_i^{\bar{H}}\}, T$ remains independent and are treated as input that specify the initial equilibrium conditions and $V_{r.v.}^{(k)}$ are free parameters of the framework. We do not attempt to endow $V_{r.v.}$ with a strict microphysical definition, instead, we treat it as a phenomenological parameter.

Operationally, $V_{r.v.}^{(k)}$ represents the effective reservoir that balances the droplet's excess strong charge k with respect to the background equilibrium composition. It may be tied to the diffusion length of charge k over the relevant time window and/or to a generic correlation length beyond which the charges cannot participate in the fluctuation. This interpretation applies to both composition fluctuations in the hadronic phase and interfacial exchange during the droplet lifetime.

We now discuss a few limiting cases.

- If $V_{r.v.}^{(k)} = V_{r.v.}$ $(k = B, C, S, \text{mec})$, without assuming $V_{r.v.} \gg V_{Q*}$, the four hadronic spherical shells collapse into a single shell of volume $V_{H\vartheta(j)} \equiv V_{H\vartheta} = V_{r.v.} - V_{Q*}$. The problem then reduces to the equilibrium between two finite, homogeneous phases with three globally conserved charges (see Appendix A).

- If $V_{r.v.}^{(k)} = V \gg V_{Q*}$ $(k = B, C, S, \text{mec})$, all particles in the system can participate in the fluctuation and nucleation; in other words, all configurations are kinematically accessible. One readily verifies that, in this limit, the reservoirs associated with the conserved charges and with mechanical equilibrium are effectively infinite. Consequently, as shown in the previous sections, the corresponding intensive quantities are not altered by the appearance of the quark droplet:

$$\mu_B^{Q*} = \mu_B^{H\vartheta} = \mu_B^{\bar{H}}, \tag{4.95}$$
$$\mu_C^{Q*} = \mu_C^{H\vartheta} = \mu_C^{\bar{H}}, \tag{4.96}$$
$$\mu_S^{Q*} = \mu_S^{H\vartheta} = \mu_S^{\bar{H}}, \tag{4.97}$$
$$P_{Q*} - \frac{2\sigma}{R_{Q*}} + P^{\text{Coul.}}_{Q*}(R_{Q*}) = P_{H\vartheta} = P_{\bar{H}}, \tag{4.98}$$

  and the thermal–fluctuation saddle–point approach is recovered.

- If $V_{r.v.}^{(k)} = V_{r.v.} = V_{Q*}$ $(k = B, C, S, \text{mec})$, then $n_i^{Q*} = n_i^{\bar{H}}$ for $i = B, C, S$. Thus, all strong charges, including B, are locally conserved. See *Case 0* in [109].

- Contrary to what one might expect, the case $V_{r.v.}^{(C)} = V_{r.v.}^{(S)} = V_{Q*}$ and $V_{r.v.}^{(B)} = V_{r.v.}^{(\text{mec})} = V \gg V_{Q*}$ does *not* reduce to the flavor–frozen approach. Indeed, C and S are not locally frozen in the sense of conserved fractions ($Y_C^{Q*} \neq Y_C^{\bar{H}}$,

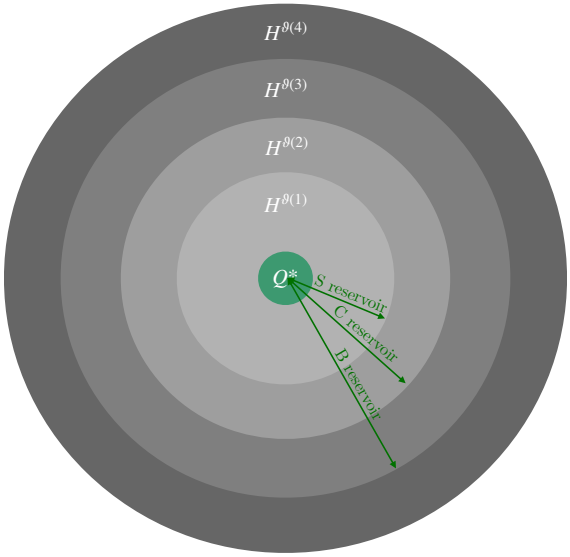

Figure 4.3: Schematic representation of the critical configuration of the system in the reduced–volume approach. See the text for details.

$Y_S^{Q*} \neq Y_S^{\bar{H}}$); rather, one has $n_C^{Q*} = n_C^{\bar{H}}$ and $n_S^{Q*} = n_S^{\bar{H}}$. To obtain the flavor–frozen limit, one must set

$$V_{r.v.}^{(C)} = V_{r.v.}^{(S)} = \frac{n_B^{Q*}}{n_B^{\bar{H}}} V_{Q*} = \frac{N_B^{Q*}}{n_B^{\bar{H}}}, \tag{4.99}$$

i.e., the volume which, in the initial equilibrium configuration, contains N_B^{Q*} baryons. Then Eqs. (4.80, 4.81) imply

$$Y_C^{Q*} = Y_C^{\bar{H}}, \tag{4.100}$$

$$Y_S^{Q*} = Y_S^{\bar{H}}. \tag{4.101}$$

Moreover, since N_C^{Q*} and N_S^{Q*} now depend on N_B^{Q*}, the minimization of W^* with respect to n_B^{Q*} changes and yields

$$\mu_B^{Q*} + Y_C^{Q*}\mu_C^{Q*} + Y_S^{Q*}\mu_S^{Q*} \;=\; \mu_B^{\bar{H}} + Y_C^{\bar{H}}\mu_C^{\bar{H}} + Y_S^{\bar{H}}\mu_S^{\bar{H}}, \tag{4.102}$$

which is identical to Eq. (4.44). Thus, the flavor–frozen limit is recovered.

To conclude, let us discuss the specific case of strangeness. In the *flavor–frozen* picture, the presence of hyperons (hence, pre–existing $Y_S^{\bar{H}} > 0$) in the hadronic phase substantially increases the stability of a flavor–frozen (Sec. 4.3.4.1) quark droplet, because the droplet must inherit the local flavor content and cannot quickly build up strangeness. One therefore expects that a sufficiently large *average* strangeness fraction in H $Y_S^{\bar{H}}$ can be required to trigger nucleation in this limit. In the composition–fluctuation saddle–point framework (Sec. 4.3.4.2), this requirement is relaxed: even if the bulk-averaged strangeness is small, thermal fluctuations can produce local regions with enhanced S $Y_S^{H*} > 0$ (without invoking weak interactions, but via strong diffusion), thereby favoring deconfinement locally. Moreover, $s\bar{s}$ pairs can be produced and separated across the interface by chemical–potential gradients ("strangeness distillation"), so that the

droplet acquires an excess of s while an equal excess of $\bar{s}$ is carried by the surroundings (*e.g.* in kaons), keeping the global net strangeness constant (even zero). The *reduced–volume* approach interpolates between these limits: to endow the droplet with extra strangeness, the compensating anti–strangeness must be supplied *within a finite reservoir* $V_{r.v.}$ around the droplet (rather than by the entire system). Thus, the ease of strangeness enrichment (and therefore the nucleation barrier) depends on the size of $V_{r.v.}$ (set by finite–time transport), with the flavor–frozen and fluctuation–assisted cases recovered as limiting scenarios.

4.3.5 Electric charge neutrality and electrostatic interaction

In astrophysical systems, electric charge neutrality has to be imposed to ensure stability. In bulk matter, pure hadronic and quark phases are taken as locally neutral, but in the mixed phase, electric charge can be shared between the two phases, and the charge neutrality can be, in principle, only global [27, 41, 109]. See Part II for a complete discussion. Whether electric charge neutrality is effectively local or only global is set by the comparison between the droplet radius R_Q and the (static) Debye screening length λ_D of each phase. The Debye screening length λ_D is the characteristic scale over which electric fields are screened, determined by the response of charged particles (the main contribution comes from electrons) to an electrostatic potential; fluctuations in electric charge density are efficiently neutralized only over distances larger than λ_D. Writing

$$\lambda_D^{-2} \;=\; 4\pi\,\alpha_{\rm em}\sum_a q_a^2\,\chi_a, \qquad \chi_a \equiv \left.\frac{\partial n_a}{\partial \mu_a}\right|_{T,\{\mu_{b\neq a}\}}, \tag{4.103}$$

with a running over all electric charge carriers, one has:

- $R_Q \gg \lambda_D$: mobile electric charges efficiently screen the electrostatic field across the interface, each phase relaxes close to local neutrality.
- $R_Q \lesssim \lambda_D$: screening is incomplete on the droplet scale, sizable charge separation persists, only global neutrality holds.

In some works, *e.g.* [43, 45, 46], it has been assumed for simplicity that the quark droplets were electrically charge neutral, fixing the electron density to ensure that. However, in principle, droplets with non-zero net electric charge are generated by spontaneous fluctuations and should be considered.

In this section, we will show the different approaches that can be used to treat charge neutrality in quark nucleation.

4.3.5.1 Local charge neutrality

Imposing local charge neutrality (LCN) inside the quark droplet,

$$Y_C^{Q*} - Y_e^{Q*} = 0, \tag{4.104}$$

and minimizing W^* with respect to Y_C^{Q*} under this constraint (see Eqs. (4.67), (4.91)) yields

$$\mu_C^{Q*} + \mu_e^{Q*} = \mu_C^H + \mu_e^H, \tag{4.105}$$

with generally $\mu_e^{Q*} \neq \mu_e^H$. Here, as in this whole section, H denotes either $\bar{H}$ or H^ϑ, depending on the adopted prescription for the flavor composition (see Sec. 4.3.4). Note that, if the flavor-frozen approach is chosen, then Y_C^{Q*} is fixed with Eq. (4.54) and not with the minimization of W^* (Eq. 4.105). Since the droplet is neutral by construction, its net Coulomb energy vanishes, $E_{Q*}^{\text{Coulomb}} = 0$, and the Coulomb pressure drop is absent, $P_{\text{Coulomb}}^{Q*} = 0$. The mechanical extremum that fixes the critical radius then reduces to

$$P_{Q*} = P_H + \frac{2\sigma}{R_{Q*}}. \tag{4.106}$$

This LCN treatment is a good approximation when electrostatic screening is efficient on the droplet scale, *i.e.* when the Debye length is much smaller than the droplet radius ($\lambda_D \ll R_{Q*}$). In this regime, each phase tends to relax toward (near) local neutrality, and Coulomb corrections to the mechanical balance are subleading.

4.3.5.2 Global charge neutrality neglecting Coulomb energy

We now allow the critical droplet to carry a net electric charge, provided that global charge neutrality holds. In this prescription, we neglect the explicit Coulomb contribution to the free energy of the configuration, $E_{Q*}^{\text{Coulomb}} = 0$, so that the only finite–size cost is the surface term. If local charge neutrality in the droplet is not imposed, the electron fraction Y_e^{Q*} must be varied on the same footing as the other composition variables to minimize W^*. Under global neutrality, this yields

$$\mu_e^{Q*} = \mu_e^H, \tag{4.107}$$

together with the other conditions (Eqs. 4.67, 4.91 or 4.54, depending on the chosen approach). At fixed T, Eq. (4.107) implies $n_e^{Q*} = n_e^H$ if electrons are described by the same EOS on both sides (hence $Y_e^{Q*} \neq Y_e^H$ in general, because $n_B^{Q*} \neq n_B^H$).

Since we neglect the Coulomb energy, there is no Coulomb pressure drop, $P_{\text{Coulomb}}^{Q*} = 0$, and the mechanical extremum of $W(R_Q)$ gives the same form as in the locally neutral case,

$$P_{Q*} = P_H + \frac{2\sigma}{R_{Q*}}. \tag{4.108}$$

This "GCN + no–Coulomb" approximation is accurate when electrostatic effects are subleading compared to bulk and surface terms, *e.g.* for sufficiently small droplets. Moreover, this approach could have a physical meaning if the electromagnetic relaxation is too slow to actually have an impact on the timescale governing the formation of the droplets.

4.3.5.3 Coulomb energy neglecting charge screening

Let us now include the Coulomb contribution. For simplicity, we assume here (and in the rest of this section) that the hadronic phase surrounding the quark droplet is homogeneous. Thus we exclude the *reduced–volume approach* (Sec. 4.3.4), in which concentric shells with different hadronic compositions (and hence different charge densities) surround the droplet.

First, consider the simple case in which the electric charge density is piecewise constant inside and outside the droplet,

$$\rho(r) = \begin{cases} \rho_Q \equiv e\, n_B^{Q*}\left(Y_C^{Q*} - Y_e^{Q*}\right), & r \le R_{Q*}, \\ \rho_H \equiv e\, n_B^{H}\left(Y_C^{\bar{H}} - Y_e^{\bar{H}}\right), & r > R_{Q*}, \end{cases} \tag{4.109}$$

where r is the radial distance from the droplet center, $e = \sqrt{4\pi\alpha_{\rm em}}$ (Heaviside–Lorentz units), and $\alpha_{\rm em} \simeq 1/137$. Note that $\rho_H = 0$ if the surroundings are electrically neutral ($Y_C^{\bar{H}} - Y_e^{\bar{H}} = 0$).

In this case, the Coulomb energy of a uniformly charged spherical droplet is (see, *e.g.*, [118, 134])

$$E_{Q*}^{\rm Coulomb} = \frac{3}{5}\,\alpha_{\rm em}\,\frac{\left(N_C^{Q*} - N_e^{Q*}\right)^2}{R_{Q*}} \tag{4.110}$$

$$= \frac{16}{15}\,\alpha_{\rm em}\,\pi^2\left[n_B^{Q*}\left(Y_C^{Q*} - Y_e^{Q*}\right)\right]^2 R_{Q*}^5, \tag{4.111}$$

where $N_i^{Q*} = n_B^{Q*} Y_i^{Q*}\,\frac{4\pi}{3} R_{Q*}^3$. If different hadronic shells surround the droplet, as in the reduced–volume scheme, additional terms appear.

The associated Coulomb pressure that enters the mechanical balance follows from the energy via

$$P_{Q*}^{\rm Coulomb} = -\frac{1}{4\pi R_{Q*}^2}\,\frac{\partial E_{Q*}^{\rm Coulomb}}{\partial R_{Q*}}\bigg|_{n_C^{Q*}, n_e^{Q*}} = -\frac{4}{3}\,\pi\,\alpha_{\rm em}\left[n_B^{Q*}\left(Y_C^{Q*} - Y_e^{Q*}\right)\right]^2 R_{Q*}^2. \tag{4.112}$$

Note that here we have taken the derivative at fixed n_C^{Q*} and n_e^{Q*}. A derivative at fixed N_C^{Q*}, N_e^{Q*} is in principle also possible. Physically, taking the derivative at fixed densities n_C^{Q*}, n_e^{Q*} means the droplet can exchange charge with its surroundings so $N \propto R_Q^3$ varies during the virtual change, whereas fixing the particle numbers N_C^{Q*}, N_e^{Q*} forces the densities to scale as $n \propto R_Q^{-3}$ with R, introducing extra implicit R–dependences and thus a different stationarity condition for the R_Q minimization.

A simple way to include the Coulomb term in the nucleation problem is to fix the thermodynamic variables of the droplet using, *e.g.*, Eqs. (4.69, 4.67, 4.68, 4.107), and then evaluate $E_{Q*}^{\rm Coulomb}$ with those values.

4.3.5.4 Coulomb energy and minimization

The previous treatment fixed the droplet composition without accounting for the Coulomb contribution in the minimization of W. If E_Q^{Coulomb} is included, the minimizing conditions read

$$\begin{aligned} \mu_B^{Q*} &= \mu_B^H, && (4.113)\\ \mu_C^{Q*} + \mu_e^{Q*} &= \mu_C^H + \mu_e^H, && (4.114)\\ \mu_S^{Q*} &= \mu_S^H, && (4.115)\\ \mu_e^{Q*} &= \mu_e^H + \frac{8}{5}\,\pi\,\alpha_{\mathrm{em}}\,R_{Q*}^2\,n_B^{Q*}\left(Y_C^{Q*} - Y_e^{Q*}\right). && (4.116) \end{aligned}$$

With this prescription, the composition that minimizes W^* (including E_Q^{Coulomb}) is selected. The electron chemical potentials experience a Coulomb shift proportional to the net charge density in the droplet, which favors droplets with a smaller net electric charge.

Replacing those conditions into W^*_{bulk} (Eq. 4.35) we obtain

$$W^*_{\mathrm{bulk}} = -\frac{4}{3}\pi R_Q^3\,(P_Q - P_H) - \frac{32}{15}\alpha_{\mathrm{em}}\pi^2\left[n_B^Q(Y_C^Q - Y_e^Q)\right]^2 R_Q^5, \tag{4.117}$$

where the second term is exactly $-2E_Q^{\mathrm{Coulomb}}$. Thus W^* (Eq. 4.30) is

$$W^* = -\frac{4}{3}\pi R_{Q*}^3\,(P_{Q*} - P_H) + 4\pi\sigma R_{Q*}^2 - \frac{16}{15}\alpha_{\mathrm{em}}\pi^2\left[n_B^{Q*}(Y_C^{Q*} - Y_e^{Q*})\right]^2 R_{Q*}^5. \tag{4.118}$$

Finally, R_{Q*} is the radius that maximizes W^*, *i.e.*, it satisfies the stationarity condition

$$P_{Q*} + \frac{4}{15}\,\pi\,\alpha_{\mathrm{em}}\left[n_B^{Q*}(Y_C^{Q*} - Y_e^{Q*})\right]^2 R_{Q*}^2 - \frac{2\sigma}{R_{Q*}} \;=\; P_H\,, \tag{4.119}$$

where the second term on the left-hand side collects the contribution from the derivative of $E_{Q*}^{\mathrm{Coul.}}$ together with the second term of W^*_{bulk} (Eq. 4.35), and can be interpreted as an effective Coulomb contribution.

Note that, in deriving Eq. (4.119), we first minimized W^* with respect to R and only afterwards imposed the relations that minimize W^* with respect to the remaining variables (Eq. 4.113–4.116), which are then substituted back into the final expression.

4.3.5.5 Coulomb energy and charge screening

We now relax the step–density assumption of Eq. (4.109), allowing electric charges to rearrange and screen the droplet charge [42, 110, 119]. For simplicity (as in [42, 119]), we assume that only electrons are mobile, so $n_e \mapsto n_e(r)$ with $n_e(r\to\infty) = n_e^{\bar{H}}$.

The charge density is therefore

$$\rho_{Q*}(r) = e\left[n_C(r) - n_e(r)\right], \tag{4.120}$$

with

$$n_C(r) = \begin{cases} n_B^{Q*} Y_C^{Q*}, & r < R_{Q*}, \\ n_B^{\bar{H}} Y_C^{\bar{H}}, & r > R_{Q*}, \end{cases} \tag{4.121}$$

while $n_e(r)$ is continuous at $r = R_{Q*}$. Electrically charged species have local chemical potentials

$$\mu_i(r) = \tilde{\mu}_i(r) + e\,\phi(r), \qquad i = C, e, \tag{4.122}$$

where $\tilde{\mu}_i$ excludes the electrostatic contribution and $\phi(r)$ is the electrostatic potential. The composition relations between the droplet and its surroundings (*e.g.* Eqs. 4.67, 4.107) are evaluated at the interface, where ϕ is continuous. In the thin–wall limit (negligible interface thickness), if Y_C^{Q*} is determined by minimization (*i.e.*, flavors are not frozen),

$$\mu_C^{Q*} + e\phi(R_{Q*}) = \mu_C^H + e\phi(R_{Q*}) \;\Rightarrow\; \mu_C^{Q*} = \mu_C^H, \tag{4.123}$$

which we then use to fix Y_C^{Q*}.

The electrostatic potential follows from Poisson's equation

$$\nabla^2\phi(r) = -\,\rho_{Q*}(r). \tag{4.124}$$

To close the problem, we linearize the electron density around vanishing potential. Define $\tilde{n}_e \equiv n_e(\phi \to 0) = n_e^{\bar{H}} = n_e^{Q*}$ (since $\phi \to 0$ for $r \to \infty$) and $\tilde{\mu}_e \equiv \mu_e(\phi \to 0) = \mu_e^{\bar{H}} = \mu_e^{Q*}$. With the susceptibility

$$\chi_e = \left.\frac{\partial n_e}{\partial \mu_e}\right|_{T,\mu_e=\tilde{\mu}_e} = \left.\frac{\partial n_e^{\bar{H}}}{\partial \mu_e^{\bar{H}}}\right|_T, \tag{4.125}$$

one has

$$\delta n_e(r) = \chi_e\,\delta\mu_e(r), \qquad n_e(r) \simeq \tilde{n}_e + \chi_e\,e\,\phi(r), \tag{4.126}$$

and the Debye length satisfies

$$\frac{1}{\lambda_D^2} = e^2\,\chi_e. \tag{4.127}$$

(If additional charged species are mobile, their contributions add to χ_e in the usual way.)

With these definitions, Poisson's equation becomes

$$\nabla^2\phi(r) = -e\Big[n_C(r) - \tilde{n}_e\Big] + e^2\chi_e\,\phi(r) \tag{4.128}$$

$$= -e\,n_B^{Q*}\left(Y_C^{Q*} - Y_e^{Q*}\right)\Theta(R_{Q*} - r) + \frac{1}{\lambda_D^2}\,\phi(r), \tag{4.129}$$

where we used Eq. (4.121), charge neutrality in the hadronic bath ($Y_C^{\bar{H}} - Y_e^{\bar{H}} = 0$), and $\tilde{n}_e = n_e^{\bar{H}} = n_e^{Q*}$. Imposing $\phi(\infty) = 0$, $\phi'(0) = 0$, and continuity at $r = R_{Q*}$, the

solution is

$$\phi(r) = \begin{cases} e\, n_B^{Q*}\left(Y_C^{Q*} - Y_e^{Q*}\right) \lambda_D^2 \left[1 - \dfrac{\left(1 + \frac{R_{Q*}}{\lambda_D}\right) e^{-R_{Q*}/\lambda_D}}{(r/\lambda_D)} \sinh\left(\dfrac{r}{\lambda_D}\right)\right], & r \leq R_{Q*}, \\ e\, n_B^{Q*}\left(Y_C^{Q*} - Y_e^{Q*}\right) \lambda_D^3 \left[\dfrac{R_{Q*}}{\lambda_D} \cosh\left(\dfrac{R_{Q*}}{\lambda_D}\right) - \sinh\left(\dfrac{R_{Q*}}{\lambda_D}\right)\right] \dfrac{e^{-r/\lambda_D}}{r}, & r \geq R_{Q*}. \end{cases} \tag{4.130}$$

The Coulomb energy of a spherical droplet is

$$E_{Q*}^{\text{Coulomb}}(R_{Q*}) = \frac{1}{2} \int d^3r\, \rho_{Q*}(r)\, \phi(r) \tag{4.131}$$

$$= \frac{16\pi^2}{15}\, \alpha_{\text{em}} \left[n_B^{Q*}\left(Y_C^{Q*} - Y_e^{Q*}\right)\right]^2 R_{Q*}^5\, f\left(\frac{R_{Q*}}{\lambda_D}\right), \tag{4.132}$$

with

$$f(x) = \frac{5}{2x^5}\left[x^3 - 3(x+1)\left(x\cosh x - \sinh x\right)e^{-x}\right], \qquad x = \frac{R_{Q*}}{\lambda_D}. \tag{4.133}$$

The corresponding contribution to the mechanical balance is

$$P_{Q*}^{\text{Coulomb}}(R_{Q*}) = -\frac{4\pi}{3}\, \alpha_{\text{em}} \left[n_B^{Q*}\left(Y_C^{Q*} - Y_e^{Q*}\right)\right]^2 R_{Q*}^2 \left[f\left(\frac{R_{Q*}}{\lambda_D}\right) + \frac{1}{5}\frac{R_{Q*}}{\lambda_D} f'\left(\frac{R_{Q*}}{\lambda_D}\right)\right]. \tag{4.134}$$

As $R_{Q*}/\lambda_D \to 0$ (unscreened limit), $f(R_{Q*}/\lambda_D) \to 1$, $f'(R_{Q*}/\lambda_D) \to -5/6$ and the Eqs. (4.132),(4.134) reduce to the homogeneous, unscreened expressions $E_{Q*}^{\text{Coulomb}} \propto R_{Q*}^5$ (Eq. 4.111) and $P_{Q*}^{\text{Coulomb}} \propto -R_{Q*}^2$ (Eq. 4.112).
For $R_{Q*}/\lambda_D \gg 1$ (strong screening), $f(R_{Q*}/\lambda_D) \sim \frac{5}{2}(\lambda_D/R)^2$ and $f'(R_{Q*}/\lambda_D) \sim -5(\lambda_D/R)^3$ so $E_{Q*}^{\text{Coul.}} \propto R_{Q*}^3 \lambda_D^2$ and $P_{Q*}^{\text{Coul.}} \propto -\lambda_D^2$. Thus, screening reduces the Coulomb cost and qualitatively restores a barrier shape similar to the locally or globally neutral cases without Coulomb interaction. Indeed, note that in the strong screening limit the Coulombian contribution can be seen as a correction to the bulk contribution, since it has the same radius dependence.

In Fig. 4.4, an energy barrier as a function of the radius with the different approaches presented in this section is shown. The red line assumes local charge neutrality (see Sec. 4.3.5.1), the purple line assumes global charge neutrality neglecting the role of Coulomb energy (see Sec. 4.3.5.2), the blue line simply add the Coulomb energy to the global charge neutrality case (see Sec. 4.3.5.3). Finally, the green and orange are the more sophisticated approaches. The former (see Sec. 4.3.5.4) assumes that the particle densities are constant inside and outside the droplet (but different between inside and outside) and their value is optimized to minimize W^* (comprehensive of the coulomb energy). The latter (see Sec. 4.3.5.5), the electron density is continuous and not constant since electrons act to screen the net electric charge.

Note that in the GCN+Coul. case, no critical radius appears: the unscreened $\propto R_{Q*}^5$ Coulomb term places the second minimum at an energy higher than that at $R_{Q*} = 0$, so the intervening maximum does not correspond to a critical droplet. In the Minimiz. and Screen. cases, electric charges are allowed to redistribute, reducing the Coulomb

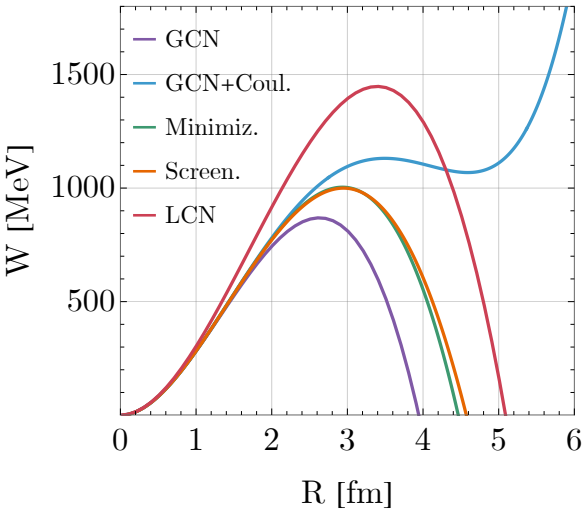

Figure 4.4: Work needed to generate a SQM droplet with a radius R. Different colors refers to different approaches in treating the electron distribution and electric charge neutrality: global charge neutrality (GCN, purple) without Coulombian energy (Sec. 4.3.5.2), GCN with Coulombian energy (blue) (Sec. 4.3.5.3),GCN with Coulombian energy and electron screening (orange) (Sec. 4.3.5.5), minimization of the energy assuming different but uniform electron densities in the two phases (green) (See. 4.3.5.4), local charge neutrality (LCN) (red) (Sec. 4.3.5.1). See the related text for details. The used EOS are the SFHO-HΔ (Sec. 2.1.2) and the unpaired α-Bag (Sec. 2.2.2). We set $n_B^H/n_0 = 7.4$, $T = 20$ MeV, $\sigma = 30$ MeVfm^{-2}, $Y_L^H = 0.25$, $B_{\rm unp}^{1/4} = 178$ MeV.

energy. As a result, the barrier regains a shape qualitatively similar to the LCN and GCN (no Coulomb) limits, with the corresponding curves lying between those two extremes.

4.3.6 Thermal nucleation rate

The rate of a spontaneous thermal fluctuation generating a critical droplet, as a function of the initial hadronic conditions $(n_B^{\bar{H}}, \{Y_i^{\bar{H}}\}, T)$, is [30, 185, 195]

$$\Gamma_{\rm th} = \Gamma_0 \exp\left[-\frac{W^*}{T}\right], \tag{4.135}$$

where W^* is the energy barrier, *i.e.*, the work required to create a critical volume V_{Q*} of quark matter in a pure H system.

This thermal nucleation rate can be derived both in a thermodynamical framework [185] and within a field-theoretic framework [30, 195] (see also *e.g.* [29, 116]).

While Eq. (4.135) is general, the prefactor Γ_0 depends on the specific properties of the system. In *Langer* nucleation theory [30, 195], the prefactor Γ_0 is expressed as the product of a statistical prefactor Ω_0 (measuring the phase-space volume of the saddle-point region) and a dynamical prefactor κ (the exponential growth rate of the droplet

at the saddle point):

$$\Gamma_0 = \frac{\kappa}{2\pi}\,\Omega_0. \tag{4.136}$$

Langer's theory provides a first-principles derivation of Eqs. (4.135, 4.136) as the decay rate of a metastable state by thermal activation. The key idea is that a coarse-grained free energy $\mathcal{F}$[order parameter] has a metastable minimum and a nearby saddle point (a single critical droplet). The nucleation rate is the steady probability current across the saddle. This formulation is applicable in the context of all classical first-order phase transitions. In particular, the derivation does *not* assume a particle accumulation in a cluster, but it applies equally well to *e.g.*, a superfluid transition via nucleation of a sufficiently large vortex ring or magnetic reversal via formation of a coherently oriented spin domain. The framework has been generalized to relativistic quantum field theories at zero and finite temperature [135, 197, 206]. In these relativistic treatments, the state-of-the-art prefactor depends on the dissipative transport coefficients of the ambient medium (thermal conductivity and shear/bulk viscosities) entering through κ, while Ω_0 reflects the static spectrum of fluctuations around the saddle.

The statistical prefactor is

$$\Omega_0 = \frac{2}{3\sqrt{3}}\left(\frac{\sigma}{T}\right)^{3/2}\left(\frac{R_{Q*}}{\xi_q}\right)^4, \tag{4.137}$$

where ξ_q is the quark correlation length, σ the surface tension, and R_{Q*} the radius of the critical droplet. The dynamical prefactor reads:

$$\kappa = \frac{2\sigma}{R_{Q*}^3\,(\Delta\omega)^2}\left[\lambda T + 2\left(\frac{4}{3}\eta + \zeta\right)\right], \tag{4.138}$$

where $\Delta\omega$ is the enthalpy density difference between the two phases at the saddle point, λ is the thermal conductivity, and η and ζ are the shear and bulk viscosities of hadronic matter, respectively. The transport coefficients η, ζ, and λ were estimated in [207]. Here, we adopt the same coefficients as in [43, 127]: namely, we set the thermal conductivity and bulk viscosity to zero, $\lambda = \zeta = 0$, because the shear–viscosity term dominates [207]. For the shear viscosity, we use the fit presented in [207]:

$$\eta = 7.6 \times 10^{26}\left(\frac{n_B^{\bar{H}}}{n_0}\right)^2\left(\frac{T}{\mathrm{MeV}}\right)^{-2}\frac{\mathrm{MeV}}{\mathrm{fm\ s}}. \tag{4.139}$$

For the statistical prefactor, we also take the quark correlation length to be $\xi_q \simeq 0.7$ fm [135], as in [127].

For a comprehensive discussion of the prefactor, see [197]. We stress, however, that the dominant physics resides in the exponential, while the prefactor plays only a subleading role. Indeed, the exponential factor changes by many orders of magnitude with the thermodynamic conditions, whereas the prefactor varies much more mildly. Thus, the dependence of the nucleation rate on the thermodynamic state is governed almost entirely by the exponential term. Since the goal is to identify the conditions under which the rate becomes large enough to trigger the phase transition, the prefactor has

a negligible impact on the results. In numerous works, the state-of-the-art prefactor is therefore replaced, for simplicity, by a dimensional estimate such as T^4 or μ^4, without qualitative changes in the conclusions (see *e.g.* [116, 117, 122]).

Finally, the nucleation time, *i.e.*, the typical waiting time for a critical fluctuation to occur in a system of volume V, is

$$\tau_{\rm th} \;=\; \frac{1}{V\,\Gamma_{\rm th}}. \tag{4.140}$$

This is neither the lifetime of an individual droplet nor the time required for a droplet to grow to the critical size. Rather, it is the expected waiting time for at least one critical droplet to appear within the system, statistically speaking.

4.3.7 Quantum nucleation rate

At sufficiently low temperatures, the decay of the metastable hadronic phase proceeds via quantum tunneling rather than thermal activation. In this regime, the dynamics of small virtual droplets is described semiclassically by a one-dimensional WKB problem for a particle of coordinate R_Q (or V_Q) moving in an effective potential $W(R_Q)$ with a radius–dependent inertia $M(R_Q)$ [208]. The droplet becomes real once it tunnels through the barrier separating the metastable and the stable configurations. The theory was developed by [208] and then extended in the relativistic regime by [42, 119]. The dynamics of the fluctuations in the variable R_Q is governed by a relativistic Lagrangian,

$$\mathcal{L}(R_Q,\dot{R}_Q) \;=\; -\,M(R_Q)\,\sqrt{1-\dot{R}_Q^2} \;+\; M(R_Q) \;-\; W(R). \tag{4.141}$$

The effective inertia follows from the hydrodynamic flow induced by a changing R_Q under (quasi-)mechanical equilibrium between the droplet and the surrounding is

$$M(R_Q) \;=\; 4\pi\,\rho_H\left(1-\frac{n_B^{Q*}}{n_B^{\bar{H}}}\right)^2 R_Q^3, \tag{4.142}$$

where $\rho_H \;=\; n_B^{\bar{H}}\sum_h Y_h^{\bar{H}} m_h$ ($h \;=$ all the hadrons) is the mass density of the ambient hadronic phase. See [119] for compressibility/dissipation corrections that enter as higher–order modifications of $M(R)$.

The quantum tunneling nucleation rate is

$$\Gamma_{\rm qt} = n_{\rm n.c.}\,\nu_0\,\exp[-A(E_0)]\,, \tag{4.143}$$

where $A(E)$ is the action under the potential barrier

$$A(E) \;=\; 2\int_{R_{Q-}}^{R_{Q+}} \sqrt{\Big[2M(R_Q)+E-W(R_Q)\Big]\,[W(R_Q)-E]}\;dR_Q, \tag{4.144}$$

where R_{Q-} and R_{Q+} are the classical turning points, namely the points in which $W(R_Q)=E$.

Near $R_Q = 0$ the potential $W(R_Q)$ has a local minimum, so the collective coordinate executes small oscillations in a bound region where $E > W(R_Q)$ between 0 and R_{Q-}. Quantization of this motion produces discrete levels, the lowest one (the ground state energy E_0) lies at $E_0 > W(0)$ because of zero–point motion (finite curvature of W at the minimum). Tunneling occurs from this bound state through the barrier segment where $W(R_Q) > E_0$ (hence the factor $[\,W - E_0\,]$ in A), and the system emerges at R_{Q+} into the classically allowed growth region.

In the semiclassical treatment, the ground-state energy E_0 and small-oscillation frequency ν_0 of the bound motion near $R_Q = 0$ are obtained from $W(R_Q)$. In particular, E_0 is fixed by the Bohr–Sommerfeld condition

$$I(E_0) \;=\; 2\pi\Big(m_0 + \tfrac{3}{4}\Big), \tag{4.145}$$

where the relativistic oscillation action is

$$I(E) \;=\; 2\int_0^{R_{Q-}} \sqrt{\Big[2M(R_Q) + E - W(R_Q)\Big]\,\Big[E - W(R_Q)\Big]}\,dR_Q. \tag{4.146}$$

The integer

$$m_0 \;=\; \left\lfloor \frac{I(E_{\min})}{2\pi} + \frac{1}{4} \right\rfloor \tag{4.147}$$

counts the number of positive–energy bound levels below the lower edge of the "relativistic continuum". Here $E_{\min}$ is the maximum of $W(R_Q) - 2M(R_Q)$, which sets the lower bound of the positive–energy continuum band (*i.e.*, the region where $2M(R_Q) + E - W(R_Q) \geq 0$ for all R_Q).

The small–oscillation frequency follows from

$$\nu_0^{-1} \;=\; \left.\frac{dI}{dE}\right|_{E_0}. \tag{4.148}$$

Finally, $n_{\rm n.c.} = N_{\rm n.c.}/V$ is the number of statistically independent nucleation centers per unit of volume. For a system of 100 m a standard estimate is $N_{\rm n.c.} \sim 10^{48}$.

For a system with a volume V and thus a number $N_{\rm n.c.}$ of independent nucleation centers, the nucleation time is

$$\tau_{\rm qt} \;=\; \frac{1}{V\,\Gamma_{\rm qt}} \;=\; \frac{1}{N_c\,\nu_0\,\exp\left[-A(E_0)\right]}. \tag{4.149}$$

4.3.8 Color-superconductivity in quark nucleation

Color–superconducting quark matter could play a role at the typical densities of compact stars [60, 209, 210].

A key issue concerns the behavior of color superconductivity in finite systems [211], such as the first nucleating quark droplet. Since the diquark coherence length is $\xi_{Qcsc} \sim$

$1/\Delta$ [54], where Δ is the pairing gap, diquark pairs can only form in droplets larger than this characteristic size (see Fig. 4.5). For example, in [211] the pairing gap vanishes if the system is smaller than ~ 3 fm. We therefore impose a minimal radius R_Δ, above which the droplet becomes superconducting [46].

For simplicity, we restrict to the CFL phase. A comprehensive treatment would include other pairing patterns (e.g., 2SC) [54, 210], but our aim here is not to analyze the competition among color–superconducting phases. Rather, we focus on how nucleation is modified when the energetically favored superconducting phase can only develop once $R \geq R_\Delta$, while smaller droplets ($R < R_\Delta$) remain in the less-stable unpaired phase. The same framework can, in principle, be applied to other color–superconducting phases.

Within this approach, the P_{Q*} and the other thermodynamic quantities of the quark phase entering the energy barrier (e.g., Eq. 4.74) become explicitly radius dependent:

$$P_Q(n_B^{Q*}, \{Y_i^{Q*}\}, T, R) = \begin{cases} P_{Q_{\rm unp}}(n_B^{Q*}, \{Y_i^{Q*}\}, T), & R \leq R_\Delta, \\ P_{Q_{\rm CFL}}(n_B^{Q*}, T), & R > R_\Delta, \end{cases} \tag{4.150}$$

where $Q_{\rm unp}$ and $Q_{\rm CFL}$ refer to the unpaired and CFL quark phases.

A possible choice for R_Δ is $R_\Delta(T) = 1/\Delta(T)$. Note that $R_\Delta(T)$ depends on temperature through the gap $\Delta(T)$ (see Eq. 2.77). In principle, it could also depend on n_B^{Q*} if the gap were consistently computed as $\Delta(n_B^{Q*}, T)$ by solving the gap equation, instead of using the simple ansatz described in Sec. 2.2.3.

The critical radius is then the value of R_Q at which $W(n_B^{\bar{H}}, \{Y_i^{\bar{H}}\}, T, R_Q)$ attains its maximum,

$$\max_{R_Q}\Big[W(n_B^{\bar{H}}, \{Y_i^{\bar{H}}\}, T, R_Q)\Big] = W(n_B^{\bar{H}}, \{Y_i^{\bar{H}}\}, T, R_{Q*}), \tag{4.151}$$

namely

$$R_{Q*}(n_B^{\bar{H}}, \{Y_i^{\bar{H}}\}, T) = \begin{cases} R_{Q*}^{\rm unp}(n_B^{\bar{H}}, \{Y_i^{\bar{H}}\}, T), & R_{Q*}^{\rm unp} \leq R_\Delta, \\ \max\Big[R_\Delta(T),\, R_{Q*}^{\rm CFL}(n_B^{\bar{H}}, T)\Big], & R_{Q*}^{\rm unp} > R_\Delta, \end{cases} \tag{4.152}$$

where $R_{Q*}^{\rm unp}$ ($R_{Q*}^{\rm CFL}$) is the critical radius computed assuming only the unpaired (CFL) phase, found by solving Eq. (4.48) with $P_Q \to P_{Q_{\rm unp}}$ ($P_Q \to P_{Q_{\rm CFL}}$). Finally, the energy barrier is obtained by substituting R_{Q*} from Eq. (4.152) into Eq. (4.74):

$$W^*(n_B^{\bar{H}}, \{Y_i^{\bar{H}}\}, T) = W\Big[n_B^{\bar{H}}, \{Y_i^{\bar{H}}\}, T,\, R_{Q*}(n_B^{\bar{H}}, \{Y_i^{\bar{H}}\}, T)\Big]. \tag{4.153}$$

This scheme will be referred to as *unp+CFL*.

Note that, alternatively, one could introduce an interpolation ansatz between the unpaired and CFL phases that depends explicitly on the droplet size. In a more realistic description, the pairing condensate would turn on smoothly as a function of R, rather than undergoing a non-smooth transition at a single radius.

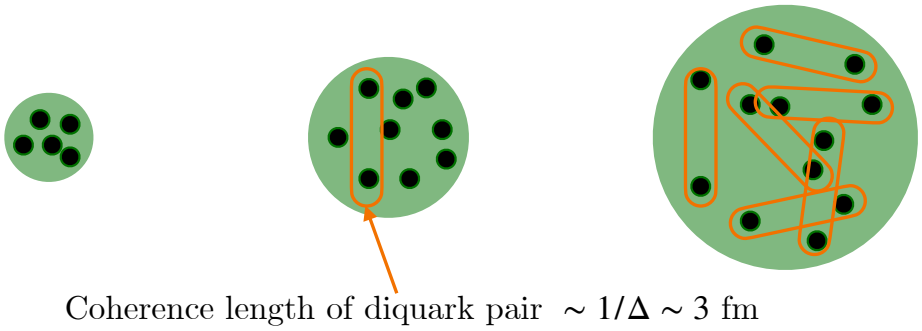

Figure 4.5: Since the diquark coherence length is $\xi_{Qcsc} \sim 1/\Delta$ [54], the color-superconducting order parameter is strongly suppressed in droplets whose radius $R \lesssim \xi_{Qcsc}$. In the nucleation stage, the first (subcritical or critical) droplet is therefore expected to be predominantly *unpaired*, with the paired condensates turning on only after the droplet grows beyond this characteristic size.

Chapter 5

Strange quark star formation

In this chapter we apply the nucleation framework developed in the previous sections to concrete astrophysical systems. We first outline how to incorporate the formalism into time–dependent simulations and how to construct approximate prescriptions that can be used even in the absence of specific simulations.

We then discuss its application to different scenarios. First, we study nucleation in hadronic PNSs and the resulting implications for the possible coexistence of NSs and QSs, using the fluctuation–assisted nucleation approach introduced in Sec. 4.3.4.2 and exploring the role of color superconductivity within the framework presented in Sec. 4.3.8.

Next, we explore qualitatively the reduced–volume approach (Sec. 4.3.4.3), obtaining hints regarding the possibility that a hadronic NS that survives the PNS phase can later convert by mass accretion, after it has already cooled and deleptonized.

Moreover, we illustrate an application to a simulation of a core–collapse supernova explosion in a compact binary, where a simplified treatment of quark–matter nucleation is implemented.

Finally, we will present qualitatively some other applications that will be explored in details in future works.

5.1 Investigating QS formation with the nucleation formalism

As discussed in the previous chapters, the macroscopic deconfinement phase transition that converts a hadronic object into a QS is triggered by nucleation.

In some works [34, 47, 94], a simple phenomenological approach is used to estimate the nucleation conditions, which does not explicitly include nucleation calculations. Within the approximate approach, the onset of deconfinement is set with a simple necessary condition is imposed by comparing the mean spacing among strange quarks inside confined matter, $d_S \sim (Y_S^H n_B^H)^{-1/3}$ to the mean nucleon spacing in cold nuclear

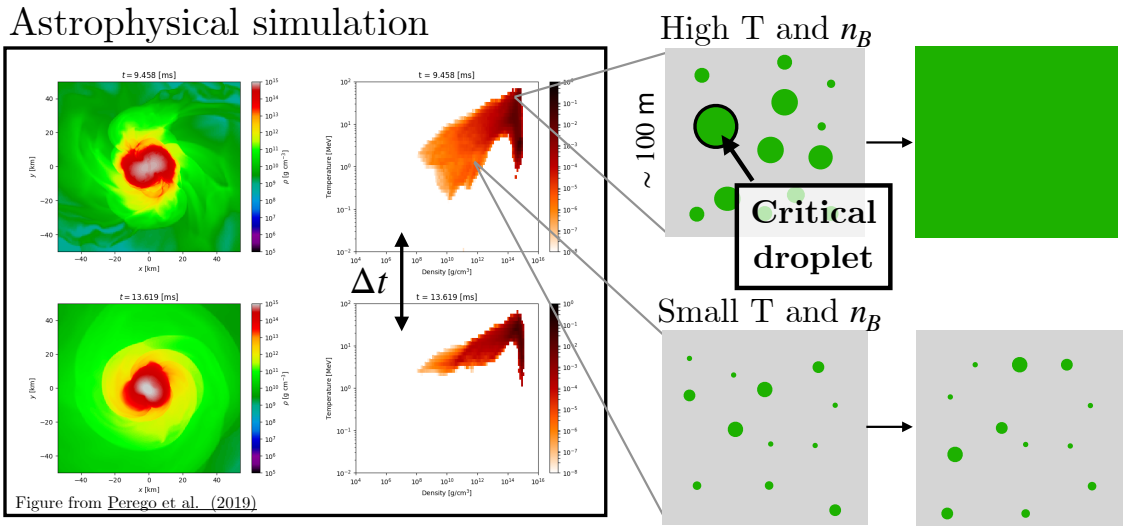

Figure 5.1: Schematic picture of how nucleation calculations can be implemented by post-processing a simulation output. Every cell in each timestep of the simulation can be considered as the system having a given average thermodynamic condition (the output of the simulation) on which we compute the nucleation rate. We can assume that the nucleation happens in a cell when at least one nucleation event is statistically expected in it. The simulation figure is from [64].

matter, $d_n = n_0^{-1/3}$: when $d_S \lesssim d_n$, strangeness is sufficiently dense to seed a critical SQM droplet. Usually, this translates into a threshold band $Y_S^H \simeq 0.2 - 0.3$.

However, a complete discussion would require the use of the nucleation rate, computed as discussed in Chapter 4.

In astrophysical applications, the system has a space- and time-dependent configuration $n_B^H(\mathbf{r},t), \{Y_i^H(\mathbf{r},t)\}, T(\mathbf{r},t)$. The expected number of nucleation events is

$$\int_{t_{\rm TOT}} dt \int_{V_{\rm TOT}} d^3\mathbf{r}\, \Gamma\left[n_B^H(\mathbf{r},t), \{Y_i^H(\mathbf{r},t)\}, T(\mathbf{r},t)\right], \tag{5.1}$$

where $t_{\rm TOT}$ and $V_{\rm TOT}$ denote the total time and volume considered.

5.1.1 Post processing astrophysical simulations

In numerical simulations of BNSMs, CCSNe, or PNSs, the system is discretized into cells of volume V (typically ~ 100 m), within which (n_B^H, Y_i^H, T) can be regarded as approximately constant over both space and time during a timestep Δt. The local nucleation rate can thus be evaluated cell by cell using the simulation output $(n_B^H, \{Y_i^H\}, T)$ as input for Γ. The phase transition is statistically triggered in cell r at time t if

$$\Delta t\, V_{t,r}\, \Gamma\left[n_B^H, \{Y_i^H\}, T\right]_{t,r} \geq 1. \tag{5.2}$$

5.1.2 Approximate approach

However, in this work, we do not have access to an astrophysical simulation that provides the input $(n_B^H, \{Y_i^H\}, T)$, and thus a different approach is required.

Our strategy is to compute the thermodynamic conditions $(n_B^H, \{Y_i^H\}, T)$ under which a nucleation event is statistically expected to occur in a hadronic system before these conditions change, *i.e.*, when the nucleation time τ (Eq. 4.140) is shorter than the dynamical timescale of the system $\tau_{\rm dyn} \simeq 10^{-4}$ s.

In principle, one should compute the local nucleation rate throughout the entire hadronic object (*e.g.* the PNS before or after the CCSN explosion) and then integrate over the volume. However, since the thermal nucleation rate depends exponentially on W^*/T (and on the action that depends on W^* in quantum nucleation), the global rate is dominated by the space–time point where the energy barrier W^* is minimized. For this reason, we restrict our analysis to the innermost region of the hadronic object, approximated as a sphere of radius 100 m (*i.e.*, $V_{\rm center} = \frac{4}{3}\pi(100\text{ m})^3 \simeq 10^{51}$ fm^3), where n_B^H reach its maximum value and the quantities are nearly spatially constant within the region. We therefore neglect the contribution from the rest of the astrophysical object.

Moreover, during the evolution, the central conditions $(n_B^H, \{Y_i^H\}, T)$ can remain approximately constant on timescales longer than $\tau_{\rm dyn}$. Our approach may therefore slightly overestimate the values of n_B^H and T at which nucleation occurs. Nevertheless, (see also [43, 45]), τ varies extremely rapidly with the thermodynamic conditions, so adopting a different reference timescale instead of $\tau_{\rm dyn}$ does not significantly affect the results.

In conclusion, we define the *nucleation conditions* as the set of parameters[1] $(n_B^H, \{Y_i^H\}, T)$ such that

$$\tau \equiv \left[V_{\rm center}\,\Gamma(n_B^H, Y_L^H, T)\right]^{-1} \leq \tau_{\rm dyn}. \tag{5.3}$$

5.1.3 Remnant and energy released

Once the nucleation conditions are reached in a hadronic object, the seed grows and a conversion front propagates outward, transforming hadronic matter into SQM. The remnant is a hot QS that subsequently cools and deleptonizes via intense neutrino emission until it settles into a hydrostatic configuration on the QS branch [10, 31, 32].

During the conversion, both strong and weak processes in the front conserve the total baryon number, while neutrinos and gravitational waves carry away energy and lepton number but not baryons. Significant deviations would require substantial mass ejection across the surface, which is unlikely in particular for PNSs since they lack an extended envelope to ablate. Thus, we assume that the total baryon number N_B is conserved during the conversion, so that the final QS has the same baryonic mass $(M_B \equiv m_b\, N_B)$[2]

[1] Note that $\{Y_i^H\}$ can be usually fixed as a function of n_B^H, T and a reduced number of fractions. For example, in a PNS evolution the independent input variables are n_B^H, Y_L^H, T.

[2] We fix the baryon mass to the atomic mass unit $m_b = 931$ MeV. Other works sometimes adopt

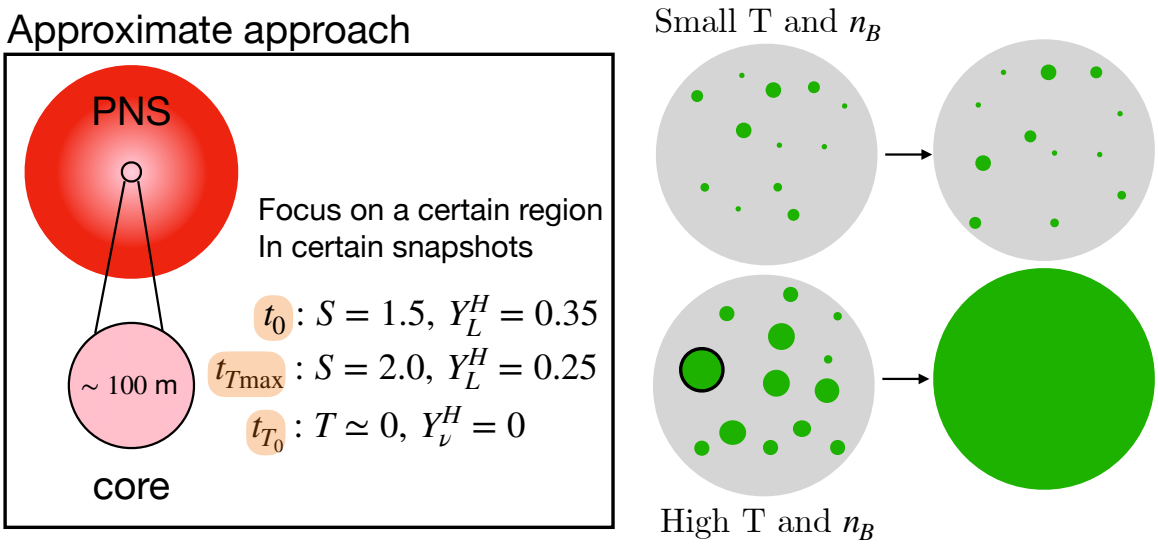

Figure 5.2: Alternative approach to compute nucleation in an astrophysical system without a proper simulation. We assume nucleation happens, triggering the macroscopic-scale conversion, when the nucleation timescale in the center of the hadronic object is smaller than the dynamical timescale of the system.

as the initial object (*e.g.* an hadronic PNS or NS),*i.e.* $M_B^{\rm QS} = M_B^{\rm PNS/NS}$ [43, 212].

This approximation is robust if the conversion proceeds as a deflagration [10, 31, 32], and remains reasonable even in a hypothetical detonative scenario, since the expelled mass is expected to be at most $\sim 10^{-2}$ $M_\odot$, negligible compared to the stellar baryon content and the total conversion energy.

By contrast, the gravitational mass of the star changes during the conversion. The total released energy is given by the difference in binding energies between the final QS and the initial PNS:

$$E_{\rm conv} = \text{B.E.}_{\rm QS} - \text{B.E.}_{\rm PNS/NS} = M^{\rm PNS/NS} - M^{\rm QS}. \tag{5.4}$$

This energy can be emitted in the form of a powerful neutrino burst, intense gravitational waves, or possibly even trigger gamma-ray bursts (GRBs) [10, 131, 133, 213]. In addition, the conversion energy could impart a "second kick" to the QS, providing a natural explanation for the bimodal distribution of pulsar velocities [214]. Finally, if the converted QS resides in a binary system, the nearly instantaneous[3] gravitational mass defect can increase the orbital eccentricity, even in systems previously circularized by tides (see [160] for a recent study in the twin-star scenario).

$m_b = 939$ MeV. This choice is arbitrary as long as it is applied consistently to all objects.

[3]The conversion timescale is much shorter than a typical orbital period.

5.2 QS formation in PNSs and implications on the QS–NS coexistence

In this chapter, we investigate the possibility that QSs are produced during the evolution of a hadronic PNS, a possible remnant of a CCSN, in the context of the two–families scenario of compact stars. In particular, we investigate whether our results are consistent with the coexistence of NSs and QSs. Since all NSs are initially born as PNSs, their existence implies that not all PNSs convert into QSs.

Conversely, the possibility that no PNS converts does not exclude the existence of QSs and therefore does not rule out the two–families scenario. Indeed, alternative channels for QS formation are possible, such as during or immediately after the BNSMs [34], through accretion onto a NS from a binary companion, via accretion of supernova ejecta in a binary system [47], or during the CCSN of a very massive progenitor star, before shock revival and the termination of core accretion.

In doing this analysis, we will also consider the role of color superconductivity and, in particular, the suppression of the color superconducting pairing in finite-size systems as presented in Sec. 4.3.8. Moreover, the nucleation rate will be computed within the formalism described in the Sec. 4.3.4.2, namely considering the thermal fluctuations in the hadronic composition, in the framework that assumes all the configurations involving only strong interactions are available. As discussed, this can be considered as an overstimation of the nucleation rate (see Sec. 4.3.4.3). Here we are, however, interested in investigating whether a parameter space for the coexistence of NSs–QSs exists even in this limit. We will focus on the thermal nucleation rate since it is expected to dominate at the typical temperature of the PNS core [43, 45]. Finally, charge neutrality will be treated as discussed in Sec. 4.3.5.4, namely, not assuming local or global charge neutrality, but setting the composition that minimizes the whole energy barrier, encompassing the Coulombian contribution. This approach provide a result qualitative similar to the screening approach, but is more in line with our general approach of having two different phases for the hadronic and quark phases.

5.2.1 PNS evolution

Hadronic PNSs are one of the possible remnants of CCSNe [63]. When stars with initial masses above ~ 8 $M_\odot$ exhaust their nuclear fuel, their cores can no longer be supported against gravity and begin to collapse. The collapse proceeds until the core baryon density approaches nuclear saturation, $n_B \simeq n_0 \simeq 0.16$ fm^{-3}, where the repulsive component of the nuclear force together with neutron degeneracy pressure halts the collapse, causing the core to bounce. This process occurs over a dynamic timescale ($\sim 10^{-4}$ s).

Immediately after bounce, the hadronic PNS is formed. It is characterized by a relatively low mass $\sim (0.5-1)$ $M_\odot$, a high lepton fraction $Y_L \simeq 0.35$–0.4, and an entropy per baryon of $S \simeq 1-1.5$ (with precise values depending on the progenitor, the EOS, and weak-interaction microphysics) [35, 36, 63]. Over the subsequent $\sim (0.5-1)$ s, the PNS accretes matter from the overlying layers. The amount of accreted mass depends

on the progenitor star characteristics (mainly its mass).

If accretion is modest (*e.g.*, for progenitors $\lesssim 20$ $M_\odot$), a neutrino-driven CCSN explosion happens, leaving a hadronic PNS remnant. For more massive progenitors, sustained accretion can be large enough that conditions for quark deconfinement may already be met during this early phase. Indeed, deconfinement has been proposed as a mechanism that can trigger CCSN explosions in cases where standard mechanism fails [35, 36]. This possibility, in the context of the two–families scenario, will be investigated in Sec. 5.5. For even more massive progenitors, continued accretion can drive the PNS above its stability limit, leading to black hole (BH) formation. In the present chapter we focus on the scenario in which a hadronic PNS survives these initial stages and becomes the remnant of a successful CCSN.

After explosion, the newly formed hadronic PNS core (typically $S \simeq 1 - 1.5$ and $Y_L \simeq 0.35 - 0.4$) is no longer strongly accreted, so its baryonic mass M_B can be taken as approximately constant for the subsequent evolution. Within ~ 10 s, the core entropy per baryon commonly rises toward $S \simeq 1.5 - 2$, while the lepton fraction decreases to $Y_L \simeq 0.25 - 0.3$ owing to neutrino diffusion (deleptonization). Finally, the PNS cools by neutrino emission, eventually reaching the cold neutrino-less β-equilibrium NS configuration after ~ 30 s.

The specific values of S and Y_L depend on the PNS baryonic mass (hence on progenitor properties), on the EOS and on the neutrino-transport treatment adopted [37, 215–218]. Note that the quoted S and Y_L refer to core values and are not necessarily uniform throughout the star.

Since the evolution of a hadronic PNS is slower than the weak equilibration timescale, we can assume that the hadronic PNS is in chemical equilibrium and thus $(n_B^H, \{Y_i^H\}, T) \to (n_B^H, Y_L^H, T)$.

Since we do not have dedicated PNS simulations for our EOS model, we discuss the time evolution of the PNS central conditions by considering two representative snapshots, with typical thermodynamic values extrapolated from existing simulations [37, 215–218]:

- (t_0) $S_H = 1.5$ and $Y_L^H = 0.35$ at the time of the CCSN explosion;
- $(t_{T\max})$ $S_H = 2$ and $Y_L^H = 0.25$ after ~ 10 s, when the central temperature reaches its maximum.

Here, $S_H = s_H/n_B^H$ denotes the entropy per baryon of the hadronic phase. In computing the PNS masses and radii, we therefore assume that the star is characterized by fixed values of S_H and Y_L^H. The corresponding central baryon density is then fixed at given S_H, Y_L^H (and thus for t_0 and $t_{T\max}$) as a function of the PNS mass.

We will then investigate whether in those two snapshots the nucleation conditions as defined in Sec. 5.1.2 are reached. In that case, we will assume that the PNS will start a conversion into a QS, eventually populating the QS branch in the two–families scenario M–R diagram. The final QS, as discussed in Sec. 5.1.3, will have the same baryon mass than the initial PNS $M_B^{\rm QS} = M_B^{\rm PNS}$, but different gravitational mass. The difference in the gravitational mass is the conversion energy that, as discussed before, could be

related to astrophysical observables, *e.g.* yielding to GRBs. Depending on the stage of the PNS evolution at which the conversion occurs, and on the timescale required to complete it, such a GRB could be delayed with respect to the CCSN explosion.

On the other hand, if the nucleation conditions are never reached during the evolution of the PNS, the remnant will instead cool and settle into a cold NS with the same baryon mass, $M_B^{\rm NS} = M_B^{\rm PNS}$.

5.2.2 Phases equilibrium and compact star families

Some characteristics of the EOS models used in this chapter are shown in Fig. 5.3.

Panel (5.3a) shows the mass–radius relations for NSs, QSs, and PNSs. For the PNSs, two representative snapshots are considered, t_0 ($S_H = 1.5$, $Y_L^H = 0.35$) and $t_{T\rm max}$ ($S_H = 2$, $Y_L^H = 0.25$), as discussed in Sec. 5.1.2.

In the two–families scenario, the hadronic EOS is generally soft because of the inclusion of hyperons and Δ resonances (see Sec. 2.1.2), which leads to relatively low maximum masses for NSs and PNSs (with our model and parametrization, $M_{\rm max}^{\rm NS} = 1.68$ M$_\odot$). Such an EOS, unable to support ~ 2 M$_\odot$, is not in conflict with observations of massive compact stars, since in this scenario the most massive objects are identified with QSs. In this work we adopt a slightly different parametrization than in [34, 47, 94, 168], resulting in a slightly stiffer EOS and therefore slightly larger NS masses and radii. The increased stiffness mainly arises from the vector field ϕ (see [23]), which introduces repulsive interactions among strange hadrons, shifting the onset of strangeness to higher baryon density. For this work, we will not consider mesons (*e.g.* pions, kaons), as their contribution does not qualitatively modify the results. Further details are given in Sec. 2.1.2.

QSs are assumed to be bare and composed of CFL SQM (αBag model). We consider two parametrizations with different maximum masses: 2.20 M$_\odot$ (Q1) and 2.57 M$_\odot$ (Q2), see Sec. 2.2.3.

Panel (5.3b) shows the gravitational mass M as a function of the baryonic mass M_B for the same set of configurations. Because M_B is conserved as a PNS cools to a NS or converts to a QS, the secular evolution of an individual star proceeds *vertically* in this diagram.

If nucleation is attained in a maximum–mass PNS at t_0 ($M_{\rm max}^{\rm PNS} = 1.78$ M$_\odot$) or at $t_{T\rm max}$ ($M_{\rm max}^{\rm PNS} = 1.74$ M$_\odot$), the corresponding QS masses are $M^{\rm QS} = 1.48$ M$_\odot$ and 1.45 M$_\odot$ for the Q1 parametrization (1.39 M$_\odot$ and 1.37 M$_\odot$ for Q2). Such conversions do not directly populate the high–mass end of the QS branch; the most massive QSs must instead arise from BCSM or CCSN remnants (*e.g.*, if nucleation occurs before or during the explosion) or from subsequent binary accretion.

Conversely, if nucleation is not reached, the same maximum–mass PNSs cool to $M^{\rm NS} = 1.68$ M$_\odot$ (from t_0) and 1.65 M$_\odot$ (from $t_{T\rm max}$). For the hadronic EOS adopted here, we find $M_{B,\rm max}^{\rm PNS}(t_{T\rm max}) < M_{B,\rm max}^{\rm NS}$; hence every PNS in $t_{T\rm max}$ in our sequences has a cold NS counterpart at the same M_B and can in principle cool stably if deconfinement does not occur. This behavior is, however, model–dependent: for other EOS choices, the reverse

inequality may hold, in which case a sufficiently massive PNS with $M_B^{\rm PNS} > M_{B,\rm max}^{\rm NS}$ would undergo a delayed collapse to a BH unless it converts to a QS. Finally, we note that $M_{B,\rm max}^{\rm PNS}(t_0) > M_{B,\rm max}^{\rm NS}(t_{T\rm max})$. Therefore, if deconfinement does not occur before $t_{T\rm max}$, a PNS born at t_0 with $M_B \simeq M_{B,\rm max}^{\rm PNS}(t_0)$ will undergo a collapse to a BH.

Panel (5.3c) shows the pressure P as a function of the initial *hadronic* baryon density n_B^H (in units of nuclear saturation, $n_0 = 0.1583\,\mathrm{fm}^{-3}$) at $T = 20$ MeV (solid) and $T = 50$ MeV (dashed). Gray curves refer to the hadronic phase, while green (red) curves give the *bulk* pressure of the CFL (unpaired) SQM phase, *i.e.* without surface and Coulomb contributions (see Sec. 4.3.5.4). The labels $Q_*^{\rm unp}$ and $Q_*^{\rm CFL}$ denote quark matter whose thermodynamic state is fixed by matching chemical potentials to those of the hadronic phase at the same (n_B^H, Y_L^H, T): $\mu_i^{Q*} = \mu_i^H$ for $i = B, C, S, e, \nu_e$ (see Sec. 4.3.5.4). Accordingly, $P_{Q_*^{\rm unp}}$ and $P_{Q_*^{\rm CFL}}$ are plotted as a function of n_B^H (the initial hadronic density); the corresponding n_B^{Q*} is not displayed. To avoid overloading notation, throughout this section, we refer to the initial hadronic state as H (denoted $\bar{H}$ in Chapter 4.3).

The more stable (i.e. energetically favorable) phase is thus the one with higher pressure at fixed n_B^H, Y_L^H, and T. In the cases shown, the CFL phase satisfies the Witten hypothesis and is consistently more stable in bulk than the hadronic phase. By contrast, unpaired SQM is more stable only under specific conditions, such as at high n_B^H for fixed T and Y_L^H. The intersections $P_H = P_{Q_*^{\rm unp}}$ mark the bulk onset of the H–$Q_{\rm unp}$ mixed phase. If $\sigma \to 0$, finite-size effects vanish and the transition starts as soon as bulk coexistence is reached. For $\sigma \neq 0$, the critical radius $R_*^{\rm unp}$ diverges at $P_H = P_{Q_*^{\rm unp}}$. When $P_{Q_*^{\rm unp}} > P_H$, the hadronic phase is metastable with respect to $Q_{\rm unp}$, $R_*^{\rm unp}$ is finite, and nucleation of unpaired SQM has a non-zero rate. The slopes of the $Q_*^{\rm unp}$ curves are only slightly steeper than the hadronic ones near the intersections. Using an even more favorable hadronic EOS or a less favorable SQM EOS, the $Q_*^{\rm unp}$ slope could become smaller than the H one, leading to the counterintuitive scenario in which the hadronic phase becomes progressively more stable than the quark phase as n_B^H increases, at least at some densities. For example, this situation arises for $\alpha_s = \frac{\pi}{2} \times 0.3$ (instead of $\frac{\pi}{2} \times 0.1$), which makes the $Q_{\rm unp}$ phase stiffer and therefore less energetically favorable.

Panel (5.3d) shows the n_B^H–T onset of the H–$Q_{\rm unp}$ mixed phase, defined by $P_H = P_{Q_*^{\rm unp}}$, for different Y_L^H. Increasing T shifts the onset to lower n_B^H[4]. At fixed T, decreasing Y_L^H also lowers the onset density, mainly because a smaller Y_L^H implies a reduced Y_C^H, which enhances the hadronic symmetry-energy contribution and disfavors the hadronic phase (see, *e.g.*, [41, 181]).

5.2.3 Role of color–superconductivity

In Fig. 5.4 we report the impact of color superconductivity, within the unp+CFL approach of Sec. 4.3.8, on the energy barrier, the critical radius, and the nucleation

[4]This behavior is not general. For some EOS models and parametrizations, in the low-Y_L^H, low-T regime, the hadronic pressure may not be monotonic with T due to the competition between thermal effects, which tend to increase the pressure, and the population of additional hadronic degrees of freedom, which tends to reduce it. This effect leads to a non-monotonic behavior of the n_B^H onset as a function of T.

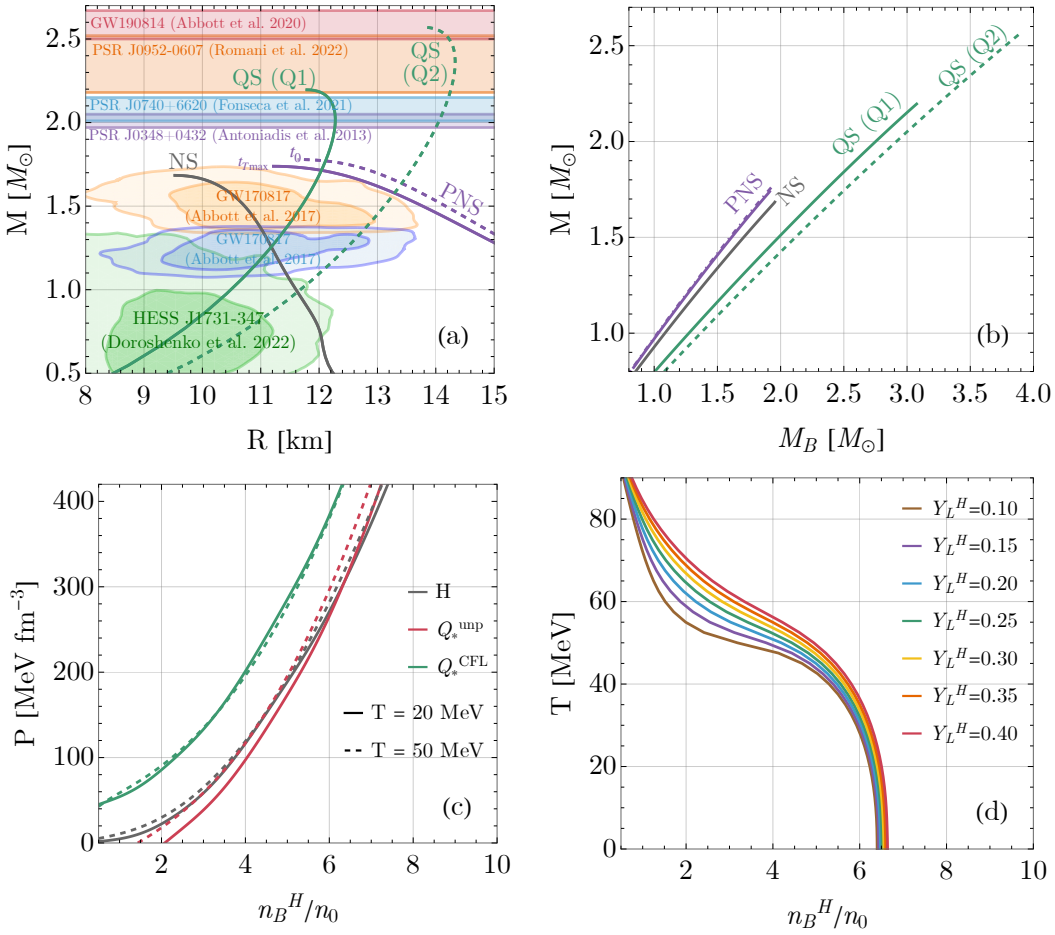

Figure 5.3: (a) Gravitational mass M vs. radius R for NSs, QSs, and PNSs. NSs are in neutrino-less β-equilibrium at $T = 0$, while PNSs are in neutrino-trapped β-equilibrium with isentropic profiles. PNSs configurations are shown in the snapshots t_0 ($Y_L^H = 0.35$, $S_H = 1.5$) and $t_{T\max}$ ($Y_L^H = 0.25$, $S_H = 2.0$). QSs are bare, at $T = 0$, and in the CFL phase. Two parametrizations are shown: Q1 with $B_{\rm CFL}^{1/4} = 145$ MeV and Q2 with $B_{\rm CFL}^{1/4} = 135$ MeV. Observational constraints are indicated [11, 13, 15, 18, 19, 76].
(b) Gravitational mass M vs. baryonic mass M_B for the same configurations as in panel (a).
(c) Pressure P vs. hadronic baryon density n_B^H in units of nuclear saturation density n_0 at fixed $Y_L^H = 0.25$. Gray: hadronic phase (H); red: unpaired SQM phase ($Q_*^{\rm unp}$); green: CFL SQM phase ($Q_*^{\rm CFL}$) with $B_{\rm CFL}^{1/4} = 145$ MeV. Solid (dashed) lines correspond to $T = 20$ MeV ($T = 50$ MeV). For Q_* phases, the x-axis is n_B^H, not n_B^{Q*} (see text).
(d) Onset of the H–$Q_{\rm unp}$ mixed phase ($P_H = P_{Q_*^{\rm unp}}$) in the n_B^H–T plane for different Y_L^H. In all panels $B_{\rm unp}^{1/4} = 178$ MeV.

time. We fix in this section $B_{\rm unp}^{1/4} = 178$ MeV, $\Delta_0 = 80$ MeV, and $\sigma = 30$ MeV fm^{-2}. A systematic analysis of parameter dependence is given in Sec. 5.2.5. Throughout this section, unless specified, results are shown at fixed $Y_L^H = 0.25$; its role will be discussed in Sec. 5.2.4.

Panel (5.4a) shows the work W required to generate a SQM droplet (Eq. 4.64) as a function of its radius R, for $n_B^H = (6.0,\, 7.2,\, 8.0)\, n_0$ at fixed T. Dotted lines correspond to the CFL-only case ($P_{Q*} \mapsto P_{Q_*^{\rm CFL}}$), dashed lines to the unpaired-only case ($P_{Q*} \mapsto P_{Q_*^{\rm unp}}$), and solid lines to the unp+CFL case (Eq. 4.150). For $R < R_\Delta = 1/\Delta$, the droplet is unpaired, since diquark pairs cannot form, and the unp+CFL curve coincides with the unpaired one. When $R > R_\Delta$, the droplet can sustain diquark pairs, so the curve follows the CFL case.

The maximum of $W(R)$ corresponds to the saddle–point configuration, *i.e.* a hadronic medium containing a critical droplet of radius R_*, with $W_* \equiv W(n_B^H, Y_L^H, T, R_*)$ representing the energy barrier. The critical radius in the CFL case ($R_*^{\rm CFL}$) is always smaller than in the unpaired case ($R_*^{\rm unp}$). Two regimes emerge: if $R_*^{\rm unp} < R_\Delta$, the droplet nucleates in the unpaired phase ($R_* = R_*^{\rm unp}$, *e.g.* $n_B^H = 8.0\, n_0$). If $R_*^{\rm unp} > R_\Delta$, the barrier is reached exactly at $R = R_\Delta$, where pairing sets in ($R_* = R_\Delta$, *e.g.* $n_B^H = 7.2\, n_0$). At $n_B^H = 6.0\, n_0$, $T = 20$ MeV, H is stable with respect to $Q_{\rm unp}$, so no $R_*^{\rm unp}$ exists (dashed blue curve rises monotonically). Nevertheless, in the unp+CFL framework, nucleation can still occur when the CFL phase appears at $R = R_\Delta$.

At fixed R, $W \propto (P_H - P_{Q*})$ decreases with increasing n_B^H, leading to smaller W_* even when R_* is unchanged (*e.g.* $n_B^H = 6.0\, n_0$ and $7.2\, n_0$). The same trend occurs for increasing T or decreasing Y_L^H, with the exceptions noted in Sec. 5.2.2. For details, see also [46].

Panel (5.4b) displays the critical radius in the unp+CFL (R_*) and unpaired-only ($R_*^{\rm unp}$) cases as a function of n_B^H/n_0, for $T = (10 - 60)$ MeV. In the unpaired-only case, $R_*^{\rm unp}$ decreases with both T and n_B^H, and diverges at the mixed-phase onset line ($P_{Q_*^{\rm unp}} = P_H$). The $R_\Delta(T) = 1/\Delta(T)$ instead increases with T. At high n_B^H, $R_*^{\rm unp}$ is small, so that $R_*^{\rm unp} < R_\Delta$ and the unp+CFL result coincides with the unpaired one ($R_* = R_*^{\rm unp}$). The same regime is found at high T, since R_Δ becomes large. Above the critical temperature $T_c^{\rm CFL} = 2^{1/3} \cdot 0.57\, \Delta_0$ (57 MeV for $\Delta_0 = 80$ MeV), $\Delta(T) \to 0$, $R_\Delta \to \infty$, and the CFL phase vanishes, so that $R_* = R_*^{\rm unp}$. At low n_B^H and T, instead, $R_*^{\rm unp} > R_\Delta$ and thus $R_* = R_\Delta$, which in this regime grows with T.

Panel (5.4c) shows W_*/T (the exponential suppression factor in Eq. 4.135) with the same layout as panel (5.4b). At high n_B^H and T, $W_* = W(R_*^{\rm unp})$, while at low n_B^H and/or T, $W_* = W(R_\Delta)$. In the former case, W_* decreases with n_B^H both explicitly and through the density dependence of R_*, whereas in the latter the critical radius no longer scales with n_B^H, so that $W_*(n_B^H)$ decreases more rapidly in the former case than in the latter. At low n_B^H, W_*/T does not vary monotonically with T; this behavior will be discussed later in this section for τ.

Panel (5.4d) shows the thermal nucleation time τ (*i.e.*, the typical timescale after which the energy barrier is overcome and a spontaneous thermal fluctuation produces a critical SQM droplet) as a function of temperature T, for different baryon densities of the hadronic phase $n_B^H = (2-8)\, n_0$. Although the plot spans many orders of magnitude

in τ for clarity, the physically relevant range is $10^{-4}\,\mathrm{s} \lesssim \tau \lesssim 10^{17}\,\mathrm{s}$, corresponding respectively to the dynamical timescale of astrophysical events and to the age of the Universe.

As discussed for R_* and W_*/T, at high n_B^H and/or high T, the critical radius is reached before diquark pairing sets in, so the unp+CFL result converges to the unpaired-only case. In the unpaired-only scenario, τ decreases steeply with increasing n_B^H and T: for instance, at $n_B^H/n_0 = 6$, τ changes from 10^{17} s to 10^{-4} s within $\Delta T \simeq 0.7$ MeV.

In the unp+CFL framework (solid lines), when $R_* = R_\Delta \neq R_*^{\mathrm{unp}}$ the nucleation time decreases less rapidly[5] with T at fixed n_B^H. The reason is that in the $R_* = R_*^{\mathrm{unp}}$ regime, increasing T reduces τ both directly and indirectly through the decrease of R_*. By contrast, in the $R_* = R_\Delta = 1/\Delta$ regime, increasing T reduces τ directly but increases it indirectly, since $\Delta(T)$ decreases with T (Eq. 2.77), enlarging R_Δ, raising W_*/T, and thus increasing τ. As a consequence, at low n_B^H the nucleation time, as well as W_*/T, is not a monotonic function of T: beyond a certain temperature, further heating increases τ because the suppression of pairing dominates over the direct thermal enhancement of nucleation (see purple and blu lines, $n_B^H = (2-5)n_0$, in panel 5.4d).

Finally, when T approaches the critical temperature of the CFL phase, T_c^{CFL}, the gap vanishes ($\Delta(T) \to 0$), $R_\Delta \to \infty$, and the unp+CFL result smoothly converges to the unpaired-only one. At high n_B^H, this non-monotonic disappears, since $R_* = R_*^{\mathrm{unp}}$ is already realized at relatively small T, before the increase in τ due to the shrinking gap becomes significant.

5.2.4 Nucleation conditions

Figure 5.5 shows the nucleation conditions (see Sec. 5.1.2), *i.e.*, the values of temperature T and baryon density n_B^H for a given lepton fraction Y_L^H in the initial hadronic phase at which the nucleation time τ equals the astrophysical dynamical timescale τ_{dyn}. By definition, these curves represent the minimum nucleation temperature at fixed n_B^H and Y_L^H: all points with T above the lines correspond to nucleation conditions.

The two panels correspond to $Y_L^H = 0.25 - 0.35$ ($t_{T\mathrm{max}}$ and t_0 respectively), while different colors represent various B_{unp} parameters. Solid lines show the results within the unp+CFL framework, dashed lines those in the unpaired-only case, and purple dot-dashed lines mark isoentropic ($S_H = 1, 1.5, 2$) trajectories of the initial hadronic phase.

The qualitative behavior of the nucleation lines (at fixed Y_L^H, B_{unp}, Δ_0, and σ) reflects the discussion of the $\tau(T)$ dependence in Fig. 5.4d. It can be summarized as follows:

(i) At low n_B^H (*e.g.*, $2\,n_0$ in Fig. 5.4d), $\tau(T)$ is non-monotonic and has a local minimum at $\tau > \tau_{\mathrm{dyn}}$. In this regime, the only solution to $\tau(T) = \tau_{\mathrm{dyn}}$ corresponds to the unpaired-only case, *i.e.*, $R_* = R_*^{\mathrm{unp}}$.

[5] Nevertheless, the variation remains sufficiently steep that defining the nucleation condition by comparing τ with the dynamical timescale or with any other PNS-relevant timestep does not affect the results qualitatively; see Sec. 5.1.2.

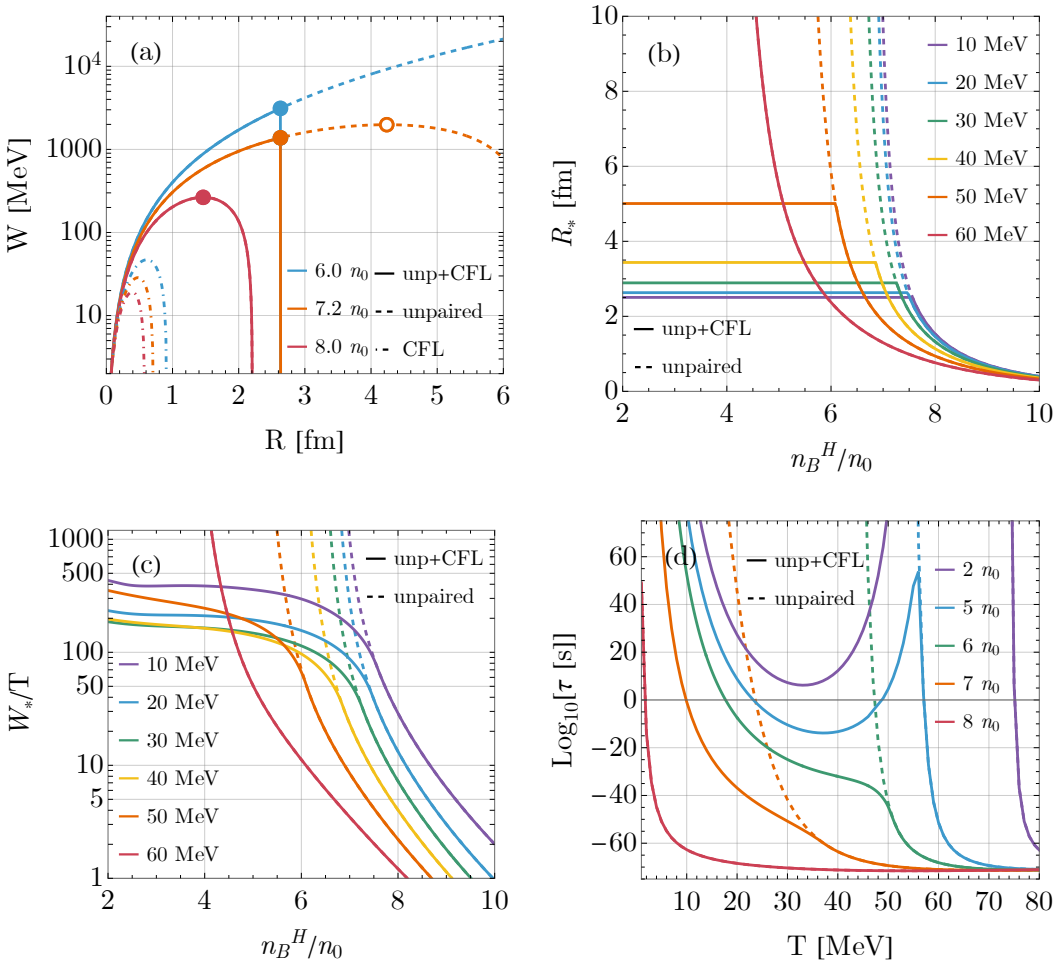

Figure 5.4: (a) Work $W(R)$ to generate a SQM droplet. Solid: unp+CFL (Sec. 4.3.8); dashed: unpaired only; dotted: CFL only. Filled (open) circles mark R_* ($R_*^{\rm unp}$). For $n_B^H = 6\,n_0$, H is stable against $Q_{\rm unp}$, so no $R_*^{\rm unp}$ exists, while for $n_B^H = 8\,n_0$ $R_* = R_*^{\rm unp}$.
(b) Critical radius R_* vs. n_B^H for different T. Solid: unp+CFL (R_*); dashed: unpaired only ($R_*^{\rm unp}$).
(c) Energy barrier over temperature, W_*/T, vs. n_B^H.
(d) Nucleation time τ vs. T, for different n_B^H.
All panels assume $Y_L^H = 0.25$, $\sigma = 30$ MeV fm^{-2}, $\Delta_0 = 80$ MeV, and $B_{\rm unp}^{1/4} = 178$ MeV.

(ii) At slightly higher n_B^H (*e.g.*, $5\,n_0$ in Fig. 5.4d), the local minimum of $\tau(T)$ lies below $\tau_{\rm dyn}$, so $\tau = \tau_{\rm dyn}$ may be satisfied at three temperatures. In this case we select the lowest-T solution, which corresponds to $R_* = R_\Delta$. The discontinuity in the $T(n_B^H)$ curves occurs at the n_B^H value where the minimum of $\tau(T)$ exactly touches $\tau = \tau_{\rm dyn}$.

(iii) At intermediate n_B^H (*e.g.*, $6 - 7\,n_0$ in Fig. 5.4d)), $\tau(T)$ becomes monotonically decreasing, and the unique solution of $\tau(T) = \tau_{\rm dyn}$ corresponds to $R_* = R_\Delta$.

(iv) At high n_B^H (*e.g.*, $8\,n_0$ in Fig. 5.4d), the critical radius is reached before diquark pairing sets in, so the unp+CFL results converge again to the unpaired-only case, $R_* = R_*^{\rm unp}$.

Thus, in regimes (i) and (iv) we are in the $R_*^{\rm unp} < R_\Delta$ regime, so the critical droplet coincides with the unpaired solution, $R_* = R_*^{\rm unp}$. At low densities this is driven by the large temperature required for nucleation (implying small or vanishing pairing gaps Δ and therefore large or diverging R_Δ), while at high densities it arises from the very small $R_*^{\rm unp}$. In contrast, in regimes (ii) and (iii) we find $R_*^{\rm unp} \geq R_\Delta$, so the critical radius is determined by the onset of diquark pairing, $R_* = R_\Delta$. In these regimes, the color-superconducting phase substantially reduces the nucleation temperature compared to the unpaired-only case.

As Y_L^H increases, both T and/or n_B^H required for nucleation also increase. This trend is associated with the rise in Y_C^H accompanying larger Y_L^H, which increases the hadronic symmetry energy and disfavors the hadronic phase (see Fig. 5.3d).

The bag constant $B_{\rm unp}$ also plays an important role: larger $B_{\rm unp}$ reduces P_{Q*}, increases W_* and τ, and thus raises the nucleation temperature at fixed n_B^H and Y_L^H.

The dependence on surface tension σ is more subtle. In the regime where $R_* = R_\Delta$, W_* depends on σ only directly, since R_* is fixed by $\Delta(T)$. In the regime $R_* = R_*^{\rm unp}$, however, W_* depends both explicitly on σ and implicitly through $R_*(\sigma)$.[6]

Finally, increasing Δ_0 reduces R_Δ and raises $T_c^{\rm CFL}$, thereby widening the range of densities where $R_* = R_\Delta$. It also reduces W_*, which in turn lowers the nucleation temperature at fixed n_B^H, Y_L^H. The explicit impact of varying Δ_0 and σ is not shown in Fig. 5.5, but will be analyzed systematically in Sec. 5.2.5.

As emphasized in [46], along the nucleation boundary condition line, the exponential factor is typically $W_*/T \sim (150 - 180)$, yielding extremely small local nucleation probabilities. Nevertheless, the nucleation rate remains astrophysically relevant because of the very large prefactor and the macroscopic volume of the system. In practice, even a single nucleation event within the central region could be sufficient to trigger deconfinement.

[6] See [46] for an analytical discussion of the σ dependence in the two regimes.

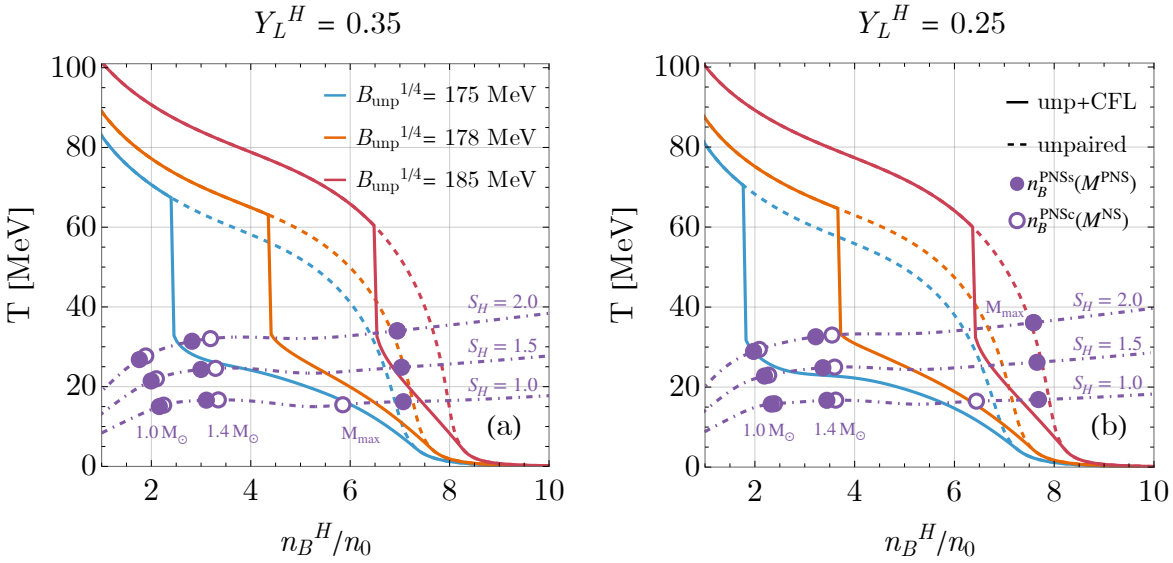

Figure 5.5: Temperature T and baryon density in the hadronic phase n_B^H (in units of n_0) at which the nucleation timescale equals the dynamical timescale, $\tau = \tau_{\rm dyn} = 10^{-4}$ s. These points define the nucleation conditions, *i.e.*, the (n_B^H, Y_L^H, T) values at which deconfinement is triggered. Each panel corresponds to a different lepton fraction: (a) $Y_L^H = 0.35$ as in t_0; (b) $Y_L^H = 0.25$ as in $t_{T\rm max}$. Colors indicate $B_{\rm unp}^{1/4}$. Solid lines: unp+CFL framework (Sec. 4.3.8); dashed lines: unpaired-only case. Purple dot-dashed curves: isoentropic trajectories of the hadronic phase. Purple filled dots: central conditions of PNSs with entropy S_H, corresponding (from left to right) to gravitational masses of 1.0 M$_\odot$, 1.4 M$_\odot$, and the maximum-mass configuration $M_{\rm max}^{\rm PNS}(Y_L^H, S_H)$. Purple empty dots: central conditions of PNSs with the same baryonic mass as cold NSs in neutrino-less β-equilibrium, with gravitational masses (from left to right) 1.0 M$_\odot$, 1.4 M$_\odot$, and the maximum-mass NS $M_{\rm max}^{\rm NS} = 1.68$ M$_\odot$. The empty dots for $S_H = 1.5, 2$ are not shown since $M_{B,\rm max}^{\rm PNS} < M_{B,\rm max}^{\rm NS}$. Parameters: $\Delta_0 = 80$ MeV, $\sigma = 30$ MeV fm^{-2}.

5.2.5 Conversion of PNSs and NS–QS coexistence

We now compare the nucleation conditions discussed above with the central conditions of PNSs.

In Fig. 5.5, the purple dot-dashed lines show the temperatures of the initial hadronic phase at fixed entropy per baryon, $S_H = (1, 1.5, 2)$. Solid purple dots mark the central conditions (n_B^H, T) of PNSs with gravitational masses $M^{\rm PNS} = (1.0, 1.4, M_{\rm max}^{\rm PNS})$ $\rm M_\odot$, where the last point corresponds to the maximum-mass configuration. Open dots mark PNSs that have the same baryonic mass as cold NSs with $M^{\rm NS} = (1.0, 1.4, M_{\rm max}^{\rm NS})$ $\rm M_\odot$, where $M_{\rm max}^{\rm NS} = 1.68$ $\rm M_\odot$. Thus, for example, if a PNS has central conditions corresponding to the open dot at 1.4 $\rm M_\odot$, it will eventually cool and deleptonize into a 1.4 $\rm M_\odot$ NS provided nucleation does not occur.

Let us examine the two representative evolutionary snapshots, t_0 and $t_{T\rm max}$ (see Sec. 5.2.1), fixing $\sigma = 30$ MeV fm^{-2} and $\Delta_0 = 80$ MeV as in Fig. 5.5.

At t_0 ($S_H = 1.5$, $Y_L^H = 0.35$; Fig. 5.5a), the nucleation criterion is satisfied for PNSs whose gravitational mass exceeds $M^{\rm PNS} \gtrsim (1.59,\ 1.75,\ 1.78)$ $\rm M_\odot$ for $B_{\rm unp}^{1/4} = (175,\ 178,\ 185)$ MeV, respectively. Thus, for a given $B_{\rm unp}$, PNSs above the quoted mass convert to QSs already in this first snapshot, whereas lighter objects continue their PNS evolution.

At $t_{T_{\rm max}}$ ($S_H = 2$, $Y_L^H = 0.25$; Fig. 5.5b), conditions are *most favorable* to deconfinement (the nucleation density is minimal), so survival as a hadronic star is correspondingly more constrained. For all shown values $B_{\rm unp}^{1/4} = (175, 178, 185)$ MeV, nucleation is triggered in part of the sequence. As an example, for $B_{\rm unp}^{1/4} = 178$ MeV, PNSs with $M^{\rm PNS} \gtrsim 1.51$ $\rm M_\odot$ convert to QSs, while lighter PNSs cool into NSs; in this case the most massive surviving NSs have $M^{\rm NS} \simeq 1.43$ $\rm M_\odot$. For smaller $B_{\rm unp}$, conversion sets in at even lower masses, leaving only low–mass NSs as survivors.

With the used hadronic EOS parametrization, the maximum baryonic mass of a PNS, evaluated both at birth and at the time of peak temperature, satisfies $M_{B,\rm max}^{\rm PNS}(t_0 \text{ and } t_{T_{\rm max}}) < M_{B,\rm max}^{\rm NS}$. Consequently, every PNS admits a cold, stable NS configuration with the same baryonic mass, into which it can cool provided that SQM nucleation is not triggered.

Since $t_{T_{\rm max}}$ corresponds to the epoch of maximum central temperature (and hence to the lowest nucleation density over the entire PNS evolution), the prospects for NS survival are essentially determined at this stage.

To formalize this, let $\tilde{M}$ be the gravitational mass of the PNS at $t_{T\rm max}$ whose central density $\tilde{n}_B^H$ lies exactly on the nucleation line, namely the crossing point between one of the solid lines and the $S = 2$ purple dot-dashed line in panel 5.5b. Namely, a PNS in $t_{T\rm max}$ with a mass $M^{\rm PNS} = M_x$ will convert into a QS if $M_x \geq \tilde{M}$ (or, equivalently, $n_{B,\rm c}^H(M_x, t_{T\rm max}) > \tilde{n}_B^H$, where $n_{B,\rm c}^H(M_x, t_x)$ is the baryon density in the center of a PNS with mass M_x at the conditions of the snapshot t_x). We further define $M_{t_x}^{\rm PNS}(M^{\rm NS} = M_x)$ as the gravitational mass of the PNS (evaluated at $t_x = t_0$, $t_{T\rm max}$) that has the same baryonic mass as NS of gravitational mass M_x. Namely, $M_{t_{T\rm max}}^{\rm PNS}(M^{\rm NS} = 1.0\ \rm M_\odot)$, $M_{t_{T\rm max}}^{\rm PNS}(M^{\rm NS} = 1.4\ \rm M_\odot)$, and $M_{t_{T\rm max}}^{\rm PNS}(M^{\rm NS} = M_{\rm max}^{\rm NS})$ denote the masses of the PNSs whose central conditions correspond to the empty dots in Fig. 5.5.

Parameters	PNS at t_0				PNS at $t_{T\max}$			Remnant		
	$M^{\rm PNS}$ [$\mathrm{M}_\odot$]	$M_B^{\rm PNS}$ [$\mathrm{M}_\odot$]	$n_{B,c}^H$ [n_0]	$Y_{S,c}^H$	$M^{\rm PNS}$ [$\mathrm{M}_\odot$]	$n_{B,c}^H$ [n_0]	$Y_{S,c}^H$	type	M [$\mathrm{M}_\odot$]	$E_{\rm conv}$ [$\times 10^{53}$ erg]
$B_{\rm unp}^{1/4} = 185$ MeV	1.40	1.48	3.00	0.01	1.39	3.19	0.03	NS	1.32	–
$B_{\rm unp}^{1/4} = 185$ MeV	1.60	1.72	3.85	0.03	1.59	4.26	0.07	NS	1.51	–
$B_{\rm unp}^{1/4} = 178$ MeV	1.40	1.48	3.00	0.01	1.39	3.19	0.03	NS	1.32	–
$B_{\rm unp}^{1/4} = 178$ MeV	1.60	1.72	3.85	0.03	1.59	4.26	0.07	QS	1.32	4.82
$B_{\rm unp}^{1/4} = 175$ MeV	1.40	1.48	3.00	0.01	1.39	3.19	0.03	QS	1.15	4.33
$B_{\rm unp}^{1/4} = 175$ MeV	1.60	1.72	3.85	0.03	–	–	–	QS	1.32	4.82

Table 5.1: Some possible outcomes of the PNS evolution given the parameters and the initial PNS mass at t_0 ($Y_L^H = 0.35$, $S_H = 1.5$). The mass, baryonic mass, central baryon density and central strangeness fraction are shown for the PNS at t_0. If the PNS remains a PNS until $t_{T\max}$ ($Y_L^H = 0.25$, $S_H = 2.0$), its mass, central baryon density and central strangeness fraction in this stage are shown. Finally, the outcome object type, its mass and the conversion energy are reported. In case of conversion the mass of the QS is computed using parametrization Q1; results for Q2 are visible in Fig. 5.3. We fix $\Delta_0 = 80$ MeV and $\sigma = 30$ MeVfm^{-2}.

The evolutionary outcomes are then classified by comparing $\tilde{M}$ with these PNS reference masses:

- If $\tilde{M} < M_{t_{T\max}}^{\rm PNS}(M^{\rm NS} \simeq 1.0\,\mathrm{M}_\odot)$: all relevant[7] PNSs lie above the nucleation line and convert to QSs (no NSs survive).
- If $M_{t_{T\max}}^{\rm PNS}(M^{\rm NS} = 1.0\,\mathrm{M}_\odot) \leq \tilde{M} \leq M_{t_{T\max}}^{\rm PNS}(M^{\rm NS} = M_{\rm max}^{\rm NS})$: PNSs with $M^{\rm PNS} < \tilde{M}$ cool into NSs with the same baryonic mass, while those with $M^{\rm PNS} \geq \tilde{M}$ convert into QSs.
- If $M_{t_{T\max}}^{\rm PNS}(M^{\rm NS} = M_{\rm max}^{\rm NS}) < \tilde{M} \leq M_{\rm max}^{\rm PNS}$: PNSs with $M^{\rm PNS} \geq \tilde{M}$ convert into QSs, while lighter ones ($M^{\rm PNS} < \tilde{M}$) collapse into BHs if $M^{\rm PNS} > M_{t_{T\max}}^{\rm PNS}(M^{\rm NS} = M_{\rm max}^{\rm NS})$ or cool into NSs otherwise. However, with the used hadronic EOS parametrization, there are not PNSs respecting this condition.
- If $\tilde{n}_B^H > n_{B,\rm c}^H(M_{\rm max}^{\rm PNS}, t_{T\max})$ all PNSs evolve either into NSs (if $M^{\rm PNS} \leq M_{t_{T\max}}^{\rm PNS}(M^{\rm NS} = M_{\rm max}^{\rm NS})$) or into BHs (if $M^{\rm PNS} > M_{t_{T\max}}^{\rm PNS}(M^{\rm NS} = M_{\rm max}^{\rm NS})$). In this case the QS branch cannot be populated directly by PNS evolution, but only through other processes (*e.g.* accretion, BNS mergers, CCSNe).

In this language, a parameter choice is *compatible with NS–QS coexistence* if $\tilde{M} \geq M_{t_{T\max}}^{\rm PNS}(M^{\rm NS} = 1.0\,\mathrm{M}_\odot)$. If one further requires that canonical 1.4 $\mathrm{M}_\odot$ compact stars be realizable as NSs, then the stronger condition $\tilde{M} \geq M_{t_{T\max}}^{\rm PNS}(M^{\rm NS} = 1.4\,\mathrm{M}_\odot)$ must be satisfied. In Table 5.1, the details of some possible scenarios are discussed, given the parameters and the PNS mass.

[7] Stable NSs with gravitational mass $\lesssim 1.17$ $\mathrm{M}_\odot$ are not expected astrophysically [86].

Finally, let us discuss the impact of the free parameters on the issue of NS–QS coexistence.

In Fig. 5.6 we show the values of the surface tension σ and of $B_{\rm unp}^{1/4}$ at which the nucleation line intersects the central densities of PNSs. The dot-dashed, dashed, and solid curves correspond respectively to $\tilde{M} = M_{t_x}^{\rm PNS}(M^{\rm NS} = 1.0\ {\rm M}_\odot)$, $\tilde{M} = M_{t_x}^{\rm PNS}(M^{\rm NS} = 1.4\ {\rm M}_\odot)$, and $\tilde{M} = M_{\rm max}^{\rm PNS}(t_x)$. Results are shown for two values of the pairing gap, $\Delta_0 = (80, 120)$ MeV (blue and orange curves, respectively). Panel 5.6b corresponds to the snapshot $t_x = t_{T\rm max}$, which is the most relevant one for NS–QS coexistence, while panel 5.6a refers to $t_x = t_0$.

The green (gray) dot-dashed line indicates the upper bound of $B_{\rm unp}$ for which three-flavor (two-flavor) unpaired quark matter is absolutely stable, namely $E/A_{Q_{\rm unp}} < E/A_{^{56}{\rm Fe}}$ ($E/A_{Q_{\rm unp}^{\rm 2flav}} < E/A_{^{56}{\rm Fe}}$). Thus, if $B_{\rm unp}^{1/4} > 154$ MeV (above the green line), unpaired quark matter does not fulfill the Witten hypothesis, even if the CFL phase does.

At fixed σ, the classification is as follows:

- If $B_{\rm unp}$ lies above the solid line, nucleation is never reached during the PNS evolution, and remnants can only be NSs or BHs. In this case, QSs must be formed via other channels (*e.g.* accretion, BNS mergers, CCSNe).
- If $B_{\rm unp}$ is between the solid and dashed lines, remnants can be either QSs or NSs with masses up to $1.4 - M_{\rm max}^{\rm NS}$ [8] .
- If $B_{\rm unp}$ is between the dashed and dot-dashed lines, only light NSs (with masses up to $1.0 - 1.4\ {\rm M}_\odot$) or QSs can survive.
- If $B_{\rm unp}$ lies below the dot-dashed line, all PNSs convert into QSs and no NSs exist.

The pairing gap Δ_0 has a crucial role: a larger Δ_0 corresponds to a smaller R_Δ, allowing nucleation to occur at lower densities and temperatures. Consequently, higher values of $B_{\rm unp}$ and/or σ are required to maintain NS–QS coexistence when Δ_0 increases.

In this work, we have allowed the unpaired and CFL phases to have different bag parameters. Within this framework, nucleation conditions are controlled by $B_{\rm unp}, \sigma$, and Δ_0, but not by $B_{\rm CFL}$. Conversely, the final mass of a CFL QS depends only on $B_{\rm CFL}$ and Δ_0 (with $M^{\rm QS}$ increasing for smaller $B_{\rm CFL}$ and larger Δ_0). If one enforces $B_{\rm unp} = B_{\rm CFL}$, the parameter space compatible with NS–QS coexistence shrinks considerably, since large σ values are then required. In particular, the interplay of parameters can be summarized as follows: at fixed σ, a large $B_{\rm CFL} = B_{\rm unp}$ requires a large Δ_0 to satisfy the $> 2\ {\rm M}_\odot$ observational constraint. However, such a large Δ_0, similarly to a small $B_{\rm CFL} = B_{\rm unp}$, facilitates nucleation, so that large σ is needed to prevent the

[8] With the hadronic EOS parametrization adopted here, the maximum baryonic mass of a cold NS exceeds that of a hot PNS, $M_{B,\rm max}^{\rm NS} > M_{B,\rm max}^{\rm PNS}(t_0$ and $t_{T\rm max})$. Hence any PNS can, in principle, cool to a stable NS with the same M_B if deconfinement does not occur. For other parametrizations the reverse inequality may hold; in that case there exists a region in the parameter space in which the nucleation conditions are not reached for $M_B^{\rm PNS} > M_{B,\rm max}^{\rm NS}$ PNS and they would thus collapse to BHs.

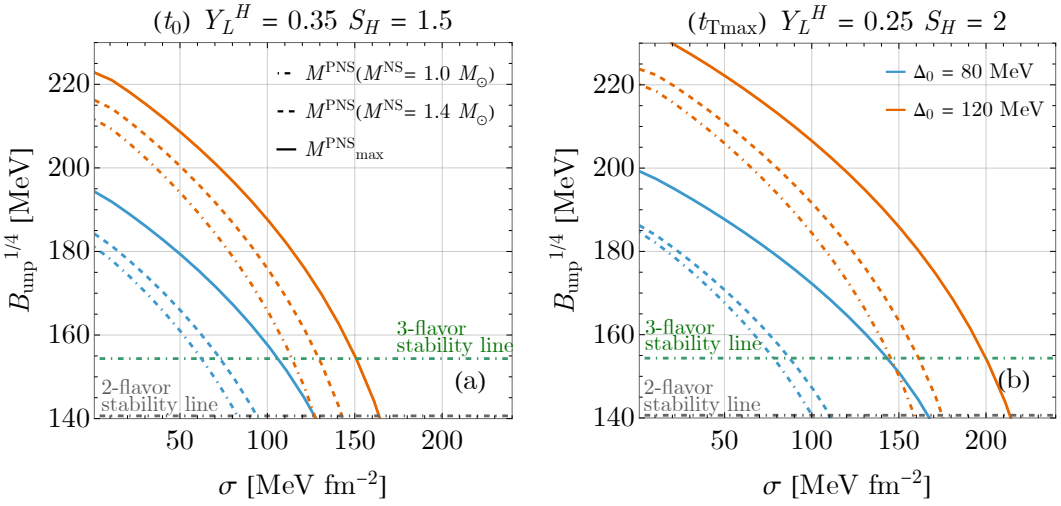

Figure 5.6: Parameter space in terms of $B_{\rm unp}^{1/4}$ and σ for two gap values, $\Delta_0 = 80$ MeV (blue) and 120 MeV (orange), at which the nucleation conditions are satisfied in the center of a PNS. Dot-dashed, dashed, and solid curves correspond to the cases where the nucleation line passes through $M^{\rm PNS}(M^{\rm NS} = 1.0\ {\rm M}_\odot)$, $M^{\rm PNS}(M^{\rm NS} = 1.4\ {\rm M}_\odot)$, and $M^{\rm PNS}_{\rm max}$. Panel (a) corresponds to $Y_L^H = 0.35$, $S_H = 1.5$ (the snapshot t_0), while (b) corresponds to $Y_L^H = 0.25$, $S_H = 2$ (the snapshot $t_{T\rm max}$, *i.e.* maximum central temperature). Since the $t_{T\rm max}$ snapshot is the most favorable for nucleation, some general constraints follow: at fixed σ, if $B_{\rm unp}^{1/4}$ lies below the dot-dashed line, no NSs with $M^{\rm NS} > 1.0\ {\rm M}_\odot$ can survive PNS evolution (all convert into QSs), while if it lies above the solid line, no QSs can be generated from hadronic PNSs. See the text for a complete discussion. The gray (green) dot-dashed curves indicate the stability boundaries for two-flavor (three-flavor) unpaired quark matter, corresponding to $E/A_{Q_{\rm unp}} = E/A_{^{56}{\rm Fe}}$.

conversion of all PNSs. For instance, consider the parametrizations of Fig. 5.3: (Q1) $B_{\rm CFL}^{1/4} = 145$ MeV, $\Delta_0 = 80$ MeV and (Q2) $B_{\rm CFL}^{1/4} = 135$ MeV, $\Delta_0 = 80$ MeV. Case (Q1), which yields $M^{\rm QS}_{\rm max} \simeq 2.20\ {\rm M}_\odot$, is compatible with $B_{\rm unp} = B_{\rm CFL}$ only if $\sigma \gtrsim 96$ MeVfm^{-2} (or $\gtrsim 107$ MeVfm^{-2} if 1.4 $\rm M_\odot$ NSs are required). Case (Q2), which yields $M^{\rm QS}_{\rm max} = 2.57\ {\rm M}_\odot$, is incompatible with $B_{\rm unp} = B_{\rm CFL}$ since it falls below the two-flavor stability line. This line could in principle be lowered by increasing α_s (here fixed to $\alpha_s = \pi/2 \times 0.1$), but larger α_s values are incompatible with the hadronic EOS used (see Sec. 5.2.2 and Fig. 5.3d), at least with the used approach for nucleation.

In conclusion, if σ is not sufficiently large, NS–QS coexistence requires $B_{\rm unp} > B_{\rm CFL}$, *i.e.* the CFL phase must be significantly more energetically favored than the unpaired phase. Possible microscopic explanations for different bag constants in the unpaired and CFL phases will be explored in future work, by computing both the bag and the gap consistently rather than treating them as free parameters. For instance, [21, 91] find different effective values of B for different Δ_0, by computing the color-superconducting phase within an NJL-like model and then mapping it onto a Bag-like parametrization [66].

5.3 QS formation from mass accretion

In this section, we briefly present some preliminary results obtained with the reduced–volume approach introduced in Sec. 4.3.4.3, and discuss their implications for nucleation in cold NSs, *e.g.* triggered by mass accretion from a companion or from the ejecta of a supernova explosion in the same binary system (see Sec. 5.4).

The questions we would like to address are the following. First, does the reduced–volume approach (which encodes the possibility that some thermodynamically allowed configurations are kinematically inaccessible because charge diffusion is inefficient on the relevant timescales) significantly modify the fluctuation–assisted approach (which, as discussed in Sec. 4.3.4.2, converges to strong chemical equilibrium)? Second, can some NSs that do not convert during the PNS evolution later convert when they are cold ($T \simeq 0$) due to mass accretion? If a viable parameter space exists, conversion in cold NSs is, in principle, possible.

In what follows, we restrict to a qualitative discussion of the impact of the finite–volume prescription and present some first hints on its application to nucleation in accreting cold NSs. A detailed analysis, including a full account of the role of color superconductivity and a complete parameter study, is deferred to future work.

Following Sec. 4.3.4.3, let us assume that the strong–conserved charges that can participate in nucleation, either via exchange during droplet formation or via prior composition fluctuations in the hadronic medium, are those contained in an effective *reduced volume* $V_{\rm r.v.} = V_{\rm r.v.}^{(k)}$ ($k = B, C, S, \mathrm{mec}$), taken for simplicity to be the same for baryon number, non–leptonic charge, strangeness and mechanical readjustment.

A possible natural way to relate $V_{\rm r.v.}$ to microphysics is to connect it to the diffusion length ℓ_D of the conserved charges, *i.e.*

$$V_{\rm r.v.} = \frac{4}{3}\,\pi\,\ell_D^3\,. \tag{5.5}$$

As discussed in Sec. 4.3.4.3, ℓ_D depends on both the diffusion coefficient D_i of the conserved charge i and on the time Δt available for diffusion, $\ell_D = \sqrt{D_i \Delta t}$. In [219] diffusion coefficients for strong–conserved charges were computed in a region of the phase diagram characterized by relatively high T and moderate μ, from which one can extrapolate an effective $\kappa_i = \frac{\partial n_i}{\partial(\mu_i/T)} D_i \sim (10^{-2}\text{–}10^{-1})\,T^2$ for $i = B, C, S$. Although extrapolation to the conditions of interest here is uncertain, this estimate is sufficient to show that the relevant uncertainty lies mainly in the choice of Δt.

Two timescales are in principle available: (i) the lifetime of a single deconfined droplet in a confined medium, $\Delta t \sim 10^{-23}\text{–}10^{-20}\,\mathrm{s}$, and (ii) the dynamical evolution time of the macroscopic system, $\Delta t \sim 10^{-4}\,\mathrm{s}$, over which the bulk thermodynamic variables remain approximately constant and composition fluctuations in the hadronic phase can develop. For the same D_i, these choices span diffusion lengths from $\ell_D \lesssim 1$ fm up to $\ell_D \sim 10^{10}$ fm. A full microphysical treatment would be required to determine which timescale is appropriate in different regimes; here we simply explore how different ℓ_D (or, equivalently, different reduced volumes) affect the nucleation conditions.

For convenience we introduce the dimensionless parameter

$$\chi \equiv \frac{V_{Q*}}{V_{\mathrm{r.v.}}} = \frac{R_{Q*}^3}{\ell_D^3}\,, \tag{5.6}$$

where V_{Q*} and R_{Q*} are the volume and radius of the critical quark droplet.

Within the reduced–volume prescription, the strong–conserved charges contained in $V_{\mathrm{r.v.}}$ obey

$$N_B^{Q*} + N_B^{H\vartheta} = N_B^{\mathrm{r.v.}} = V_{\mathrm{r.v.}}\, n_B^H\,, \tag{5.7}$$
$$N_C^{Q*} + N_C^{H\vartheta} = N_C^{\mathrm{r.v.}} = V_{\mathrm{r.v.}}\, n_B^H Y_C^H\,, \tag{5.8}$$
$$N_S^{Q*} + N_S^{H\vartheta} = N_S^{\mathrm{r.v.}} = V_{\mathrm{r.v.}}\, n_B^H Y_S^H\,, \tag{5.9}$$

where (n_B^H, Y_C^H, Y_S^H) are the bulk–equilibrium baryon density, non–leptonic charge fraction and strangeness fraction of the initial hadronic phase, and the superscripts Q^* and H^ϑ label, respectively, the quark droplet and the hadronic surroundings within the reduced volume.

Dividing by $V_{\mathrm{r.v.}}$ and expressing the charges in terms of densities, these relations can be written as

$$\chi\, n_B^{Q*} + (1-\chi)\, n_B^{H\vartheta} = n_B^H\,, \tag{5.10}$$
$$\chi\, n_C^{Q*} + (1-\chi)\, n_C^{H\vartheta} = n_B^H Y_C^H\,, \tag{5.11}$$
$$\chi\, n_S^{Q*} + (1-\chi)\, n_S^{H\vartheta} = n_B^H Y_S^H\,. \tag{5.12}$$

For simplicity, in this exploratory study we restrict to electrically neutral fluctuations, imposing $n_C^{Q*} - n_e^{Q*} = 0$ and $n_C^{H\vartheta} - n_e^{H\vartheta} = 0$, since the main goal here is to isolate finite–volume effects.

The saddle–point conditions for the reduced–volume configuration (see Sec. 4.3.4.3) read

$$\mu_B^{Q*} = \mu_B^{H\vartheta}\,, \tag{5.13}$$
$$\mu_C^{Q*} + \mu_e^{Q*} = \mu_C^{H\vartheta} + \mu_e^{H\vartheta}\,, \tag{5.14}$$
$$\mu_S^{Q*} = \mu_S^{H\vartheta}\,. \tag{5.15}$$

For a given χ, the solution of these eight equations, together with the mean-field equations in both phases, determines the full thermodynamic state of the system as a function of the initial bulk hadronic conditions.

Figure 5.7 shows the strangeness fraction of the quark droplet, Y_S^{Q*}, as a function of the bulk hadronic density n_B^H for several temperatures and for different choices of χ. The blue curves correspond to the flavor–frozen (FF) limit (Sec. 4.3.4.1), the red ones to the strong–equilibrium (SE) limit obtained from the saddle–point fluctuation approach when all configurations are assumed to be available (Sec. 4.3.4.2), and the grey curves to the reduced–volume (RV) prescription for different $\chi = V_{Q*}/V_{\mathrm{r.v.}}$.

Several features are worth noting.

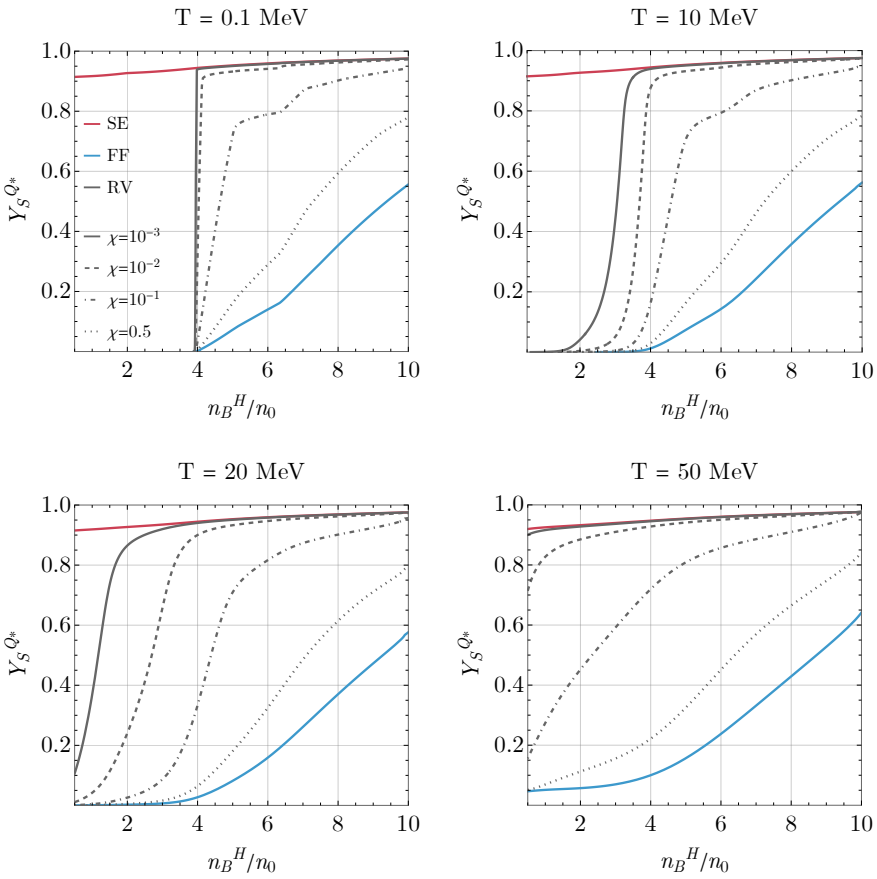

Figure 5.7: Strangeness fraction of the quark droplet Y_S^{Q*} as a function of the baryon density of the initial hadronic phase n_B^H in units of n_0. Each panel corresponds to a different temperature $T = (0.1\text{–}50)$ MeV. The blue line shows the flavor–frozen (FF) limit (Sec. 4.3.4.1); the red line, the strong chemical–equilibrium (SE) limit obtained from the saddle–point fluctuation approach (Sec. 4.3.4.2); and the grey lines, the reduced–volume (RV) prescription (Sec. 4.3.4.3) for several values of $\chi = V_{Q*}/V_{\text{r.v.}}$. The initial hadronic phase is taken in neutrinoless β equilibrium.

- At $T = 0.1$ MeV, the initial hadronic phase has essentially no strangeness ($Y_S^H = 0$) for $n_B^H \lesssim 4\,n_0$. In this regime, the production of strangeness via distillation (an excess of s quarks inside the droplet compensated by kaons with negative strangeness in the hadronic surroundings) is inefficient even for $\chi \ll 1$. This behaviour is *not* captured in the SE prescription of Sec. 4.3.4.2, where $\mu_S^{Q*} = \mu_S^H$ is enforced.
- Once strangeness appears in the hadronic phase, even moderately small values $\chi \lesssim 0.01$ (corresponding to $\ell_D \sim 10$ fm) are sufficient for the RV curves to approach the SE limit. As χ is increased (smaller ℓ_D and $V_{\rm r.v.}$) the RV results approach the FF limit.
- At higher temperatures, some strangeness is already present in the initial hadronic phase and can be redistributed more efficiently as χ decreases, enhancing the strangeness content of the droplet. In the temperature range considered here, hyperons provide the dominant contribution to $Y_S^{H\vartheta}$; kaons yield only minor corrections, except at low n_B^H and large χ, where K^+ and K^0 can become comparable to hyperons in the hadronic sector.

A similar qualitative behaviour is found for other thermodynamic quantities. The example shown in Fig. 5.7 refers to an unpaired quark phase and to neutrinoless β equilibrium in the hadronic phase, but the same trends hold when these assumptions are relaxed (*e.g.* for CFL quark matter).

These results justify *a posteriori* the use of the SE prescription in Sec. 5.2: for the PNS conditions relevant there ($T \gtrsim 20$ MeV and $n_B^H \gtrsim 2\,n_0$), the SE limit is recovered already for $\chi \lesssim 10^{-2}$–10^{-3}, *i.e.* for diffusion lengths $\ell_D \sim 10$–100 fm, which are plausible when thermal fluctuations in the hadronic phase are efficient during a timescale $\sim 10^{-4}$ s prior to droplet formation.

By contrast, at low temperature the reduced–volume effects can be much more important. Once a NS has survived the PNS phase and cooled down, a neutrinoless β–equilibrated description becomes appropriate already after approximately a minute after the supernova explosion. In this regime strangeness is absent in the core up to relatively large densities.

Figure 5.8 shows the conditions in the (T, n_B^H) plane at which the nucleation timescale equals 10^{-4} s for a neutrinoless β–equilibrated system. Green curves correspond to the SE limit and red curves to the FF limit. Solid (dashed) lines refer to quantum (thermal) nucleation. The two dots on the $T = 0$ axis indicate the central conditions of a 1.4 $M_\odot$ NS and of the maximum–mass NS for the adopted EOS parameters.

For the illustrative choice $\sigma = 100$ MeV fm^{-2}, $\Delta_0 = 80$ MeV and $B_{\rm unp}^{1/4} = B_{\rm CFL}^{1/4} = 145$ MeV (compatible with the existence of NSs up to 1.4 $M_\odot$, see Sec. 5.2 and Fig. 5.6), the SE curves would predict very efficient nucleation, with most NSs converting. The reduced–volume analysis, however, indicates that at $T = 0$ the SE limit can only be reached once some strangeness is already present in the initial system. Before strangeness appears in the hadronic phase ($n_B^H \lesssim 4\,n_0$), the system effectively follows the FF curves, so conversion is possible only for NSs whose cores reach such high densities. Additional effects, such as the behaviour of color superconductivity in small

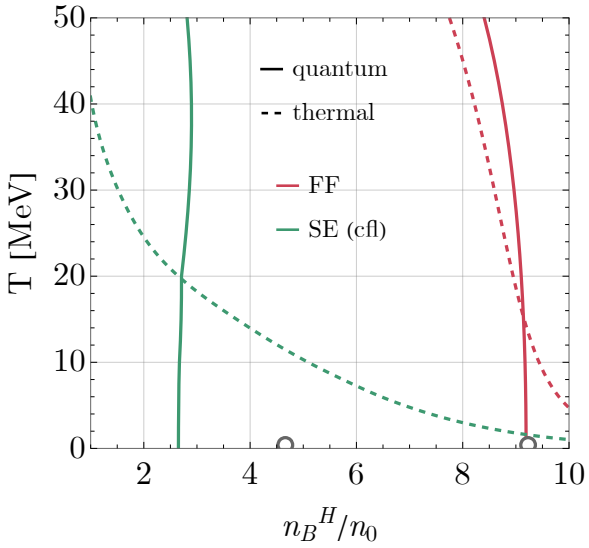

Figure 5.8: Temperature T and baryon density of the initial hadronic phase n_B^H at which the nucleation timescale equals 10^{-4} s, considering quantum nucleation (solid lines) and thermal nucleation (dashed lines) in the flavor–frozen (FF, red) and strong–equilibrium (SE, green) limits. The two dots on the $T = 0$ axis mark the central conditions of a 1.4 $M_\odot$ NS and of the maximum–mass NS. The parameters are $\sigma = 100$ MeV fm^{-2}, $\Delta_0 = 80$ MeV and $B^{1/4} = 145$ MeV.

systems (Secs. 4.3.8 and 5.2), will further delay conversion. Nevertheless, even in the FF limit, quantum nucleation remains possible in the core of the most massive NSs. This suggests that a region of parameter space should exist in which a $\sim$ (1.3–1.4) $M_\odot$ NS survives the PNS phase (as ensured by the parameters adopted, given the results reported in Sec. 5.2) and later converts into a QS as a consequence of mass accretion on a longer timescale.

A detailed quantitative exploration of this possibility, including a full CFL treatment within the framework presented in Sec. 4.3.8 as used in Sec. 5.2, together with a systematic scan of the parameter space, is left for future work. The qualitative lesson from this preliminary analysis is that finite–volume effects are likely to play a crucial role in determining whether a cold, accreting NS can convert into a QS, and that the answer depends sensitively on currently poorly known microphysical inputs.

5.4 QS formation from CCSN in compact binaries

In this section, we investigate whether the accretion that follows a CCSN in a tight binary containing an evolved progenitor (*e.g.*, a CO or Wolf–Rayet star) and a NS can drive one or both NSs to convert into QSs.

The scenario is as follows. The evolved star undergoes core collapse and explodes as a CCSN in a compact orbit with an NS companion. The collapse of the iron core forms a newborn NS, while part of the SN ejecta is gravitationally captured and accreted both by the newborn NS and by the pre–existing NS companion.

$M_{\rm zams}$ ($M_\odot$)	$M_{\rm CO}$ ($M_\odot$)	$M_B^{\rm new}$ ($M_\odot$)	$M^{\rm new}$ ($M_\odot$)	$M_{\rm ej}$ ($M_\odot$)	M ($M_\odot$)	$P_{\rm orb}$ (min)
30	8.89	1.75	1.58	7.14	1.40	4.88
25	4.80	1.80	1.62	3.00	1.40	4.80
15	3.00	1.40	1.29	1.60	1.40	4.47

Table 5.2: Properties of the CO–NS progenitors. The CO star is the pre–SN configuration obtained from `KEPLER` stellar evolution code evolution [225] of a ZAMS star of mass $M_{\rm zams}$. Its mass is the sum of the mass ejected by the SN, $M_{\rm ej}$, and the collapsed iron core mass, assumed equal to the baryonic mass $M_B^{\rm new}$ of the newborn NS. The newborn NS gravitational mass $M^{\rm new}$ is inferred from the universal relation between binding energy and gravitational mass of [226].

If, during this accretion phase, the central density of either object exceeds the critical value for SQM nucleation, a first quark seed can form and, under the Bodmer–Witten hypothesis, the entire star subsequently converts into a QS. The possible compact remnants of such events are therefore NS–NS, NS–QS, or QS–QS binaries.

This section summarizes the analysis presented in [47].

5.4.1 Simulation setup

As a first step, we compute the time–dependent accretion rates onto the newborn NS and its NS companion using three–dimensional smoothed–particle hydrodynamics (SPH) simulations with the `SNSPH` code [220], adapted to CO–NS binaries as in [221]. The code has been extensively tested in studies of binary–driven hypernovae and long GRBs (see *e.g.* [221–223]).

The SPH simulations are initialized at the time when the SN shock reaches the surface of the pre–SN CO star. At that stage, a 1D core–collapse calculation [224] has already produced a newborn NS of baryonic mass $M_B^{\rm new}$ and gravitational mass $M^{\rm new}$, and the CO envelope is in the process of being ejected. The companion NS is modeled as a point mass of baryonic mass M_B and gravitational mass M. Both compact objects interact only gravitationally with the SPH particles and with each other. Accretion onto each NS is modeled following [221]: SPH particles that satisfy the accretion criteria within an accretion (capture) radius are removed from the simulation and their properties are added to the corresponding point mass.

We consider binaries in which the companion has initial mass $M = 1.4\ M_\odot$ and the exploding star is a CO core produced by ZAMS progenitors of 15, 25, and 30 $M_\odot$. The main properties of these CO–NS progenitors are summarized in Table 5.2.

Figure 5.9 shows density snapshots of the SN ejecta in the orbital plane for the three CO progenitors. The NS companion captures part of the ejecta, which forms a trailing stream that circularizes into a thick disk around it. Simultaneously, fallback from the innermost ejecta produces accretion onto the newborn NS. After roughly one orbital period, both compact objects are surrounded by accretion disks.

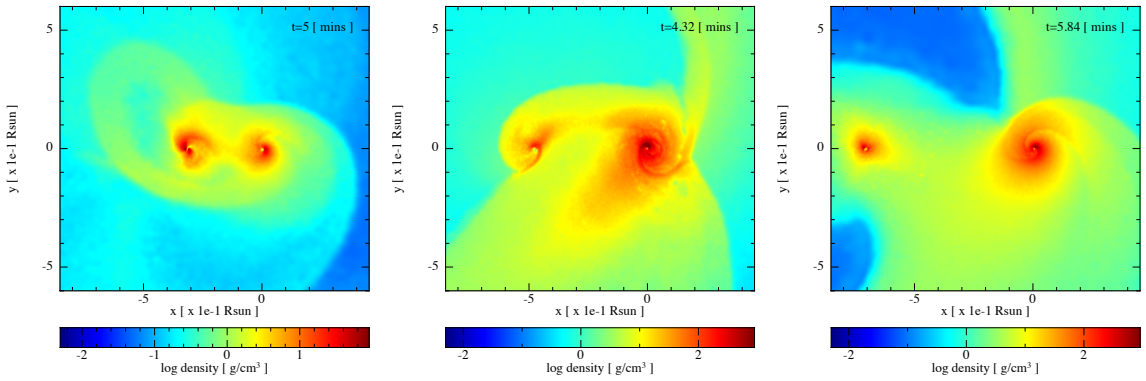

Figure 5.9: SPH simulations of a CO–NS binary with an initial 1.4 $M_\odot$ NS companion and a CO star produced from ZAMS progenitors of 15 $M_\odot$ (left), 25 $M_\odot$ (center), and 30 $M_\odot$ (right). The orbital periods are 4.47, 4.80, and 4.88 min, respectively. Each panel shows the mass density in the equatorial plane at selected times; $t = 0$ is the SN shock breakout at the CO surface. The origin is at the NS companion, and the x–axis is along the line joining the two stars. The captured ejecta circularizes into a thick disk around the companion; fallback material forms a disk around the newborn NS. Figure from [47].

The resulting accretion rates onto the newborn NS and onto the companion are shown in Fig. 5.10. The fallback rate onto the newborn NS peaks at early times; for the 25 and 30 $M_\odot$ progenitors a second peak appears later, induced by the gravitational influence of the companion [221]. The accretion onto the NS companion exhibits a broad main peak plus smaller, shorter fluctuations as the star orbits through denser and rarer regions of the SN ejecta. The noisy structure at late times is likely of numerical origin.

To follow the structural evolution of the newborn NS and the NS companion during accretion, we couple the SPH–derived accretion histories to a relativistic stellar-structure code based on `RNS` [227], including the quadrupole corrections of [226]. Given an EOS, a baryonic mass M_B, and an angular momentum J, the code computes rigidly rotating,

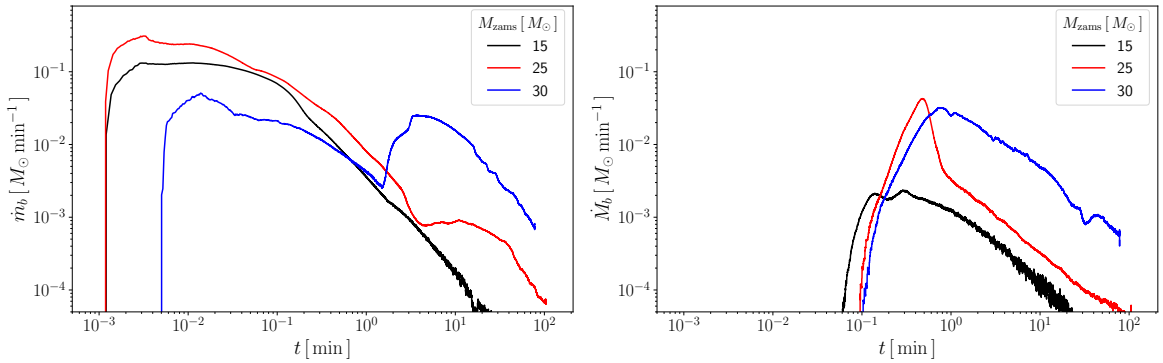

Figure 5.10: Baryonic mass accretion rate onto the newborn NS (left) and the NS companion (right) as a function of time for the three CO progenitors in Table 5.2. The explosion energies are $E_{\rm sn} = 1.08 \times 10^{51}$ erg (15 $M_\odot$), 5.67×10^{50} erg (25 $M_\odot$), and 7.85×10^{50} erg (30 $M_\odot$). Figure from [47].

axisymmetric equilibrium configurations[9].

At each simulation time step, the baryonic masses of the newborn NS and of the companion are updated according to the SPH accretion rates, $\dot{M}_B^{\rm new}$ and $\dot{M}_B$, respectively. The stellar angular momenta evolve according to angular momentum conservation,

$$\dot{J} = \tau_{\rm acc}, \tag{5.16}$$

where $\tau_{\rm acc}$ is the torque exerted by the accretion flow. The SPH simulations indicate that the inflowing matter circularizes into a disk before being accreted; we therefore take the torque to be

$$\tau_{\rm acc} = \begin{cases} \chi\, l\, \dot{M}_B^{\rm new}, & \text{for the newborn NS,} \\ \chi\, l\, \dot{M}_B, & \text{for the companion,} \end{cases} \tag{5.17}$$

where $0 < \chi \leq 1$ is the angular–momentum transfer efficiency and l is the specific angular momentum of matter at the inner disk radius $R_{\rm in}$ (fixed in this work to $\chi = 0.5$),

$$l = \begin{cases} l_{\rm isco}, & R_{\rm in} \geq R, \\ \Omega R^2, & R_{\rm in} < R, \end{cases} \tag{5.18}$$

with $l_{\rm isco}$ the specific angular momentum at the innermost stable circular orbit, and R and Ω the stellar radius and angular velocity, respectively, provided by `RNS`. In this work we neglect magnetic torques (spin–down), which are expected to be subdominant at the very high accretion rates and small magnetospheric radii relevant here [223].

5.4.2 Equations of state and deconfinement criterion

The hadronic EOS is modeled with the SFHo–HΔ RMF model (Sec. 2.1.2). Here we adopt the parametrization used in [34, 94, 168], in which the vector ϕ–meson coupling to hyperons is set to zero, $x_{\phi H} = 0$.

The newborn NS is initially a hot PNS, with entropy per baryon $S \sim 1 - 2$ and trapped neutrinos; it cools and deleptonizes to a cold, neutrinoless β–equilibrated NS in $\sim$ 30–60 s (see Sec. 5.2). In our problem, the accretion phase lasts minutes, and the detailed thermal/leptonic evolution is not followed in the SPH simulations. To bracket the thermal state of the stars when deconfinement may occur, we therefore consider two limiting hadronic EOSs: (EOS1) $T = 0$, neutrinoless β–equilibrium; (EOS2) $S = 1$, neutrinoless β–equilibrium.

Accretion does not appreciably heat the stellar interiors thanks to efficient neutrino cooling in the accretion atmosphere [228, 229], so describing the accreting companion stars by cold EOS is a reasonable approximation.

[9]The `RNS` code uses as input the pressure P and energy density ε, from which it computes the log–enthalpy via $d(\log h) = dP/(\varepsilon + P)$ and then the baryon density $n_B = (\varepsilon + P)\exp(-h)/m_p$ with $m_p = 939$ MeV and integrate from the surface to the center. For hadronic EOSs we start from $\log h(p = 0) = 1$, whereas for quark matter we modify the starting point to $\log h(P = 0) = \varepsilon(P = 0)/[m_p\, n_B(P = 0)]$.

EOS	$M_{\rm max}^{J=0}$ ($M_\odot$)	$M_{\rm max}^{K}$ ($M_\odot$)	$M^{J=0}(n_{\rm crit})$ ($M_\odot$)
EOS1: SFHo–HΔ ($T=0$)	1.585	1.884	1.545–1.566
EOS2: SFHo–HΔ ($S=1$)	1.576	1.850	1.519–1.550
Quark EOS1 (αBag unpaired)	2.116	3.042	–
Quark EOS2 (αBag CFL)	2.586	3.719	–

Table 5.3: Maximum gravitational masses for static ($M_{\rm max}^{J=0}$) and Keplerian ($M_{\rm max}^{K}$) sequences, and static masses at which the central density reaches the critical value $n_{\rm crit}$ for hadronic EOS1 and EOS2.

In this section, the nucleation conditions are estimated using the approximate criterion of [34, 94] (see also Sec. 5.1): we assume that the conversion starts when the average distance between strange quarks in the hadronic phase is comparable to the average nucleon spacing at nuclear saturation, *i.e.* when the total strangeness fraction reaches

$$Y_S \equiv \frac{n_S}{n_B} \sim 0.2 - 0.3, \tag{5.19}$$

or equivalently when the strangeness density is of order the saturation density. Denoting by $n_{\rm crit}$ the baryon density at which Y_S enters this range, we take the first SQM seed to form once the stellar central density satisfies $n_c \geq n_{\rm crit}$ during the accretion–driven evolution. For the EOSs used here, this corresponds to static stellar masses $M^{J=0}(n_{\rm crit})$ in the ranges given in Table 5.3.

Since the subsequent conversion lasts only seconds, whereas the accretion we investigate operates on a typical timescale of several minutes, we adopt a simplified prescription: once the central density n_c reaches $n_{\rm crit}$, we assume an instantaneous conversion of the entire star into a QS, conserving baryon number and angular momentum. A detailed treatment of the conversion dynamics is beyond the scope of this work.

To explore the dependence on the SQM properties, we consider two cold quark EOSs:

- Quark EOS1: αBag unpaired; see Sec. 2.2.2) with parameters $B^{1/4} = 137.5$ MeV and $\alpha_s = (\pi/2) \times 0.25$, and $m_u = m_d = 0$, $m_s = 100$ MeV;

- Quark EOS2: αBag CFL (Sec. 2.2.3), with parameters as in [94]: $B^{1/4} = 135$ MeV, $\alpha_s = (\pi/2) \times 0.3$, pairing gap $\Delta_0 = 80$ MeV, and the same quark masses.

In both cases we treat the post–conversion QS as cold, which is appropriate on the timescale of our accretion evolution.

The main static and Keplerian properties of the hadronic and quark EOSs, as well as the static masses at $n_{\rm crit}$, are summarized in Table 5.3.

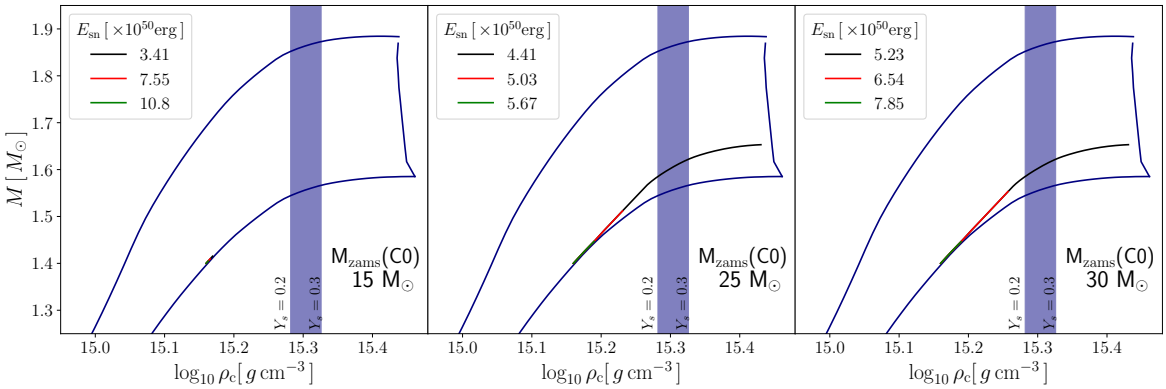

Figure 5.11: Evolution of the NS companion in the (ρ_c, M) plane using EOS1 (cold hadronic EOS). The companion is initially non–rotating with $M = 1.4$ M$_\odot$. The three panels correspond to CO progenitors from ZAMS stars of 15 M$_\odot$ (left), 25 M$_\odot$ (center), and 30 M$_\odot$ (right), with pre–SN orbital periods as in Table 5.2. Different colors show different SN explosion energies E_{sn}. The dark–blue solid curves bound the stability region (static to Keplerian). The shaded band indicates central densities where the strangeness fraction reaches $Y_S = 0.2 - 0.3$. Figure from [47].

5.4.3 Evolution of the NSs

We first consider the evolution of an initially non–rotating NS companion of gravitational mass 1.4 M$_\odot$ for the three CO progenitors in Table 5.2. For each progenitor we explore three SN kinetic energies E_{sn} chosen such that the ejecta is unbound and the velocity profile spans $\sim 10^3$–few $\times 10^4$ km s^{-1} [221]. The accretion histories shown in Fig. 5.10 are then used to evolve the stellar structure with the cold hadronic EOS (EOS1).

The trajectories of the NS companion in the (M, ρ_c) plane are shown in Fig. 5.11 (where ρ_c here is the energy density). As accretion proceeds, both the gravitational mass and the central density increase, while the rotation frequency grows from zero. For a given progenitor, lower explosion energies correspond to higher accretion rates and thus to larger increases in central density.

Also displayed are the static, secular–instability, and Keplerian sequences, and the band of central densities where $Y_S = 0.2$–0.3, *i.e.* where the quark–nucleation criterion is met. For the lightest CO progenitor ($M_{zams} = 15$ M$_\odot$), the accretion is too weak for the companion to reach n_{crit} for any of the E_{sn} considered. For $M_{zams} = 25$ and 30 M$_\odot$, and for the lowest explosion energy in each case, the central density crosses into the Y_S band before any rotational instability is reached; in our scenario these companions would then convert to QSs.

We now turn to the newborn NS formed from the CO core collapse. Here we fix E_{sn} for each progenitor, $E_{sn} = (3.41,\ 4.41,\ 5.23) \times 10^{50}$ erg for $M_{zams} = (15,\ 25,\ 30)$ M$_\odot$, respectively, and vary the initial stellar angular momentum J_0 along the constant–baryonic–mass sequence determined by M_B^{new} in Table 5.2. It is convenient to parametrize J_0 via the dimensionless specific angular momentum $j_{ns,0} \equiv cJ_0/(GM_\odot^2)$.We perform the evolution with both EOS1 ($T = 0$) and EOS2 ($S/A = 1$).

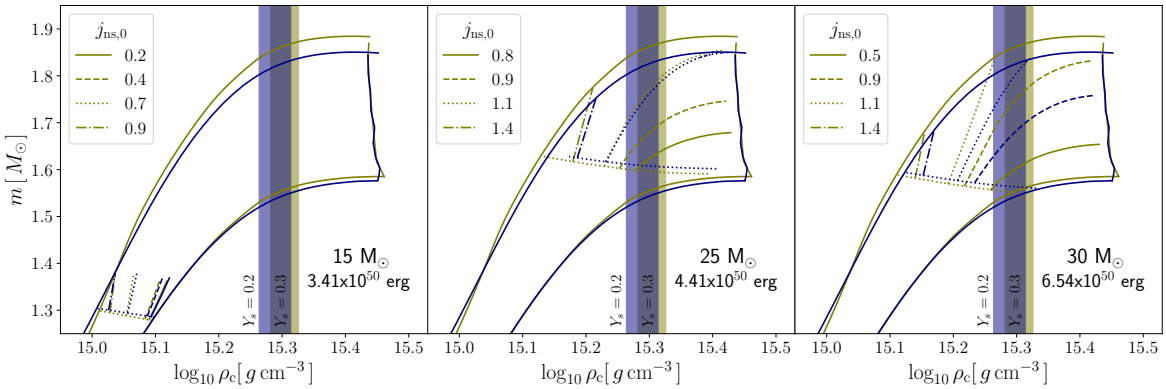

Figure 5.12: Same as Fig. 5.11, but for the newborn NS, evolved along constant baryonic mass sequences ($M_B^{\rm new} = 1.4,\ 1.80,\ 1.75\ \mathrm{M}_\odot$ for $M_{\rm zams} = 15,\ 25,\ 30\ \mathrm{M}_\odot$, respectively). Different curves correspond to different initial specific angular momenta $j_{\rm ns,0}$. Yellow curves show EOS1 ($T = 0$), dark blue curves EOS2 ($S = 1$). Figure from [47].

Figure 5.12 shows the evolutionary tracks of the newborn NS in the (ρ_c, M) plane. For rapidly rotating initial configurations (*e.g.* $j_{\rm ns,0} \gtrsim 1.2$, corresponding to $\nu \sim 1$ kHz), accretion is more efficient at spinning up the star than compressing it: the mass and J grow substantially, but the central density increases only modestly. In these cases the star reaches the Keplerian limit before crossing the deconfinement band, and no conversion occurs. In contrast, for more slowly rotating initial conditions the central density grows more strongly and the star can reach $n_{\rm crit}$ before hitting any instability, especially for the 25 and 30 $\mathrm{M}_\odot$ progenitors. In very slowly rotating cases, the PNS may even be *born* above $n_{\rm crit}$, in which case deconfinement would begin already during the early PNS phase; such situations require a dedicated treatment and are not modeled here.

5.4.4 Conversion and released energy

The time evolution of the central baryon density in the cases where deconfinement is reached is shown in Fig. 5.13. The upper panel refers to the NS companion (varying $E_{\rm sn}$, zero initial spin), while the lower panel refers to the newborn NS (fixed $E_{\rm sn}$, varying $j_{\rm ns,0}$). We omit the 15 $\mathrm{M}_\odot$ progenitor in the newborn–NS panel since in those models no star reaches $n_{\rm crit}$.

The figure highlights two points. First, for fixed progenitor and EOS, a smaller $E_{\rm sn}$ yields a higher accretion rate and a shorter time to reach $n_{\rm crit}$. Second, for fixed $E_{\rm sn}$ the newborn NS typically reaches $n_{\rm crit}$ earlier and more easily than the companion, because it is immersed in dense fallback and is also fed by material initially captured by the companion. Thus, for the parameter set explored here, conversion of the *newborn* NS to a QS is generally favored over conversion of the companion.

Once a star crosses $n_{\rm crit}$, we switch its interior description from the hadronic EOS to one of the quark EOSs while conserving baryon number and angular momentum. The top panels of Fig. 5.14 show the resulting configurations in the $(M, R_{\rm eq})$ plane for selected models, comparing the hadronic branch (EOS1) to the QS branches for quark

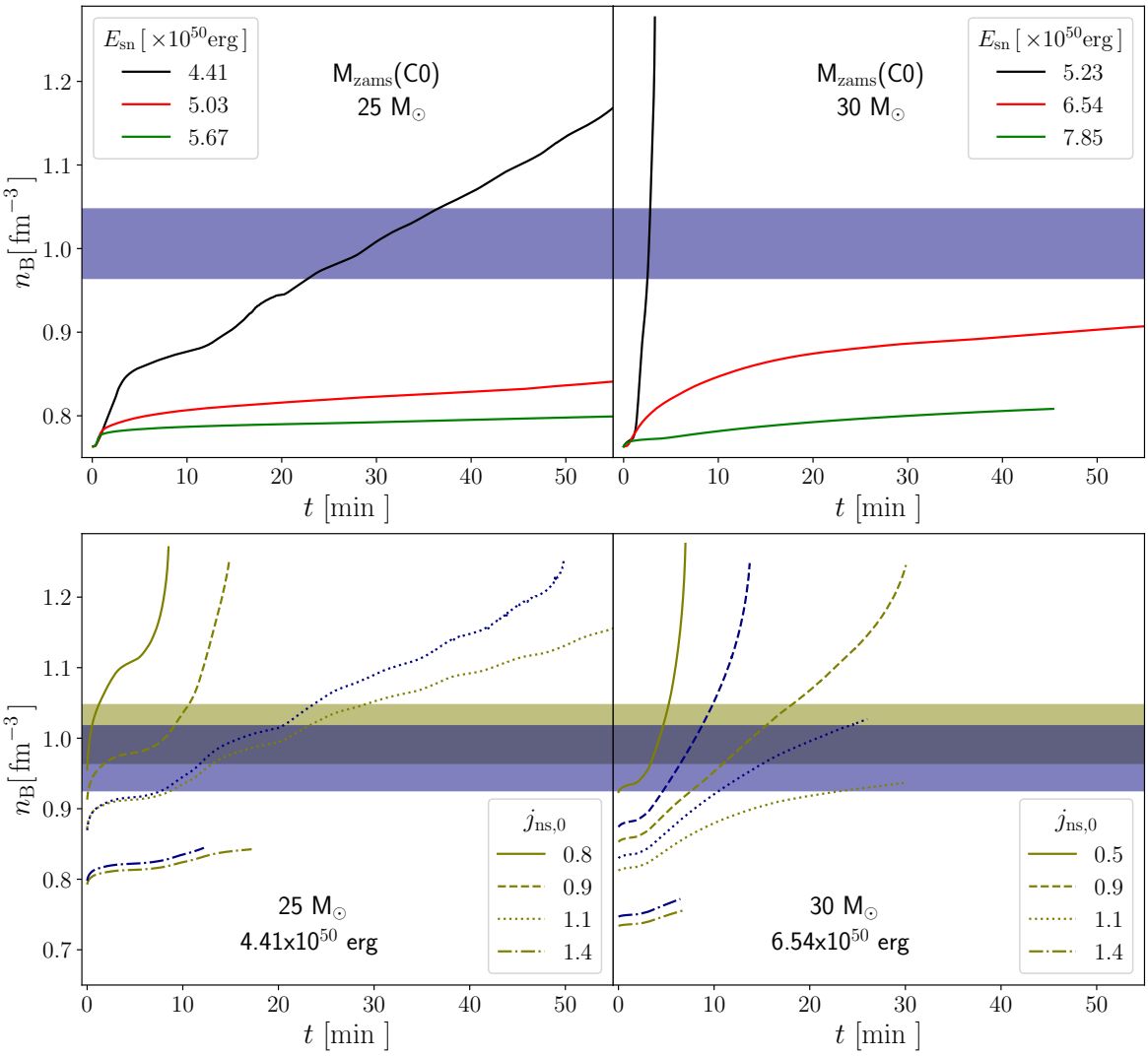

Figure 5.13: Time evolution of the central baryon density. *Upper panel:* NS companion, for the models of Fig. 5.11 (fixed initial spin, varying E_{sn}). *Lower panel:* newborn NS, for the models of Fig. 5.12 (fixed E_{sn}, varying $j_{ns,0}$). Only cases that reach n_{crit} are shown. For the 15 $M_\odot$ progenitor, no deconfinement occurs in the newborn NS and the corresponding curves are omitted. Figure from [47].

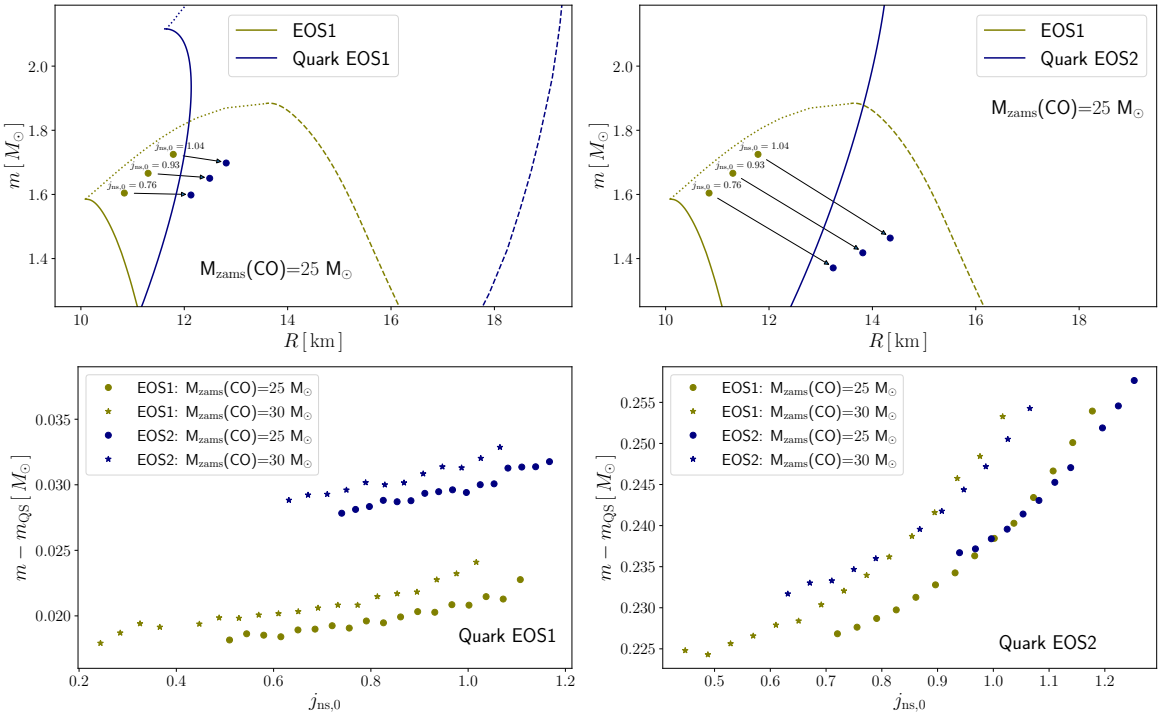

Figure 5.14: *Upper panels:* Mass–radius relations for hadronic EOS1 (NS branch) and quark EOS1 (left) or quark EOS2 (right) (QS branches). Solid, dotted, and dashed curves indicate static, secular–instability, and Keplerian sequences, respectively. Yellow points correspond to newborn NS configurations at the onset of deconfinement ($Y_S = 0.2$); blue points show the QSs with the same (M_b, J). The example corresponds to a CO progenitor with $M_{\rm zams} = 25\ \mathrm{M}_\odot$ and $E_{\rm sn} \simeq 3.4 \times 10^{50}$ erg. *Lower panels:* Change in gravitational mass ΔM upon conversion, as a function of the initial stellar angular momentum $j_{\rm ns,0}$, for quark EOS1 (left) and quark EOS2 (right). The range of $j_{\rm ns,0}$ corresponds to initial spin frequencies between ~ 500 and 1100 Hz. Figure from [47].

EOS1 (left) and quark EOS2 (right). Yellow points mark the hadronic configurations at the moment they reach $Y_S = 0.2$; dark–blue points show the corresponding QSs with the same (M_B, J). In all cases the conversion leads to a *larger* equatorial radius and a *smaller* gravitational mass, consistent with the higher binding energy of SQM [8].

The bottom panels of Fig. 5.14 quantify the change in gravitational mass, $\Delta M = M_{\rm NS} - M_{\rm QS}$, as a function of the initial stellar angular momentum, for the 25 and 30 $\mathrm{M}_\odot$ progenitors and both quark EOSs. For quark EOS1, we find $\Delta M \simeq (0.02 - 0.025)\ \mathrm{M}_\odot$ for EOS1 and about 50% larger for EOS2 (hot case). For quark EOS2, the larger stiffness and binding yield to a nearly temperature independent $\Delta M \simeq (0.22 - 0.25)\ \mathrm{M}_\odot$. These correspond to conversion energies

$$E_{\rm conv} \sim (4 \times 10^{52}\ \mathrm{erg})\ \ \text{(Quark EOS1)}, \quad E_{\rm conv} \sim (4 \times 10^{53}\ \mathrm{erg})\ \ \text{(Quark EOS2)}.$$

Such energies are sufficient to power highly energetic transients (*e.g.* GRBs) if a significant fraction is channeled into observable radiation [10, 31]. A detailed modeling of the conversion front, neutrino and photon emission, and their observable signatures is beyond the scope of this thesis.

$M_{\rm CO}$ ($M_\odot$)	$M_{\rm zams}$ ($M_\odot$)	$E_{\rm sn}$ (10^{50} erg)	Companion fate	Newborn NS fate	Remnant binary
3.0	15	3.41–10.8	NS	NS	NS–NS
4.8	25	4.41	QS	QS if $j_{\rm ns,0} < 1.25$ NS if $j_{\rm ns,0} > 1.25$	QS–QS QS–NS
4.8	25	5.03	NS	NS	NS–NS
4.8	25	5.67	NS	NS	NS–NS
8.9	30	5.23	QS	QS	QS–QS
8.9	30	6.54	NS	QS if $j_{\rm ns,0} < 1.05$ NS if $j_{\rm ns,0} > 1.05$	NS–QS NS–NS
8.9	30	7.85	NS	NS	NS–NS

Table 5.4: Qualitative outcomes of the simulations for selected combinations of CO mass, SN energy, and initial spin of the newborn NS.

5.4.5 Binary outcomes

Table 5.4 summarizes the qualitative outcomes of the simulations, in terms of whether each star converts and what type of compact binary remains at the end of the accretion phase. For each CO progenitor mass we list the SN explosion energies considered, and indicate the final nature of the NS companion and the newborn NS. For the newborn NS, the outcome may depend on the initial spin $j_{\rm ns,0}$; this is explicitly indicated.

These results show that, for suitably massive progenitors and moderate SN explosion energies, both the newborn NS and the NS companion can reach the deconfinement threshold, leading to NS–QS or QS–QS binaries. If such systems remain bound, they are potential sources of compact–object mergers involving QSs. In the two–families scenario, such mergers may exhibit gravitational–wave and electromagnetic signatures distinct from those of purely hadronic NS–NS mergers [34].

In this work, we have neglected the dynamical impact of the conversion energy release on the surrounding disks and on the binary orbit. Qualitatively, one expects that additional energy injection could reduce the amount of bound ejecta (hindering conversion of the second star) or, conversely, that neutrino irradiation could enhance mass transfer onto the companion. A consistent treatment of these effects requires radiation–hydrodynamic simulations in the post–SN environment, and is left to future work.

5.5 Deconfinement–driven supernova explosions

In this section, we briefly and qualitatively discuss how the mechanism for deconfinement–driven CCSN explosions proposed in [35, 36] for the one–family scenario could be adapted to the two–families picture.

The main features of the deconfinement–driven mechanism are as follows. For relatively low zero–age main–sequence (ZAMS) masses (of order 10–12 $M_\odot$), the post–bounce

evolution is fairly standard: after core bounce, the shock stalls at a few hundred kilometers and is subsequently revived by neutrino heating on timescales of a few 100 ms. The central density of the PNS grows only moderately and remains below the onset density of the mixed phase, so that the inner core never experiences deconfinement. The explosion is powered by the usual neutrino mechanism, the remnant is a purely hadronic NS with typical mass, and the neutrino signal shows a single main burst associated with shock revival.

For much more massive progenitors (ZAMS masses $\gtrsim$ 40–50 $M_\odot$), the situation changes qualitatively. The post–bounce accretion rate onto the PNS is very large, so that its central density and temperature continue to rise. If only a purely hadronic EOS were available (and no hadron–quark transition or SQM nucleation were possible), the PNS would soon exceed its maximum mass and undergo direct collapse to a BH, without a successful explosion. When a first–order hadron–quark phase transition is included, however, the central density eventually enters the mixed phase at a few times nuclear saturation density. The associated softening of the EOS triggers a rapid, dynamical recollapse of the PNS core on a timescale of a few milliseconds. This secondary collapse continues until the innermost region is converted to pure quark matter, at which point the EOS stiffens again. The sudden restiffening halts the infall and produces a second "quark–core bounce" inside the already formed PNS. A new shock wave is launched at the quark–hadron interface and propagates outward, eventually leading to a successful, energetic explosion rather than BH formation. The remnant is a massive HS, and the dynamics are accompanied by a characteristic second neutrino burst and by a modification of the gravitational–wave signal associated with the quark–core bounce.

To reproduce, at least qualitatively, a similar mechanism in the two–families scenario, one still needs an initial softening of the EOS followed by a subsequent restiffening capable of halting the gravitational collapse on a millisecond timescale. In the two–families picture, the first softening would not be caused by the hadron–quark mixed phase but by the appearance of hyperons in hadronic matter once density and temperature become sufficiently high due to the strong mass accretion. Hyperon production softens the hadronic EOS and can induce a mini–collapse of the PNS. Along the expected approximately isentropic trajectory, the temperature decreases as the density increases, in close analogy with what happens when the mixed phase appears in the one–family scenario.

For the mechanism to work in this context, two conditions must be satisfied. First, the accretion must be strong enough that the nucleation conditions are met while the PNS is still undergoing contraction; in practice, the nucleation timescale must be much shorter than the dynamical collapse timescale, of order a millisecond. Second, within this collapse window, a sufficiently large amount of PNS matter must be converted to SQM so that the EOS stiffens enough to halt the collapse and launch a new shock. Simulations of the conversion process after nucleation [31, 32] suggest a rapid burning phase, acting on millisecond timescales, that converts the central part of the star into SQM and ends when the hadronic and quark phases reach equal pressure and energy density (while still being out of full thermal and chemical equilibrium). The resulting configuration is an out–of–equilibrium hybrid object that relaxes on a longer, diffusive timescale.

From the nucleation perspective, the requirement is that, for at least some of the most massive PNSs, the nucleation rate becomes so large that a critical droplet forms on a timescale much shorter than a millisecond. Whether the subsequent rapid burning is indeed fast enough to convert enough matter and produce a stiffening sufficient to halt the collapse and generate a strong shock ultimately demands fully dynamical simulations that couple nucleation and conversion to multidimensional CCSN hydrodynamics. The discussion presented here should therefore be viewed as qualitative, outlining a plausible extension of deconfinement–powered explosions to the two–families scenario and motivating future dedicated simulations.

Conclusions

The behavior of strongly interacting matter at densities above nuclear saturation and the associated deconfinement transition between hadronic and quark matter remain among the central open questions in contemporary nuclear physics and astrophysics. Compact stars and related high–energy transients provide unique laboratories in which to probe this poorly known regime of the QCD phase diagram, where several charges (baryon number, electric charge, strangeness, lepton number) may play a role and where the ground state of matter itself might differ from ordinary nuclear matter.

In this context, the aim of this thesis has been to investigate the deconfinement transition under conditions relevant for compact stars, with particular emphasis on (i) how to describe a first–order phase transition in multi–component matter in a thermodynamically consistent way in the context of the one-family scenario, and (ii) how nucleation and non–equilibrium conversion can operate in the two–families scenario, where NSs are metastable with respect to QSs.

Part I reviewed the present understanding of strongly interacting matter, the QCD phase diagram and the Bodmer–Witten hypothesis, and summarized the main phenomenological scenarios for compact stars. In the *one–family* picture, all cold compact stars lie on a single sequence of NSs and HSs described by a unique equilibrium EOS. Deconfinement can then be modeled as an equilibrium phase transition, and nucleation effects may, in principle, provide only relatively small corrections to the equilibrium onset of the mixed phase. In the *two–families* scenario, by contrast, bulk hadronic matter is always metastable with respect to bulk SQM. A family of metastable NSs coexists with a family of stable QSs, and macroscopic deconfinement is realized through the decay of the metastable hadronic state via nucleation and subsequent out–of–equilibrium conversion. In this case, nucleation is not a secondary refinement but the central ingredient that determines the conditions and astrophysical scenario under which a hadronic object converts into a QS.

Part I also introduced the EOS models for hadronic and quark matter, leptons and thermal bosons used in this work, and outlined the astrophysical systems in which a hadron–quark transition might occur: proto neutron stars (PNSs), core–collapse supernovae (CCSNe), binary compact star mergers (BCSMs) and accreting binaries. These systems span a broad region of the QCD phase diagram and provide complementary constraints on deconfinement.

Part II addressed the problem of how to describe a first–order phase transition in multi–component matter in a thermodynamically consistent way, with a focus on HSs in

the one–family scenario. In neutrinoless β–equilibrated matter, the traditional Maxwell and Gibbs constructions correspond to two limiting assumptions about charge neutrality: fully local charge neutrality in each phase (Maxwell) and fully global charge neutrality in the mixed phase (Gibbs). However, realistic astrophysical systems may realize intermediate regimes in which only a fraction of the electric charge is effectively tied to each phase, while the remaining fraction can rearrange globally and can feature additional conserved charges (such as the lepton number).

To capture this physics, a general framework has been developed that interpolates continuously between local and global charge neutrality by introducing a control parameter that quantifies the fraction of leptons participating in local versus global neutrality. The framework is formulated through free–energy minimization under the appropriate conservation laws and it is applicable at finite temperature and both in and out of β-equilibrium. In the neutrinoless β–equilibrium limit, the usual Maxwell and Gibbs constructions are recovered as two limiting cases of the mixed–phase EOS.

A central point of Part II is that once more than one global conserved quantity is present (for example baryon number and non–leptonic electric charge), a strict Maxwell construction is *not* a proper thermodynamic equilibrium solution, even if local charge neutrality is enforced in each phase. In this situation, imposing phase coexistence via an effective Maxwell construction, as often done in CCSN and merger simulations with EOSs tabulated in terms of (n_B, Y_e, T), may artificially strengthen the transition by unphysically enhancing jumps in pressure, and entropy. The framework introduced here provides a controlled way to tune the strength and the extent of the mixed phase while maintaining full thermodynamic consistency.

Applied to a representative hadron–quark model, the formalism showed that the mixed phase pressure is not constant even under local charge neutrality when additional conserved charges are present, and that the sound speed, thermal index and composition can be significantly modified with respect to standard Maxwell/Gibbs limits. This could have direct implications for the structure of HSs and for the interpretation of gravitational–wave and electromagnetic signals from mergers and CCSNe.

Looking ahead, the mixed–phase framework opens up several avenues for future work. It can be coupled to more sophisticated hadronic and quark EOSs, including hyperons, delta resonances and color superconducting phases, and embedded directly in dynamical simulations of CCSNe and BCSMs. This would allow one to explore, within a thermodynamically consistent setting, how astrophysical observables respond to variations in the strength and in the extent of the hadron–quark transition, instead of relying on ad hoc Maxwell constructions. In particular, it will be interesting to quantify the impact on post–merger gravitational–wave spectra and on the conditions for deconfinement–triggered core–collapse explosions.

Part III focused on the two–families scenario and on the decay of the metastable hadronic phase via nucleation. Chapter 4 developed a thermodynamic description of SQM nucleation in compact star conditions. The nucleation problem was formulated in terms of an energy barrier in the configuration space spanned by the droplet volume (the order parameter) and the thermodynamic variables of the quark phase (baryon density, charge fraction, strangeness fraction). A metastable hadronic configuration

corresponds to a local minimum of the relevant thermodynamic potential, while the fully converted SQM configuration corresponds to the global minimum. The critical SQM droplet is identified with a saddle point: a maximum along the droplet–volume direction and a minimum along all other accessible directions. Both thermal nucleation (overcoming the barrier through thermal fluctuations) and quantum nucleation (tunnelling through the barrier) were discussed.

A key aspect of the analysis is the role of time scales and conserved quantities. Deconfinement is mediated by strong interactions, which act on time scales $\tau_{\rm strong} \sim 10^{-23}$ s and are many orders of magnitude faster than weak processes. As a consequence, the system can explore only those configurations that respect strong–interaction conservation laws (baryon number, non–leptonic electric charge and strangeness, or equivalently the net u, d, s quark numbers). Whether these conserved numbers are enforced locally in each phase or only globally across the system is not fixed a priori and depends on the efficiency of transport and of interfacial exchange of conserved charges. A standard approach in the literature is the *frozen–flavor* limit, in which the droplet simply inherits the local composition of the surrounding hadronic phase. In this picture, the hadronic phase is assumed to be uniform in composition, *i.e.* its local composition is taken to coincide everywhere with the bulk–equilibrium average.

The thesis investigates the role of *thermal (statistical) fluctuations* of the hadronic composition. At the temperatures characteristic of PNSs and merger remnants, the hadronic composition fluctuates around its bulk–equilibrium values. Since nucleation is a local process, the first critical droplet tends to form in subregions whose instantaneous composition is, by chance, more favorable to SQM than the global average. This was captured in a "thermal–fluctuation" approach, in which charge and flavor fluctuations are included in the construction of the barrier. It was found that allowing for composition fluctuations systematically lowers the nucleation barrier, increases the nucleation rate and broadens the range of stellar conditions compatible with conversion to QSs.

However, not all thermodynamically allowed configurations are necessarily dynamically accessible on the finite dynamical timescales of compact star evolution. To encode these kinematic constraints, a *reduced–volume* prescription was introduced, in which fluctuations and exchange of conserved charges are allowed only within a finite reservoir surrounding the droplet. This construction interpolates between the frozen–flavor and fluctuation–assisted limits and yields more realistic estimates of nucleation rates in astrophysical conditions. The impact of electric charge neutrality, Coulomb energy, charge screening and color superconductivity in the quark phase on the structure of the critical droplet and on the nucleation conditions was also investigated, showing that color superconductivity can significantly modify the barrier and hence the available parameter space for nucleation.

Chapter 5 applied the nucleation formalism to specific astrophysical scenarios and illustrated how it can be coupled to time–dependent evolutions, given a thermodynamic trajectory (either from a full hydrodynamical simulation or from a simplified evolutionary model). In the context of astrophysical simulations, the formalism can be used locally in each cell and at each timestep to compute the expected number of nucleation events, so that conversion is triggered stochastically whenever at least one critical

droplet forms in the computational domain. In the absence of a full simulation, one can instead compute the nucleation rate along a prescribed evolutionary path and compare the corresponding nucleation timescale with the dynamical timescale of the system at a given stage, thereby identifying whether and when a critical droplet is likely to form and translating microphysical assumptions into macroscopic outcomes (conversion or no conversion).

The latter strategy was first employed to study PNS evolution in the two–families scenario. Using fluctuation–assisted nucleation and an approximate treatment of color superconductivity, the thesis explored the conditions under which a PNS can convert to a QS before cooling and deleptonization. The analysis showed that nucleation is highly sensitive to the poorly known microphysical parameters, such as the Bag constant of the unpaired phase, the surface tension between hadronic matter and SQM, and the pairing gap in the color–superconducting phase. For plausible parameter choices, there exist regions of parameter space where a fraction of PNSs convert to QSs while lighter PNSs remain as NSs, leading to a natural coexistence of NSs and QSs. Other regions correspond to nearly complete conversion, where all sufficiently massive PNSs become QSs, or to no conversion at all. Color superconductivity was found to play a particularly important role, often shrinking the parameter space compatible with long–lived metastable NSs unless different effective Bag constants characterize the unpaired and superconducting phases.

The reduced–volume approach was then explored to address the possibility that a hadronic NS surviving the PNS phase can later convert by mass accretion, after it has cooled and deleptonized. Preliminary applications of this scheme to cold, accreting NSs indicate that finite diffusion volumes can substantially modify the nucleation conditions, opening a plausible channel for delayed conversion of massive NSs into QSs while highlighting the need for a more systematic exploration of this scenario in future work.

Finally, a simplified nucleation prescription was employed in simulations of CCSNe in compact progenitor–NS binaries, where a newborn NS and its NS companion accrete matter from the SN ejecta. Hydrodynamics simulations were used to compute the time–dependent accretion histories, which were then coupled to an approximate nucleation criterion based on a critical central density (or strangeness content) for SQM formation. If this threshold is crossed during the minutes–long accretion phase, one or both NSs can convert into QSs, yielding NS–NS, NS–QS or QS–QS remnants and releasing substantial energy long after the original core collapse. This provides a concrete example of how NS–QS or QS–QS binary systems may form.

The nucleation approach developed in this thesis is necessarily approximate. The description is formulated at the level of thermodynamic potentials and mean–field EOSs. A full treatment would require a unified Lagrangian for hadronic and quark degrees of freedom, a self–consistent computation of surface tension and pairing properties, and an explicit treatment of fluctuations beyond mean field, including the dynamics of the relevant order parameters. Likewise, a complete understanding of which configurations are dynamically accessible would demand detailed calculations of reaction rates, transport coefficients and diffusion lengths on the relevant timescales.

Moreover, several key parameters entering the nucleation problem (such as the surface tension at the hadron–quark interface, the effective Bag constants of the unpaired and color–superconducting phases, and the magnitude and density dependence of the pairing gap) are still poorly constrained. Color superconductivity has been included here via an approximate prescription that is adequate for assessing its qualitative impact but should be refined in future work. Because of these uncertainties, nucleation studies cannot yet provide sharp, model–independent predictions; instead, they delineate regions of parameter space compatible with, or excluded by, various astrophysical outcomes.

Despite these limitations, some qualitative lessons should be kept in mind. If the deconfinement transition in dense matter is indeed of first order, it need not to follow the equilibrium mixed–phase trajectory: it can proceed out of equilibrium through the decay of a metastable hadronic state. In the two–families scenario this is the defining feature, but even in the standard one–family picture it would be interesting to quantify whether nucleation truly provides only minor corrections to the equilibrium construction, or whether, in some regions of parameter space, it can significantly delay deconfinement. Moreover, it could be possible that some astrophysical phenomena usually associated with very sharp transitions in the EOS, and often modelled via ad hoc Maxwell constructions, might instead be explained by nucleation and subsequent non–equilibrium conversion, even in situations where a strict Maxwell construction is thermodynamically inconsistent. The mixed–phase and nucleation frameworks developed in this thesis provide concrete tools for exploring this idea.

Looking ahead, several directions appear particularly interesting. On the microphysical side, it will be important to couple the mixed–phase and nucleation formalisms to more advanced EOSs in which hadrons and quarks are treated within a unified approach, and to compute surface tension, pairing and fluctuation effects as self–consistent outputs rather than external inputs. On the astrophysical side, the nucleation module can be embedded directly into multidimensional simulations of CCSNe and BCSMs, or used to post–process their thermodynamic histories to model the phase–transition trigger in a consistent way. A natural next step is to improve the description of the subsequent out–of–equilibrium conversion (or burning) after the decay of the metastable state, coupling the microphysics of front propagation to the global dynamics of the system. Beyond compact stars, it would also be valuable to investigate how analogous nucleation mechanisms might operate in heavy–ion collisions or in the early Universe, and to explore possible analogue laboratory systems in which the decay of a metastable phase can be studied under controlled conditions.

Finally, the rapid development of multi–messenger astronomy, including the advent of third–generation gravitational–wave detectors and improved X–ray missions, will provide increasingly detailed data on compact stars and their transients. To take full advantage of these observations, complemented by constraints from heavy–ion collisions and the early Universe, it will be essential to identify deconfinement signatures as robust and model–independent as possible, so as to turn deconfinement from a purely theoretical possibility into a testable property of dense QCD matter.

Appendix A

Phase–equilibrium conditions in first–order phase transitions

In this appendix, we derive the equilibrium conditions for a multi–component system in which two phases, hadronic (H) and quark (Q), can coexist in a first–order phase transition. We track all conserved charges relevant to compact star applications and allow for the possibility that some charges are conserved globally (shared between phases) while others are conserved locally (separately in each phase).

We consider the quark phase to occupy a spherical droplet of volume $V_Q = \frac{4\pi}{3}R^3$ and surface area $\mathcal{S}_Q = 4\pi R^2$, embedded in an extended hadronic phase of volume V_H; the total volume is $V = V_H + V_Q$. This can be generalized to arbitrary geometries by replacing $\mathcal{S}_Q(R)$ with the appropriate surface functional and, if needed, including Coulomb terms (see Sec. 4.3.5). In the usual bulk mixed–phase constructions, surface and Coulomb contributions are dropped and their effect is mimicked by imposing either local or global charge neutrality (Sec. 1.3.1).

Throughout this appendix, we use the total particle numbers N_i as independent variables. Equivalent derivations can be done in terms of number densities n_i or chemical potentials μ_i, provided the appropriate thermodynamic potential is used.

A.1 Free energy and charges

The total free energy of the two–phase system is

$$F\Big(\{N_h^H\},\{N_q^Q\},V_H,V_Q,T\Big) = F_H\Big(\{N_h^H\},V_H,T\Big) + F_Q\Big(\{N_q^Q\},V_Q,T\Big) + \mathcal{S}_Q(V_Q)\,\sigma, \tag{A.1}$$

where N_i^I is the net number of particles i in phase $I = H, Q$, V_I the volume of that phase, and σ the surface tension between the two phases. The sets $h = p, n, \Lambda, \ldots, e, \nu_e$ and $q = u, d, s, e, \nu_e$ include all hadronic and quark degrees of freedom considered in the EOSs. The bulk contributions F_H and F_Q are computed from the homogeneous EOSs while finite–size effects are included only for the quark droplet through the surface term. We neglect here the Coulomb self–energy of a charged droplet; its effect is discussed in

Sec. 4.3.5.

It is convenient to trade the detailed particle content for conserved charges. We consider (as in Sec. 2.5):

- baryon number B,
- nonleptonic (hadronic+quark) electric charge C,
- strangeness S (defined such that $S_s = +1$),
- total electric charge $Q_{\rm tot}$ (including leptons),
- electron–family lepton number L.

The corresponding global conserved numbers are

$$N_i = N_i^H + N_i^Q, \qquad i = B, C, S, L, Q_{\rm tot}, \tag{A.2}$$

$$V = V_H + V_Q. \tag{A.3}$$

In each phase, we define charge fractions with respect to the phase baryon number N_B^I and global fractions with respect to the total baryon number N_B:

$$Y_i^I = \frac{N_i^I}{N_B^I}, \qquad i = B, C, S, L, Q_{\rm tot}, \quad I = H, Q, \tag{A.4}$$

$$Y_i = \frac{N_i}{N_B}, \qquad i = B, C, S, L, Q_{\rm tot}. \tag{A.5}$$

(Any positive conserved number could play the role of the denominator; B is the most natural choice.)

A crucial step in any phase–equilibrium analysis is to specify which charges are conserved and whether they are conserved *globally* (shared between phases) or *locally* (separately in each phase) [109]. For each charge one may have:

$$\text{global conservation:} \qquad \bar{N}_i = N_i^H + N_i^Q = \text{const}, \tag{A.6}$$

$$\text{local conservation:} \qquad \bar{Y}_i = Y_i^H = Y_i^Q = \text{const}. \tag{A.7}$$

A bar indicates that the corresponding quantity is externally fixed.

In terms of densities, Eq. (A.6) becomes

$$V\,\bar{n}_i = V_H n_i^H + V_Q n_i^Q, \tag{A.8}$$

$$\bar{n}_i = (1-\chi)\, n_i^H + \chi\, n_i^Q, \tag{A.9}$$

where $\chi \equiv V_Q/V$ is the volume fraction occupied by the quark phase, and $n_i^I = N_i^I/V_I$ is the density of charge i in the *homogeneous* phase I. The true mixed–phase densities are $(1-\chi)\, n_i^H$ and $\chi\, n_i^Q$.

The free energy per unit volume is

$$f\Big(\{n_h^H\},\{n_q^Q\},\chi,T\Big) = (1-\chi)\, f_H\Big(\{n_h^H\},T\Big) + \chi\, f_Q\Big(\{n_q^Q\},T\Big) + \frac{\mathcal{S}_Q(V_Q)}{V}\,\sigma, \quad \text{(A.10)}$$

where $f_I = F_I/V_I$ is the bulk free energy density in phase $I = H, Q$. Again, n_i^I are the homogeneous–phase densities; the mixed–phase contribution of each region is weighted by $(1-\chi)$ and χ.

Which set of charges is effectively conserved depends on the reactions allowed to proceed. Strong interactions conserve $B, C, S, L, Q_{\rm tot}$; weak nonleptonic reactions such as $u + d \leftrightarrow u + s$ violate S but conserve $B, C, L, Q_{\rm tot}$; semileptonic (β) reactions such as $u + e^- \leftrightarrow d + \nu_e$ violate C but conserve $B, L, Q_{\rm tot}$. In general, one expects the system to rearrange globally conserved charges between the phases in order to minimize its free energy [27]. Local conservation (e.g., local charge neutrality) must be imposed only when transfer of the corresponding charge between phases is suppressed, for example by charge–screening or by slow reaction rates compared to the system lifetime.

A careful discussion including weak–interaction timescales can be found in [109]. Mixed local/global electric charge neutrality constraints and their impact on phase transitions at $T = 0$ and $T \neq 0$ are discussed in [40, 41].

In what follows, we assume global electric neutrality, $Q_{\rm tot} = 0$, which is relevant for compact–star matter, but the derivation can be generalized to $Q_{\rm tot} \neq 0$.

Finally, we stress that the equilibrium conditions derived below identify the *state* that minimizes F under the specified constraints. Whether a real system actually reaches that state depends on microphysics: reaction rates, transport, screening, etc. Full equilibrium is attained only if the relevant reactions occur at a rate that is sufficiently fast compared to the system's lifetime.

A.2 Equilibrium conditions

Let us compute the equilibrium conditions explicitly. We will carry out all steps in detail for the first case; the remaining cases are treated with the same method and will not be reported here.

A.2.1 Global $B, C, S, L, Q_{\rm tot}$

We start from the most general case in which all charges $B, C, S, L, Q_{\rm tot}$ are globally conserved. The independent extensive variables are then $\{N_i^I\}$ and V_I ($i = B, C, S, L, Q_{\rm tot}$, $I = H, Q$), while the fixed input quantities are $\bar{N}_B$, $\bar{N}_C$, $\bar{N}_S$, $\bar{N}_L$, $\bar{N}_{Q_{\rm tot}} = 0$, the total volume V, and the temperature T. Using the global conservation

relations (A.6) and $V = V_H + V_Q$ we can eliminate

$$N_B^Q = \bar{N}_B - N_B^H, \tag{A.11}$$
$$N_C^Q = \bar{N}_C - N_C^H, \tag{A.12}$$
$$N_S^Q = \bar{N}_S - N_S^H, \tag{A.13}$$
$$N_L^Q = \bar{N}_L - N_L^H, \tag{A.14}$$
$$N_{Q_{\rm tot}}^Q = \bar{N}_{Q_{\rm tot}} - N_{Q_{\rm tot}}^H = -N_{Q_{\rm tot}}^H, \tag{A.15}$$
$$V_Q = V - V_H. \tag{A.16}$$

and we remain with the independent variables $\{N_i^H\}$ and V_H.

Equilibrium is obtained by minimizing F with respect to all independent variables at fixed $\bar{N}_i$, V, and T. The derivative with respect to N_B^H gives

$$0 = \left.\frac{\partial F}{\partial N_B^H}\right|_{\{N_{j\neq B}^H\},V_H,T} \tag{A.17}$$
$$= \left.\frac{\partial F_H}{\partial N_B^H}\right|_{\{N_{j\neq B}^H\},V_H,T} + \left.\frac{\partial F_Q}{\partial N_B^Q}\right|_{\{N_{j\neq B}^Q\},V_Q,T} \frac{\partial N_B^Q}{\partial N_B^H} \tag{A.18}$$
$$= \mu_B^H - \mu_B^Q, \tag{A.19}$$

so that

$$\mu_B^H = \mu_B^Q. \tag{A.20}$$

Here $\mu_i^I \equiv \partial F_I / \partial N_i^I$ is the chemical potential conjugate to charge i in phase I. Repeating the argument for N_C^H, N_S^H, N_L^H, and $N_{Q_{\rm tot}}^H$ yields

$$\mu_C^H = \mu_C^Q, \tag{A.21}$$
$$\mu_S^H = \mu_S^Q, \tag{A.22}$$
$$\mu_L^H = \mu_L^Q, \tag{A.23}$$
$$\mu_{Q_{\rm tot}}^H = \mu_{Q_{\rm tot}}^Q. \tag{A.24}$$

Thus, for each globally conserved charge there is a corresponding common chemical potential across the two phases.

Mechanical equilibrium follows from the minimization with respect to V_H:

$$0 = \left.\frac{\partial F}{\partial V_H}\right|_{\{N_i^H\},T} \tag{A.25}$$
$$= \left.\frac{\partial F_H}{\partial V_H}\right|_{\{N_i^H\},T} + \left.\frac{\partial F_Q}{\partial V_Q}\right|_{\{N_i^Q\},T} \frac{\partial V_Q}{\partial V_H} + \sigma \frac{\partial \mathcal{S}_Q}{\partial R} \left(\frac{\partial V_Q}{\partial R}\right)^{-1} \frac{\partial V_Q}{\partial V_H}. \tag{A.26}$$

Using

$$P_I = -\left.\frac{\partial F_I}{\partial V_I}\right|_{\{N_i^I\},T}, \qquad V_Q = \frac{4\pi}{3}R^3, \quad \mathcal{S}_Q = 4\pi R^2, \tag{A.27}$$

we obtain

$$P_H = P_Q - \frac{2\sigma}{R}. \tag{A.28}$$

The above conditions are written in terms of the conjugate potentials $\mu_B, \mu_C, \mu_S, \mu_L, \mu_{Q_{\rm tot}}$. For practical applications, it is often more convenient to rewrite them in terms of particle chemical potentials.

For example, note that B, C and S can be uniquely mapped to the quark flavor numbers u, d, s:

$$N_B^Q = \tfrac{1}{3}(N_u^Q + N_d^Q + N_s^Q), \tag{A.29}$$
$$N_C^Q = \tfrac{2}{3}N_u^Q - \tfrac{1}{3}N_d^Q - \tfrac{1}{3}N_s^Q, \tag{A.30}$$
$$N_S^Q = N_s^Q, \tag{A.31}$$

which can be inverted to

$$N_u^Q = N_B^Q + N_C^Q, \tag{A.32}$$
$$N_d^Q = 2N_B^Q - N_C^Q - N_S^Q, \tag{A.33}$$
$$N_s^Q = N_S^Q. \tag{A.34}$$

Using the chain rule, one finds

$$\left.\frac{\partial F_Q}{\partial N_B^Q}\right|_{\{N_{j\neq B}^Q\},V_Q,T} = \left.\frac{\partial F_Q}{\partial N_u^Q}\right|_{N_d^Q,N_s^Q,V_Q,T} \left.\frac{\partial N_u^Q}{\partial N_B^Q}\right|_{N_C^Q,N_S^Q} + \tag{A.35}$$
$$+ \left.\frac{\partial F_Q}{\partial N_d^Q}\right|_{N_u^Q,N_s^Q,V_Q,T} \left.\frac{\partial N_d^Q}{\partial N_B^Q}\right|_{N_C^Q,N_S^Q} + \tag{A.36}$$
$$+ \left.\frac{\partial F_Q}{\partial N_s^Q}\right|_{N_u^Q,N_d^Q,V_Q,T} \left.\frac{\partial N_s^Q}{\partial N_B^Q}\right|_{N_C^Q,N_S^Q} \tag{A.37}$$
$$\mu_B^Q = \mu_u^Q + 2\mu_d^Q, \tag{A.38}$$

and in the same way

$$\mu_C^Q = \mu_u^Q - \mu_d^Q, \tag{A.39}$$
$$\mu_S^Q = \mu_s^Q - \mu_d^Q. \tag{A.40}$$

In the hadronic phase, a minimal mapping onto (n, p, Λ) gives

$$\mu_B^H = \mu_n^H, \tag{A.41}$$
$$\mu_C^H = \mu_p^H - \mu_n^H, \tag{A.42}$$
$$\mu_S^H = \mu_\Lambda^H - \mu_n^H. \tag{A.43}$$

Combining these with the equalities of μ_B, μ_C, μ_S across the phases one recovers the

familiar quark–hadron equilibrium relations, e.g.

$$\mu_n^H = \mu_u^Q + 2\mu_d^Q, \tag{A.44}$$
$$\mu_p^H = 2\mu_u^Q + \mu_d^Q, \tag{A.45}$$
$$\mu_\Lambda^H = \mu_u^Q + \mu_d^Q + \mu_s^Q. \tag{A.46}$$

Similarly, we can remap $(C, L, Q_{\rm tot})$ into (C, e, ν_e) using

$$N_C^I = N_C^I \tag{A.47}$$
$$N_L^I = N_e^I + N_{\nu_e}^I, \tag{A.48}$$
$$N_{Q_{\rm tot}}^I = N_C^I - N_e^I, \tag{A.49}$$

so that one finds, using again the chain rule as above,

$$\mu_L^I = \mu_{\nu_e}^I, \tag{A.50}$$
$$\mu_{Q_{\rm tot}}^I = -\mu_e^I + \mu_{\nu_e}^I, \tag{A.51}$$

and the equalities of μ_L and $\mu_{Q_{\rm tot}}$ between phases translate into $\mu_{\nu_e}^H = \mu_{\nu_e}^Q$ and $\mu_e^H = \mu_e^Q$.

Up to this point, we have treated all N_i as *net* numbers, so for instance $N_s^Q = 0$ does not preclude a finite density of s and $\bar{s}$, only that they are equal. One may separate explicitly particle and antiparticle numbers $N_{i(+)}^I$, $N_{i(-)}^I$ with $N_i^I = N_{i(+)}^I - N_{i(-)}^I$ and redo the minimization. This yields the additional relations

$$\mu_{i(-)}^I = -\mu_{i(+)}^I \equiv -\mu_i^I, \tag{A.52}$$

as expected for chemical equilibrium between particles and antiparticles.

A.2.2 Global B, C, S, L and local charge neutrality

Let us now consider the case in which the total electric charge $Q_{\rm tot}$ is *locally* conserved and vanishes in each phase, so that $\bar{Y}_{Q_{\rm tot}} = 0$ and

$$Y_{Q_{\rm tot}}^H = Y_{Q_{\rm tot}}^Q = 0. \tag{A.53}$$

Compared to the fully global case, the global constraint $\bar{N}_{Q_{\rm tot}} = N_{Q_{\rm tot}}^H + N_{Q_{\rm tot}}^Q$ is replaced by two local constraints,

$$\bar{Y}_{Q_{\rm tot}} = \frac{N_{Q_{\rm tot}}^H}{N_B^H} = \frac{N_{Q_{\rm tot}}^Q}{N_B^Q}, \tag{A.54}$$

so we gain one additional constraint and thus lose one independent variable. Using the global constraints on B, C, S, L and the fixed total volume V, we can eliminate

$N_B^Q, N_C^Q, N_S^Q, N_{Q_{\rm tot}}^H, N_{Q_{\rm tot}}^Q, V_Q$ in favour of $N_B^H, N_C^H, N_S^H, N_L^H, V_H$:

$$N_B^Q = \bar{N}_B - N_B^H, \tag{A.55}$$
$$N_C^Q = \bar{N}_C - N_C^H, \tag{A.56}$$
$$N_S^Q = \bar{N}_S - N_S^H, \tag{A.57}$$
$$N_{Q_{\rm tot}}^H = N_B^H \bar{Y}_{Q_{\rm tot}} = 0, \tag{A.58}$$
$$N_{Q_{\rm tot}}^Q = (N_B - N_B^H)\, \bar{Y}_{Q_{\rm tot}} = 0, \tag{A.59}$$
$$V_Q = V - V_H. \tag{A.60}$$

The equilibrium conditions are obtained, as before, by minimizing the free energy with respect to the remaining independent variables. The only stationarity condition that changes with respect to the fully global case is the one with respect to N_B^H:

$$0 = \left.\frac{\partial F}{\partial N_B^H}\right|_{\{N_{i\neq B}^H\},V_H,T} \tag{A.61}$$
$$= \left.\frac{\partial F_H}{\partial N_B^H}\right|_{\{N_{i\neq B}^H\},V_H,T} + \left.\frac{\partial F_H}{\partial N_{Q_{\rm tot}}^H}\right|_{\{N_{i\neq Q_{\rm tot}}^H\},V_H,T} \frac{\partial N_{Q_{\rm tot}}^H}{\partial N_B^H} \tag{A.62}$$
$$+ \left.\frac{\partial F_Q}{\partial N_B^Q}\right|_{\{N_{i\neq B}^Q\},V_Q,T} \frac{\partial N_B^Q}{\partial N_B^H} + \left.\frac{\partial F_Q}{\partial N_{Q_{\rm tot}}^Q}\right|_{\{N_{i\neq Q_{\rm tot}}^Q\},V_Q,T} \frac{\partial N_{Q_{\rm tot}}^Q}{\partial N_B^H}. \tag{A.63}$$

Using $N_{Q_{\rm tot}}^H = N_B^H \bar{Y}_{Q_{\rm tot}}$ and $N_{Q_{\rm tot}}^Q = (N_B - N_B^H)\bar{Y}_{Q_{\rm tot}}$, this can be written as

$$\mu_B^H + \bar{Y}_{Q_{\rm tot}} \mu_{Q_{\rm tot}}^H = \mu_B^Q + \bar{Y}_{Q_{\rm tot}} \mu_{Q_{\rm tot}}^Q. \tag{A.64}$$

Since local neutrality implies $\bar{Y}_{Q_{\rm tot}} = 0$, we recover

$$\mu_B^H = \mu_B^Q. \tag{A.65}$$

The remaining chemical–equilibrium conditions are unchanged with respect to the fully global case, *except* that we no longer have $\mu_{Q_{\rm tot}}^H = \mu_{Q_{\rm tot}}^Q$:

$$\mu_C^H = \mu_C^Q, \tag{A.66}$$
$$\mu_S^H = \mu_S^Q, \tag{A.67}$$
$$\mu_L^H = \mu_L^Q. \tag{A.68}$$

It is instructive to rewrite these conditions in terms of particle chemical potentials by mapping

$$(N_C^I, N_L^I, N_{Q_{\rm tot}}^I) \longrightarrow (N_C^I, N_e^I, N_{\nu_e}^I),$$

and using Eqs. (A.50)–(A.51). Inserting those relations into the above equilibrium

conditions one finds

$$\mu_B^H - \bar{Y}_{Q_{\rm tot}}\mu_e^H = \mu_B^Q - \bar{Y}_{Q_{\rm tot}}\mu_e^Q \;\Rightarrow\; \mu_B^H = \mu_B^Q \quad (\bar{Y}_{Q_{\rm tot}} = 0), \tag{A.69}$$

$$\mu_C^H + \mu_e^H = \mu_C^Q + \mu_e^Q, \tag{A.70}$$

$$\mu_S^H = \mu_S^Q, \tag{A.71}$$

$$\mu_{\nu_e}^H = \mu_{\nu_e}^Q. \tag{A.72}$$

Thus, when $Q_{\rm tot}$ is locally conserved (local charge neutrality in each phase), there remain four independent continuity relations between the particle chemical potentials, corresponding to the four globally conserved charges B, C, S, L.

A.2.3 Global $B, C, L, Q_{\rm tot}$ and local S

We now consider the case in which baryon number, nonleptonic charge, lepton number and total electric charge are globally conserved, while strangeness is conserved *locally* in each phase. This means that the strangeness fraction is the same in H and Q,

$$Y_S^H = Y_S^Q = \bar{Y}_S, \tag{A.73}$$

so that S cannot be exchanged between the phases.

Repeating the minimization of the free energy with the corresponding set of constraints we obtain the chemical–equilibrium conditions

$$\mu_B^H + \bar{Y}_S\,\mu_S^H = \mu_B^Q + \bar{Y}_S\,\mu_S^Q, \tag{A.74}$$

$$\mu_C^H = \mu_C^Q, \tag{A.75}$$

$$\mu_L^H = \mu_L^Q, \tag{A.76}$$

$$\mu_{Q_{\rm tot}}^H = \mu_{Q_{\rm tot}}^Q. \tag{A.77}$$

Thus, the locally conserved charge S does not lead to a separate equality $\mu_S^H = \mu_S^Q$; instead, it appears in the combination $\mu_B + \bar{Y}_S\mu_S$ that is common to both phases.

If we remap the variables in each phase as

$$(N_B^I, N_C^I, N_S^I, N_L^I, N_{Q_{\rm tot}}^I) \;\longrightarrow\; (N_B^I, N_C^I, N_S^I, N_e^I, N_{\nu_e}^I),$$

and use the relations derived in the previous subsection between $(\mu_B, \mu_C, \mu_S, \mu_L, \mu_{Q_{\rm tot}})$ and $(\mu_B, \mu_C, \mu_S, \mu_e, \mu_{\nu_e})$, the above conditions become

$$\mu_B^H + \bar{Y}_S\,\mu_S^H = \mu_B^Q + \bar{Y}_S\,\mu_S^Q, \tag{A.78}$$

$$\mu_C^H = \mu_C^Q, \tag{A.79}$$

$$\mu_e^H = \mu_e^Q, \tag{A.80}$$

$$\mu_{\nu_e}^H = \mu_{\nu_e}^Q. \tag{A.81}$$

This explicitly shows that a locally conserved charge (here S) does not acquire its own continuity condition $\mu_S^H = \mu_S^Q$, but is effectively "absorbed" into the equilibrium

condition for another conjugate potential, in this case the baryon chemical potential via the combination $\mu_B + \bar{Y}_S \mu_S$.

A.2.4 Allowing nonleptonic weak reactions: S not conserved

If nonleptonic weak reactions such as

$$u + d \leftrightarrow u + s \tag{A.82}$$

have time to equilibrate, strangeness S is no longer conserved, neither globally nor locally. The corresponding constraints are removed, and minimization of F with respect to N_S^H and N_S^Q now yields

$$\mu_S^H = 0, \qquad \mu_S^Q = 0, \tag{A.83}$$

i.e.

$$\mu_\Lambda^H = \mu_n^H, \qquad \mu_s^Q = \mu_d^Q, \tag{A.84}$$

the usual nonleptonic–equilibrium conditions. The other relations (for $B, C, L, Q_{\rm tot}$) remain as in the chosen global/local pattern.

A.2.5 Allowing β reactions: C not conserved

If in addition β reactions such as

$$u + e^- \leftrightarrow d + \nu_e \tag{A.85}$$

equilibrate, the charge C is no longer conserved. Removing the associated constraints and minimizing with respect to N_C^H and N_C^Q gives

$$\mu_C^H = 0, \qquad \mu_C^Q = 0, \tag{A.86}$$

which in particle language is just chemical β–equilibrium:

$$\mu_p^H + \mu_e^H = \mu_n^H + \mu_{\nu_e}^H, \tag{A.87}$$

$$\mu_u^Q + \mu_e^Q = \mu_d^Q + \mu_{\nu_e}^Q. \tag{A.88}$$

Again, the remaining relations for $B, S, L, Q_{\rm tot}$ follow from the chosen conservation pattern.

A.2.6 CFL matter

For a quark droplet in the CFL phase, the quark number densities satisfy

$$N_u^Q = N_d^Q = N_s^Q, \tag{A.89}$$

which implies

$$N_C^Q = 0, \qquad N_S^Q = N_B^Q. \tag{A.90}$$

In this case the minimization with respect to N_B^H and N_S^H leads to

$$\mu_B^H + \mu_S^H = \mu_B^Q + \mu_S^Q = \mu_u^Q + \mu_d^Q + \mu_s^Q, \tag{A.91}$$

i.e. equality of the Gibbs energy per baryon including strangeness between the hadronic phase and the CFL droplet. The lepton conditions are the same as in the chosen global/local pattern.

A.2.7 General conditions

For any set of globally conserved charges, the chemical equilibrium conditions are:

- one common chemical potential

$$\mu_i^H = \mu_i^Q \tag{A.92}$$

  for each globally conserved charge N_i;

- no chemical potential equality for locally conserved charges. Instead, the local constraints $Y_i^H = \bar{Y}_i = Y_i^Q$ enter in the relation between the remaining chemical potentials:

$$\mu_B^H + \sum_i \bar{Y}_i \mu_i^H = \mu_B^Q + \sum_i \bar{Y}_i \mu_i^Q \quad i = \text{all local conserved charges} \tag{A.93}$$

$$\mu_j^H = \mu_j^Q \quad j = \text{all globally conserved charges except } B \tag{A.94}$$

- mechanical equilibrium $P_H = P_Q - 2\sigma/R$ if surface tension is included.

When only a single global charge is conserved, the chemical equilibrium condition can always be written as

$$\sum_{i=B,C,S,e,\nu_e} Y_i^H \, \mu_i^H = \sum_{i=B,C,S,e,\nu_e} Y_i^Q \, \mu_i^Q, \tag{A.95}$$

where

$$\sum_i Y_i^I \, \mu_i^I = \frac{\varepsilon_I + P_I - T s_I}{n_B^I} \equiv \mu_I \tag{A.96}$$

is the Gibbs free energy per baryon in phase $I = H, Q$.

Appendix B

TOV equations

Nonrotating, spherically symmetric compact stars in general relativity are described by the Tolman–Oppenheimer–Volkoff (TOV) equations, which express hydrostatic equilibrium and mass conservation for a given equation of state (EOS) $P(\varepsilon)$ [65]:

$$\frac{dP(r)}{dr} = -\frac{G\,\varepsilon(r)\,m(r)}{r^2}\left[1+\frac{P(r)}{\varepsilon(r)}\right]\left[1+\frac{4\pi r^3 P(r)}{m(r)}\right]\left[1-\frac{2Gm(r)}{r}\right]^{-1}, \tag{B.1}$$

$$\frac{dm(r)}{dr} = 4\pi r^2 \varepsilon(r), \tag{B.2}$$

where $m(r)$ is the gravitational mass enclosed within radius r, $P(r)$ is the pressure, and $\varepsilon(r)$ is the energy density. The TOV system is solved together with an EOS $P(\varepsilon)$ by specifying the central energy density $\varepsilon_c \equiv \varepsilon(0)$ (or equivalently $P(0) = P(\varepsilon_c)$) and integrating outward until the pressure vanishes at $r = R$, which defines the stellar surface. The total gravitational mass is then $M \equiv m(R)$.

In the presence of an external gravitational field due to another compact object, a compact star is tidally deformed. The leading effect is a quadrupolar deformation characterized by the (dimensionless) tidal deformability [230, 231]

$$\Lambda = \frac{2}{3}\,k_2\,\mathcal{C}^{-5}, \tag{B.3}$$

which relates the tidally induced quadrupole moment Q_{ij} to the external quadrupolar tidal field E_{ij} through [232, 233]

$$Q_{ij} = -\Lambda\,G^4 M^5\,E_{ij}. \tag{B.4}$$

Here $\mathcal{C}$ is the compactness,

$$\mathcal{C} = G\frac{M}{R}, \tag{B.5}$$

and k_2 is the (dimensionless) quadrupolar tidal Love number, which depends on the

stellar mass and on the EOS:

$$k_2 = \frac{8}{5}\mathcal{C}^5(1-2\mathcal{C})^2\Big[2+2\mathcal{C}(Y-1)-Y\Big] \times\Bigg\{2\mathcal{C}\Big[6-3Y+3\mathcal{C}(5Y-8)\Big]+4\mathcal{C}^3\Big[13-11Y+\mathcal{C}(3Y-2)+2\mathcal{C}^2(1+Y)\Big] +3(1-2\mathcal{C})^2\Big[2-Y+2\mathcal{C}(Y-1)\Big]\ln(1-2\mathcal{C})\Bigg\}. \tag{B.6}$$

The quantity Y is defined as $Y \equiv y(R)$, where $y(r)$ satisfies the first–order differential equation

$$r\,\frac{dy(r)}{dr} + y^2(r) + y(r)\,F(r) + r^2 Q(r) = 0, \tag{B.7}$$

integrated simultaneously with Eq. (B.1). Regularity at the center imposes the boundary condition $y(0) = 2$ [231].

The functions $F(r)$ and $Q(r)$ are given by [231]

$$F(r) = \Big[1 - 4\pi G r^2\Big(\varepsilon(r) - P(r)\Big)\Big]\left[1 - \frac{2Gm(r)}{r}\right]^{-1}, \tag{B.8}$$

and

$$r^2 Q(r) = 4\pi G r^2\left[5\varepsilon(r) + 9P(r) + \frac{\varepsilon(r)+P(r)}{\partial P(r)/\partial\varepsilon(r)}\right]\left[1-\frac{2Gm(r)}{r}\right]^{-1} - 6\left[1-\frac{2Gm(r)}{r}\right]^{-1} - \frac{4G^2m^2(r)}{r^2}\left[1+\frac{4\pi r^3 P(r)}{m(r)}\right]^2\left[1-\frac{2Gm(r)}{r}\right]^{-2}. \tag{B.9}$$

An equivalent formulation for computing the tidal Love number is discussed in [28].

Finally, the total baryon number N_B of the star is obtained by integrating the proper baryon density $n_B(r)$ over the curved spacetime volume,

$$N_B = 4\pi\int_0^R dr\; r^2\, n_B(r)\,\left[1-\frac{2Gm(r)}{r}\right]^{-1/2}, \tag{B.10}$$

and the corresponding baryon mass is

$$M_B = m_B\, N_B. \tag{B.11}$$

In this work we fix the baryon mass to the atomic mass unit $m_B = 931$ MeV. Other works sometimes adopt $m_B = 939$ MeV. This choice is arbitrary as long as it is applied consistently to all objects.

Appendix C

Numeric solutions of Fermi and Bose integrals

Many of the EOS models used in this thesis require repeated evaluation of relativistic Fermi and Bose integrals over a wide range of masses, chemical potentials, and temperatures. At $T = 0$ these integrals admit simple analytic expressions, but at finite temperature $T > 0$ they must, in general, be computed numerically. Here we summarize the notation, collect the $T = 0$ formulas, and describe the finite–temperature treatment based on the Johns–Ellis–Lattimer (JEL) scheme [234], which we adopt throughout this work.

Throughout this appendix, m denotes the mass of the particle, μ its chemical potential, g_d its degeneracy factor (e.g. $g_d = 2$ for spin-1/2 baryons and leptons, $g_d = 4$ for spin-3/2 baryons, $g_d = 6$ for quarks with three colors, $g_d = 1$ for neutrinos), and

$$E(k) = \sqrt{k^2 + m^2} \tag{C.1}$$

the single–particle energy. In RMF models, the quantities that enter the integrals are the effective ones, $m \to m^*$ and $\mu \to \mu^*$.

C.1 Relativistic Fermi integrals

For a fermion species with degeneracy g_d, mass m, and chemical potential μ, the Fermi–Dirac distribution for particles is

$$\mathbf{f}(k, \mu, T, m) = \frac{1}{\exp\left[\dfrac{E(k) - \mu}{T}\right] + 1}, \tag{C.2}$$

and for antiparticles it is obtained by $\mu \to -\mu$. The thermodynamic quantities for a free relativistic Fermi gas can be written as

$$n(\mu,T) = g_d \int \frac{d^3k}{(2\pi)^3} \Big[\mathbf{f}(k,\mu,T,m) - \mathbf{f}(k,-\mu,T,m)\Big], \tag{C.3}$$

$$P(\mu,T) = g_d \int \frac{d^3k}{(2\pi)^3} \frac{k^2}{3E(k)} \Big[\mathbf{f}(k,\mu,T,m) + \mathbf{f}(k,-\mu,T,m)\Big], \tag{C.4}$$

$$\varepsilon(\mu,T) = g_d \int \frac{d^3k}{(2\pi)^3} E(k) \Big[\mathbf{f}(k,\mu,T,m) + \mathbf{f}(k,-\mu,T,m)\Big], \tag{C.5}$$

$$n_s(\mu,T) = g_d \int \frac{d^3k}{(2\pi)^3} \frac{m}{E(k)} \Big[\mathbf{f}(k,\mu,T,m) + \mathbf{f}(k,-\mu,T,m)\Big], \tag{C.6}$$

where n is the *net* number density (particles minus antiparticles), P the pressure, ε the energy density, and n_s the scalar density. The entropy density follows from

$$s(\mu,T) = \frac{\varepsilon(\mu,T) + P(\mu,T) - \mu\, n(\mu,T)}{T}. \tag{C.7}$$

Using spherical symmetry, Eqs. (C.3)–(C.6) reduce to one–dimensional integrals:

$$n(\mu,T) = \frac{g_d}{2\pi^2} \int_0^\infty k^2 \Big[\mathbf{f}(k,\mu,T,m) - \mathbf{f}(k,-\mu,T,m)\Big]\, dk, \tag{C.8}$$

$$P(\mu,T) = \frac{g_d}{2\pi^2} \frac{1}{3} \int_0^\infty \frac{k^4}{E(k)} \Big[\mathbf{f}(k,\mu,T,m) + \mathbf{f}(k,-\mu,T,m)\Big]\, dk, \tag{C.9}$$

$$\varepsilon(\mu,T) = \frac{g_d}{2\pi^2} \int_0^\infty k^2 E(k) \Big[\mathbf{f}(k,\mu,T,m) + \mathbf{f}(k,-\mu,T,m)\Big]\, dk, \tag{C.10}$$

$$n_s(\mu,T) = \frac{g_d}{2\pi^2} \int_0^\infty k^2 \frac{m}{E(k)} \Big[\mathbf{f}(k,\mu,T,m) + \mathbf{f}(k,-\mu,T,m)\Big]\, dk. \tag{C.11}$$

C.1.1 Zero temperature

At $T = 0$ the Fermi–Dirac distribution becomes a step function,

$$\mathbf{f}(k,\mu,T{=}0,m) = \Theta\Big(\mu - E(k)\Big), \tag{C.12}$$

and antiparticles are absent. The Fermi momentum is

$$k_F = \sqrt{\mu^2 - m^2}, \qquad (\mu \geq m), \tag{C.13}$$

and the integrals can be evaluated analytically. The standard results for a zero–temperature relativistic Fermi gas are

$$n(\mu,0) = \frac{g_d}{6\pi^2} k_F^3, \tag{C.14}$$

$$n_s(\mu,0) = \frac{g_d\, m}{4\pi^2}\left[k_F\,\mu - m^2 \ln\!\left(\frac{k_F+\mu}{m}\right)\right], \tag{C.15}$$

$$P(\mu,0) = \frac{g_d}{48\pi^2}\left[(2k_F^3 - 3m^2 k_F)\,\mu + 3m^4 \ln\!\left(\frac{k_F+\mu}{m}\right)\right], \tag{C.16}$$

$$\varepsilon(\mu,0) = \frac{g_d}{16\pi^2}\left[(2k_F^3 + m^2 k_F)\,\mu - m^4 \ln\!\left(\frac{k_F+\mu}{m}\right)\right]. \tag{C.17}$$

C.1.2 Finite temperature

At $T > 0$ the integrals (C.8)–(C.11) must, in general, be evaluated numerically. Direct numerical integration in (μ, T)–space can be computationally expensive and numerically delicate in highly degenerate and/or ultrarelativistic limits. To overcome this, we adopt the analytic approximation developed by Johns, Ellis, and Lattimer (JEL) [234], which expresses the thermodynamic integrals in terms of simple polynomials of suitably chosen dimensionless variables.

For fermions, the JEL scheme introduces the dimensionless quantities

$$t \equiv \frac{T}{m}, \qquad \psi \equiv \frac{\mu - m}{T}, \tag{C.18}$$

and defines a mapping $\psi \mapsto f$ through the implicit relation

$$\psi = 2\sqrt{1 + \frac{f}{a}} + \ln\!\left(\frac{\sqrt{1+f/a}-1}{\sqrt{1+f/a}+1}\right), \tag{C.19}$$

with a constant parameter a. For each (μ, T) one first computes ψ, then inverts Eq. (C.19) numerically to obtain $f(\psi)$, and finally defines the auxiliary variable

$$\phi \equiv t\,\sqrt{1 + f(\psi)}. \tag{C.20}$$

The thermodynamic quantities are then written as

$$n^{(+)}(\mu,T) = \frac{g_d}{2\pi^2}\, m^3\, \mathcal{N}_F\Big(f(\psi), \phi(\psi,t)\Big), \tag{C.21}$$

$$P^{(+)}(\mu,T) = \frac{g_d}{2\pi^2}\, m^4\, \mathcal{P}_F\Big(f(\psi), \phi(\psi,t)\Big), \tag{C.22}$$

$$\varepsilon^{(+)}(\mu,T) = \frac{g_d}{2\pi^2}\, m^4\, \mathcal{E}_F\Big(f(\psi), \phi(\psi,t)\Big) + m\, n^{(+)}(\mu,T), \tag{C.23}$$

where the superscript $(+)$ denotes the particle contribution (antiparticles are added

below), and the dimensionless functions $\mathcal{N}_F$, $\mathcal{P}_F$, and $\mathcal{E}_F$ are explicit polynomials in f and ϕ.

The pressure is approximated as

$$\mathcal{P}_F(f,\phi) = \frac{f\,\phi^{5/2}(1+\phi)^{3/2}}{(1+f)^{M+1}(1+\phi)^N} \sum_{i=0}^{M}\sum_{j=0}^{N} p_{ij}\, f^i \phi^j. \tag{C.24}$$

The number density is

$$\mathcal{N}_F(f,\phi) = \frac{f\,\phi^{3/2}(1+\phi)^{3/2}}{(1+f)^{M+\frac{1}{2}}(1+\phi)^N\sqrt{1+f/a}} \sum_{i=0}^{M}\sum_{j=0}^{N} p_{ij}\, f^i \phi^j\, \mathcal{A}_{ij}(f,\phi), \tag{C.25}$$

$$\mathcal{A}_{ij}(f,\phi) \equiv 1 + i + \left(\tfrac{1}{4} + \tfrac{j}{2} - M\right)\frac{f}{1+f} + \left(\tfrac{3}{4} - \tfrac{N}{2}\right)\frac{f\,\phi}{(1+f)(1+\phi)}. \tag{C.26}$$

The energy density is obtained from

$$\mathcal{E}_F(f,\phi) = \frac{f\,\phi^{5/2}(1+\phi)^{3/2}}{(1+f)^{M+1}(1+\phi)^N} \sum_{i=0}^{M}\sum_{j=0}^{N} p_{ij}\, f^i \phi^j\, \mathcal{B}_{ij}(\phi), \tag{C.27}$$

$$\mathcal{B}_{ij}(\phi) \equiv \frac{3}{2} + j + \left(\frac{3}{2} - N\right)\frac{\phi}{1+\phi}. \tag{C.28}$$

In this thesis we use the "constrained" JEL parameter set with

$$M = N = 3, \qquad a = 0.433, \tag{C.29}$$

and coefficients p_{ij} given by (Table 5 of [234])

$$p_{ij} = \begin{pmatrix} 5.34689 & 18.0517 & 21.3422 & 8.53240 \\ 16.8441 & 55.7051 & 63.6901 & 24.6213 \\ 17.4708 & 56.3902 & 62.1319 & 23.2602 \\ 6.07364 & 18.9992 & 20.0285 & 7.11153 \end{pmatrix}. \tag{C.30}$$

With this choice, the JEL approximation reproduces the exact Fermi integrals with relative errors $\lesssim 10^{-4}$ over the entire (μ, T) range of interest. The coefficients and prefactors are constructed so that the nonrelativistic and ultrarelativistic, degenerate and nondegenerate limits are all recovered, including the $T = 0$ expressions in Eqs. (C.14)–(C.17).

The scalar density is not fitted independently; instead, we exploit the exact relation for a free relativistic gas

$$n_s(\mu,T) = \frac{\varepsilon(\mu,T) - 3P(\mu,T)}{m}, \tag{C.31}$$

which can be easily shown analytically by replacing Eqs. (C.9, C.10), and holds for any T, μ for quasiparticles with dispersion $E(k) = \sqrt{k^2+m^2}$. In RMF applications, this relation remains valid if m is interpreted as the effective mass m^* and ε, P are

computed consistently from the quasiparticle spectrum.

In practice, we compute first the *particle* contribution $n^{(+)}(\mu,T)$, $P^{(+)}(\mu,T)$, $\varepsilon^{(+)}(\mu,T)$ using the JEL formulas, and obtain the contribution of antiparticles by the replacement $\mu \to -\mu$:

$$n(\mu,T) = n^{(+)}(\mu,T) - n^{(+)}(-\mu,T), \tag{C.32}$$

$$P(\mu,T) = P^{(+)}(\mu,T) + P^{(+)}(-\mu,T), \tag{C.33}$$

$$\varepsilon(\mu,T) = \varepsilon^{(+)}(\mu,T) + \varepsilon^{(+)}(-\mu,T), \tag{C.34}$$

and similarly for s and n_s.

C.2 Relativistic Bose integrals

For a boson species with degeneracy g_d, mass m, and chemical potential μ, the Bose–Einstein distribution for particles is

$$\mathbf{b}(k,\mu,T,m) = \frac{1}{\exp\!\left[\dfrac{E(k)-\mu}{T}\right] - 1}, \tag{C.35}$$

with the usual constraint $|\mu| \le m$ (for massive bosons) to avoid Bose–Einstein condensation. The antiparticle distribution is obtained by $\mu \to -\mu$.

The thermodynamic quantities are

$$n_b(\mu,T) = g_d \int \frac{d^3k}{(2\pi)^3} \Big[\mathbf{b}(k,\mu,T,m) - \mathbf{b}(k,-\mu,T,m)\Big], \tag{C.36}$$

$$P_b(\mu,T) = g_d \int \frac{d^3k}{(2\pi)^3} \frac{k^2}{3E(k)} \Big[\mathbf{b}(k,\mu,T,m) + \mathbf{b}(k,-\mu,T,m)\Big], \tag{C.37}$$

$$\varepsilon_b(\mu,T) = g_d \int \frac{d^3k}{(2\pi)^3} E(k) \Big[\mathbf{b}(k,\mu,T,m) + \mathbf{b}(k,-\mu,T,m)\Big], \tag{C.38}$$

and the entropy density is

$$s_b(\mu,T) = \frac{\varepsilon_b(\mu,T) + P_b(\mu,T) - \mu\, n_b(\mu,T)}{T}. \tag{C.39}$$

In one–dimensional form:

$$n_b(\mu,T) = \frac{g_d}{2\pi^2} \int_0^\infty k^2 \Big[\mathbf{b}(k,\mu,T,m) - \mathbf{b}(k,-\mu,T,m)\Big]\, dk, \tag{C.40}$$

$$P_b(\mu,T) = \frac{g_d}{2\pi^2} \frac{1}{3} \int_0^\infty \frac{k^4}{E(k)} \Big[\mathbf{b}(k,\mu,T,m) + \mathbf{b}(k,-\mu,T,m)\Big]\, dk, \tag{C.41}$$

$$\varepsilon_b(\mu,T) = \frac{g_d}{2\pi^2} \int_0^\infty k^2 E(k) \Big[\mathbf{b}(k,\mu,T,m) + \mathbf{b}(k,-\mu,T,m)\Big]\, dk. \tag{C.42}$$

In this thesis we mostly use massive bosons (mesons and, in some cases, thermal gluons) in regimes where Bose–Einstein condensation does not occur, so $|\mu| < m$ is always enforced. As in the fermionic case, it is convenient to compute first the "particle–only" integrals and then add the antiparticle contributions via $\mu \to -\mu$.

The JEL scheme has also been extended to relativistic Bose integrals [234]. For bosons one again introduces t and ψ (Eq. C.18) but uses a different mapping $\psi \mapsto h$ defined by

$$\psi = \frac{h}{\sqrt{a_b} + h} - \ln\left(\frac{\sqrt{a_b} + h}{\sqrt{a_b}}\right), \tag{C.43}$$

with a parameter a_b. For each (μ, T) we compute ψ, invert Eq. (C.43) numerically to obtain $h(\psi)$ (with μ clamped to $|\mu| < m$), and then express the thermodynamic quantities as

$$n_b^{(+)}(\mu, T) = \frac{g_d}{2\pi^2}\, m^3\, \mathcal{N}_b\Big(h(\psi), t\Big), \tag{C.44}$$

$$P_b^{(+)}(\mu, T) = \frac{g_d}{2\pi^2}\, m^4\, \mathcal{P}_b\Big(h(\psi), t\Big), \tag{C.45}$$

$$\varepsilon_b^{(+)}(\mu, T) = \frac{g_d}{2\pi^2}\, m^4\, \mathcal{E}_b\Big(h(\psi), t\Big) + m\, n_b^{(+)}(\mu, T), \tag{C.46}$$

where $\mathcal{N}_b$, $\mathcal{P}_b$, and $\mathcal{E}_b$ are again low–order polynomials in h and t. Schematically, the pressure takes the form

$$\mathcal{P}_b(h, t) = \frac{t^{5/2}(1+t)^{3/2}}{(1+h)^{M_b+1}(1+t)^{N_b}} \sum_{i=0}^{M_b} \sum_{j=0}^{N_b} p_{ij}^{(b)}\, h^i t^j, \tag{C.47}$$

with M_b, N_b and $p_{ij}^{(b)}$ chosen so that the correct nonrelativistic and ultrarelativistic limits at small and large t are exactly reproduced.

In this work we adopt the constrained bosonic JEL parameter set with

$$M_b = 3, \qquad N_b = 4, \qquad a_b = 1.040, \tag{C.48}$$

and coefficients $p_{ij}^{(b)}$ corresponding to Table 11 of [234].

$$p_{ij}^{(b)} = \begin{pmatrix} 1.68130 & 6.85060 & 10.8539 & 7.81762 & 2.16465 \\ 4 \times 1.68130 & 4 \times 6.85060 & 4 \times 10.8539 & 4 \times 7.81762 & 4 \times 2.16465 \\ 8.51373 & 35.6576 & 57.7975 & 42.4049 & 11.8321 \\ 3.47433 & 15.1995 & 25.6536 & 19.3811 & 5.54423 \end{pmatrix}.$$

As for fermions, this choice guarantees a relative accuracy better than $\sim 10^{-4}$ for the pressure and comparable accuracy for the other thermodynamic quantities over the parameter range relevant to high–energy astrophysics.

The antiparticles contribution is again obtained with $\mu \mapsto -\mu$.

References

[1] M. Buballa. "NJL model analysis of quark matter at large density". In: *Phys. Rept.* 407 (2005), pp. 205–376. DOI: 10.1016/j.physrep.2004.11.004. arXiv: hep-ph/0402234.

[2] G. Baym, T. Hatsuda, T. Kojo, P. D. Powell, Y. Song, and T. Takatsuka. "From hadrons to quarks in neutron stars: a review". In: *Rept. Prog. Phys.* 81.5 (2018), p. 056902. DOI: 10.1088/1361-6633/aaae14. arXiv: 1707.04966 [astro-ph.HE].

[3] A. R. Bodmer. "Collapsed nuclei". In: *Phys. Rev. D* 4 (1971), pp. 1601–1606. DOI: 10.1103/PhysRevD.4.1601.

[4] E. Witten. "Cosmic Separation of Phases". In: *Phys. Rev. D* 30 (1984), pp. 272–285. DOI: 10.1103/PhysRevD.30.272.

[5] M. Oertel, M. Hempel, T. Klähn, and S. Typel. "Equations of state for supernovae and compact stars". In: *Rev. Mod. Phys.* 89.1 (2017), p. 015007. DOI: 10.1103/RevModPhys.89.015007. arXiv: 1610.03361 [astro-ph.HE].

[6] C. Alcock, E. Farhi, and A. Olinto. "Strange stars". In: *Astrophys. J.* 310 (1986), pp. 261–272. DOI: 10.1086/164679.

[7] F. Weber. "Strange quark matter and compact stars". In: *Prog. Part. Nucl. Phys.* 54 (2005), pp. 193–288. DOI: 10.1016/j.ppnp.2004.07.001. arXiv: astro-ph/0407155.

[8] A. Drago, A. Lavagno, and G. Pagliara. "Can very compact and very massive neutron stars both exist?" In: *Phys. Rev. D* 89.4 (2014), p. 043014. DOI: 10.1103/PhysRevD.89.043014. arXiv: 1309.7263 [nucl-th].

[9] A. Drago, A. Lavagno, G. Pagliara, and D. Pigato. "The scenario of two families of compact stars: 1. Equations of state, mass-radius relations and binary systems". In: *Eur. Phys. J. A* 52.2 (2016), p. 40. DOI: 10.1140/epja/i2016-16040-3. arXiv: 1509.02131 [astro-ph.SR].

[10] A. Drago and G. Pagliara. "The scenario of two families of compact stars: 2. Transition from hadronic to quark matter and explosive phenomena". In: *Eur. Phys. J. A* 52.2 (2016), p. 41. DOI: 10.1140/epja/i2016-16041-2. arXiv: 1509.02134 [astro-ph.SR].

[11] J. Antoniadis et al. "A Massive Pulsar in a Compact Relativistic Binary". In: *Science* 340 (2013), p. 6131. DOI: 10.1126/science.1233232. arXiv: 1304.6875 [astro-ph.HE].

[12] M. C. Miller et al. "The Radius of PSR J0740+6620 from NICER and XMM-Newton Data". In: *Astrophys. J. Lett.* 918.2 (2021), p. L28. DOI: 10.3847/2041-8213/ac089b. arXiv: 2105.06979 [astro-ph.HE].

[13] R. W. Romani, D. Kandel, A. V. Filippenko, T. G. Brink, and W. Zheng. "PSR J0952−0607: The Fastest and Heaviest Known Galactic Neutron Star". In: *Astrophys. J. Lett.* 934.2 (2022), p. L17. DOI: 10.3847/2041-8213/ac8007. arXiv: 2207.05124 [astro-ph.HE].

[14] B. P. Abbott et al. "GW170817: Observation of Gravitational Waves from a Binary Neutron Star Inspiral". In: *Phys. Rev. Lett.* 119.16 (2017), p. 161101. DOI: 10.1103/PhysRevLett.119.161101. arXiv: 1710.05832 [gr-qc].

[15] B. P. Abbott et al. "GW170817: Measurements of neutron star radii and equation of state". In: *Phys. Rev. Lett.* 121.16 (2018), p. 161101. DOI: 10.1103/PhysRevLett.121.161101. arXiv: 1805.11581 [gr-qc].

[16] L. Mauviard et al. "A NICER view of the 1.4 solar-mass edge-on pulsar PSR J0614–3329". In: (June 2025). arXiv: 2506.14883 [astro-ph.HE].

[17] P. Danielewicz, R. Lacey, and W. G. Lynch. "Determination of the equation of state of dense matter". In: *Science* 298 (2002), pp. 1592–1596. DOI: 10.1126/science.1078070. arXiv: nucl-th/0208016.

[18] V. Doroshenko, V. Suleimanov, G. Pühlhofer, and A. Santangelo. "A strangely light neutron star within a supernova remnant". In: *Nature Astron.* 6.12 (2022), pp. 1444–1451. DOI: 10.1038/s41550-022-01800-1.

[19] R. Abbott et al. "GW190814: Gravitational Waves from the Coalescence of a 23 Solar Mass Black Hole with a 2.6 Solar Mass Compact Object". In: *Astrophys. J. Lett.* 896.2 (2020), p. L44. DOI: 10.3847/2041-8213/ab960f. arXiv: 2006.12611 [astro-ph.HE].

[20] S. Han, M. A. A. Mamun, S. Lalit, C. Constantinou, and M. Prakash. "Treating quarks within neutron stars". In: *Phys. Rev. D* 100.10 (2019), p. 103022. DOI: 10.1103/PhysRevD.100.103022. arXiv: 1906.04095 [astro-ph.HE].

[21] D. Blaschke, U. Shukla, O. Ivanytskyi, and S. Liebing. "Effect of color superconductivity on the mass of hybrid neutron stars in an effective model with perturbative QCD asymptotics". In: *Phys. Rev. D* 107.6 (2023), p. 063034. DOI: 10.1103/PhysRevD.107.063034. arXiv: 2212.14856 [nucl-th].

[22] L. Brandes and W. Weise. "Implications of latest NICER data for the neutron star equation of state". In: *Phys. Rev. D* 111.3 (2025), p. 034005. DOI: 10.1103/PhysRevD.111.034005. arXiv: 2412.05923 [nucl-th].

[23] M. Fortin, M. Oertel, and C. Providência. "Hyperons in hot dense matter: what do the constraints tell us for equation of state?" In: *Publ. Astron. Soc. Austral.* 35 (2018), p. 44. DOI: 10.1017/pasa.2018.32. arXiv: 1711.09427 [astro-ph.HE].

[24] I. Vidaña. "Neutron stars and the hyperon puzzle". In: *EPJ Web Conf.* 271 (2022), p. 09001. DOI: 10.1051/epjconf/202227109001.

[25] A. W. Steiner, M. Hempel, and T. Fischer. "Core-collapse supernova equations of state based on neutron star observations". In: *Astrophys. J.* 774 (2013), p. 17. DOI: 10.1088/0004-637X/774/1/17. arXiv: 1207.2184 [astro-ph.SR].

[26] R. O. Gomes, P. Char, and S. Schramm. "Constraining strangeness in dense matter with GW170817". In: *Astrophys. J.* 877.2 (2019), p. 139. DOI: 10.3847/1538-4357/ab1751. arXiv: 1806.04763 [nucl-th].

[27] N. K. Glendenning. "First order phase transitions with more than one conserved charge: Consequences for neutron stars". In: *Phys. Rev. D* 46 (1992), pp. 1274–1287. DOI: 10.1103/PhysRevD.46.1274.

[28] S. Typel et al. "CompOSE Reference Manual". In: *Eur. Phys. J. A* 58.11 (2022), p. 221. DOI: 10.1140/epja/s10050-022-00847-y. arXiv: 2203.03209 [astro-ph.HE].

[29] A. Bessa, E. S. Fraga, and B. W. Mintz. "Phase conversion in a weakly first-order quark-hadron transition". In: *Phys. Rev. D* 79 (2009), p. 034012. DOI: 10.1103/PhysRevD.79.034012. arXiv: 0811.4385 [hep-ph].

[30] J. S. Langer. "Statistical theory of the decay of metastable states". In: *Annals Phys.* 54 (1969), pp. 258–275. DOI: 10.1016/0003-4916(69)90153-5.

[31] A. Drago and G. Pagliara. "Combustion of a hadronic star into a quark star: the turbulent and the diffusive regimes". In: *Phys. Rev. C* 92.4 (2015), p. 045801. DOI: 10.1103/PhysRevC.92.045801. arXiv: 1506.08337 [nucl-th].

[32] G. Pagliara, M. Herzog, and F. K. Röpke. "Combustion of a neutron star into a strange quark star: The neutrino signal". In: *Phys. Rev. D* 87.10 (2013), p. 103007. DOI: 10.1103/PhysRevD.87.103007. arXiv: 1304.6884 [astro-ph.HE].

[33] A. Prakash, I. Gupta, M. Breschi, R. Kashyap, D. Radice, S. Bernuzzi, D. Logoteta, et al. "Detectability of QCD phase transitions in binary neutron star mergers: Bayesian inference with the next generation gravitational wave detectors". In: *Phys. Rev. D* 109.10 (2024), p. 103008. DOI: 10.1103/PhysRevD.109.103008. arXiv: 2310.06025 [gr-qc].

[34] R. De Pietri, A. Drago, A. Feo, G. Pagliara, M. Pasquali, S. Traversi, and G. Wiktorowicz. "Merger of compact stars in the two-families scenario". In: *Astrophys. J.* 881.2 (2019), p. 122. DOI: 10.3847/1538-4357/ab2fd0. arXiv: 1904.01545 [astro-ph.HE].

[35] T. Fischer, N.-U. F. Bastian, M.-R. Wu, P. Baklanov, E. Sorokina, S. Blinnikov, S. Typel, et al. "Quark deconfinement as a supernova explosion engine for massive blue supergiant stars". In: *Nature Astron.* 2.12 (2018), pp. 980–986. DOI: 10.1038/s41550-018-0583-0. arXiv: 1712.08788 [astro-ph.HE].

[36] T. Kuroda, T. Fischer, T. Takiwaki, and K. Kotake. "Core-collapse Supernova Simulations and the Formation of Neutron Stars, Hybrid Stars, and Black Holes". In: *Astrophys. J.* 924.1 (2022), p. 38. DOI: 10.3847/1538-4357/ac31a8. arXiv: 2109.01508 [astro-ph.HE].

[37] J. A. Pons, A. W. Steiner, M. Prakash, and J. M. Lattimer. "Evolution of protoneutron stars with quarks". In: *Phys. Rev. Lett.* 86 (2001), pp. 5223–5226. DOI: 10.1103/PhysRevLett.86.5223. arXiv: astro-ph/0102015.

[38] M. Hempel and J. Schaffner-Bielich. "Statistical Model for a Complete Supernova Equation of State". In: *Nucl. Phys. A* 837 (2010), pp. 210–254. DOI: 10.1016/j.nuclphysa.2010.02.010. arXiv: 0911.4073 [nucl-th].

[39] E. R. Most, L. J. Papenfort, V. Dexheimer, M. Hanauske, S. Schramm, H. Stöcker, and L. Rezzolla. "Signatures of quark-hadron phase transitions in general-relativistic neutron-star mergers". In: *Phys. Rev. Lett.* 122.6 (2019), p. 061101. DOI: 10.1103/PhysRevLett.122.061101. arXiv: 1807.03684 [astro-ph.HE].

[40] C. Constantinou, T. Zhao, S. Han, and M. Prakash. "Framework for phase transitions between the Maxwell and Gibbs constructions". In: *Phys. Rev. D* 107.7 (2023), p. 074013. DOI: 10.1103/PhysRevD.107.074013. arXiv: 2302.04289 [nucl-th].

[41] C. Constantinou, M. Guerrini, T. Zhao, S. Han, and M. Prakash. "Framework for phase transitions between the Maxwell and Gibbs constructions at finite temperature". In: *Phys. Rev. D* 112.9 (2025), p. 094014. DOI: 10.1103/8l3m-tdlc. arXiv: 2506.20418 [nucl-th].

[42] K. Iida and K. Sato. "Quantum nucleation of two flavor quark matter in neutron stars". In: *Prog. Theor. Phys.* 98 (1997), pp. 277–282. DOI: 10.1143/PTP.98.277. arXiv: astro-ph/9705211.

[43] I. Bombaci, D. Logoteta, I. Vidaña, and C. Providência. "Quark matter nucleation in neutron stars and astrophysical implications". In: *Eur. Phys. J. A* 52.3 (2016), p. 58. DOI: 10.1140/epja/i2016-16058-5. arXiv: 1601.04559 [astro-ph.HE].

[44] G. Lugones and A. G. Grunfeld. "Quark matter nucleation at neutron star cores: Relevance of energy-density fluctuations". In: *Int. J. Mod. Phys. E* 20 (2011). Ed. by A. Perez Martinez, C. A. Z. Vasconcellos, D. Hadjimichef, H. Perez Rojas, J. Horvath, and W. Greiner, pp. 167–174. DOI: 10.1142/S0218301311040219.

[45] M. Guerrini, G. Pagliara, A. Drago, and A. Lavagno. "Thermal Fluctuations of Matter Composition and Quark Nucleation in Compact Stars". In: *Astrophys. J.* 974.1 (2024), p. 45. DOI: 10.3847/1538-4357/ad67cc. arXiv: 2404.06463 [nucl-th].

[46] M. Guerrini, G. Pagliara, A. Lavagno, and A. Drago. "Role of thermal fluctuations in nucleation of three-flavor quark matter". In: *Universe* 11 (2025), p. 258. DOI: 10.3390/universe11080258. arXiv: 2506.00139 [nucl-th].

[47] L. M. Becerra, F. Cipolletta, A. Drago, M. Guerrini, A. Lavagno, G. Pagliara, and J. A. Rueda. "On the formation of strange quark stars from supernova in compact binaries". In: *JHEAp* 50 (2026), p. 100491. DOI: 10.1016/j.jheap.2025.100491. arXiv: 2507.22033 [astro-ph.HE].

[48] M. Mannarelli. "Meson condensation". In: *Particles* 2.3 (2019), pp. 411–443. DOI: 10.3390/particles2030025. arXiv: 1908.02042 [hep-ph].

[49] K. Aryal, C. Constantinou, R. L. S. Farias, and V. Dexheimer. "The Effect of Charge, Isospin, and Strangeness in the QCD Phase Diagram Critical End Point". In: *Universe* 7.11 (2021), p. 454. DOI: 10.3390/universe7110454. arXiv: 2109.14787 [nucl-th].

[50] C. Drischler, K. Hebeler, and A. Schwenk. "Chiral interactions up to next-to-next-to-next-to-leading order and nuclear saturation". In: *Phys. Rev. Lett.* 122.4 (2019), p. 042501. DOI: 10.1103/PhysRevLett.122.042501. arXiv: 1710.08220 [nucl-th].

[51] C. Drischler, J. W. Holt, and C. Wellenhofer. "Chiral Effective Field Theory and the High-Density Nuclear Equation of State". In: *Ann. Rev. Nucl. Part. Sci.* 71 (2021), pp. 403–432. DOI: 10.1146/annurev-nucl-102419-041903. arXiv: 2101.01709 [nucl-th].

[52] S. Borsanyi, Z. Fodor, J. N. Guenther, R. Kara, S. D. Katz, P. Parotto, A. Pasztor, et al. "QCD Crossover at Finite Chemical Potential from Lattice Simulations". In: *Phys. Rev. Lett.* 125.5 (2020), p. 052001. DOI: 10.1103/PhysRevLett.125.052001. arXiv: 2002.02821 [hep-lat].

[53] A. Sorensen et al. "Dense nuclear matter equation of state from heavy-ion collisions". In: *Prog. Part. Nucl. Phys.* 134 (2024), p. 104080. DOI: 10.1016/j.ppnp.2023.104080. arXiv: 2301.13253 [nucl-th].

[54] M. G. Alford, A. Schmitt, K. Rajagopal, and T. Schäfer. "Color superconductivity in dense quark matter". In: *Rev. Mod. Phys.* 80 (2008), pp. 1455–1515. DOI: 10.1103/RevModPhys.80.1455. arXiv: 0709.4635 [hep-ph].

[55] J. C. Collins and M. J. Perry. "Superdense Matter: Neutrons Or Asymptotically Free Quarks?" In: *Phys. Rev. Lett.* 34 (1975), p. 1353. DOI: 10.1103/PhysRevLett.34.1353.

[56] E. Annala, T. Gorda, A. Kurkela, J. Nättilä, and A. Vuorinen. "Evidence for quark-matter cores in massive neutron stars". In: *Nature Phys.* 16.9 (2020), pp. 907–910. DOI: 10.1038/s41567-020-0914-9. arXiv: 1903.09121 [astro-ph.HE].

[57] J. Madsen. "Physics and astrophysics of strange quark matter". In: *Lect. Notes Phys.* 516 (1999). Ed. by J. Cleymans, H. B. Geyer, and F. G. Scholtz, pp. 162–203. DOI: 10.1007/BFb0107314. arXiv: astro-ph/9809032.

[58] R. Anglani, R. Casalbuoni, M. Ciminale, N. Ippolito, R. Gatto, M. Mannarelli, and M. Ruggieri. "Crystalline color superconductors". In: *Rev. Mod. Phys.* 86 (2014), pp. 509–561. DOI: 10.1103/RevModPhys.86.509. arXiv: 1302.4264 [hep-ph].

[59] E. Farhi and R. L. Jaffe. "Strange Matter". In: *Phys. Rev. D* 30 (1984), p. 2379. DOI: 10.1103/PhysRevD.30.2379.

[60] S. Weissenborn, I. Sagert, G. Pagliara, M. Hempel, and J. Schaffner-Bielich. "Quark Matter In Massive Neutron Stars". In: *Astrophys. J. Lett.* 740 (2011), p. L14. DOI: 10.1088/2041-8205/740/1/L14. arXiv: 1102.2869 [astro-ph.HE].

[61] F. Di Clemente, M. Casolino, A. Drago, M. Lattanzi, and C. Ratti. "Strange quark matter as dark matter: 40 yr later, a reappraisal". In: *Mon. Not. Roy. Astron. Soc.* 537.2 (2025), pp. 1056–1069. DOI: 10.1093/mnras/staf087. arXiv: 2404.12094 [hep-ph].

[62] L. Formaggio, F. Di Clemente, G. Yadav, A. Drago, and C. Ratti. "Cosmic Trajectories calculation with state of the art lattice QCD equation of state". In: (July 2025). arXiv: 2508.00094 [astro-ph.CO].

[63] M. Prakash, I. Bombaci, M. Prakash, P. J. Ellis, J. M. Lattimer, and R. Knorren. "Composition and structure of protoneutron stars". In: *Phys. Rept.* 280 (1997), pp. 1–77. DOI: 10.1016/S0370-1573(96)00023-3. arXiv: nucl-th/9603042.

[64] A. Perego, S. Bernuzzi, and D. Radice. "Thermodynamics conditions of matter in neutron star mergers". In: *Eur. Phys. J. A* 55.8 (2019), p. 124. DOI: 10.1140/epja/i2019-12810-7. arXiv: 1903.07898 [gr-qc].

[65] N. K. Glendenning. *Compact stars: Nuclear physics, particle physics, and general relativity*. 1997.

[66] M. Alford, M. Braby, M. W. Paris, and S. Reddy. "Hybrid stars that masquerade as neutron stars". In: *Astrophys. J.* 629 (2005), pp. 969–978. DOI: 10.1086/430902. arXiv: nucl-th/0411016.

[67] A. Kurkela, E. S. Fraga, J. Schaffner-Bielich, and A. Vuorinen. "Constraining neutron star matter with Quantum Chromodynamics". In: *Astrophys. J.* 789 (2014), p. 127. DOI: 10.1088/0004-637X/789/2/127. arXiv: 1402.6618 [astro-ph.HE].

[68] L. Bonanno and A. Sedrakian. "Composition and stability of hybrid stars with hyperons and quark color-superconductivity". In: *Astron. Astrophys.* 539 (2012), A16. DOI: 10.1051/0004-6361/201117832. arXiv: 1108.0559 [astro-ph.SR].

[69] M. G. Alford, S. Han, and M. Prakash. "Generic conditions for stable hybrid stars". In: *Phys. Rev. D* 88.8 (2013), p. 083013. DOI: 10.1103/PhysRevD.88.083013. arXiv: 1302.4732 [astro-ph.SR].

[70] S. Benic, D. Blaschke, D. E. Alvarez-Castillo, T. Fischer, and S. Typel. "A new quark-hadron hybrid equation of state for astrophysics - I. High-mass twin compact stars". In: *Astron. Astrophys.* 577 (2015), A40. DOI: 10.1051/0004-6361/201425318. arXiv: 1411.2856 [astro-ph.HE].

[71] G. Montana, L. Tolos, M. Hanauske, and L. Rezzolla. "Constraining twin stars with GW170817". In: *Phys. Rev. D* 99.10 (2019), p. 103009. DOI: 10.1103/PhysRevD.99.103009. arXiv: 1811.10929 [astro-ph.HE].

[72] J. P. Carlomagno, G. A. Contrera, A. G. Grunfeld, and D. Blaschke. "Thermal twin stars within a hybrid equation of state based on a nonlocal chiral quark model compatible with modern astrophysical observations". In: *Phys. Rev. D* 109.4 (2024), p. 043050. DOI: 10.1103/PhysRevD.109.043050. arXiv: 2312.01975 [nucl-th].

[73] A. L. Watts and S. Reddy. "Magnetar oscillations pose challenges for strange stars". In: *Mon. Not. Roy. Astron. Soc.* 379 (2007), p. L63. DOI: 10.1111/j.1745-3933.2007.00336.x. arXiv: astro-ph/0609364.

[74] M. Mannarelli, G. Pagliaroli, A. Parisi, and L. Pilo. "Electromagnetic signals from bare strange stars". In: *Phys. Rev. D* 89.10 (2014), p. 103014. DOI: 10.1103/PhysRevD.89.103014. arXiv: 1403.0128 [hep-ph].

[75] M. Mannarelli, G. Pagliaroli, A. Parisi, L. Pilo, and F. Tonelli. "Torsional oscillations of nonbare strange stars". In: *Astrophys. J.* 815.2 (2015), p. 81. DOI: 10.1088/0004-637X/815/2/81. arXiv: 1504.07402 [astro-ph.SR].

[76] E. Fonseca et al. "Refined Mass and Geometric Measurements of the High-mass PSR J0740+6620". In: *Astrophys. J. Lett.* 915.1 (2021), p. L12. DOI: 10.3847/2041-8213/ac03b8. arXiv: 2104.00880 [astro-ph.HE].

[77] D. Chatterjee and I. Vidaña. "Do hyperons exist in the interior of neutron stars?" In: *Eur. Phys. J. A* 52.2 (2016), p. 29. DOI: 10.1140/epja/i2016-16029-x. arXiv: 1510.06306 [nucl-th].

[78] L. Tolos and L. Fabbietti. "Strangeness in Nuclei and Neutron Stars". In: *Prog. Part. Nucl. Phys.* 112 (2020), p. 103770. DOI: 10.1016/j.ppnp.2020.103770. arXiv: 2002.09223 [nucl-ex].

[79] A. Drago, A. Lavagno, G. Pagliara, and D. Pigato. "Early appearance of Δ isobars in neutron stars". In: *Phys. Rev. C* 90.6 (2014), p. 065809. DOI: 10.1103/PhysRevC.90.065809. arXiv: 1407.2843 [astro-ph.SR].

[80] B. P. Abbott et al. "Properties of the binary neutron star merger GW170817". In: *Phys. Rev. X* 9.1 (2019), p. 011001. DOI: 10.1103/PhysRevX.9.011001. arXiv: 1805.11579 [gr-qc].

[81] S. Vinciguerra et al. "An Updated Mass–Radius Analysis of the 2017–2018 NICER Data Set of PSR J0030+0451". In: *Astrophys. J.* 961.1 (2024), p. 62. DOI: 10.3847/1538-4357/acfb83. arXiv: 2308.09469 [astro-ph.HE].

[82] D. Choudhury et al. "A NICER View of the Nearest and Brightest Millisecond Pulsar: PSR J0437–4715". In: *Astrophys. J. Lett.* 971.1 (2024), p. L20. DOI: 10.3847/2041-8213/ad5a6f. arXiv: 2407.06789 [astro-ph.HE].

[83] T. E. Riley et al. "A NICER View of the Massive Pulsar PSR J0740+6620 Informed by Radio Timing and XMM-Newton Spectroscopy". In: *Astrophys. J. Lett.* 918.2 (2021), p. L27. DOI: 10.3847/2041-8213/ac0a81. arXiv: 2105.06980 [astro-ph.HE].

[84] J. Nättilä, M. C. Miller, A. W. Steiner, J. J. E. Kajava, V. F. Suleimanov, and J. Poutanen. "Neutron star mass and radius measurements from atmospheric model fits to X-ray burst cooling tail spectra". In: *Astron. Astrophys.* 608 (2017), A31. DOI: 10.1051/0004-6361/201731082. arXiv: 1709.09120 [astro-ph.HE].

[85] A. Nathanail, E. R. Most, and L. Rezzolla. "GW170817 and GW190814: tension on the maximum mass". In: *Astrophys. J. Lett.* 908.2 (2021), p. L28. DOI: 10.3847/2041-8213/abdfc6. arXiv: 2101.01735 [astro-ph.HE].

[86] Y. Suwa, T. Yoshida, M. Shibata, H. Umeda, and K. Takahashi. "On the minimum mass of neutron stars". In: *Mon. Not. Roy. Astron. Soc.* 481.3 (2018), pp. 3305–3312. DOI: 10.1093/mnras/sty2460. arXiv: 1808.02328 [astro-ph.HE].

[87] F. Di Clemente, A. Drago, and G. Pagliara. "Is the Compact Object Associated with HESS J1731-347 a Strange Quark Star? A Possible Astrophysical Scenario for Its Formation". In: *Astrophys. J.* 967.2 (2024), p. 159. DOI: 10.3847/1538-4357/ad445b. arXiv: 2211.07485 [astro-ph.HE].

[88] V. Sagun, E. Giangrandi, T. Dietrich, O. Ivanytskyi, R. Negreiros, and C. Providência. "What Is the Nature of the HESS J1731-347 Compact Object?" In: *Astrophys. J.* 958.1 (2023), p. 49. DOI: 10.3847/1538-4357/acfc9e. arXiv: 2306.12326 [astro-ph.HE].

[89] T. Salmi et al. "A NICER View of PSR J1231−1411: A Complex Case". In: *Astrophys. J.* 976.1 (2024), p. 58. DOI: 10.3847/1538-4357/ad81d2. arXiv: 2409.14923 [astro-ph.HE].

[90] O. Ivanytskyi and D. Blaschke. "Density functional approach to quark matter with confinement and color superconductivity". In: *Phys. Rev. D* 105.11 (2022), p. 114042. DOI: 10.1103/PhysRevD.105.114042. arXiv: 2204.03611 [nucl-th].

[91] C. Gärtlein, O. Ivanytskyi, V. Sagun, and D. Blaschke. "Hybrid star phenomenology from the properties of the special point". In: *Phys. Rev. D* 108.11 (2023), p. 114028. DOI: 10.1103/PhysRevD.108.114028. arXiv: 2301.10765 [nucl-th].

[92] C. Gärtlein, O. Ivanytskyi, V. Sagun, and I. Lopes. "Color-superconducting quarkyonic matter". In: (Sept. 2025). arXiv: 2509.03517 [nucl-th].

[93] A. Ayriyan, O. Ivanytskyi, and D. Blaschke. "Bayesian inference favors quark matter in neutron star interiors". In: (Sept. 2025). arXiv: 2509.02554 [nucl-th].

[94] I. Bombaci, A. Drago, D. Logoteta, G. Pagliara, and I. Vidaña. "Was GW190814 a Black Hole–Strange Quark Star System?" In: *Phys. Rev. Lett.* 126.16 (2021), p. 162702. DOI: 10.1103/PhysRevLett.126.162702. arXiv: 2010.01509 [nucl-th].

[95] D. Logoteta, I. Vidana, and I. Bombaci. "Impact of chiral hyperonic three-body forces on neutron stars". In: *Eur. Phys. J. A* 55.11 (2019), p. 207. DOI: 10.1140/epja/i2019-12909-9. arXiv: 1906.11722 [nucl-th].

[96] A. Sedrakian, J.-J. Li, and F. Weber. "Heavy baryons in compact stars". In: *Prog. Part. Nucl. Phys.* 131 (2023), p. 104041. DOI: 10.1016/j.ppnp.2023.104041. arXiv: 2212.01086 [nucl-th].

[97] V. Parmar, V. B. Thapa, M. Sinha, and I. Bombaci. "Exploring the Δ-resonance in neutron stars: Implications from astrophysical and nuclear observations". In: *Phys. Rev. D* 112.2 (2025), p. 023016. DOI: 10.1103/643w-c2ly. arXiv: 2503.07256 [astro-ph.HE].

[98] C. Constantinou, S. Han, P. Jaikumar, and M. Prakash. "g modes of neutron stars with hadron-to-quark crossover transitions". In: *Phys. Rev. D* 104.12 (2021), p. 123032. DOI: 10.1103/PhysRevD.104.123032. arXiv: 2109.14091 [astro-ph.HE].

[99] M. C. Miller et al. "PSR J0030+0451 Mass and Radius from *NICER* Data and Implications for the Properties of Neutron Star Matter". In: *Astrophys. J. Lett.* 887.1 (2019), p. L24. DOI: 10.3847/2041-8213/ab50c5. arXiv: 1912.05705 [astro-ph.HE].

[100] T. E. Riley et al. "A *NICER* View of PSR J0030+0451: Millisecond Pulsar Parameter Estimation". In: *Astrophys. J. Lett.* 887.1 (2019), p. L21. DOI: 10.3847/2041-8213/ab481c. arXiv: 1912.05702 [astro-ph.HE].

[101] T. Salmi et al. "The Radius of the High-mass Pulsar PSR J0740+6620 with 3.6 yr of NICER Data". In: *Astrophys. J.* 974.2 (2024), p. 294. DOI: 10.3847/1538-4357/ad5f1f. arXiv: 2406.14466 [astro-ph.HE].

[102] A. J. Dittmann et al. "A More Precise Measurement of the Radius of PSR J0740+6620 Using Updated NICER Data". In: *Astrophys. J.* 974.2 (2024), p. 295. DOI: 10.3847/1538-4357/ad5f1e. arXiv: 2406.14467 [astro-ph.HE].

[103] A. Abac et al. "The Science of the Einstein Telescope". In: (Mar. 2025). arXiv: 2503.12263 [gr-qc].

[104] K. Fukushima, T. Kojo, and W. Weise. "Hard-core deconfinement and soft-surface delocalization from nuclear to quark matter". In: *Phys. Rev. D* 102.9 (2020), p. 096017. DOI: 10.1103/PhysRevD.102.096017. arXiv: 2008.08436 [hep-ph].

[105] K. Masuda, T. Hatsuda, and T. Takatsuka. "Hadron-Quark Crossover and Massive Hybrid Stars with Strangeness". In: *Astrophys. J.* 764 (2013), p. 12. DOI: 10.1088/0004-637X/764/1/12. arXiv: 1205.3621 [nucl-th].

[106] J. I. Kapusta and T. Welle. "Neutron stars with a crossover equation of state". In: *Phys. Rev. C* 104.1 (2021), p. L012801. DOI: 10.1103/PhysRevC.104.L012801. arXiv: 2103.16633 [nucl-th].

[107] L. McLerran and S. Reddy. "Quarkyonic Matter and Neutron Stars". In: *Phys. Rev. Lett.* 122.12 (2019), p. 122701. DOI: 10.1103/PhysRevLett.122.122701. arXiv: 1811.12503 [nucl-th].

[108] T. Zhao and J. M. Lattimer. "Quarkyonic Matter Equation of State in Beta-Equilibrium". In: *Phys. Rev. D* 102.2 (2020), p. 023021. DOI: 10.1103/PhysRevD.102.023021. arXiv: 2004.08293 [astro-ph.HE].

[109] M. Hempel, G. Pagliara, and J. Schaffner-Bielich. "Conditions for Phase Equilibrium in Supernovae, Proto-Neutron and Neutron Stars". In: *Phys. Rev. D* 80 (2009), p. 125014. DOI: 10.1103/PhysRevD.80.125014. arXiv: 0907.2680 [astro-ph.HE].

[110] H. Heiselberg. "Screening in quark droplets". In: *Phys. Rev. D* 48 (1993), pp. 1418–1423. DOI: 10.1103/PhysRevD.48.1418.

[111] D. N. Voskresensky, M. Yasuhira, and T. Tatsumi. "Charge screening at first order phase transitions and hadron quark mixed phase". In: *Nucl. Phys. A* 723 (2003), pp. 291–339. DOI: 10.1016/S0375-9474(03)01313-7. arXiv: nucl-th/0208067.

[112] K. Maslov, N. Yasutake, A. Ayriyan, D. Blaschke, H. Grigorian, T. Maruyama, T. Tatsumi, et al. "Hybrid equation of state with pasta phases and third family of compact stars". In: *Phys. Rev. C* 100.2 (2019), p. 025802. DOI: 10.1103/PhysRevC.100.025802. arXiv: 1812.11889 [nucl-th].

[113] M. Ju, X. Wu, F. Ji, J. Hu, and H. Shen. "Hadron-quark mixed phase in the quark-meson coupling model". In: *Phys. Rev. C* 103.2 (2021), p. 025809. DOI: 10.1103/PhysRevC.103.025809. arXiv: 2102.12276 [nucl-th].

[114] M. G. Alford and S. P. Harris. "Beta equilibrium in neutron star mergers". In: *Phys. Rev. C* 98.6 (2018), p. 065806. DOI: 10.1103/PhysRevC.98.065806. arXiv: 1803.00662 [nucl-th].

[115] M. G. Alford, A. Haber, S. P. Harris, and Z. Zhang. "Beta Equilibrium Under Neutron Star Merger Conditions". In: *Universe* 7.11 (2021), p. 399. DOI: 10.3390/universe7110399. arXiv: 2108.03324 [nucl-th].

[116] B. W. Mintz, E. S. Fraga, G. Pagliara, and J. Schaffner-Bielich. "Nucleation of quark matter in protoneutron star matter". In: *Phys. Rev. D* 81 (2010), p. 123012. DOI: 10.1103/PhysRevD.81.123012. arXiv: 0910.3927 [hep-ph].

[117] M. L. Olesen and J. Madsen. "Nucleation of quark matter bubbles in neutron stars". In: *Phys. Rev. D* 49 (1994), pp. 2698–2702. DOI: 10.1103/PhysRevD.49.2698. arXiv: astro-ph/9401002.

[118] H. Heiselberg, C. J. Pethick, and E. F. Staubo. "Quark matter droplets in neutron stars". In: *Phys. Rev. Lett.* 70 (1993), pp. 1355–1359. DOI: 10.1103/PhysRevLett.70.1355.

[119] K. Iida and K. Sato. "Effects of hyperons on the dynamical deconfinement transition in cold neutron star matter". In: *Phys. Rev. C* 58 (1998), pp. 2538–2559. DOI: 10.1103/PhysRevC.58.2538. arXiv: nucl-th/9808056.

[120] I. Bombaci, G. Lugones, and I. Vidana. "Effects of color superconductivity on the nucleation of quark matter in neutron stars". In: *Astron. Astrophys.* 462 (2007), pp. 1017–1022. DOI: 10.1051/0004-6361:20065259. arXiv: astro-ph/0603644.

[121] I. Vidana, G. Lugones, and I. Bombaci. "Role of color superconductivity on the nucleation of quark matter in neutron stars". In: *J. Phys. G* 35 (2008), p. 014054. DOI: 10.1088/0954-3899/35/1/014054.

[122] T. A. S. d. Carmo, G. Lugones, and A. G. Grunfeld. "Nucleation rate of color superconducting droplets in protoneutron stars". In: *J. Phys. G* 40 (2013), p. 035201. DOI: 10.1088/0954-3899/40/3/035201. arXiv: 1301.3483 [hep-ph].

[123] G. Lugones and I. Bombaci. "Deconfinement and color superconductivity in cold neutron stars". In: *Phys. Rev. D* 72 (2005), p. 065021. DOI: 10.1103/PhysRevD.72.065021. arXiv: astro-ph/0504564.

[124] G. Lugones. "From quark drops to quark stars: some aspects of the role of quark matter in compact stars". In: *Eur. Phys. J. A* 52.3 (2016), p. 53. DOI: 10.1140/epja/i2016-16053-x. arXiv: 1508.05548 [astro-ph.HE].

[125] T. Norsen. "Strangeness nucleation in neutron star matter". In: *Phys. Rev. C* 65 (2002), p. 045805. DOI: 10.1103/PhysRevC.65.045805. arXiv: astro-ph/0201126.

[126] I. Bombaci. "Quark matter nucleation in neutron stars". In: *Int. J. Mod. Phys. D* 19 (2010). Ed. by J. E. Horvath, M. M. B. Malheiro de Oliveira, B. E. J. Bodmann, C. A. Z. Vasconcellos, H. Stoecker, and W. Greiner, pp. 1491–1498. DOI: 10.1142/S0218271810017548.

[127] I. Bombaci, D. Logoteta, P. K. Panda, C. Providencia, and I. Vidana. "Quark matter nucleation in hot hadronic matter". In: *Phys. Lett. B* 680 (2009), pp. 448–452. DOI: 10.1016/j.physletb.2009.09.039. arXiv: 0910.4109 [astro-ph.SR].

[128] I. Bombaci, D. Logoteta, C. Providencia, and I. Vidana. "Effects of quark matter nucleation on the evolution of proto-neutron stars". In: *Astron. Astrophys.* 528 (2011), A71. DOI: 10.1051/0004-6361/201015783. arXiv: 1102.1665 [astro-ph.SR].

[129] I. Bombaci, D. Logoteta, C. Providencia, and I. Vidana. "Evolution of newborn neutron stars: Role of quark matter nucleation". In: *J. Phys. Conf. Ser.* 336 (2011). Ed. by I. Bombaci, A. Covello, L. E. Marcucci, and S. Rosati, p. 012021. DOI: 10.1088/1742-6596/336/1/012021.

[130] I. Bombaci and D. Logoteta. "Quark deconfinement in neutron stars and astrophysical implications". In: *Int. J. Mod. Phys.* 1.02 (2017). Ed. by M. Bianchi, R. T. Jantzen, and R. Ruffini, pp. 904–923. DOI: 10.1142/S021827181730004X.

[131] Z. Berezhiani, I. Bombaci, A. Drago, F. Frontera, and A. Lavagno. "Gamma-ray bursts from delayed quark deconfinement phase transition in neutron stars". In: *Nucl. Phys. B Proc. Suppl.* 113 (2002). Ed. by R. Battiston and F. Cervelli, pp. 268–274. DOI: 10.1016/S0920-5632(02)01851-0.

[132] Z. Berezhiani, I. Bombaci, A. Drago, F. Frontera, and A. Lavagno. "Quark matter formation in neutron stars and implications for gamma-ray bursts". In: *AIP Conf. Proc.* 644.1 (2002). Ed. by S. Costa, A. Insolia, and C. Tuve, pp. 239–246. DOI: 10.1063/1.1523198.

[133] Z. Berezhiani, I. Bombaci, A. Drago, F. Frontera, and A. Lavagno. "Gamma-ray bursts from delayed collapse of neutron stars to quark matter stars". In: *Astrophys. J.* 586 (2003), pp. 1250–1253. DOI: 10.1086/367756. arXiv: astro-ph/0209257.

[134] M. Di Toro, A. Drago, T. Gaitanos, V. Greco, and A. Lavagno. "Testing deconfinement at high isospin density". In: *Nucl. Phys. A* 775 (2006), pp. 102–126. DOI: 10.1016/j.nuclphysa.2006.04.007. arXiv: nucl-th/0602052.

[135] L. P. Csernai and J. I. Kapusta. "Nucleation of relativistic first order phase transitions". In: *Phys. Rev. D* 46 (1992), pp. 1379–1390. DOI: 10.1103/PhysRevD.46.1379.

[136] K. Kajantie and H. Kurki-Suonio. "Bubble Growth and Droplet Decay in the Quark Hadron Phase Transition in the Early Universe". In: *Phys. Rev. D* 34 (1986), pp. 1719–1738. DOI: 10.1103/PhysRevD.34.1719.

[137] R. Cominotti, C. Baroni, C. Rogora, D. Andreoni, G. Guarda, G. Lamporesi, G. Ferrari, et al. "Observation of Temperature Effects on False Vacuum Decay in Atomic Quantum Gases". In: *Phys. Rev. Lett.* 135.18 (2025), p. 183401. DOI: 10.1103/l396-yysb. arXiv: 2504.03528 [cond-mat.quant-gas].

[138] A. Zenesini, A. Berti, R. Cominotti, C. Rogora, I. G. Moss, T. P. Billam, I. Carusotto, et al. "False vacuum decay via bubble formation in ferromagnetic superfluids". In: *Nature Phys.* 20.4 (2024), pp. 558–563. DOI: 10.1038/s41567-023-02345-4. arXiv: 2305.05225 [hep-ph].

[139] M. Guerrini, G. Pagliara, A. Drago, and A. Lavagno. "Deconfinement phase transition in proto-neutron stars: testing the coexistence of strange quark stars and neutron stars". In: *in preparation* ().

[140] E. R. Most, L. Jens Papenfort, V. Dexheimer, M. Hanauske, H. Stoecker, and L. Rezzolla. "On the deconfinement phase transition in neutron-star mergers". In: *Eur. Phys. J. A* 56.2 (2020), p. 59. DOI: 10.1140/epja/s10050-020-00073-4. arXiv: 1910.13893 [astro-ph.HE].

[141] A. Bauswein, N.-U. F. Bastian, D. B. Blaschke, K. Chatziioannou, J. A. Clark, T. Fischer, and M. Oertel. "Identifying a first-order phase transition in neutron star mergers through gravitational waves". In: *Phys. Rev. Lett.* 122.6 (2019), p. 061102. DOI: 10.1103/PhysRevLett.122.061102. arXiv: 1809.01116 [astro-ph.HE].

[142] S. Blacker, N.-U. F. Bastian, A. Bauswein, D. B. Blaschke, T. Fischer, M. Oertel, T. Soultanis, et al. "Constraining the onset density of the hadron-quark phase transition with gravitational-wave observations". In: *Phys. Rev. D* 102.12 (2020), p. 123023. DOI: 10.1103/PhysRevD.102.123023. arXiv: 2006.03789 [astro-ph.HE].

[143] S. Blacker. "Impact of a first-order phase transition on neutron star merger simulations". In: *J. Phys. Conf. Ser.* 1667.1 (2020). Ed. by M. Destefanis, T. Galatyuk, A. Bauswein, C. Ratti, and L. Tolos, p. 012003. DOI: 10.1088/1742-6596/1667/1/012003.

[144] M. Breschi, S. Bernuzzi, F. Zappa, M. Agathos, A. Perego, D. Radice, and A. Nagar. "kiloHertz gravitational waves from binary neutron star remnants: time-domain model and constraints on extreme matter". In: *Phys. Rev. D* 100.10 (2019), p. 104029. DOI: 10.1103/PhysRevD.100.104029. arXiv: 1908.11418 [gr-qc].

[145] A. Bauswein and N. Stergioulas. "Spectral classification of gravitational-wave emission and equation of state constraints in binary neutron star mergers". In: *J. Phys. G* 46.11 (2019), p. 113002. DOI: 10.1088/1361-6471/ab2b90. arXiv: 1901.06969 [gr-qc].

[146] S. Vretinaris, N. Stergioulas, and A. Bauswein. "Empirical relations for gravitational-wave asteroseismology of binary neutron star mergers". In: *Phys. Rev. D* 101.8 (2020), p. 084039. DOI: 10.1103/PhysRevD.101.084039. arXiv: 1910.10856 [gr-qc].

[147] L. R. Weih, M. Hanauske, and L. Rezzolla. "Postmerger Gravitational-Wave Signatures of Phase Transitions in Binary Mergers". In: *Phys. Rev. Lett.* 124.17 (2020), p. 171103. DOI: 10.1103/PhysRevLett.124.171103. arXiv: 1912.09340 [gr-qc].

[148] A. Prakash, D. Radice, D. Logoteta, A. Perego, V. Nedora, I. Bombaci, R. Kashyap, et al. "Signatures of deconfined quark phases in binary neutron star mergers". In: *Phys. Rev. D* 104.8 (2021), p. 083029. DOI: 10.1103/PhysRevD.104.083029. arXiv: 2106.07885 [astro-ph.HE].

[149] Y. Fujimoto, K. Fukushima, K. Hotokezaka, and K. Kyutoku. "Gravitational Wave Signal for Quark Matter with Realistic Phase Transition". In: *Phys. Rev. Lett.* 130.9 (2023), p. 091404. DOI: 10.1103/PhysRevLett.130.091404. arXiv: 2205.03882 [astro-ph.HE].

[150] S. Hensh, Y.-J. Huang, T. Kojo, L. Baiotti, K. Takami, S. Nagataki, and H. Sotani. "Neutron-quark Stars: Discerning Viable Alternatives for the Higher-density Part of the Equation of State of Compact Stars". In: *Astrophys. J. Lett.* 991.1 (2025), p. L12. DOI: 10.3847/2041-8213/ae0031. arXiv: 2407.09446 [astro-ph.HE].

[151] S. Tootle, C. Ecker, K. Topolski, T. Demircik, M. Järvinen, and L. Rezzolla. "Quark formation and phenomenology in binary neutron-star mergers using V-QCD". In: *SciPost Phys.* 13 (2022), p. 109. DOI: 10.21468/SciPostPhys.13.5.109. arXiv: 2205.05691 [astro-ph.HE].

[152] T. Demircik, C. Ecker, M. Järvinen, L. Rezzolla, S. Tootle, and K. Topolski. "Exploring the Phase Diagram of V-QCD with Neutron Star Merger Simulations". In: *EPJ Web Conf.* 274 (2022), p. 07006. DOI: 10.1051/epjconf/202227407006. arXiv: 2211.10118 [astro-ph.HE].

[153] A. Bauswein, R. Oechslin, and H. .-. Janka. "Discriminating Strange Star Mergers from Neutron Star Mergers by Gravitational-Wave Measurements". In: *Phys. Rev. D* 81 (2010), p. 024012. DOI: 10.1103/PhysRevD.81.024012. arXiv: 0910.5169 [astro-ph.SR].

[154] Z. Zhu and L. Rezzolla. "Fully general-relativistic simulations of isolated and binary strange quark stars". In: *Phys. Rev. D* 104.8 (2021), p. 083004. DOI: 10.1103/PhysRevD.104.083004. arXiv: 2102.07721 [astro-ph.HE].

[155] E. Zhou, K. Kiuchi, M. Shibata, A. Tsokaros, and K. Uryu. "Evolution of equal mass binary bare quark stars in full general relativity: Could a supramassive merger remnant experience prompt collapse?" In: *Phys. Rev. D* 106.10 (2022), p. 103030. DOI: 10.1103/PhysRevD.106.103030. arXiv: 2111.00958 [astro-ph.HE].

[156] F. Grippa, A. Prakash, D. Logoteta, D. Radice, and I. Bombaci. "General relativistic hydrodynamic simulations of binary strange star mergers". In: *Phys. Rev. D* 111.8 (2025), p. 083009. DOI: 10.1103/PhysRevD.111.083009. arXiv: 2407.11143 [astro-ph.HE].

[157] E. Zhou, A. Tsokaros, K. Uryu, R. Xu, and M. Shibata. "Differentially rotating strange star in general relativity". In: *Phys. Rev. D* 100.4 (2019), p. 043015. DOI: 10.1103/PhysRevD.100.043015. arXiv: 1902.09361 [astro-ph.HE].

[158] N. Bucciantini, A. Drago, G. Pagliara, S. Traversi, and A. Bauswein. "Formation and evaporation of strangelets during the merger of two compact stars". In: *Phys. Rev. D* 106.10 (2022), p. 103032. DOI: 10.1103/PhysRevD.106.103032. arXiv: 1908.02501 [astro-ph.HE].

[159] I. Sagert, T. Fischer, M. Hempel, G. Pagliara, J. Schaffner-Bielich, A. Mezzacappa, F. .-. Thielemann, et al. "Signals of the QCD phase transition in core-collapse supernovae". In: *Phys. Rev. Lett.* 102 (2009), p. 081101. DOI: 10.1103/PhysRevLett.102.081101. arXiv: 0809.4225 [astro-ph].

[160] S. Chanlaridis, D. Ohse, D. E. Alvarez-Castillo, J. Antoniadis, D. Blaschke, V. Danchev, N. Langer, et al. "Formation of twin compact stars in low-mass X-ray binaries - Implications for eccentric and isolated millisecond pulsar populations". In: *Astron. Astrophys.* 695 (2025), A16. DOI: 10.1051/0004-6361/202452259. arXiv: 2409.04755 [astro-ph.HE].

[161] A. Drago, G. Pagliara, and S. Traversi. "A multi-messenger analysis of neutron star mergers". In: *Mem. Soc. Ast. It.* 89.2 (2018). Ed. by L. Amati, E. Bozzo, M. Della Valle, D. Gotz, and P. O'Brien, pp. 236–244. arXiv: 1802.01696 [astro-ph.HE].

[162] A. Drago, G. Pagliara, S. B. Popov, S. Traversi, and G. Wiktorowicz. "The merger of two compact stars: a tool for dense matter nuclear physics". In: *Universe* 4.3 (2018). Ed. by D. Blaschke, A. Ayriyan, A. Friesen, and H. Grigorian, p. 50. DOI: 10.3390/universe4030050. arXiv: 1802.02495 [astro-ph.HE].

[163] P. Char, A. Drago, and G. Pagliara. "How to Test the Two-Families Scenario". In: *AIP Conf. Proc.* 2127.1 (2019). Ed. by A. Li, B.-A. Li, and F. Xu, p. 020026. DOI: 10.1063/1.5117816. arXiv: 1905.04681 [astro-ph.HE].

[164] J. M. Lattimer. "Neutron Stars and the Nuclear Matter Equation of State". In: *Ann. Rev. Nucl. Part. Sci.* 71 (2021), pp. 433–464. DOI: 10.1146/annurev-nucl-102419-124827.

[165] P. Moller, J. R. Nix, and K. L. Kratz. "NUCLEAR PROPERTIES FOR ASTROPHYSICAL AND RADIOACTIVE-ION-BEAM APPLICATIONS". In: *Atom. Data Nucl. Data Tabl.* 66 (1997), pp. 131–343. DOI: 10.1006/adnd.1997.0746. arXiv: nucl-th/9601043.

[166] P. Jaikumar, A. Semposki, M. Prakash, and C. Constantinou. "g-mode oscillations in hybrid stars: A tale of two sounds". In: *Phys. Rev. D* 103.12 (2021), p. 123009. DOI: 10.1103/PhysRevD.103.123009. arXiv: 2101.06349 [nucl-th].

[167] T. Zhao, C. Constantinou, P. Jaikumar, and M. Prakash. "Quasinormal g modes of neutron stars with quarks". In: *Phys. Rev. D* 105.10 (2022), p. 103025. DOI: 10.1103/PhysRevD.105.103025. arXiv: 2202.01403 [gr-qc].

[168] G. F. Burgio, A. Drago, G. Pagliara, H. .-. Schulze, and J. .-. Wei. "Are Small Radii of Compact Stars Ruled out by GW170817/AT2017gfo?" In: *Astrophys. J.* 860.2 (2018), p. 139. DOI: 10.3847/1538-4357/aac6ee. arXiv: 1803.09696 [astro-ph.HE].

[169] A. W. Steiner, M. Prakash, J. M. Lattimer, and P. J. Ellis. "Isospin asymmetry in nuclei and neutron stars". In: *Phys. Rept.* 411 (2005), pp. 325–375. DOI: 10.1016/j.physrep.2005.02.004. arXiv: nucl-th/0410066.

[170] J. Schaffner, C. B. Dover, A. Gal, C. Greiner, and H. Stoecker. "Strange hadronic matter". In: *Phys. Rev. Lett.* 71 (1993), pp. 1328–1331. DOI: 10.1103/PhysRevLett.71.1328.

[171] J. Schaffner and I. N. Mishustin. "Hyperon rich matter in neutron stars". In: *Phys. Rev. C* 53 (1996), pp. 1416–1429. DOI: 10.1103/PhysRevC.53.1416. arXiv: nucl-th/9506011.

[172] A. Lavagno. "Hot and dense hadronic matter in an effective mean field approach". In: *Phys. Rev. C* 81 (2010), p. 044909. DOI: 10.1103/PhysRevC.81.044909. arXiv: 1004.0822 [nucl-th].

[173] A. Lavagno and D. Pigato. "Strangeness thermodynamic instabilities in hot and dense nuclear matter". In: *Eur. Phys. J. A* 58.12 (2022), p. 237. DOI: 10.1140/epja/s10050-022-00885-6. arXiv: 2301.06909 [nucl-th].

[174] K. Fukushima. "Chiral effective model with the Polyakov loop". In: *Phys. Lett. B* 591 (2004), pp. 277–284. DOI: 10.1016/j.physletb.2004.04.027. arXiv: hep-ph/0310121.

[175] C. Ratti, M. A. Thaler, and W. Weise. "Phases of QCD: Lattice thermodynamics and a field theoretical model". In: *Phys. Rev. D* 73 (2006), p. 014019. DOI: 10.1103/PhysRevD.73.014019. arXiv: hep-ph/0506234.

[176] H. J. Pirner, G. Chanfray, and O. Nachtmann. "A Color Dielectric Model for the Nucleus". In: *Phys. Lett. B* 147 (1984), pp. 249–252. DOI: 10.1016/0370-2693(84)90110-2.

[177] D. Logoteta, I. Bombaci, C. Providencia, and I. Vidana. "A Chiral model approach to quark matter nucleation in neutron stars". In: *Phys. Rev. D* 85 (2012), p. 023003. DOI: 10.1103/PhysRevD.85.023003. arXiv: 1203.4159 [nucl-th].

[178] T. Klahn and T. Fischer. "Vector interaction enhanced bag model for astrophysical applications". In: *Astrophys. J.* 810.2 (2015), p. 134. DOI: 10.1088/0004-637X/810/2/134. arXiv: 1503.07442 [nucl-th].

[179] M. B. Albino, R. Fariello, G. Lugones, and F. S. Navarra. "The sharpness of the quark-hadron transition and the properties of hybrid stars". In: *Int. J. Mod. Phys. D* 34.15 (2025), p. 2550073. DOI: 10.1142/S0218271825500737. arXiv: 2510.02053 [nucl-th].

[180] G. Lugones and A. G. Grunfeld. "Scaling and universality in strange quark stars". In: *Phys. Rev. D* 111.12 (2025), p. 123027. DOI: 10.1103/59d4-4x9m. arXiv: 2503.11515 [nucl-th].

[181] T. Fischer, I. Sagert, G. Pagliara, M. Hempel, J. Schaffner-Bielich, T. Rauscher, F. K. Thielemann, et al. "Core-collapse supernova explosions triggered by a quark-hadron phase transition during the early post-bounce phase". In: *Astrophys. J. Suppl.* 194 (2011), p. 39. DOI: 10.1088/0067-0049/194/2/39. arXiv: 1011.3409 [astro-ph.HE].

[182] A. Schmitt. *Dense matter in compact stars: A pedagogical introduction*. Vol. 811. 2010. DOI: 10.1007/978-3-642-12866-0. arXiv: 1001.3294 [astro-ph.SR].

[183] E. Loffredo, A. Perego, D. Logoteta, and M. Branchesi. "Muons in the aftermath of neutron star mergers and their impact on trapped neutrinos". In: *Astron. Astrophys.* 672 (2023), A124. DOI: 10.1051/0004-6361/202244927. arXiv: 2209.04458 [astro-ph.HE].

[184] G. Guo, G. Martínez-Pinedo, A. Lohs, and T. Fischer. "Charged-Current Muonic Reactions in Core-Collapse Supernovae". In: *Phys. Rev. D* 102.2 (2020), p. 023037. DOI: 10.1103/PhysRevD.102.023037. arXiv: 2006.12051 [hep-ph].

[185] L. D. Landau and E. M. Lifshitz. *Statistical Physics, Part 1*. Vol. 5. Course of Theoretical Physics. Oxford: Butterworth-Heinemann, 1980.

[186] S. Blacker, A. Bauswein, and S. Typel. "Exploring thermal effects of the hadron-quark matter transition in neutron star mergers". In: *Phys. Rev. D* 108.6 (2023), p. 063032. DOI: 10.1103/PhysRevD.108.063032. arXiv: 2304.01971 [astro-ph.HE].

[187] S. Blacker. "Exploring thermal effects in neutron star mergers". PhD thesis. Tech. U., Dortmund (main), 2024. DOI: 10.26083/tuprints-00026530.

[188] M. Herzog and F. K. Ropke. "Three-dimensional hydrodynamic simulations of the combustion of a neutron star into a quark star". In: *Phys. Rev. D* 84 (2011), p. 083002. DOI: 10.1103/PhysRevD.84.083002. arXiv: 1109.0539 [astro-ph.HE].

[189] S. Furusawa, T. Sanada, and S. Yamada. "Hydrodynamical study on the conversion of hadronic matter to quark matter: I. Shock-induced conversion". In: *Phys. Rev. D* 93.4 (2016), p. 043018. DOI: 10.1103/PhysRevD.93.043018. arXiv: 1511.08148 [nucl-th].

[190] A. V. Olinto. "On the Conversion of Neutron Stars Into Strange Stars". In: *Phys. Lett. B* 192 (1987), p. 71. DOI: 10.1016/0370-2693(87)91144-0.

[191] S. Furusawa, T. Sanada, and S. Yamada. "Hydrodynamical study on the conversion of hadronic matter to quark matter. II. Diffusion-induced conversion". In: *Phys. Rev. D* 93.4 (2016), p. 043019. DOI: 10.1103/PhysRevD.93.043019. arXiv: 1511.08153 [nucl-th].

[192] G. E. Brown, V. Thorsson, K. Kubodera, and M. Rho. "A Novel mechanism for kaon condensation in neutron star matter". In: *Phys. Lett. B* 291 (1992), pp. 355–362. DOI: 10.1016/0370-2693(92)91386-N.

[193] A. Gal, E. V. Hungerford, and D. J. Millener. "Strangeness in nuclear physics". In: *Rev. Mod. Phys.* 88.3 (2016), p. 035004. DOI: 10.1103/RevModPhys.88.035004. arXiv: 1605.00557 [nucl-th].

[194] M. Alford, A. Harutyunyan, and A. Sedrakian. "Bulk viscosity from Urca processes: npeμ matter in the neutrino-trapped regime". In: *Phys. Rev. D* 104.10 (2021), p. 103027. DOI: 10.1103/PhysRevD.104.103027. arXiv: 2108.07523 [astro-ph.HE].

[195] J. S. Langer. "Metastable states". In: *Physica* 73.1 (1974), pp. 61–72. DOI: 10.1016/0031-8914(74)90226-2.

[196] E. S. Fraga, M. Hippert, and A. Schmitt. "Surface tension of dense matter at the chiral phase transition". In: *Phys. Rev. D* 99.1 (2019), p. 014046. DOI: 10.1103/PhysRevD.99.014046. arXiv: 1810.13226 [hep-ph].

[197] J. I. Kapusta and C. Gale. *Finite-Temperature Field Theory : Principles and Applications, 2nd edition*. Cambridge University Press, 2007. DOI: 10.1017/9781009401968.

[198] G. Lugones and A. G. Grunfeld. "Surface tension of hot and dense quark matter under strong magnetic fields". In: *Phys. Rev. C* 99.3 (2019), p. 035804. DOI: 10.1103/PhysRevC.99.035804. arXiv: 1811.09954 [astro-ph.HE].

[199] A. G. Grunfeld, M. F. Izzo Villafañe, and G. Lugones. "Surface and Curvature Tensions of Cold, Dense Quark Matter: A Term-by-Term Analysis Within the Nambu–Jona–Lasinio Model". In: *Universe* 11.2 (2025), p. 29. DOI: 10.3390/universe11020029. arXiv: 2407.05606 [nucl-th].

[200] M. G. Alford, K. Rajagopal, S. Reddy, and F. Wilczek. "The Minimal CFL nuclear interface". In: *Phys. Rev. D* 64 (2001), p. 074017. DOI: 10.1103/PhysRevD.64.074017. arXiv: hep-ph/0105009.

[201] L. F. Palhares and E. S. Fraga. "Droplets in the cold and dense linear sigma model with quarks". In: *Phys. Rev. D* 82 (2010), p. 125018. DOI: 10.1103/PhysRevD.82.125018. arXiv: 1006.2357 [hep-ph].

[202] M. B. Pinto, V. Koch, and J. Randrup. "The Surface Tension of Quark Matter in a Geometrical Approach". In: *Phys. Rev. C* 86 (2012), p. 025203. DOI: 10.1103/PhysRevC.86.025203. arXiv: 1207.5186 [hep-ph].

[203] A. Schmitt. "Chiral pasta: Mixed phases at the chiral phase transition". In: *Phys. Rev. D* 101.7 (2020), p. 074007. DOI: 10.1103/PhysRevD.101.074007. arXiv: 2002.01451 [hep-ph].

[204] C. Greiner, P. Koch, and H. Stoecker. "Separation of Strangeness from Antistrangeness in the Phase Transition from Quark to Hadron Matter: Possible Formation of Strange Quark Matter in Heavy Ion Collisions". In: *Phys. Rev. Lett.* 58 (1987), pp. 1825–1828. DOI: 10.1103/PhysRevLett.58.1825.

[205] C. Greiner and H. Stoecker. "Distillation and survival of strange quark matter droplets in ultrarelativistic heavy ion collisions". In: *Phys. Rev. D* 44 (1991), pp. 3517–3529. DOI: 10.1103/PhysRevD.44.3517.

[206] J. I. Kapusta, A. P. Vischer, and R. Venugopalan. "Nucleation of quark - gluon plasma from hadronic matter". In: *Phys. Rev. C* 51 (1995), pp. 901–910. DOI: 10.1103/PhysRevC.51.901. arXiv: nucl-th/9408029.

[207] P. Danielewicz. "TRANSPORT PROPERTIES OF EXCITED NUCLEAR MATTER AND THE SHOCK WAVE PROFILE". In: *Phys. Lett. B* 146 (1984), pp. 168–175. DOI: 10.1016/0370-2693(84)91010-4.

[208] I. M. Lifshits and Y. Kagan. "QUANTUM KINETICS OF PHASE TRANSITIONS AT TEMPERATURES CLOSE TO ABSOLUTE ZERO." In: *Zh. Eksp. Teor. Fiz. 62: No. 1, 385-402(Jan 1972).* (Dec. 1971). URL: https://www.osti.gov/biblio/4691022.

[209] M. Alford and S. Reddy. "Compact stars with color superconducting quark matter". In: *Phys. Rev. D* 67 (2003), p. 074024. DOI: 10.1103/PhysRevD.67.074024. arXiv: nucl-th/0211046.

[210] D. Blaschke, S. Fredriksson, H. Grigorian, A. M. Oztas, and F. Sandin. "The Phase diagram of three-flavor quark matter under compact star constraints". In: *Phys. Rev. D* 72 (2005), p. 065020. DOI: 10.1103/PhysRevD.72.065020. arXiv: hep-ph/0503194.

[211] P. Amore, M. C. Birse, J. A. McGovern, and N. R. Walet. "Color superconductivity in finite systems". In: *Phys. Rev. D* 65 (2002), p. 074005. DOI: 10.1103/PhysRevD.65.074005. arXiv: hep-ph/0110267.

[212] I. Bombaci and B. Datta. "Conversion of neutron stars to strange stars as the central engine of gamma-ray bursts". In: *Astrophys. J. Lett.* 530 (2000), p. L69. DOI: 10.1086/312497. arXiv: astro-ph/0001478.

[213] A. Drago, A. Lavagno, B. Metzger, and G. Pagliara. "Quark deconfinement and the duration of short Gamma Ray Bursts". In: *Phys. Rev. D* 93.10 (2016), p. 103001. DOI: 10.1103/PhysRevD.93.103001. arXiv: 1510.05581 [astro-ph.HE].

[214] I. Bombaci and S. B. Popov. "On the nature of bimodal initial velocity distribution of neutron stars". In: *Astron. Astrophys.* 424 (2004), pp. 627–633. DOI: 10.1051/0004-6361:20041142. arXiv: astro-ph/0405250.

[215] J. A. Pons, S. Reddy, M. Prakash, J. M. Lattimer, and J. A. Miralles. "Evolution of protoneutron stars". In: *Astrophys. J.* 513 (1999), p. 780. DOI: 10.1086/306889. arXiv: astro-ph/9807040.

[216] L. F. Roberts. "A New Code for Proto-Neutron Star Evolution". In: *Astrophys. J.* 755 (2012), p. 126. DOI: 10.1088/0004-637X/755/2/126. arXiv: 1205.3228 [astro-ph.HE].

[217] G. Camelio. "Early evolution of newly born proto-neutron stars". PhD thesis. Rome U., 2017. arXiv: 1801.01350 [gr-qc].

[218] G. Camelio, A. Lovato, L. Gualtieri, O. Benhar, J. A. Pons, and V. Ferrari. "Evolution of a proto-neutron star with a nuclear many-body equation of state: Neutrino luminosity and gravitational wave frequencies". In: *Phys. Rev. D* 96.4 (2017), p. 043015. DOI: 10.1103/PhysRevD.96.043015. arXiv: 1704.01923 [astro-ph.HE].

[219] J. A. Fotakis, M. Greif, C. Greiner, G. S. Denicol, and H. Niemi. "Diffusion processes involving multiple conserved charges: A study from kinetic theory and implications to the fluid-dynamical modeling of heavy ion collisions". In: *Phys. Rev. D* 101.7 (2020), p. 076007. DOI: 10.1103/PhysRevD.101.076007. arXiv: 1912.09103 [hep-ph].

[220] C. L. Fryer, G. Rockefeller, and M. S. Warren. "Snsph: a parallel 3d smoothed particle radiation hydrodynamics code". In: *Astrophys. J.* 643 (2006), pp. 292–305. DOI: 10.1086/501493. arXiv: astro-ph/0512532.

[221] L. Becerra, C. L. Ellinger, C. L. Fryer, J. A. Rueda, and R. Ruffini. "SPH simulations of the induced gravitational collapse scenario of long gamma-ray bursts associated with supernovae". In: *Astrophys. J.* 871.1 (2019), p. 14. DOI: 10.3847/1538-4357/aaf6b3. arXiv: 1803.04356 [astro-ph.HE].

[222] L. M. Becerra, R. Moradi, J. A. Rueda, R. Ruffini, and Y. Wang. "First minutes of a binary-driven hypernova". In: *Phys. Rev. D* 106.8 (2022), p. 083002. DOI: 10.1103/PhysRevD.106.083002. arXiv: 2208.03069 [astro-ph.HE].

[223] L. M. Becerra, F. Cipolletta, C. L. Fryer, D. P. Menezes, C. Providência, J. A. Rueda, and R. Ruffini. "Occurrence of Gravitational Collapse in the Accreting Neutron Stars of Binary-driven Hypernovae". In: *Astrophys. J.* 976.1 (2024), p. 80. DOI: 10.3847/1538-4357/ad82ea. arXiv: 2409.05767 [astro-ph.HE].

[224] C. L. Fryer, S. Andrews, W. Even, A. Heger, and S. Safi-Harb. "Parameterizing the Supernova Engine and Its Effect on Remnants and Basic Yields". In: *Astrophys. J.* 856.1 (2018), p. 63. DOI: 10.3847/1538-4357/aaaf6f. arXiv: 1712.03415 [astro-ph.HE].

[225] A. Heger and S. E. Woosley. "Nucleosynthesis and Evolution of Massive Metal-Free Stars". In: *Astrophys. J.* 724 (2010), pp. 341–373. DOI: 10.1088/0004-637X/724/1/341. arXiv: 0803.3161 [astro-ph].

[226] F. Cipolletta, C. Cherubini, S. Filippi, J. A. Rueda, and R. Ruffini. "Fast Rotating Neutron Stars with Realistic Nuclear Matter Equation of State". In: *Phys. Rev. D* 92.2 (2015), p. 023007. DOI: 10.1103/PhysRevD.92.023007. arXiv: 1506.05926 [astro-ph.SR].

[227] N. Stergioulas and J. L. Friedman. "Comparing models of rapidly rotating relativistic stars constructed by two numerical methods". In: *Astrophys. J.* 444 (1995), p. 306. DOI: 10.1086/175605. arXiv: astro-ph/9411032.

[228] L. Becerra, C. L. Bianco, C. L. Fryer, J. A. Rueda, and R. Ruffini. "On the induced gravitational collapse scenario of gamma-ray bursts associated with supernovae". In: *Astrophys. J.* 833.1 (2016), p. 107. DOI: 10.3847/1538-4357/833/1/107. arXiv: 1606.02523 [astro-ph.HE].

[229] L. Becerra, M. M. Guzzo, F. Rossi-Torres, J. A. Rueda, R. Ruffini, and J. D. Uribe. "Neutrino Oscillations Within the Induced Gravitational Collapse Paradigm of Long Gamma-Ray Bursts". In: *Astrophys. J.* 852.2 (2018), p. 120. DOI: 10.3847/1538-4357/aaa296. arXiv: 1712.07210 [astro-ph.HE].

[230] T. Hinderer. "Tidal Love numbers of neutron stars". In: *Astrophys. J.* 677 (2008). [Erratum: Astrophys.J. 697, 964 (2009)], pp. 1216–1220. DOI: 10.1086/533487. arXiv: 0711.2420 [astro-ph].

[231] T. Hinderer, B. D. Lackey, R. N. Lang, and J. S. Read. "Tidal deformability of neutron stars with realistic equations of state and their gravitational wave signatures in binary inspiral". In: *Phys. Rev. D* 81 (2010), p. 123016. DOI: 10.1103/PhysRevD.81.123016. arXiv: 0911.3535 [astro-ph.HE].

[232] E. E. Flanagan and T. Hinderer. "Constraining neutron star tidal Love numbers with gravitational wave detectors". In: *Phys. Rev. D* 77 (2008), p. 021502. DOI: 10.1103/PhysRevD.77.021502. arXiv: 0709.1915 [astro-ph].

[233] K. S. Thorne. "Tidal stabilization of rigidly rotating, fully relativistic neutron stars". In: *Phys. Rev. D* 58 (1998), p. 124031. DOI: 10.1103/PhysRevD.58.124031. arXiv: gr-qc/9706057.

[234] S. M. Johns, P. J. Ellis, and J. M. Lattimer. "Numerical approximation to the thermodynamic integrals". In: *Astrophys. J.* 473 (1996), pp. 1020–1028. DOI: 10.1086/178212. arXiv: nucl-th/9604004.